UNIVERSITY OF BIRMINGHAM

PLASTIC DEFORMATION OF Ti-6Al-4V AT SMALL SCALE: A MICROSTRUCTURAL AND MECHANISTIC STUDY

By

Rayan Basheer Mohammed Ameen

A thesis submitted to the University of Birmingham

for the degree of Doctor of Philosophy

School of Metallurgy and Materials

University of Birmingham

March 2017

Abstract

Two phase alpha/beta titanium alloys are used in a wide variety of applications such as aerospace, biomedical, gas turbine engine, sport and energy. These alloys have high specific strength and specific modulus as compared to magnesium and aluminium alloys as well as excellent corrosion resistance. The Ti-6Al-4V (α+β) alloy is the most widely used and the best known of all the Ti alloys. Although there are a number of observations in the literature reporting the mechanical responses of these two phase alloys, there exists very little understanding of the mechanisms of the individual phases and the alpha/beta interface's role in strengthening. Additionally, it has often been reported in the literature that 'smaller is stronger' for different metals due to the presence of a size effect. There is no real understanding of the mechanism of the size effect in the alpha-beta titanium and HCP and its dependence on orientation.

Single alpha, beta and alpha-beta colony micro-pillars have been manufactured from a polycrystalline commercial Ti-6Al-4V sample using Focused Ion Beam (FIB). Alpha/beta pillar contained two alpha lamellae separated by a thin fillet of beta phase. A nano-indenter was then used to conduct uniaxial micro-compression tests on Ti alloy single crystals, using a diamond flat tip as a compression platen.

By controlling the crystal orientation along the micro-pillar using Electron Back Scattering Diffraction (EBSD) different slip systems have been selectively activated. The advantage of the micro-compression method over conventional mechanical testing techniques is the ability to localize a single crystal volume which is characterisable after deformation.

This study makes a contribution to knowledge in several key areas, including an understanding of the mechanical response of different crystals at micro/submicro-scale, the

effect of phase interfaces on deformation, and an understanding of the strengthening mechanism in two-phase Ti alloys, the orientation size effect in HCP metals and the CRSSs for each phase in Ti-6Al-4V. Therefore, in order to evaluate the behaviour of these alloys for future applications, it is imperative that the microstructural features and characteristics be quantified and examined on a small scale.

The results showed that the beta phase in between alpha lamellae caused strengthening deformation. When the surface normal is parallel to the [0001] of the single alpha crystal, the material deforms with difficulty in the [0001] direction of the single alpha phase.

The mechanical responses of the alpha, beta, and alpha/beta crystals not only depended on the size of the pillars, but also on the crystallographic orientation, the initial dislocation density and the relationship between the two phases in the case of α/β crystals.

Extensive electron microscopy investigation revealed that the anisotropy in basal and prismatic slip systems can be directly correlated with the transmission of dislocations across the single crystal, the beta laths, and the accumulation of residual dislocation content near the interfaces and in the single beta phase. This information is essential in order to better model mechanical deformation in these materials. In addition, dislocation analysis indicated that the deformation of individual grains conformed to the Schmid factor (SF) analysis where slip primarily occurs on those slip systems where the resolved shear stress (SF) values are highest.

The results presented in this thesis bring to light several concerns for designing with titanium alloys and identify a number of phenomena of strong scientific interest. They will allow for the development of realistic models for the mechanical behaviour and provide a comprehensive analysis that can contribute to the theoretical development of the design and enhancement of the titanium allows. Moreover, the role of crystallography in plastic

deformation provides a novel insight into the nature of the orientation size effect in HCP. This work points towards the need for further investigations into the higher and lower temperature deformation behaviour of Ti-64 to fully understand the phenomena identified within this study.

ACKNOWLEDGEMENTS

I am sincerely grateful to my supervisors, Prof. Ian Jones, for his guidance, research support, and encouragement during this research project. His foresight and suggestions towards research lead me into not only the field of metallurgy and microscopy but also the whole world of materials science and research. Above all at a personal level he has always treated me with great kindness and I respect him for everything that I have learnt from him.

Next, I would like to thank my Co-Supervisor Dr. Yu-Lung Chiu for his timely and untiring guidance towards my work.

I would also like to extend my sincere gratitude to Prof. Michael Loretto and Dr Rengen Ding for their inspiring discussions and valuable thoughts on the project.

Thanks to all my colleagues and friends in the department of materials science and engineering.

I would like to give my special thanks to my family for their patience and encouragement. In particular, I would like to thank my wife who always gave me her support and understanding during my studies.

Financial support from the Kurdistan Regional Government / HCDP programme is gratefully acknowledged.

This thesis is dedicated to

my father Basheer and my mother Fattima

my wife Dilveen and

my lovely kids Shayan & Shadiyar.

1. Contents

Chapter One

1.1. Introduction

Two phase alpha/beta titanium alloys are used in a variety of aerospace, energy, marine, sports and biomedical applications. Titanium alloys are attractive for these applications because of their high specific modulus and specific strength as compared to other ferrous and non-ferrous materials (e.g Mg and Al alloys), high melting point and low density as well as excellent corrosion resistance [1].

Recently, the widespread availability of focussed ion beam (FIB) microscopy has made micro scale mechanical testing a practicable option [2–6]. Quantifying the stress-strain behaviour of micro-scale specimens is a challenge. Indentation techniques have been developed that enable the measurement of strength. A micro-pillar compression test is a novel way to measure the mechanical properties of materials. Micro-compression testing, particularly *in-situ* is attractive due to its ability to probe localized material properties (i.e. measure the 'single-crystal' response of individual colonies and grains in a polycrystalline material) and to search for intrinsic size effects [6].

Over the past two decades, an increase in the flow strength of a material is often reported for small scale tests due to size effects on plasticity [6–10]. However, there is no real understanding of the mechanism of plasticity at the micro-scale, especially in HCP metals. Most studies concentrate on BCC [9] and FCC [5,11], although a few studies have been

carried out to investigate the properties of HCP metals [12]. Also, no studies have been carried out on the effect of micro-scale crystal orientation for HCP.

Although, a number of papers in the literature have tried to determine the influence of the alpha/beta microstructural features on the mechanical properties of titanium alloys [2–4,13,14], there still exists little understanding of the mechanisms of strengthening in these alloys, and most of these microstructural (alpha and beta) features directly influence each other. Due to these interrelationships, it is essential to study individual microstructural features in order to investigate accurately the alpha/beta interface effect on mechanical properties. Especially, in the light of the uncertainty in the CRSS values in the Ti alloys, measuring micromechanical parameters on cubic (BCC) and non-cubic (HCP) metals utilising customary single-crystal methodologies would appear attractive.

Since the alpha/beta interfaces must play a significant role in the mechanical behaviour, it is of critical importance to characterize the constitutive behaviour of the colonies as a function of the operative slip system [14–17]. This work attempts to investigate the micromechanical properties and the effect of alpha/beta interfaces on the deformation behaviour due to the relative misalignment of the slip systems in the alpha and the beta phases and the differences in the lengths of the Burgers vector in the two phases. Micromechanical properties for Ti-64 from each of the two categories (alpha single crystal and alpha/beta/alpha tri-crystal) were studied on a micron size scale to determine if orientation and size effect exists in HCP.

Extensive scanning electron microscopy (SEM) investigation is essential in order to understand the functional dependencies of mechanical properties on the microstructural

features of a specimen undergoing a micro-compression test for several different orientations of crystal. SEM investigation provides insight into the observed anisotropy in resolving shear stress and strength behaviour. Qualitatively these results can be explained on the basis of the Burgers orientation relationship which is obeyed in these alloys.

Furthermore, detailed transmission electron microscopy (TEM) investigations of the dislocation structures in these deformation microsamples and the slip transmission mechanisms, in particular slip transmission through alpha/beta boundaries of Ti6Al4V at a small scale and at several orientations have been carried out.

The dissertation is organized into nine chapters.

The current understanding of Ti alloys is presented in Chapter Two. A review of the current understanding of the microstructure, slip behaviour, crystallographic information, mechanical properties and size effects is given.

Chapter Three covers the experimental methods employed: heat treatment, sample preparation (micro-pillars and TEM sample from pillar), scanning electron microscopy (SEM), energy dispersive X-ray spectroscopy (EDS), electron backscattered diffraction (EBSD), focused ion beam (FIB), transmission electron microscopy (TEM) and *in-situ* nano-indentation.

Chapter Four covers the micro-mechanical properties of three different orientations in Ti-64. The influence of initial crystal orientation and specimen geometry on deformation behaviour was observed in alpha/beta/alpha tri-crystal and single alpha and beta crystals.

Chapter Five describe the SEM observations of the deformed micropillars.

Chapter Six focuses on the TEM observations of slip nucleation, propagation and transmission through the α/β interfaces in the basal and pyramidal orientations.

Chapter Seven discusses the microscopic features of deformation in these colonies which were characterized using scanning electron microscopy (SEM), focussed ion beam (FIB) and transmission electron microscopy (TEM). The various factors contributing to the different interface resistances to slip transmission in the single colony and triple colonies crystals are analysed and discussed.

Chapter Eight summarizes results gained throughout this research, and draws important conclusions.

The last chapter (Chapter Nine) presents perspectives for future work.

Chapter Two

2. Literature Review

2.1. History of titanium and titanium alloys

Titanium is the fourth most abundant structural metal, constituting about 0.62 % of the earth's crust, following aluminium, iron and magnesium [18]. In the natural state titanium occurs mostly in the form of oxides: ilmenite ($FeTiO_3$) and rutile (TiO_2). Titanium metal was first discovered in 1791 by chemist William Gregor in the dark magnetic sand ilmenite. The analysis of rutile and identification of it as an oxide of an unknown element was first achieved by the German chemist Klaproth in 1795 [19], who named the element titanium after the Titans, of Greek mythology. Many efforts were made to separate the metal from oxygen and nitrogen, in order to develop cost-effective commercially available titanium metal but this proved difficult. The first commercial process to produce titanium was developed by Krolls in Luxembourg 1937-1940 [19]. Krolls demonstrated that the reduction of titanium tetrachloride with magnesium in an inert gas atmosphere could be used to extract titanium commercially. Interest in this metal and its alloys began commercially after the Second World War, due to their excellent properties: for instance they have relatively high strength and low density, good corrosion and erosion resistance and remarkable oxidation resistance, and there has been high demand since for the manufacture of critical components in the aerospace and chemical industries.

2.2. **Physical metallurgy of titanium and titanium alloys**

Titanium is a chemical element with atomic number 22 [1]. It has an incomplete 3d orbital and easily forms solid solutions with many substitional elements having atomic diameter within ±20 % of that of titanium [18]. In addition, titanium is an allotropic element with more than one crystallographic form. Pure titanium has a hexagonal closed packed (hcp) crystal structure, stable at low temperature. This structure is called the alpha phase (α-phase) (space group: $P6_3mmc$). The lattice parameters of pure α-Titanium 'a' and 'c' are 0.295 nm and 0.468 nm respectively (Figure 2-1a). Therefore, the c/a ratio is 1.587, which is low compared with the ideal value of 1.633 for the HCP crystal structure [2,4].

Different HCP metals deform via different deformation modes which depend on the c/a ratio and strongly influence texture development[1,19,21]. Body centred cubic (bcc) crystal structure (space group: $Im\bar{3}m$) β phase exists above ~882ºC which is called the beta-transus temperature. The lattice parameter of pure β-titanium, 'a' is 0.332 nm (Figure 2-1b). The crystal structure of beta phase has more symmetry than the α phase. Therefore, it has a larger configuration entropy, which leads it to be the more stable phase at high temperature. The two phases have different properties, given their structures. The β-transus temperature is the limiting temperature between the two phases. It may be adjusted through the addition of alloying elements. The β-phase remains stable up to its melting point of about 1670°C [1,19,21].

As is obvious from Figure 2-1, the hcp structure of the α phase is considerably more anisotropic than the bcc structure of the high temperature β phase, which leads to the anisotropic elastic behaviour of single crystals of α titanium. When a stress is applied parallel to the c-axis, Young's modulus takes its highest possible value of 145 GPa; the smallest value of Young's modulus (100 GPa) is achieved when the stress direction is perpendicular to c as illustrated in Figure 2-2 [2,4].

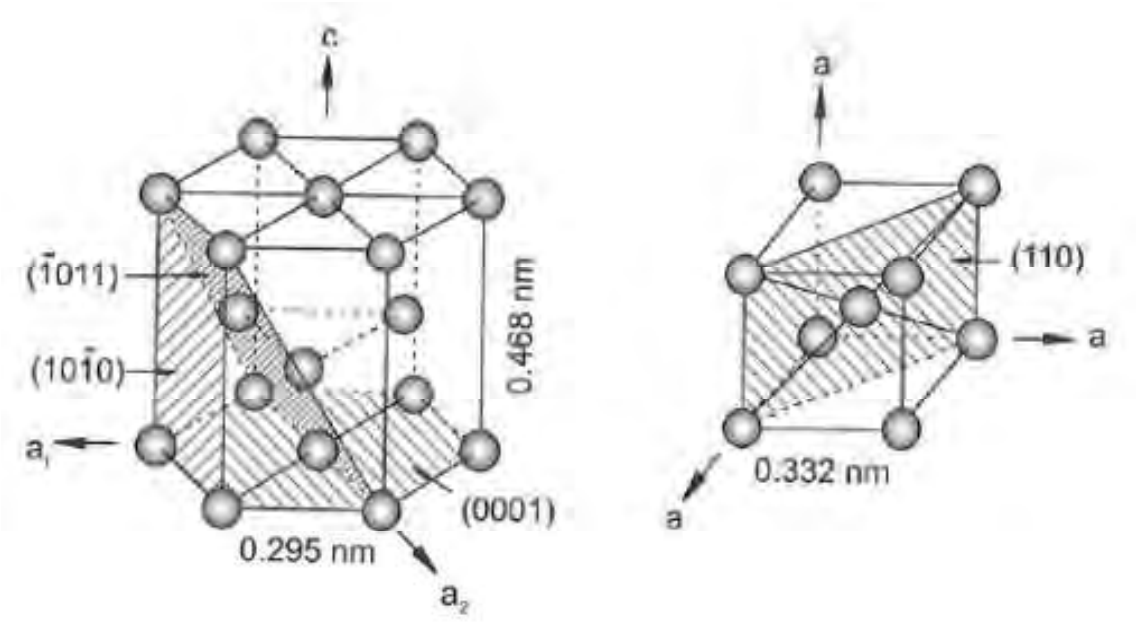

Figure 2-1 The crystal structure of (a) α- phase and (b) β-phase [19].

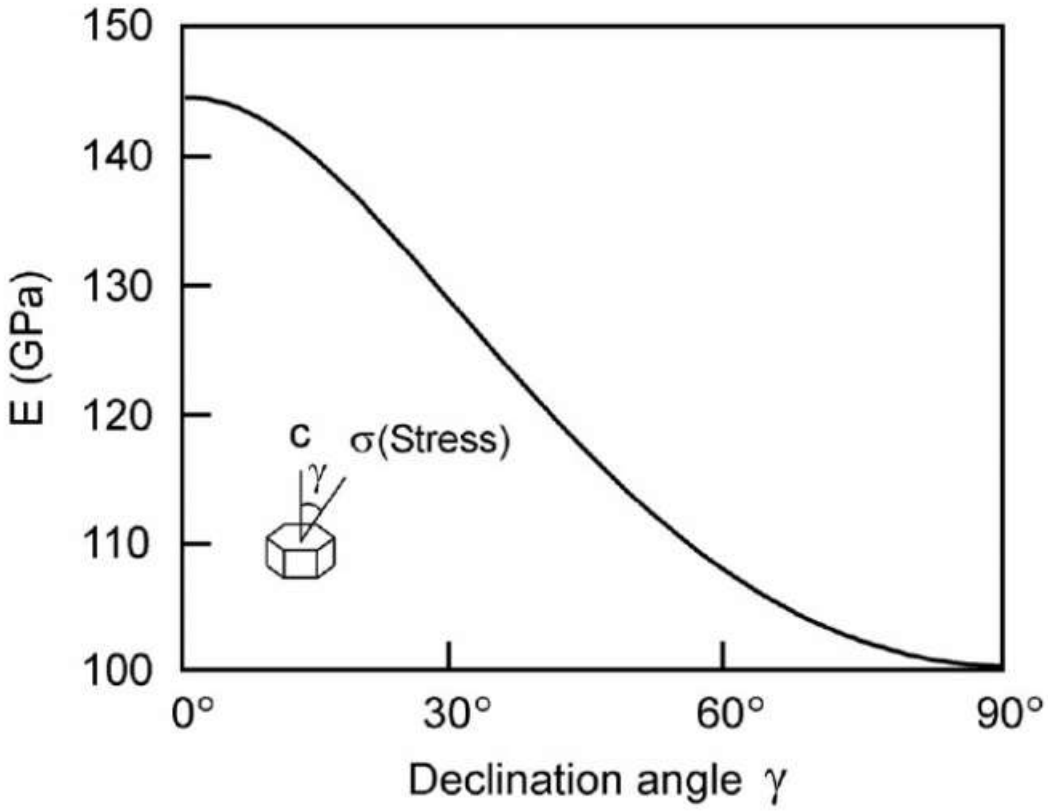

Figure 2-2 The anisotropic elastic behaviour of α phase for different declination angles [2].

2.3. **Applications and Properties of Titanium and Titanium Alloys**

Titanium and its alloys constitute one of the major groups of commercial metals. Titanium is often chosen for its high temperature mechanical properties, low density and good corrosion resistance and as a result is used in the aerospace, chemical processing and power generation industries, marine and offshore applications and medical implants [1]. Titanium and its alloys are also used for jewellery, sports and leisure. However, the strength of titanium decreases

significantly when it is heated above 430 °C. Titanium is fairly hard, non-magnetic and a poor conductor of heat and electricity. It has a lower coefficient of thermal expansion than steel and less than half that of aluminium. Titanium and its alloys have a fairly high melting point. Titanium's melting temperature is higher than those of steel and aluminium, which often makes it the material of choice over steels and aluminium [22]. Titanium has strong passivation tendencies which impart a high degree of resistance to attack by most mineral acids and chlorides. Titanium and many of its alloys are nontoxic, which helps them to be compatible with human tissue and bone. Titanium is available in all mill product forms, including castings, sheet, tube, wrought plate wire and bar as shown in Figure 2-3 (typical applications of titanium alloys).

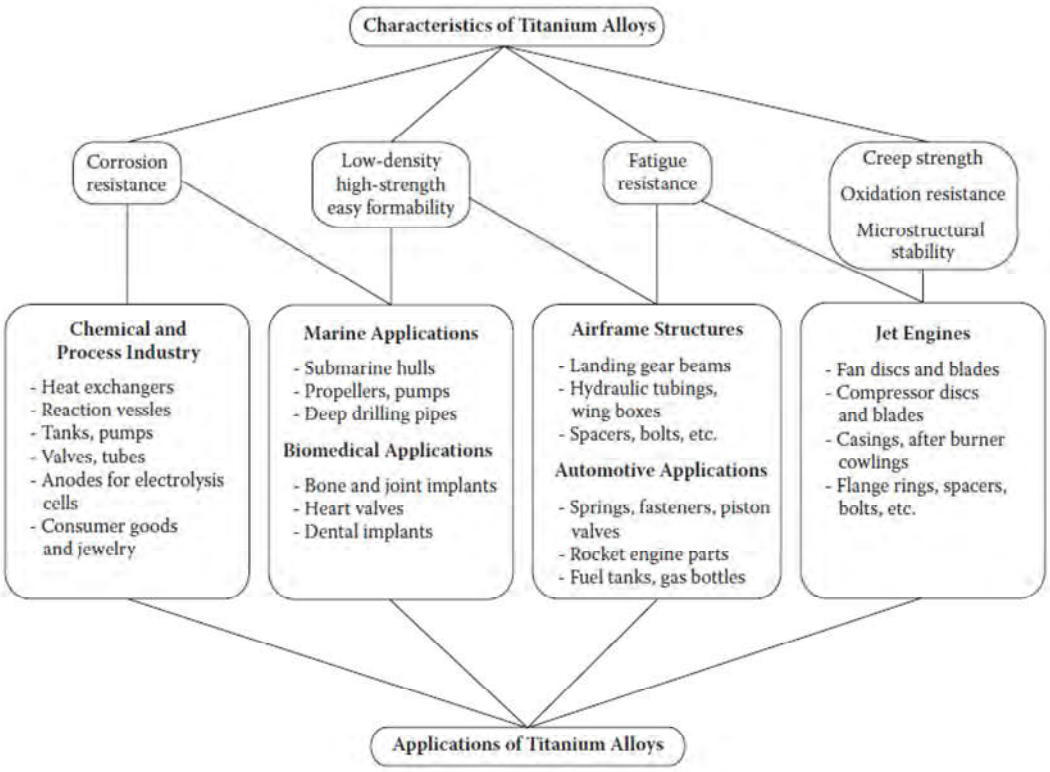

2.4. **Stabilization of Phases**

Alloying elements can be categorized according to their effect on the stabilities of the α and β phases [2] and therefore alloying elements are classified as raising the transformation temperature, thereby stabilizing the α phase (α-stabilizers), or lowering the transformation temperature, thereby stabilizing the β phase (β-stabilizers) or neutral if they do not specifically stabilize either the α or β phase [3,2,5].

2.4.1. Alpha Stabilizing Elements

α-stabilizers are those elements which increase the beta transus temperature by stabilizing the alpha phase. The elements aluminium (Al), oxygen (O), nitrogen (N) and carbon (C) are strong α stabilizing elements. Aluminium (Al) is one of the most widely used alloying elements; it is the only common metal that can raise the transition temperature exhibiting a significant solid solubility in the α phase in two phase microstructures. The structure of Al at room temperature, for example, is FCC, alpha phase which has the same packing fraction and coordination number as HCP, the structure of α titanium.

2.4.2. Beta Stabilizing Elements

β-stabilizing elements decrease the beta transus temperature by stabilizing the beta phase. Examples include vanadium (V), molybdenum (Mo), tantalum (Ta), iron (Fe) and niobium (Nb). All have body centered cubic structures at room temperature and they extend the β-phase field to lower temperatures. Generally, β stabilizers are chosen because they lower the β transus temperature and do not readily promote the formation of metastable phases. β stabilizing elements are categorized as being β-isomorphous or β-eutectoid elements, depending on whether or not a solid solution or eutectoid compound exists [1].

2.4.2.1. Isomorphous β Stablizing Elements

The β isomorphous stabilizing elements in titanium alloys decrease the β transus temperature. β isomorphous stabilizing elements, such as vanadium (V), molybdenum (Mo) and niobium (Nb) in sufficient concentration enable the β phase to be stabilized to room temperature. Tantalum (Ta) and rhenium (Re) also belong to this group, but they are not very commonly used owing to their high density [1,19,20]. β isomorphous stabilizing elements are preferred for alloying in order to improve hardenability and enhance heat treatment response, for example vanadium (V) and molybdenum (Mo).

2.4.2.2. Eutectoid β Stabilizing Elements

The most commonly used and preferred eutectoid β stabilizing elements in titanium alloys are iron (Fe), silicon (Si) and chromium (Cr) plus certain elements, including nickel (Ni),

manganese (Mn), copper (Cu), palladium (Pd), tungsten (W), and bismuth (Bi). There are some other β eutectoid forming elements, which are not used as alloying elements in titanium, such as cobalt (Co), platinum (Pt), gold (Au), silver (Ag), beryllium (Be) and uranium (U) [19]. With an increase in group number the eutectoid temperature increases, while maximum solubility in β titanium decreases [1].

2.4.3. Neutral

There has been a growing interest in using neutral elements such as zirconium and tin as alloying elements for a wide range of applications. Although they have a slight effect only on the transformation temperature in titanium, they have a high solubility in the α phase and can strengthen it [1,19,20]. The effects of these various elements on titanium phase diagrams can be found in Figure 2-4.

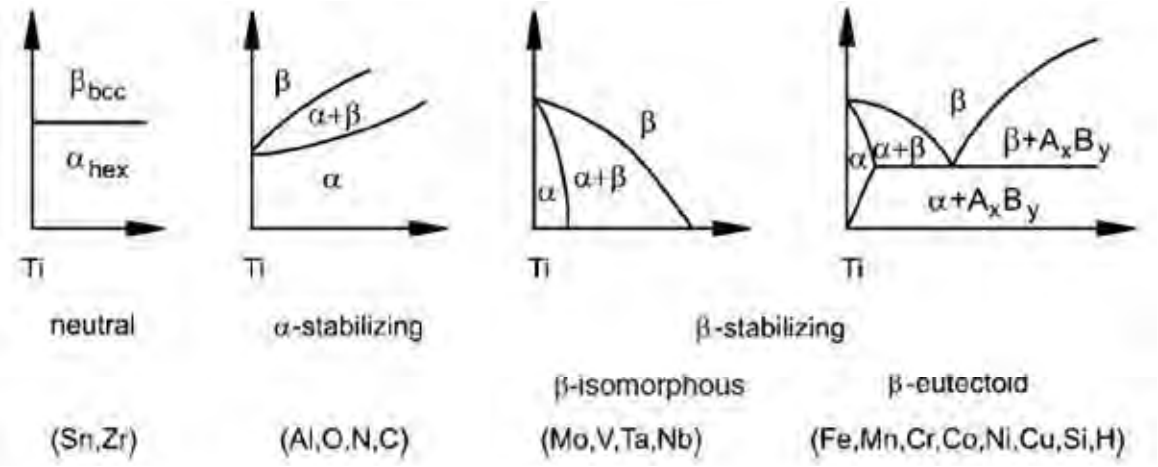

Consequently, according to the alloying element addition, titanium alloys are classified into five categories: α-alloys, near α-alloys, α + β alloys, metastable β-alloys and β-alloys.

2.5. Classification of titanium alloys

The attributes of titanium alloys of main importance to the design engineer are outstanding corrosion resistance, excellent erosion resistance, superior strength-to-weight ratio, low thermal expansion co-efficient, non-magnetic character, fire resistance and short radioactive half-life.

2.5.1. Alloy Classification

The foundation for identifying the classes of titanium alloys are the HCP and BCC crystal structures [19]: the dominant phase of the alloy determines the categorization.

2.5.1.1. Alpha Alloys

Alpha alloys contain entirely α stabilizer which raises the beta transus temperature of the alloy so that the alpha phase is stable to higher temperatures. Alpha alloys have α as their major phase at low temperatures [20]. Alpha alloys are single phase and, therefore, cannot be heat-treated to develop a variety of microstructures and mechanical property combinations [1,21]. The α titanium alloys have medium strength and relatively good creep resistance and

toughness. To strengthen α alloys there are relatively few mechanisms available and, therefore, practically, the extent of their usage is limited [19]. Some mechanisms to strengthen α alloys are grain size strengthening, solid solution strengthening by interstitial and substitutional elements, precipitation hardening by α_2 phase formation and texture strengthening [19]. Alpha alloys are quite stable until 650°C and resist corrosion up to 1100°C, that is they are used in applications where corrosion resistance and weldability are desired properties [23].

2.5.1.2. Near α Alloys

The addition of small amounts (about 1 to 2 wt. %) of β stabilizer leads to near α alloys. The microstructure is similar to that in α+β alloys, but they are primarily α alloys and are more like α alloys than α+β alloys [20]. Since near α alloys contain some β stabilizers, the strength and workability can be improved and they are preferred for elevated temperature applications up to about 600°C [1].

2.5.1.3. Metastable β alloys

These alloys contain 10 to 15% of β stabilizer; β phase is retained in a metastable state at room temperature. These alloys can not only offer high specific strength and good cold formability, since they contain small amounts of α stabilizer element, but have also been specially designed for improved burn resistance and oxidation resistance. They have formability over a wide range of temperatures [1].

2.5.1.4. β alloys

With the addition of large amounts (30%) of β stabilizer, β phase is retained at room temperature as a stable phase [21]. Typically, these alloys are fully heat treatable, weldable and capable of high strength, with excellent formability in the solution treated condition [1] .

2.5.1.5. Alpha + Beta Alloys

As can be seen from their names, the α+β titanium alloys usually contain both α and β phases at room-temperature in equilibrium. They combine the strength of the α phase with the ductility of the β phase [20]. The microstructure and properties of these alloys are susceptible to heat treatment, resulting in a wide range of microstructure and mechanical property combinations. These alloys can be processed to maximize strength through grain boundary strengthening and solution treatment plus aging [21]. They are limited to a maximum temperature of about 300°C. These alloys, which account for about half of all the titanium that is produced are widely used in engineering applications and the most common example is Ti-6Al-4V. Figure 2-5 shows a schematic three-dimensional phase diagram to classify titanium alloys.

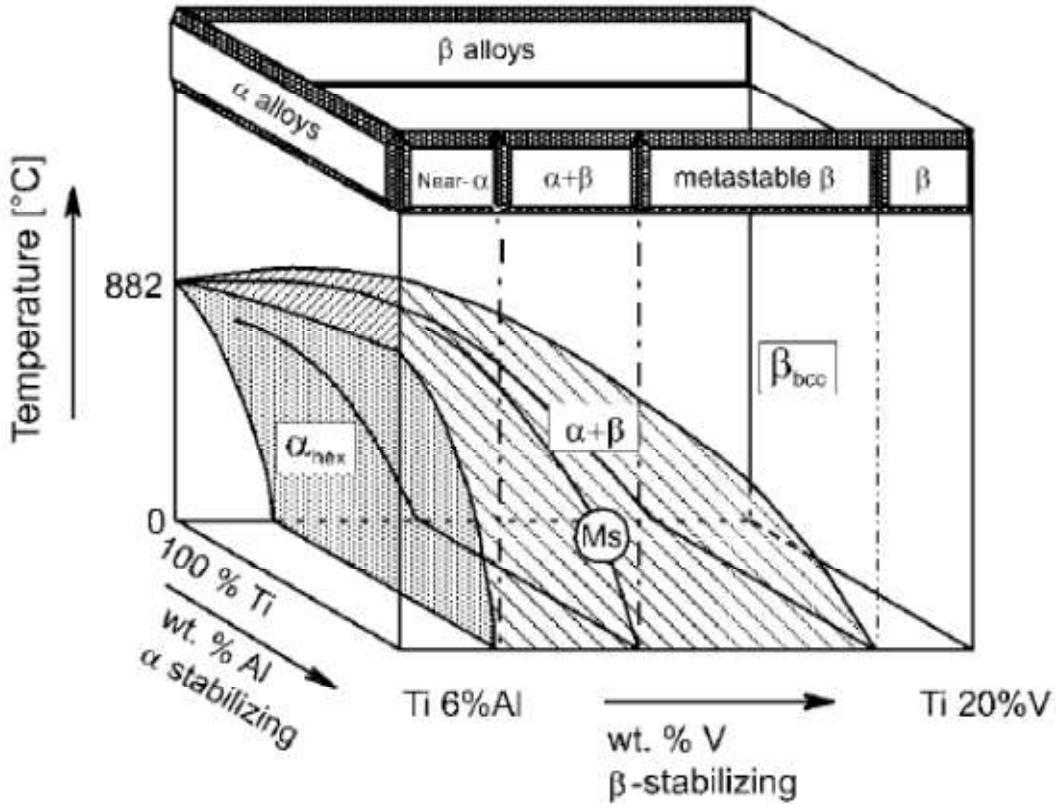

Figure 2-5 Three-dimensional phase diagram to classify Ti alloys (schematically) [20]**.**

Besides these two phases, other phases can be observed in titanium alloys, depending on the thermo mechanical treatment.

2.5.1.5.1. Martensite (α')

This martensite product is usually hexagonal close packed. α' is a non-equilibrium phase. This phase is obtained when the alloy is quenched from the body centred cubic (BCC) β phase

region: a part of the β-phase will transform to α'. Martensite produced by quenching increases with decreasing beta-stabilizing alloy content.

2.5.1.5.2. Orthorhombic martensite (α")

α'' martensite has an orthorhombic structure. It is another non-equilibrium phase. With increasing β stabilizer, there is an increasing tendency for this phase to form in preference to α'. α'' is the result of quenching the β phase (below ~900°C). Because the atoms will not have enough time to rearrange, the β-phase will either remain in its metastable state or transform to soft α''. In addition, orthorhombic martensite is softer than hexagonal close packed martensite [21].

2.5.1.5.3. Omega (ω)

The presence of oxygen prevents the formation of omega phase in Ti alloys. It is impossible to observe ω phase in Ti6Al4V. However, ω phase can occur when the β phase contains more than 15% of vanadium during aging between 200°C and 350°C or during room temperature aging in rapidly solidified material [24].

2.6. Microstructure of Ti Alloys

In Ti (α+β) alloys three different classes of microstructures can be roughly distinguished: lamellar microstructure, bimodal microstructure and equiaxed microstructure. In general, the

different microstructures are generated by appropriate heat treatment and thermomechanical processing.

2.6.1. Fully Lamellar Microstructure

During transformation the β phase field usually consists of large prior β grains in which α phase grows on cooling, usually as laths or plates. The resultant microstructure is referred to as 'lamellar' and these plate-like precipitates are also called α laths as shown in Figure 2-6. The lamellar microstructure can be achieved easily by cooling through the beta-transus temperature at intermediate rate (air-cooling) or slow rate (furnace-cooling). The beta phase transforms by diffusion-controlled partitioning of alpha-stabilizing alloy elements into alpha lamellae and beta-stabilizing elements into the remaining volume. The α phase grows faster along these planes away from the β grain boundaries because of the low interfacial energy on certain atomic planes.

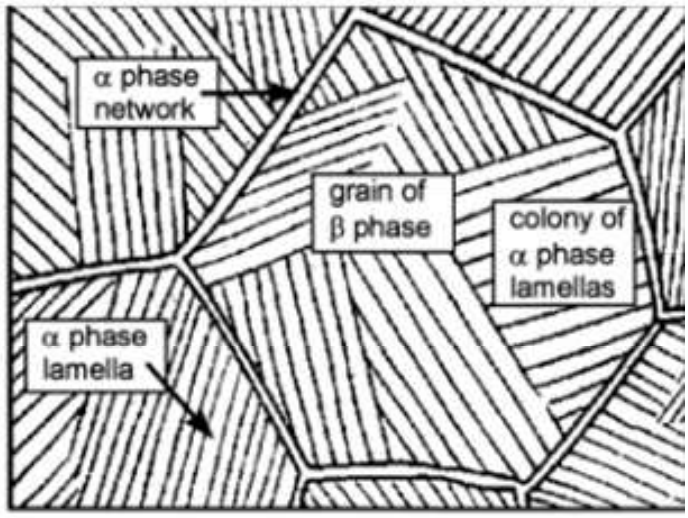

Figure 2-6 Schematic representation of α+β titanium alloys [25]

According to the Burgers orientation relationship the alpha-phase lamellar microstructures have orientations that are related to the beta phase while the beta-phase regions have the same crystal orientation as the original large beta grains as depicted in Figure 2-7.

As a result, colonies within a prior beta grain can be generated in 12 possible different orientations. These α colonies with multiple orientations often have a Widmanstätten structure or "basketweave" characteristic as illustrated in Figure 2-8. This structure has low ductility and intermediate strength with relatively good creep resistance and fracture toughness.

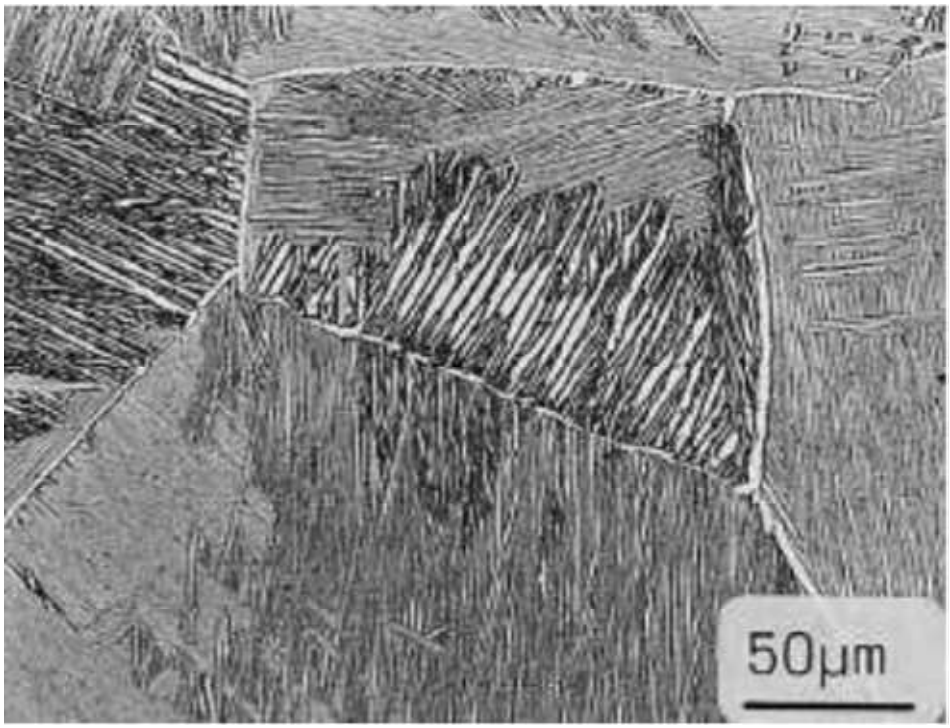

Figure 2-7 Typical SEM images of a fully lamellar microstructure [26]**.**

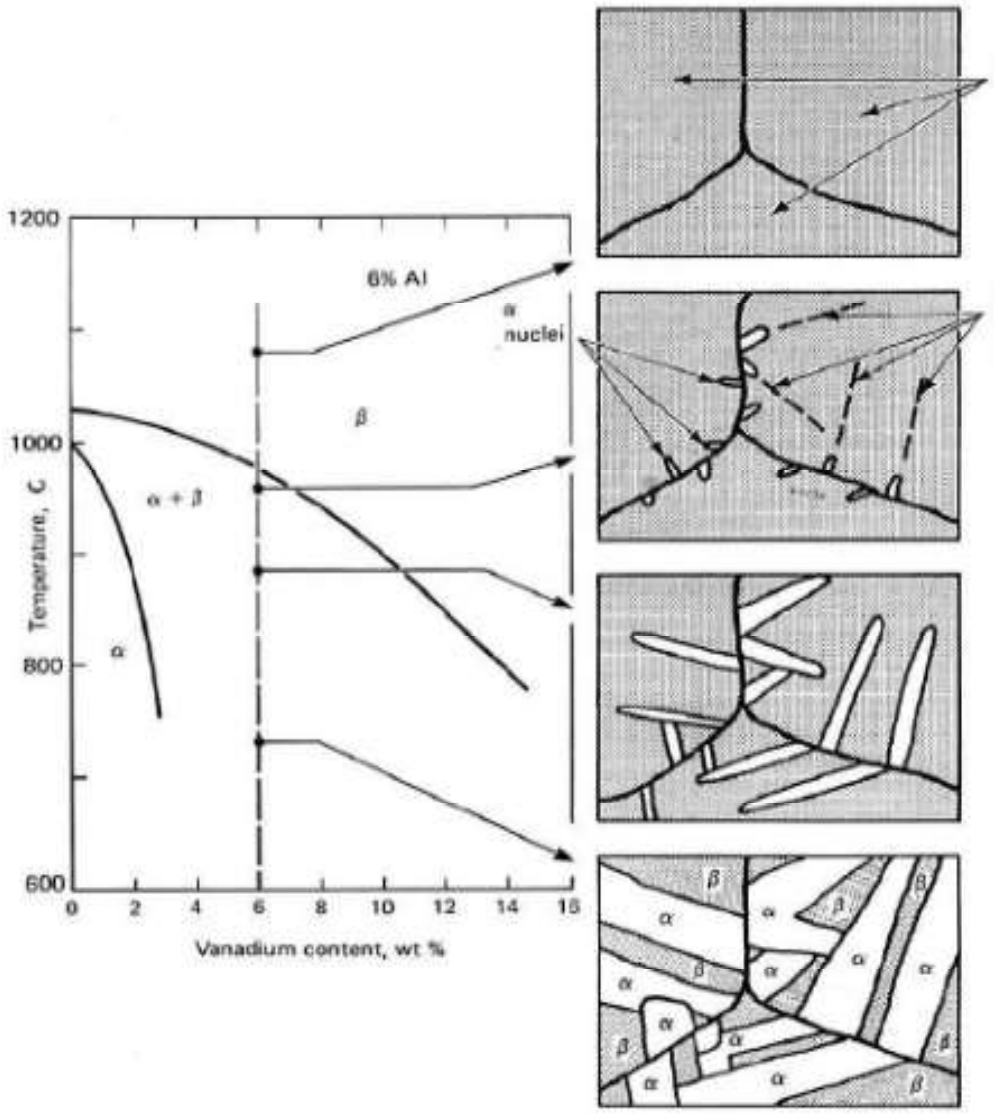

Figure 2-8 Widmanstätten structure in a Ti-6Al-4V alloy [27]**.**

There are many factors affecting the lamellar microstructure. The most important is the cooling rate [28]. Previously, Lütjering and Albrecht reported that the lamellar interfaces are heavily influenced by cooling rate from the β phase field [29]. A schematic diagram of a typical process to achieve the lamellar microstructure is shown in Figure 2-9.

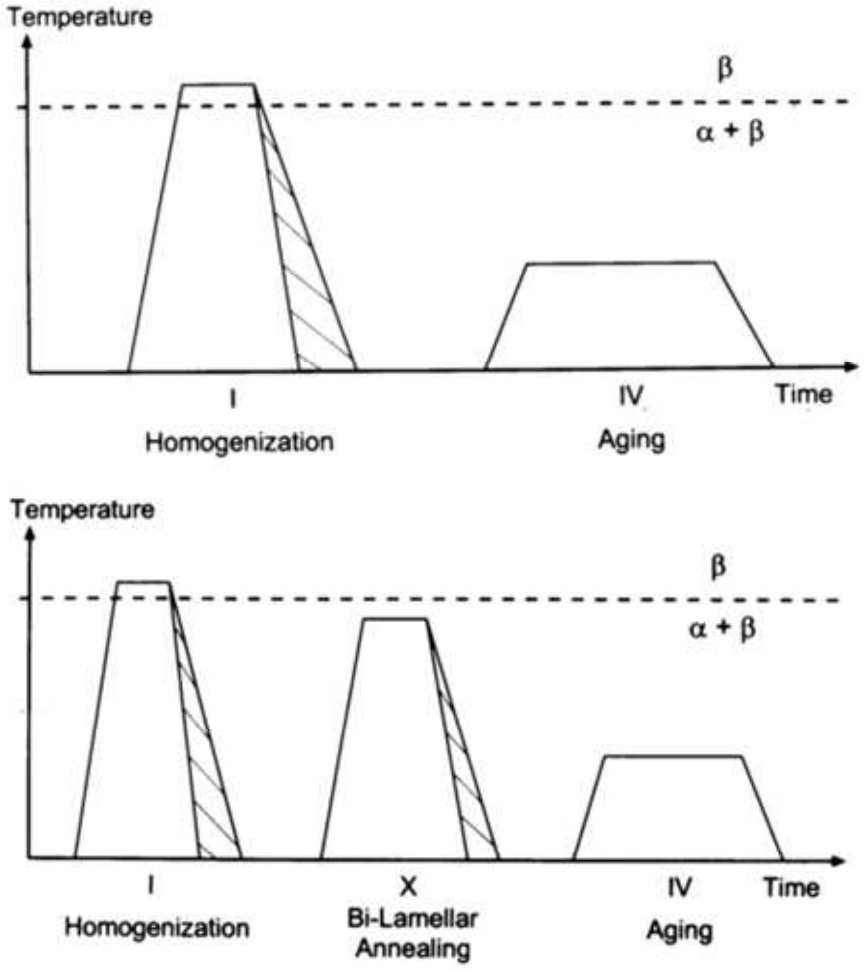

Figure 2-9 Schematic processing steps to obtain the lamellar microstructure [28]**.**

A typical lamellar microstructure can be obtained after deformation either in the β phase field or α+β phase field. Homogenization is carried out in the β phase field [28]. An aging, stress relieving treatment usually follows. When alloys are heat-treated in the high temperature β region and then cooled down to room temperature at different cooling rates, the microstructure is significantly affected as is illustrated in Figure 2-10.

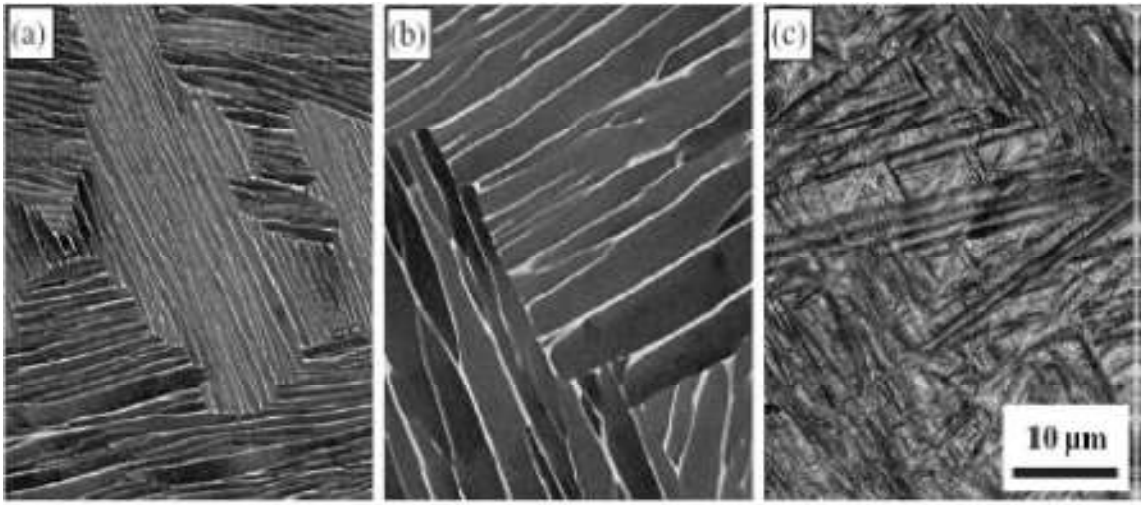

Figure 2-10 SEM images of Ti-6Al-4V alloys with different cooling rates: (a) intermediate cooling (air cooling), (b) slow cooling (cooling in vermiculite), and (c) rapid cooling (water quenching) [20]**.**

Another important feature is grain boundary α because the α forms a thin, continuous, strong layer along the prior β boundaries. With increasing cooling rate the width of the α laths will decrease. Furthermore, numerous studies have attempted to explain how the amount of β stabilizer can affect the microstructure. For example Kearns and Ward-Close [30] compare the lamellar microstructures of a Ti-4Al-4Mo-2Sn-0.5Si alloy and a Ti-6Al-4V alloy in the same condition. They found that the Ti-4Al-4Mo-2Sn-0.5Si which is a more β stabilized alloy than Ti-6Al-4V exhibits a thinner grain boundary α layer and a finer α lamellar structure.

2.6.2. Bimodal microstructure

The bimodal microstructure, which consists of globular primary α and transformed β, begins to form when the Ti alloys are heat treated below the β transus temperature [28]. Figure 2-11 shows an example of the bimodal microstructure.

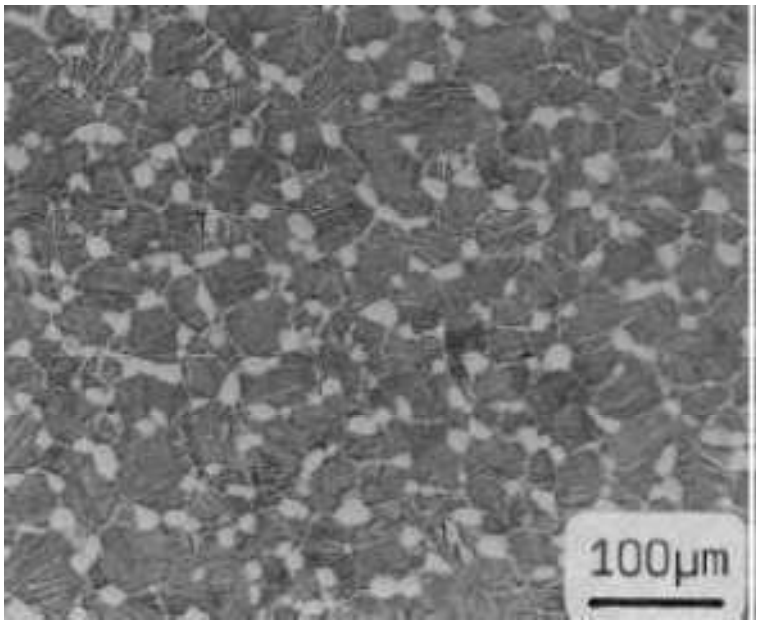

Figure 2-11 Typical SEM images of a bimodal microstructure [20]**.**

Figure 2-12 shows typical processing steps to obtain the bimodal microstructure [10,11]. A homogenization treatment is carried out in the β phase field and the material is deformed in the α+β phase field. During the deformation, crystallographic textures can be formed, depending on the degree of deformation, the deformation temperature and deformation mode. Then, a recrystallization step is carried out following an aging treatment to relieve residual stress [28].

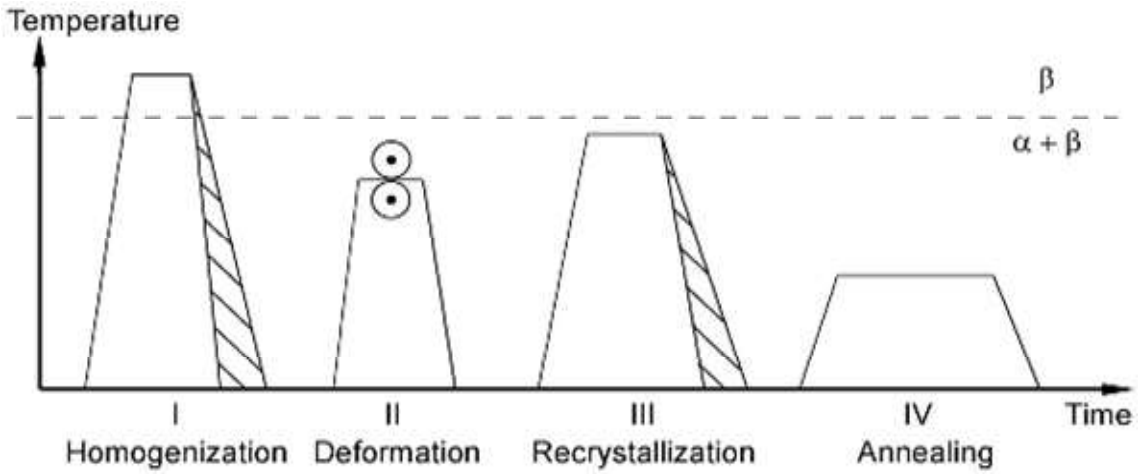

The bimodal microstructure can be affected by several factors. Firstly, the solution heat treatment or the temperature of recrystallization after the forging procedure (step III in Figure 2-12) is able to influence the volume fraction of the primary α phase [28]. Different volume fractions of the primary α phase can be obtained in Ti alloys when the temperature of solution heat treatment is changed, as shown in Figure 2-13.

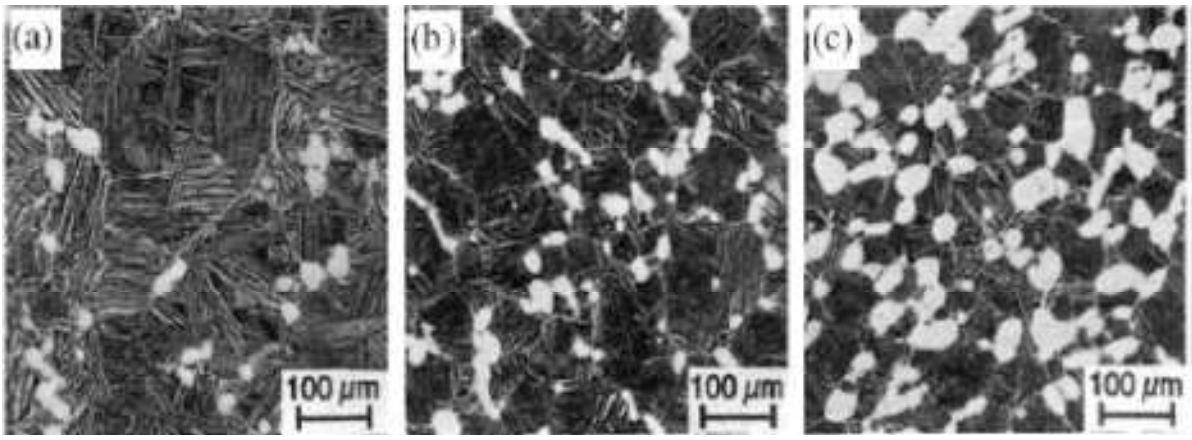

Figure 2-13 Bimodal microstructures of IMI 834 alloy with different volume fractions of the primary phase: (a) 5%, (b) 15%, and (c) 25% [20]**.**

In step II, the starting lamellar structure is "upset" in the deformation process. The size of the primary α grains (step I in Figure 2-12) is affected by the cooling rate from the β homogenization heat treatment as shown in Figure 2-14, which also determines the thickness of the grain boundary α layer and the width of the α lamellae, as reviewed previously.

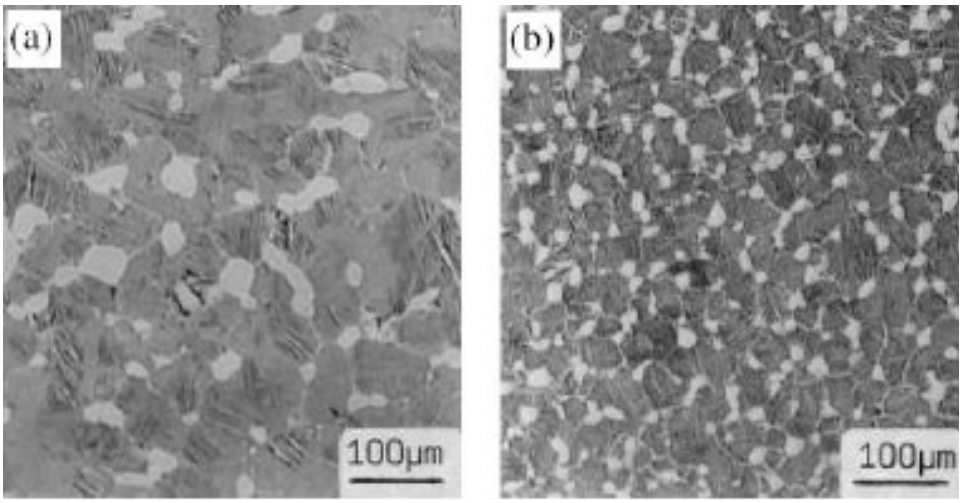

Figure 2-14 Bimodal microstructures of IMI 834 alloy with different cooling rates after beta homogenization heat treatment: (a) slower, and (b) faster [28]**.**

In summary, the most important factors determining the microstructural features in the bimodal microstructure are the cooling rates from the β homogenization heat treatment and from the solution heat treatment, as well as the recrystallization temperature.

2.6.3. Equiaxed microstructures

Equiaxed microstructures can be obtained by extensive mechanical working in the (α + β) phase region as shown in Figure 2-15 [19]. They can be obtained by simply modifying the process route for obtaining a bi-modal microstructure up until the recrystallization in the α+β phase region. There are two possible process routes to obtain a fully equiaxed microstructure (Figure 2-12). The first possibility is controlling the cooling rate after recrystallization of the bi-modal structure (III) to make it low enough that the α primary grains will grow during the cooling process and that α lamellae are not formed within the β grains [19].

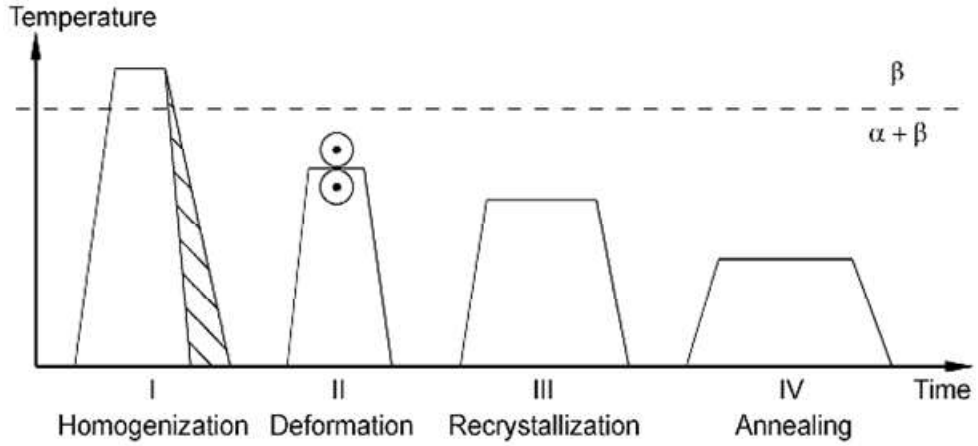

Figure 2-15 Processing route for fully equiaxed microstructures of α+β titanium alloys recrystallized at low temperatures [20]**.**

Another way to generate an equiaxed microstructure is to lower the temperature of step (III): the solution heat treatment temperature itself determines the volume fraction of the primary α phase. It is high enough to form this microstructure directly from the deformed lamellar structure during the recrystallization process [19] as shown in Figure 2-16.

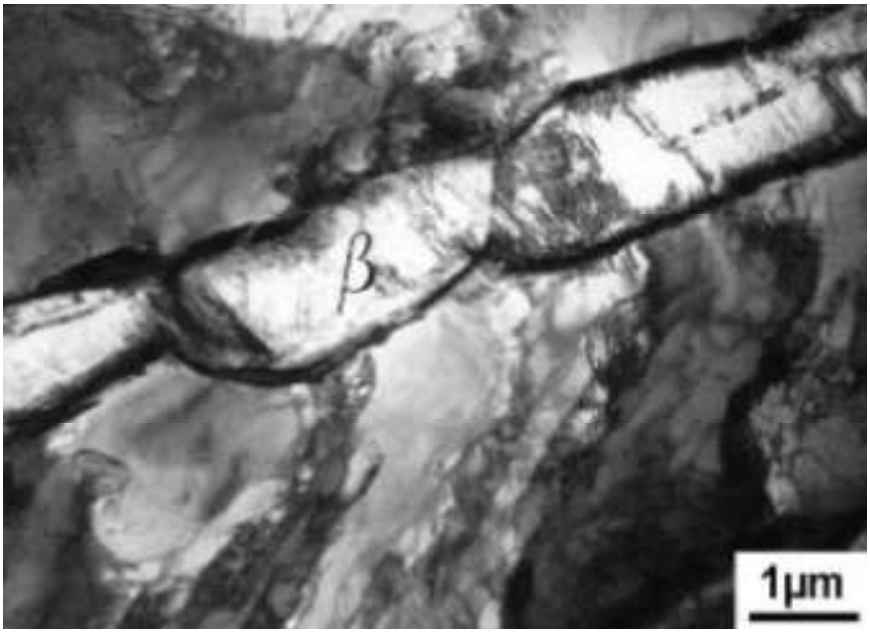

Figure 2-16 TEM micrograph for fully equiaxed microstructure at 800°C, Ti-6Al-4V [20]**.**

2.7. **The α+β phase Ti alloys: (Ti-6Al-4V)**

Ti-6Al-4V is the most commercially used α+β alloy; it has been used in this project. α+β alloys usually contain both α and β stabilizers. The amount of β stabilizer is about 4 %. α+β alloys combine the strength of the α phase with the ductility of the β phase. Figure 2-17 shows the approximate position of α+β phase in a schematic pseudobinary β-isomorphous phase diagram. The α/β Ti alloys are all the more interesting because these alloys are susceptible to

heat treatment, resulting in a wide range of microstructures and thus they can be processed in a variety of ways to get very different mechanical property combinations.

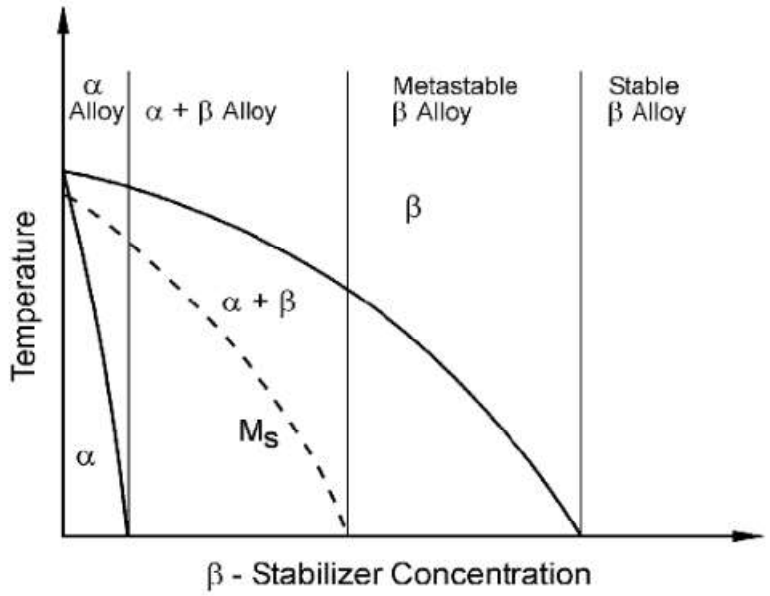

Figure 2-17 Pseudo-binary schematic illustrating effect β-isomorphous phase diagram for Ti alloys [20]**.**

The basic properties of the main alloying elements in Ti6Al4V are listed in Table 2-1[1].

Table 2-1 Basic properties of Ti6Al4V.

	Basic properties		
Element	Ti	Al	V
Atomic radius (Å)	2.0	1.82	1.92
stabilizing element	--	Alpha stabilizer	Beta stabilizer
Crystal structure	HCP	FCC	BCC
Electron Configuration:	$1s^2\ 2s^2p^6\ 3s^2p^6d^2\ 4s^2$	$1s^2\ 2s^2p^6\ 3s^2p^1$	$1s^2\ 2s^2p^6\ 3s^2p^6d^3\ 4s^2$
Atomic number	22	13	23
Melting point (℃)	1670	660	1900

2.7.1. Aluminium alloying element

Ti-6Al-4V is an alloy that includes six weight percent aluminium (Al) to stabilize the α phase. Al is the main α stabilizing element in titanium alloys [31] and provides strengthening. Figure 2-5 shows that addition of aluminium increases the β transus temperature to about 998 ± 10 °C [32]. However, the effect of aluminium on titanium alloys (such as increase in strength and changes in other properties) is much lower than that caused by interstitials such as oxygen (O), since Al is substitutional.

2.7.2. Vanadium alloying element

Vanadium (V) is a β phase stabilizer. The amount of β stabilizer is about 4 % and this content is sufficient to strengthen the β phase and refine the microstructure [19]. It is believed that the phase transformation process $\beta \rightarrow \alpha$ is primarily controlled by diffusional redistribution of vanadium between the two phases. The strengthening by V is slightly higher than that by molybdenum (Mo) although V is a weaker β stabilizer than Mo [33]. Therefore, V is the most widely used alloying element in titanium.

2.8. Deformation Mechanisms and Barrier Strengthening

2.8.1. Deformation mechanisms

As engineering devices have reduced to nano-metre and micron scales, materials behaviour at these scales has attracted attention because of the devices' interesting structural and mechanical properties. When a force is applied to a material, deformation occurs, leading to a proportional increase in stress until the yield point is reached. Elastic deformation of the material occurs before the yield point, meaning the material returns to its original shape when the force is removed. On the other hand, after the yield point, the material is plastically deformed, meaning the material will not return to its original shape when a force is taken away. It is permanently deformed. The movement of dislocations produces plastic deformation. Dislocations are defects within a crystal structure. The plastic deformation behaviour of most polycrystals is affected by the alloying elements, strain rate and temperature [34].

Dislocations are defined as a crystallographic defect, or irregularity, within a crystal structure. There are some basic types of dislocations: edge, screw and mixed dislocations [35].

The process by which plastic deformation is produced by dislocation motion is called slip, which is glide or conservative motion, and involves local shear [35]. The movement of dislocations in crystalline solids allows plastic deformation to occur at much lower stresses than what would be normally required to move one plane of atoms over another [35].

For an edge dislocation, the Burgers vector is perpendicular to the dislocation line direction; for the screw it is parallel to the dislocation line [35].

An alternative mechanism of dislocation motion is called dislocation climb or non-conservative motion. It occurs when the dislocation moves out of the glide surface. An atom closest at the bottom of the edge half plane can fill a vacancy during the movement of vacancies through a crystal lattice. At higher temperature, climb can occur more rapidly than at low temperature by reason of an increase in the mobility of vacancies [35].

The dislocation density is a measure of the length of dislocation in a unit volume of material, which increases with increasing strain in a crystal [35]. The presence of geometrically necessary dislocations that result from non-uniform strain increases the dislocation density in polycrystals.

It is known that dislocation movement can also be impeded by the presence of grain boundaries [35]. The way in which dislocations pass through these grain boundaries and move into neighbouring grains has an effect on the numbers of dislocations within a grain and the force required to move them. This is explained in more detail in the following section.

2.8.2. Grain-boundary strengthening

The grain boundary acts as a strong barrier to dislocation motion. In the early 1950s Hall [36] and Petch [37] established in independently conducted work the same relationship between the grain size and the stress required to deform the material.

The empirical relationship is named after both scientists as grain boundary strengthening (or Hall-Petch strengthening). However, the real physical mechanism underlying this relationship

remains unclear. Plastic deformation in polycrystalline materials involves a wide range of interaction phenomena between dislocations and grain boundaries, which are still the subject of extensive research. Several physically based models have been proposed in the literature. The concept of grain boundaries acting as barriers to dislocation motion are the most cited dislocation explanation of the Hall–Petch relationship [17,32,38].

It is based on the observation that grain boundaries act as natural barriers to the movement of dislocations and that the amount of dislocations trapped within a grain directly influence how easily dislocations can cross grain boundaries and propagate into an adjacent grain. Let us consider a grain where a shear stress is acting on a slip system with a sufficiency of mobile dislocations. Dislocations will move along the slip plane until they reach a grain boundary, where they are blocked due to the barrier generated by the lattice orientation mismatch between adjacent crystals. As plastic activity takes place, more dislocations will pileup against the grain boundary. Glissile dislocations generate repulsive stress fields on each other, so the more dislocations accumulate at the boundary the higher the repulsive force becomes, acting as a driving force to reduce the energetic barrier for propagation across the boundary. By decreasing the grain size the possible amount of dislocations piling-up decreases, which increases the applied shear stress (τ) required to propagate a dislocation into an adjacent grain (see Figure 2-18). For n dislocations in the pileup, the effective shear stress (τ_e) at the boundary is $n.\tau_i$, where τ_i is the resolved shear stress, n the number of dislocations in the pileup with a grain diameter D, is given by.

$$n = \frac{\kappa \pi \tau_i D}{4Gb} \qquad \textbf{2-1}$$

where G is the shear modulus, *b* is the magnitude of the Burgers vector and κ reflects the character of the dislocations: κ is equal to 1 for screw dislocations and (1- ν) for edge dislocations [35].

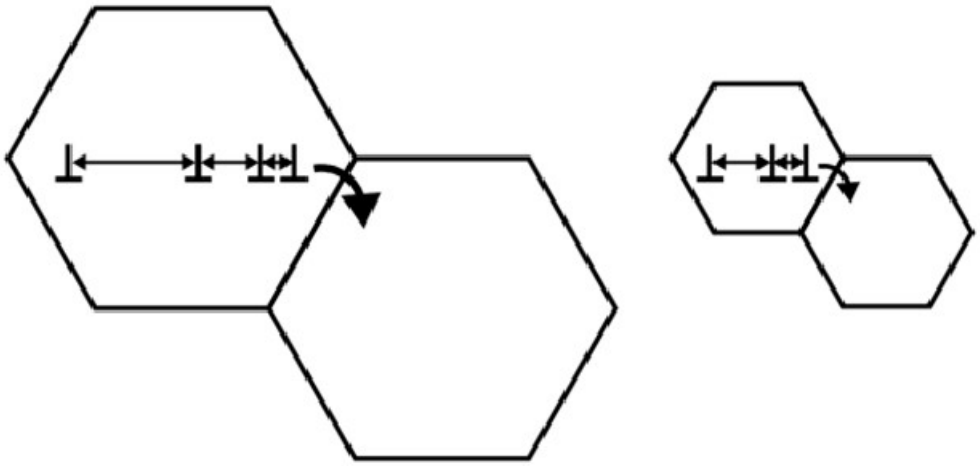

Figure 2-18 Dislocation pile-up, seen as a size effect. Larger grains are capable of holding more dislocations piled-up, generating a higher driving force for dislocations to move into adjacent grains. Thus less force is required to move a dislocation from a larger than from a smaller grain, leading materials with smaller grains to exhibit a higher yield stress.

When the pileup stress reaches or exceeds a critical stress (τ_c), as shown in Figure 2-19, then dislocations can be generated in the neighbouring grain, slip will continue and macroscopic plastic deformation results.

$$\tau_c = \tau_e = n.\tau_i = \frac{(\kappa \,.\, \pi \,.\, \tau_i^2 \,.\, D)}{(4\, G \,.\, b)} \qquad \textbf{2-2}$$

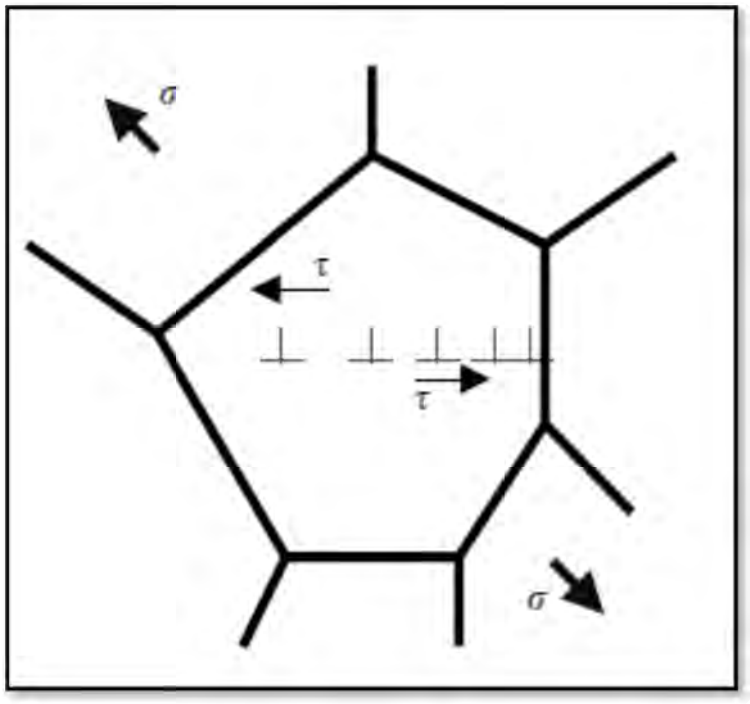

Figure 2-19 Schematic of the dislocation pileup model.

In order to overcome the influence of the grain boundary, the resolved shear stress can be taken as the applied stress (τ) less the friction stress to overcome the intrinsic dislocation resistance $\boldsymbol{\tau}_o$

$$\boldsymbol{\tau_i = \tau - \tau_o} \qquad \textbf{2-3}$$

Substituting into Equation (2-2) gives

$$\boldsymbol{\tau_c = n\tau_i = \frac{\kappa\pi(\tau - \tau_i)^2 D}{4Gb}} \qquad \textbf{2-4}$$

and rearranging yields

$$\boldsymbol{\tau = \tau_o + \left(\frac{4\tau_c Gb}{\pi D}\right)^{1/2} = \tau_o + \check{k} D^{-1/2}} \qquad \textbf{2-5}$$

Expressing Equation (2-5) in terms of the normal stress (σ), the typical Hall-Petch formalism results:

$$\boldsymbol{\sigma_y = \sigma_o + k\sqrt{D}} \qquad \textbf{2-6}$$

where σ_y is the yield stress, σ_o is the friction stress or resistance to dislocation movement, k is the strengthening coefficient and D is the mean grain size.

The stress to move mobile dislocations in the absence of grain boundaries is known as the frictional stress (σ_0). It has been shown that the frictional stress depends strongly on strain rate [5,6], temperature and the additions of alloying elements [41]. It is not affected by the grain size [39] or by second phase particles [42].

Decreasing grain size decreases the amount of possible pile up at the boundary, increasing the amount of applied stress necessary to move a dislocation across the grain boundary. This causes an increase in the amount of applied stress necessary to continue the movement of dislocations to grain boundaries and across, consequently increasing the yield strength (σ_y). Thus, there is an inverse relationship between grain size and strength.

The Hall-Petch relation is well obeyed by a variety of structural alloys over several orders of magnitude in grain sizes [43].

2.8.3. Polycrystal deformation mechanisms

Due to the lower symmetry of (HCP) titanium alloys, the number of active slip systems is more limited as compared to cubic titanium (BCC). Dislocation slip is an important deformation mode in (HCP) titanium alloys. The strict Burgers orientation relationship between alpha phase (HCP) and beta phase (BCC) [44] and the limited numbers of easy slip systems transmitted through boundaries result in dislocation pile-ups at grain boundaries and other barriers to glide.

Leyens and Peters [20] concluded that there can only be three slip systems involving the basal and prismatic planes. However, there are only two independent slip systems in the basal and prismatic planes. Therefore, the available independent slip systems are only four in hcp materials. The number of independent slip planes is not increased by pyramidal <a> slip Table 2-2 shows the active slip systems in titanium alloys. However, according to the Von Mises criterion at least five independent slip systems are required for homogeneous plastic deformation of polycrystals, i.e. the von Mises–Taylor criterion cannot be satisfied by <a> dislocations alone. Both <a> and <c+a> slip are therefore important.

<c + a> slip in pure titanium is more difficult compared to twinning activated due to the higher critical resolved shear stress associated with <c + a> slip systems. At high homologous temperature deformation twinning is not activated and therefore cannot be the dominant deformation mechanism [45]. Therefore, at elevated temperature deformation slip is dominant. Figure 2-20 shows the slip systems in titanium alloys.

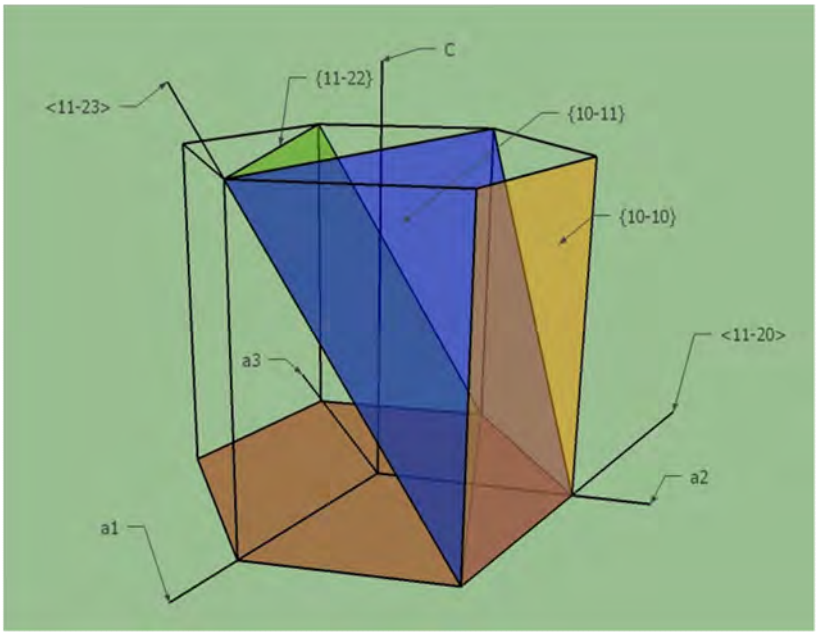

Figure 2-20 Schematic shows important slip planes and slip directions of the hcp crystal structure.

The preferential activation of slip systems is strongly dependent on two factors: the critical resolved shear stress and the Schmid factor as a function of grain orientation relative to loading direction.

Table 2-2 The active slip systems in titanium alloys (for example Ti6Al4V).

Slip System type	Burgers Vector type	Slip plane	Slip direction	No. Of slip systems	
				Total	Independent
Basal	$\vec{a}$	(0002)	$\langle 11\bar{2}0\rangle$	3	2
Prismatic	$\vec{a}$	$\{10\bar{1}0\}$	$\langle 11\bar{2}0\rangle$	3	2
1st Pyramidal	$\vec{c}+\vec{a}$	$\{10\bar{1}1\}$	$\langle 11\bar{2}3\rangle$	6	5

Lütjering and Williams reviewed the various slip systems in titanium alloys. The main close packed directions and Burgers vectors are the three $\langle 11\bar{2}0\rangle$ slip directions which can occupy the basal, prismatic and first order pyramidal slip planes; deformation can also occur in slip directions $\langle 11\bar{2}3\rangle$ on the first order pyramidal planes [19]. The various slip planes and slip directions in alpha titanium alloys are illustrated in Figure 2-21. The slip planes in titanium alloys are the basal plane (0002), the three prismatic planes $\{10\bar{1}0\}$ and the first order pyramidal planes $\{10\bar{1}1\}$ for six <c+a>.

The critical resolved shear stress required to activate these slip systems is different for each system. The smallest critical resolved shear stress value at low temperatures is for slip on the prismatic plane. The basal slip plane is the second easiest slip plane. Slip can occur on the pyramidal planes, but it has a higher critical resolved shear stress than for the other planes. As a result of plastic deformation, the crystal shape remains unchanged along the c-axis.

The <a> close packed direction is perpendicular to the c-axis and is not able to produce strain along the c direction. Therefore, to allow homogeneous deformation of a polycrystal additional non-basal slip systems are needed.

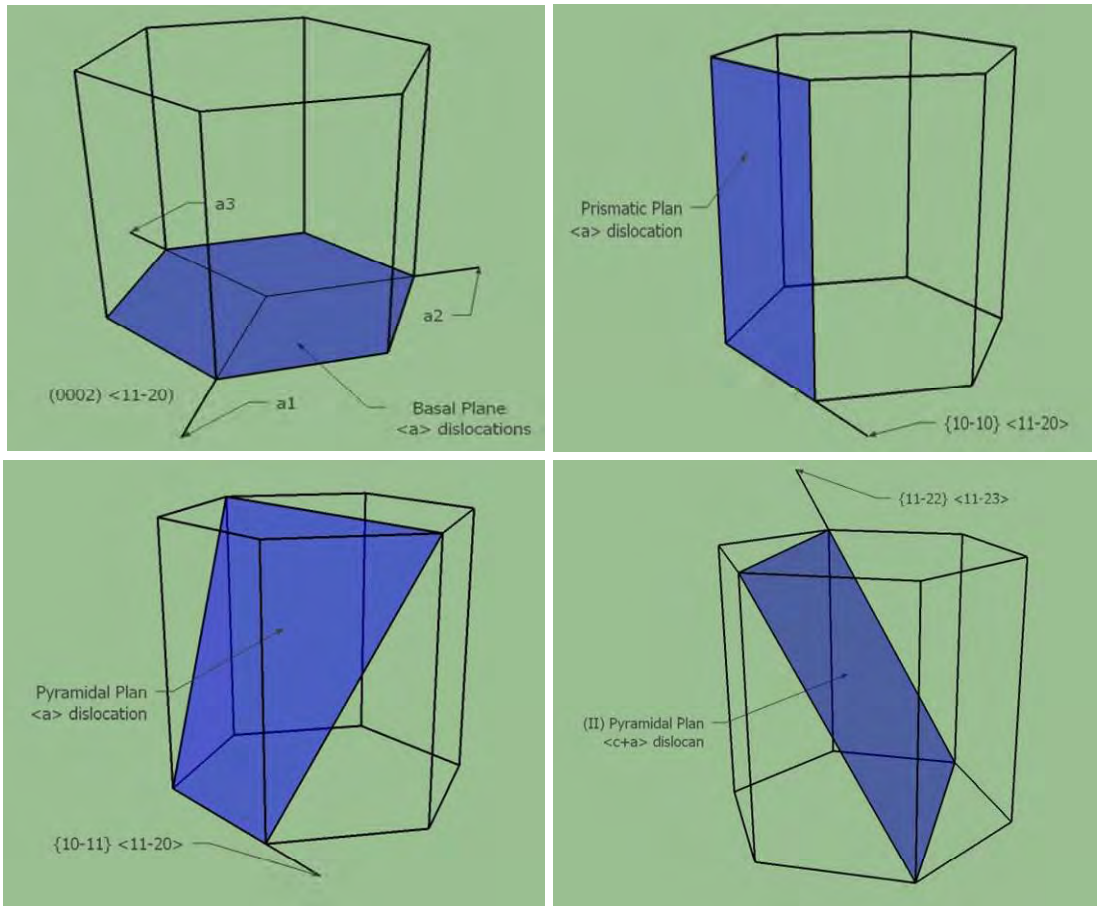

(A)

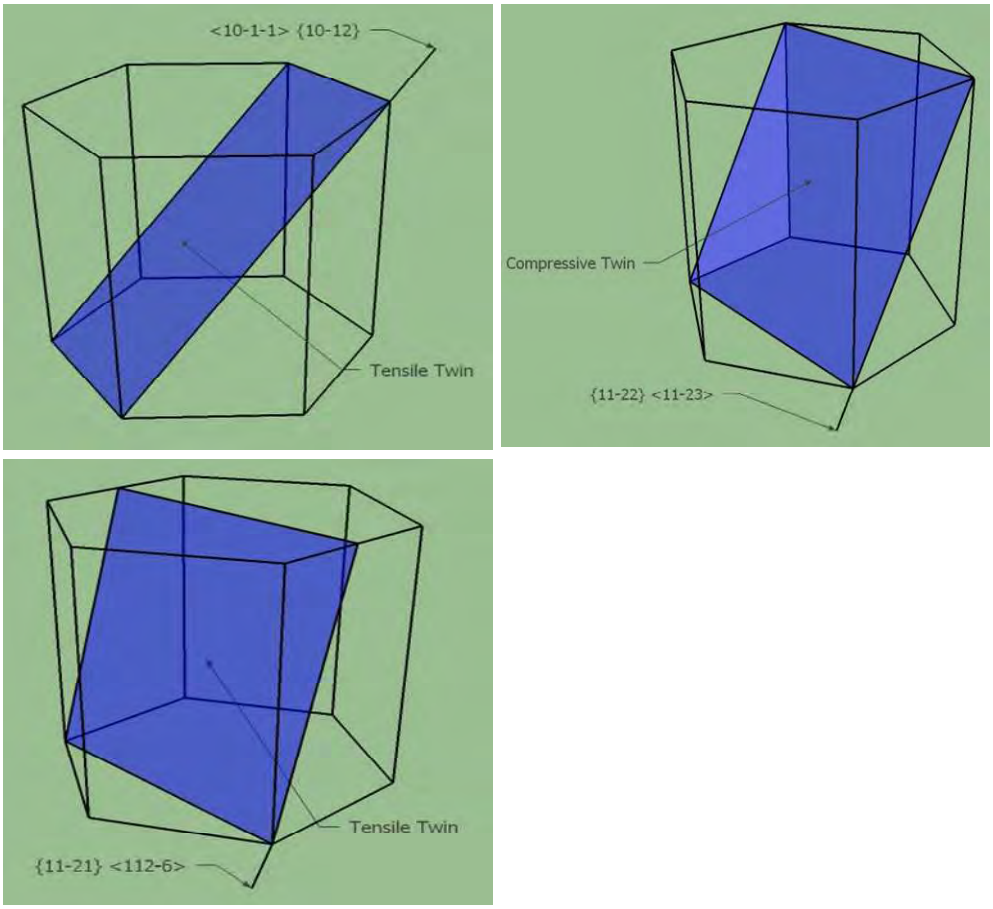

(B)

Figure 2-21 (A) Possible slip systems (B) Tensile and compression twinning systems in titanium alloys.

The calculation of Schmid factor is not well known in the case of hcp materials. The four Miller-indices of hcp materials and the c/a ratio make the calculation difficult in comparison to BCC and FCC materials. Therefore, we will present a summary of the calculation of Schmid factors in hcp materials and, more generally, some useful equations are given. In order to define the indices of directions and planes in hcp, usually Millier-Bravais notation with 4 axes has been used. The 4-axis system is based on the vectors a_1, a_2, a_3 and c; a_3 is redundant since $a_3 = -(a_1+a_2)$. With respect to this four vector basis, an arbitrary crystal vector can be written as

$$\mathbf{r} = \mathbf{u}\mathbf{a_1} + \mathbf{v}\mathbf{a_2} + \mathbf{t}\mathbf{a_3} + \mathbf{w}\mathbf{c} \qquad \textbf{2-7}$$

with the constraint

$$\mathbf{u} + \mathbf{v} + \mathbf{t} = \mathbf{0} \qquad \textbf{2-8}$$

Line directions are usually written [uvtw] and planes as (hkil). The relationship between a line direction and the parallel plane normal is given in equation **(**2-9**)**, where r is the normal vector to the plane.

$$\mathbf{[\ uvtw\ ] = [\ hkil]^{*} = [\ hki\lambda^{-2}\,l\ ]} \qquad \textbf{2-9}$$

where, $\lambda^2 = 2/3\ (\ c/a\ )^2$, * indicates the reciprocal lattice.

Conversely, the plane (hkil) to the direction [uvtw] is given by equation (2-10).

$$\mathbf{(\ hkil\ ) = (\ uvtw\ )^{*} = (uvt\lambda^{2}w\ )} \qquad \textbf{2-10}$$

To obtain the Schmid factor, it is necessary to calculate the inner product of the loading axis and the slip direction as well as the loading axis and the slip plane. The angle between the two vectors

$$\mathbf{r_1} = [\mathbf{u_1 v_1 t_1 w_1}] \textbf{ and } \mathbf{r_2} = [\mathbf{u_2 v_2 t_2 w_2}], \textbf{ is given by}$$

$$\cos(\mathbf{r_1} \cdot \mathbf{r_2}) = \frac{r_1}{|r_1|} \cdot \frac{r_2}{|r_2|} = \frac{\mathbf{u_1 u_2 + v_1 v_2 + t_1 t_2 + \lambda^2 w_1 w_2}}{\left(\mathbf{u_1^2 + v_1^2 + t_1^2 + \lambda^2 w_1^2}\right)^{1/2}\left(\mathbf{u_2^2 + v_2^2 + t_2^2 + \lambda^2 w_2^2}\right)^{1/2}} \quad \textbf{2-11}$$

$$\textbf{where,} \quad \mathbf{r_1} \cdot \mathbf{r_2} = \frac{\mathbf{3a^2}}{\mathbf{2}}(\mathbf{u_1 u_2 + v_1 v_2 + t_1 t_2 + \lambda^2 w_1 w_2})$$

By combining equation (2-8) and equation (2-11), we can also derive the angle between the line direction $\mathbf{r_1}$ =[u_1 v_1 t_1 w_1] and the plane $\mathbf{p_1}$ =[h_1 k_1 i_1 l_1] :

$$\cos(r_1 \cdot p_1) = \frac{r_1}{|r_1|} \cdot \frac{p_1}{|p_1|} = \frac{\mathbf{u_1 h_1 + v_1 k_1 + t_1 i_1 + w_1 l_1}}{\left(\mathbf{u_1^2 + v_1^2 + t_1^2 + \lambda^{-2} w_1^2}\right)^{1/2}\left(\mathbf{h_1^2 + k_1^2 + i_1^2 + \lambda^{-2} l_1^2}\right)^{1/2}} \quad \textbf{2-12}$$

Similarly, the angle between two planes, $p_1 = [h_1 k_1 i_1 l_1]$ and $p_2 = [h_2 k_2 i_2 l_2]$, is as follows,

$$\cos(p_1 \cdot p_2) = \frac{p_1}{|p_1|} \cdot \frac{p_2}{|p_2|} = \frac{\mathbf{h_1 h_2 + k_1 k_2 + i_1 i_2 + l_1 l_2}}{\left(\mathbf{h_1^2 + k_1^2 + i_1^2 + \lambda^{-2} l_1^2}\right)^{1/2}\left(\mathbf{h_2^2 + k_2^2 + i_2^2 + \lambda^{-2} l_2^2}\right)^{1/2}} \quad \textbf{2-13}$$

where, $\boldsymbol{g_1 . g_2 = \frac{2}{3a^2}(h_1 h_2 + k_1 k_2 + i_1 i_2 + \lambda^{-2} l_1 l_2)}$

As a result, the Schmid factor can be derived by multiplying equations (2-11) and (2-12).

When the load is applied along the direction $\mathbf{r_1} = [u_1\ v_1\ t_1\ w_1]$, with a slip plane of $\mathbf{p_1} = (h_1\ k_1\ i_1\ l_1)$ and slip direction $\mathbf{r_2} = [u_2\ v_2\ t_2\ w_2]$, the Schmid factor is given by equation (2-14):

$$\begin{aligned} &\cos(\mathbf{r_1}.\mathbf{r_2}) \times \cos(\mathbf{r_1}.\mathbf{p_1}) \\ &= \left(\frac{\mathbf{r_1}}{|\mathbf{r_1}|}.\frac{\mathbf{r_2}}{|\mathbf{r_2}|}\right) \times \left(\frac{\mathbf{r_1}}{|\mathbf{r_1}|}.\frac{\mathbf{p_1}}{|\mathbf{p_1}|}\right) \\ &= \frac{u_1u_2 + v_1v_2 + t_1t_2 + \lambda^2 w_1w_2}{\left(u_1^2 + v_1^2 + t_1^2 + \lambda^2 w_1^2\right)^{1/2}\left(u_2^2 + v_2^2 + t_2^2 + \lambda^2 w_2^2\right)^{1/2}} \\ &\times \frac{u_1h_1 + v_1k_1 + t_1i_1 + w_1l_1}{\left(u_1^2 + v_1^2 + t_1^2 + \lambda^{-2} w_1^2\right)^{1/2}\left(h_1^2 + k_1^2 + i_1^2 + \lambda^{-2} l_1^2\right)^{1/2}} \end{aligned} \qquad \textbf{2-14}$$

As mentioned above, when the applied stress reaches or exceeds the critical resolved shear stress, then slip is initiated in the grain. Schmid's law appears as equation (2-15) and Figure 2-22

$$\boldsymbol{\tau = \sigma \cos \emptyset \cos \lambda} \qquad \textbf{2-15}$$

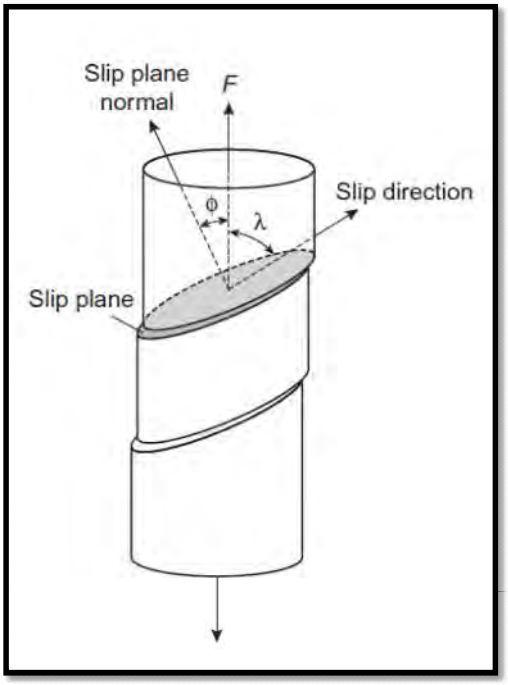

Figure 2-22 Schematic explanation of how the Schmid factor is calculated.

where τ is the resolved shear stress in the slip direction, σ is the applied stress, φ is the angle between the slip plane normal and loading direction and λ is the angle between the loading direction and slip direction.

The maximum value of (cosφ cosλ) corresponds to φ = λ = 45° ⇒ cosφ cosλ = 0.5 ⇒

$$\sigma_y = 2\tau \, \mathbf{CRSS} \qquad \textbf{2-16}$$

Slip will occur first in slip systems oriented close to the angles (φ = λ = 45°) with respect to the applied stress.

2.9. **Phase Transformation**

The transition of a system from one phase into another is called a phase transformation. During the process of phase transformation, there are usually physical and/or chemical property changes. These physical or chemical properties can be used to identify and analyse the phase transformation, for instance to study the transition start temperature and transition finish temperature.

Titanium alloys can undergo all types of solid state phase transformations. The important phase transformation concerned with the current research is the $\beta \rightarrow \alpha+\beta$ transformation, because titanium properties are highly dependent on the size, shape, and distribution of the two primary crystallographic phases: hexagonal close packed (HCP) alpha (α) and body centred cubic (BCC) beta (β).

2.9.1. Nucleation and growth in the titanium alloys

The nucleation and growth of the α phase in titanium alloys is the most practically important phase transformation. When the titanium alloy is slowly cooled down from the single β phase regime, this reaction occurs first at certain prior β grain boundaries. Depending on the cooling rate, α precipitates exhibit different morphology, volume fraction, size scale and distribution. The α phase may nucleate in β phase as a series of parallel plates, or laths, belonging to the same variant of the Burgers relationship (called an α colony), that are separated by the retained β phase as illustrated in Figure 2-23. The similarly oriented lath groups are recognized as α colonies and they grow into the β grain until encountering competing α colonies.

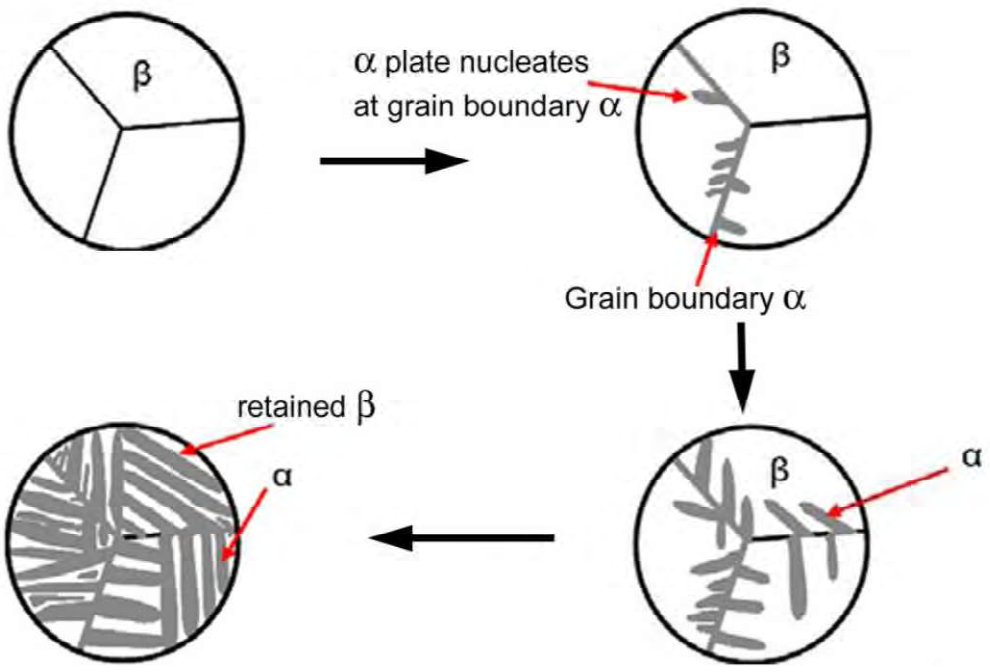

Figure 2-23 Schematic diagram showing the diffusional β → α phase transformation process, including the formation of grain boundary α colonies in the β grain [46].

With slow cooling rates and large prior β grains, like in investment castings, the colony size increases until it reaches lengths of hundreds of microns. As the cooling rate becomes higher, the lamellae get finer; this leads to decreases in the colony size until it contains only one or a few α laths and the microstructure changes from colony to a Widmanstatten or "basket-weave" structure as illustrated in Figure 2-24. In addition to nucleating α from a grain boundary, there is a possibility for new colonies to nucleate inside the β grain.

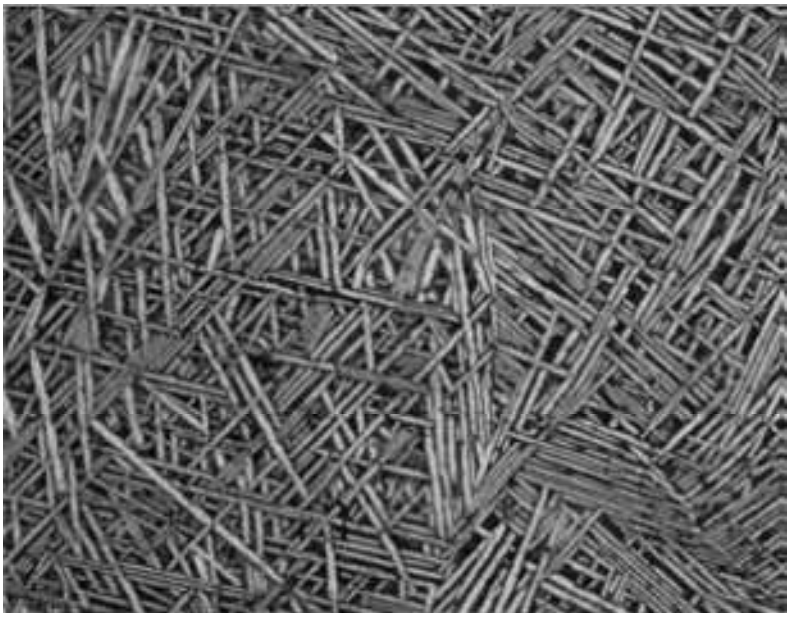

Figure 2-24 Widmanstatten or basket weave microstructure.

There are three main types of hcp/bcc orientation relationship: Burgers, Pitsch-Schrader and Potter, as can be seen in Table 2-3 [14,17]. There is a large volume of published studies describing various titanium alloys, which show that alpha phase prefers a near Burgers orientation relationship with the parent β phase [18,19,20,1,13,6]. The orientation relationships between the β and the α phases has been studied first by Burgers in 1934 [44].

He studied the orientation relationship for the bcc → hcp structural phase transformation in zirconium and this is also obeyed by titanium alloys [19].

It has been shown that the Burgers orientation relationship for two phase hcp-bcc provides low energy inter-phase boundaries, with an interface containing $[0001]$ and $\langle 11\bar{2}0\rangle$ dislocations. This can be one reason for a frequent occurrence of the Burgers orientation relationship in such structures [44].

Table 2-3 Table of orientation relationships that exist between hcp+bcc phases.

Orientation relationship	**Description**
Burgers orientation relationship	$\{101\}_\beta \parallel (0001)_\alpha, \langle 1\bar{1}1\rangle \parallel \langle 2\bar{1}\bar{1}0\rangle$
Pitsch-Schrader orientation relationship	$\{110\}_\beta \parallel (0001)_\alpha, \langle 001\rangle \parallel \langle 11\bar{2}0\rangle$
Potter orientation relationship	$\{110\}_\beta \parallel \{10\bar{1}1\}_\alpha, \langle 1\bar{1}1\rangle \parallel \langle 11\bar{2}0\rangle$

Thus the crystallographic relationship between α phase and β phase follows the Burgers orientation relationship (OR) (see Appendix A). This should allow easy slip transmission between the two phases. The (a_1) slip system is defined as the close packed $[2\bar{1}\bar{1}0]$ direction. It is nearly parallel (0.5°) to a $< 111 >_\beta$ slip direction in the β phase, thus resulting in easy slip transmission across the α/β interface. The second slip vector (a_2) $[\bar{1}2\bar{1}0]$ is misaligned ~11° from the corresponding $< 111 >_\beta$ slip direction in the β phase, leading to increased CRSS and thus more difficult slip transmission while the third slip vector has no closely aligned β phase slip system at all [2,15]. Figure 2-25 shows the alignment of the basal plane

and (101) plane. Some dislocations can easily transmit through the α/β interface by the relatively small misorientations between the grains.

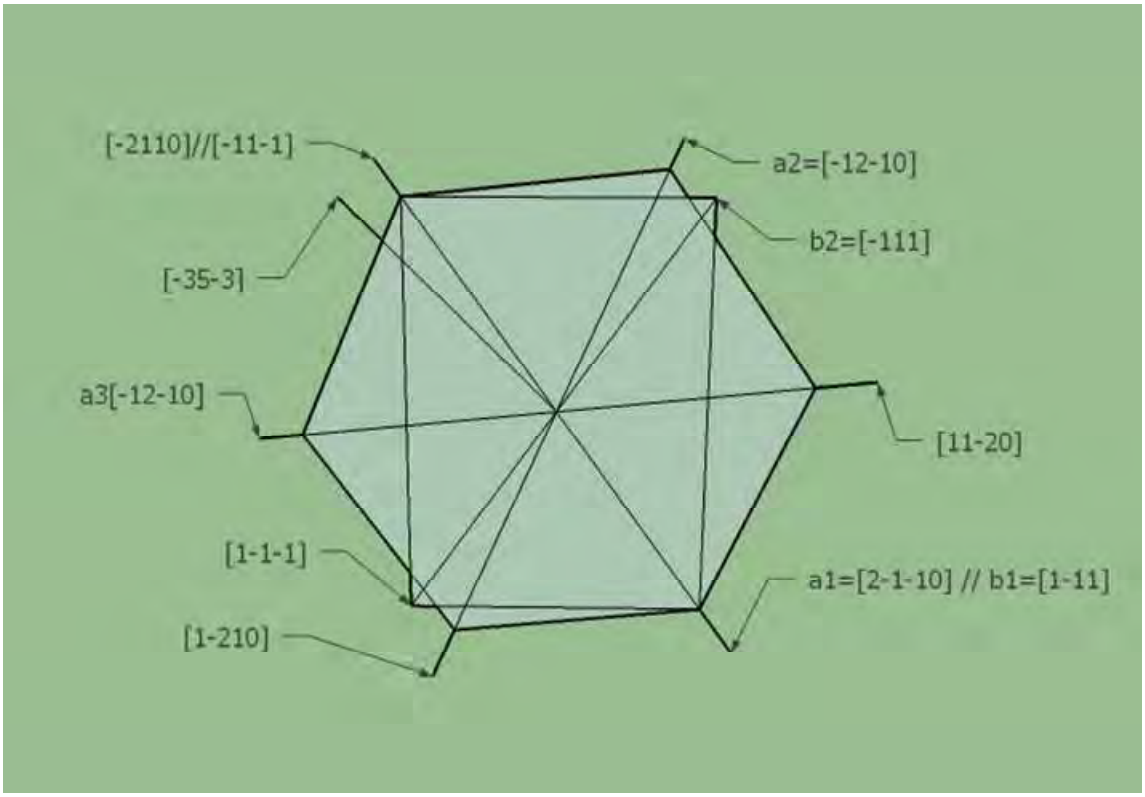

Figure 2-25 The crystallographic relationships between α and β phases in the Burgers Orientation Relationship.

During the transformation from beta to alpha+beta, following the same nucleation events, the different alpha orientations formed inside the grain are called variants. The individual β grains transform into 24 equivalent combinations and permutations of α phase according to the Burgers orientation relationship. However, these 24 variants are not always equally favoured. Obviously only one such variant is observed within each individual colony.

2.9.2. Nature of the α/β interface in Ti alloys

Perovic and Weatherly [48] were the first to study the structure of the α → β HCP:BCC interface in a Zr-2.5%Nb alloy. Two sets of dislocations were identified at the interface. The first set had a Burgers vector of <c+a> type with a spacing of 6 nm, while the second set was of <a> type. The interactions of the two sets of dislocations led to the formation of steps at the interface. The presence of steps may in fact be due to structural ledges at the interface as reported in a Ti-Cr system by Furahara et. al. [49].

Furahara and Aaronson (1991) [49] used a structural ledge approach to model the interface. A graphical technique that allows plotting of the interfacial structure as a function of orientation relationships and lattice parameter ratios was used to determine the coherency across the interface. A coherent atom pair was described as one that is within 15% of the average interatomic distance along a close packed direction in the two phases. The coherent atom pairs are then replaced by a single atom and coherent patches were plotted for a Burgers orientation relationship. Two sets of edge dislocations of <c> and <a> type at the interface result. Structural ledges were reported to increase the coherency of the interface and to eliminate the need for an <a> type dislocation (further detailed information about the coherence of the interface can be found in Ref. [49]). The interface then consists of structural ledges with a terrace plane corresponding to $\{10\bar{1}0\}_\alpha||\{112\}_\beta$ which has a <c> type edge misfit dislocation on its surface (Figure 2-26).

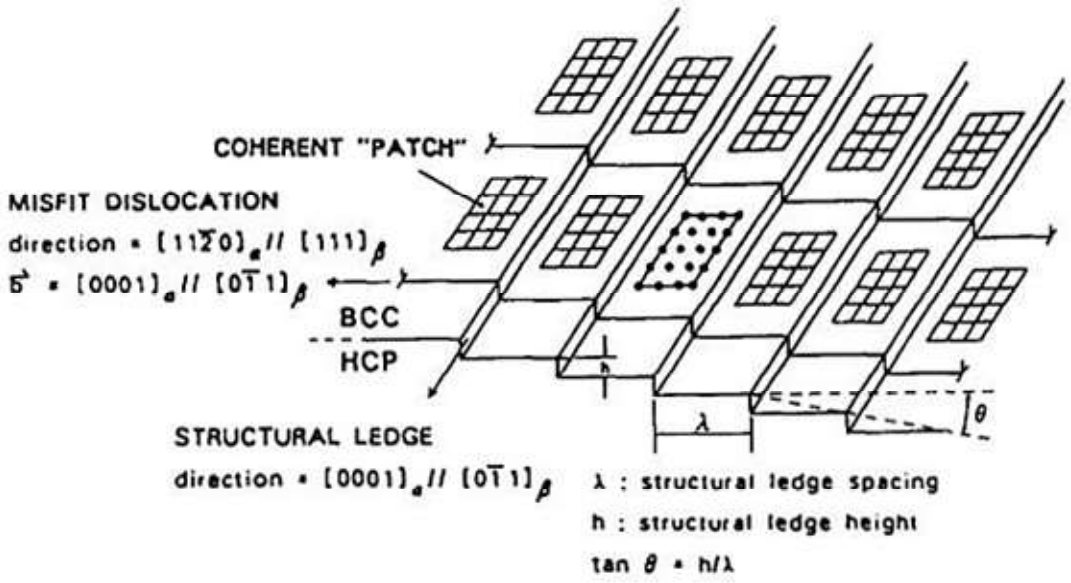

Figure 2-26 The α/β interface with structural ledges. The terraces of the ledges have <c> type edge dislocations on them [49]**.**

Furahara *et al*. [37, 38] report an almost Burgers orientation relationship between the α and β phases in a Ti-Cr alloy. However, according to Dahmen [51] the precipitate should tend to obey a Potter orientation relationship for the particular ratio of a_α/a_β. A Potter orientation relationship causes the basal and prismatic slip planes in the α to be misoriented through a small angle with the corresponding slip planes in β making slip transmission a bit more difficult. Several studies investigating the interface by TEM have been carried out on Ti alloys (Furuhara *et al*. [50], Mou and Aaronson [52], Zherebtsov *et al*. [53] and Cabibbo *et al*.[54]). An isometric sketch shown in Figure 2-27 summarizes the TEM observations of Furahara et. al. [37,38,42] who studied the interphase boundary structures of intragranular α laths formed in the β matrix in a Ti-Cr alloy. They studied the interface by TEM and decided that each lath has three sides: a side face, an edge face and a broad face, which contains structural ledges and terrace planes, and that the interface contains misfit compensating defects (dislocations or ledges) as illustrated in Figure 2-28. A broad face with misfit

dislocations having a Burgers vector of <c/2> was identified. These dislocations were observed to lie on the terraces of structural ledges as identified using high resolution TEM. The plane (terrace) of these structural ledges was $\{10\bar{1}0\}_\alpha||\{112\}_\beta$.

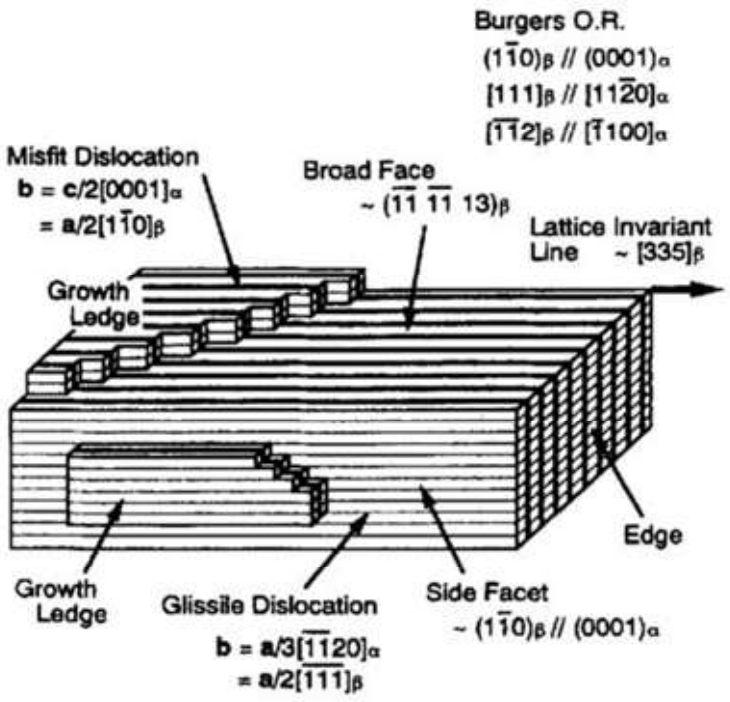

Figure 2-27 Schematic of the α/β interface. The schematic is based on TEM observations of the broad face, the side face and the edge face of the α lath. The <c> type edge dislocations are present on the broad face and <a> type dislocations loop around the side face of the α lath [50]**.**

The average habit plane of the broad face is close to $\{\overline{11}\ \overline{11}\ 13\}_\beta$ and contains the invariant line $< 335 >$. The broad face in addition to the growth ledges on its surface contains structural ledges whose terrace planes are parallel to $\{10\bar{1}0\}_\alpha||\{112\}_\beta$ as shown in Figure 2-29. On the terrace planes, misfit edge dislocations with a Burgers vector of c/2 [0001] are present. These dislocations loop around the α lath. The habit plane of the side face is close to $(0001)_\alpha||\{110\}_\beta$. The shear strain of the transformation, $a/12\ [11\bar{1}]$ is accommodated by

dislocation loops of $a/2\,[11\bar{1}]$ type with a line direction parallel to <335> on every sixth $\{10\bar{1}0\}_a$. These dislocations are perfect screws on the terrace of structural ledges and nearly perfect edges on the risers of the ledges. These dislocations are glissile on $\{10\bar{1}0\}_a || \{112\}_\beta$.

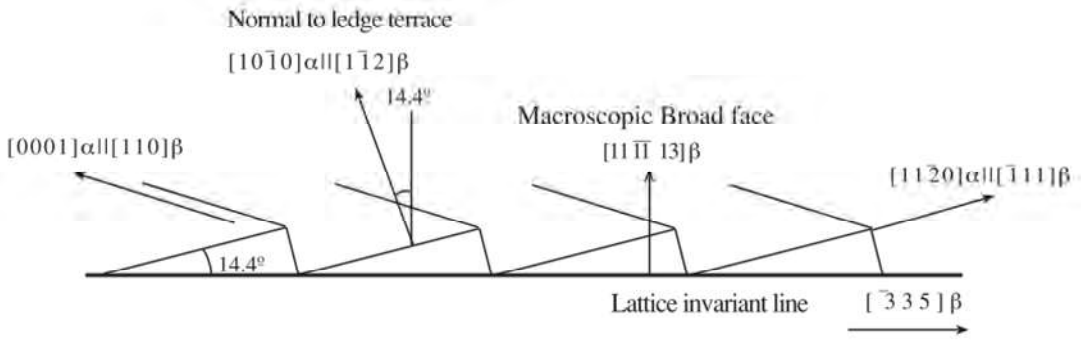

Figure 2-28 The α/β interface forming the broad face of an α lamella in an ideal lath [26].

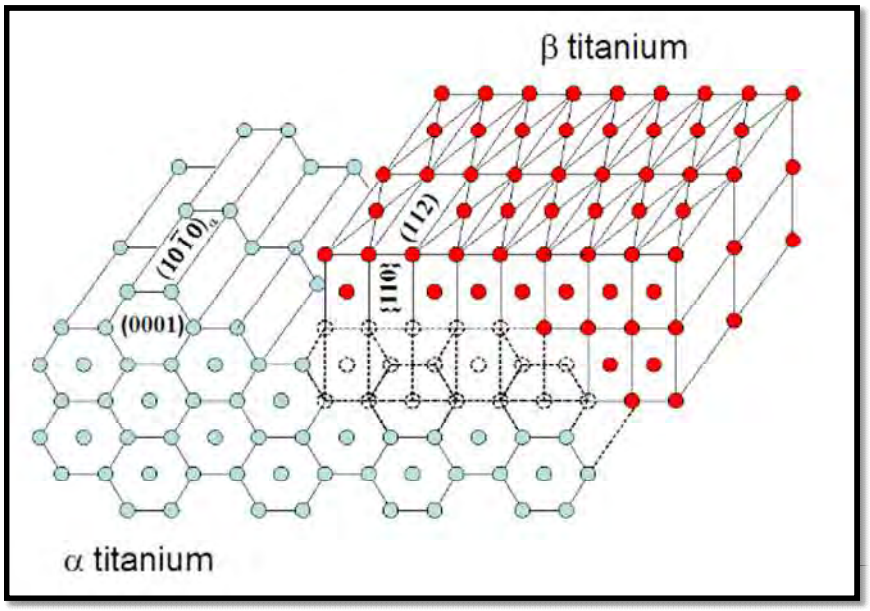

Figure 2-29 Schematic of the α-ß titanium interface via stacking of unit cells, and the resulting formation of laths.

From Figure 2-29 it can be seen that the basal plane is parallel to {101} and $\{10\bar{1}0\}_a || \{112\}_\beta$. The structural ledges on the broad face are parallel to the invariant line, the calculation of which was carried out as will the described in Chapter 5. The long faces of the interface are parallel to particular $\langle\bar{3}53\rangle_\beta$ and $\langle\bar{7}250\rangle_\alpha$, which is called the invariant line direction [31,18,32,33,34]. This is the α/β interface [26,35].

Dahmen (1982) [51] maintains that precipitate and matrix are related by an invariant line, which is one of the essential vectors to define the habit planes in numerous alloys during phase transformation. It was observed that an α precipitate which is lath shaped usually exhibits a single growth direction parallel to the invariant line direction [50]. In the early stages of growth and during nucleation, the interfacial energy affects the α precipitates, which tends to be coherent with the matrix. According to definition, structural ledges could not appear in the coherent nucleus because they localize strain in the form of dislocations, which leads to a semi-coherent α/β interface.

2.10. **Mechanisms of Slip Transmission**

Chan *et al*. [59] have studied the deformation behaviour of a colony structured α/β Ti alloy, Ti–8Al–1Mo–1V, in compression. Compression experiments on single colony samples revealed that significant yield stress variations were found with respect to the angle between the compression axis and the slip direction: they observe a failure of Schmid's law for every orientation except the specific case when slip occurred parallel to the broad face of the β phase. Interestingly, they also revealed that slip system activity strongly influences stress–strain behaviour. If boundaries are assumed to provide little resistance to slip, this hardening is likely to arise from dislocation interactions as a result of cross slip. However, no attempt to confirm the occurrence of cross slip was made in characterizing the dislocation structures in the deformed single colonies (for instance, TEM studies of dislocation activity).

The easiest activated slip system should correspond to the highest critical resolved shear stress (CRSS). Therefore, numerous studies have attempted to explain the CRSS values of Ti6Al4V under various conditions, both experimentally and computationally [29, 32, 34, 47, 48, 52–65]. However, there is no consensus on the CRSS values, particularly as they change as a function of alloy content and testing conditions. Table 2-4 presents a number of reported values for the CRSS of slip systems in single-crystal and polycrystal at room temperature for Ti6Al4V (E: experimental; S: simulated).

Table 2-4 List of the CRSS values of slip systems at room temperature for Ti-64.

Materials/testing method	Basal	Prismatic	Pyramidal <a>	Pyramidal <c+a>	Ref.
Ti-64(E)	444 MPa (Compression)	376 MPa (Tension) 392 MPa (Compression)	404 MPa (Compression)	441 MPa (Tension) 631 MPa (Compression)	[13]
Polycrystal Ti-64(E)	494 MPa (Tension) 513 MPa (Compression)	395 MPa (Tension)	395 MPa (Tension)	494 MPa (Tension) 612 MPa (Compression)	[70]
Polycrystal Ti-64(E)	373 MPa	388 MPa	-	-	[71]
Polycrystal Ti-64(S)	400 MPa	380 MPa	-	640 MPa	[72]

Table 2-4 presents the variation of the CRSS values, at the same deformation temperature and under the same test conditions. Prismatic slip is easier to activate than the other deformation modes and basal slip is much more easily activated than pyramidal <c + a> slip [2,4,12,13,15,17,56,64,73].

In the light of this uncertainty in the CRSS values in the Ti alloys, measuring these parameters on non-cubic metals utilising customary single-crystal methodologies would appear attractive.

To date, the CRSS values have been determined from single crystal CP Ti [14,74–76], Ti1.4Al [77], Ti-2.9Al [77], Ti-5Al [77], Ti-6.6Al [77], Ti-6Al [12] and Ti-6Al-4V [2–4,12,14,16,62,73,78] at temperatures ranging from room temperature to 727°C.

Nevertheless, it is not always possible to determine the CRSS values for all slip systems using routine uniaxial tests. Even for high Schmid factors, it might be difficult to generate slip on some systems when the CRSS is considerably lower on other systems. Additionally, numerous commercial metals are not available in single crystal form; they are polycrystalline or multiphase materials, making conventional methodologies difficult for understanding fundamental materials behaviour for instance, to determine the effects of the alpha/beta interface in Ti64.

The experiments performed by Suri *et al*. [17] and Savage *et al*. [15] on crystals carefully oriented for maximum resolved shear stresses have studied the room temperature deformation of single α–β colony crystals orientated for activation of a single slip system in macroscopic (3mm x 3mm x 8mm) compression of Ti-5–2.5–0.5 and Ti-6–2–4–2, respectively. Transmission electron microscopy (TEM) was used to associate the observed anisotropy to the relative Burgers orientation relationship (BOR) between the slip vectors in the alpha and beta phases, which has proven useful in providing answers to certain questions. In this regard, Suri *et al*. [17] and Savage *et al*. [15,69] demonstrated that anisotropy in deformation behaviour occurs between the three <a> slip directions in the alpha phase, which was caused by the relative misalignment of the slip systems in the beta phase. The first and second <a> slip vectors in the alpha phase had misalignments of 0.7° and ~11.5°, respectively, with the corresponding <111> slip directions in the beta phase, thus enabling easier $[a_1]$ slip transmission across the alpha/beta interface than $[a_2]$ and $[a_3]$.

Previous research tended to focus on the deformation mechanisms in macroscopic polycrystalline two-phase Ti alloy samples rather than on small-scale experiments on a localised, confined area suitable to improve our understanding of the fundamental mechanisms on the level of the individual microstructural constituents.

Current technological developments, such as the widespread availability of focused ion beam (FIB) microscopes combined with a nanoindenter or similar high sensitivity mechanical testing device have been used to determine quantitatively the CRSS for different slip systems for Ti alloys using micro-scale mechanical testing [6,79].

Specifically, Gong *et al*. [12,14,62] examined room temperature plastic deformation for the major slip systems in various Ti alloys under constant strain rate compressive loading conditions. The focus of this work was to compare the mechanical response and deformation modes in microcantilevers oriented for the different slip systems, which can be studied individually and their CRSS determined; also how the micro-cantilever width, and therefore depth, influences the CRSS values.

In Ding *et al*'s. [2–4] work FIB was used to make thin foils for TEM analysis of the dislocation structures obtained. The micro-cantilever bending experiments require crystal plasticity finite-element simulations to quantitatively determine the CRSS values for different slip systems through a procedure using modelling and comparison with experiment.

Micro-mechanical testing was applied to hcp materials to investigate the plastic behaviour of hexagonal α/β Ti alloy, where deformation by dislocations is known to be a relevant deformation mode. The relative CRSSs were determined for individual grains with visible slip bands, based on the Schmid factors on the activated slip system.

In this research, micropillar compression has been used for measurements on Ti alloys in different slip systems and crystal structures. Generally, true stress and strain can be obtained more easily than for a microcantiliever by converting load and displacement from measurements of the pillar cross-section and height, although the strains are typically overestimated owing to deformation of the top of the pillar which effectively acts as a blunt punch.

2.11. **Size effects**

In recent years there have been numerous research works on the deformation of samples at the micron and submicron scale, which exhibit higher strength compared with bulk crystals when subjected to uniaxial compression and tension [80–84].

A methodology for performing uniaxial compression tests on samples of micron size was first introduced by Uchic *et al*. [6]. They reported increasing strength with decreasing sample size. Following this approach Greer *et al*. [85] extended this fabrication technique to much smaller nanopillars and achieved reliable measurements of the higher compressive strengths attained by focused ion beam (FIB) machined cylindrical single crystalline Au nanopillars with diameters below 1 micron.

Current developments in the field of micro-mechanical testing have led to a renewed interest in a range of materials, including Au [86,87], Cu [88], Al [89,90], Ni [91–93], Mg [60,68,94–99], CP Ti [14,62,74–76,80,100], Ti6Al and Ti6Al4V [2–4,12,14,16,62,73,78].

The size effect is described a simple power-law relationship of the form

$$\boldsymbol{\sigma_y = \sigma_o + kd^n}$$

where σ_y is the flow stress, $\sigma_\circ$ is a scale independent yield stress, d is the pillar cross-section diameter, k is a constant and n is a constant parameter of the distribution known as the exponent or scaling parameter, with values ranging from 0 to 1; the magnitude of n is different for different materials.

Uchic *et al*. [8] suggested in an overview article that the relative importance of crystal orientation diminishes as the sample diameter decreases, corresponding to qualitatively similar stress-strain curves for both single slip and multiple slip orientations. Thus, some research has been carried out on the effect of crystal orientation on the deformation of FCC and BCC [9,101]; no single study exists which adequately covers HCP.

Recently, a few studies have been carried out to investigate the properties of single-crystalline HCP metals. For example, Byer *et al*. [102] and Lilleodden [95] concurrently published similar compression experiments on Mg [0001] oriented micropillars, though the two groups report diametrically opposite size-dependent strengths. The microcompression tests along [0001] on Mg carried out by Byer concluded that there was no size effect [102]. On the contrary, Lilleodden performed microcompression tests on (0001) oriented Mg, and showed a size effect on the flow stress, while no size effect on strain hardening was found [95]. Both studies concluded that deformation occurred via multiple slip on pyramidal planes. Most recently, Yu *et al*. [100] performed microcompression tests on a Ti alloy. Yu reported two

size-dependent strength regimes: one dominating at the micro-scale (pillar diameters in the range 1 to 10 μm) and strongly dependent on the sample size, where deformation is accommodated by twinning; the other size-independent and controlled by crystallographic slip, for pillar diameters <1 μm [100]. In addition, many computational efforts have been made to understand size effects in plastic flow using FEM and dislocation dynamics [12,75,80]. Undoubtedly, more definitive studies are required to understand deformation processes in HCP metals and their interactions in confined dimensions with orientation.

A commonly used explanation for size effects on mechanical properties is the strain gradient plasticity models developed by Nix and Gao [103], which could be applicable to microbending tests, as there is a size dependent strain gradient present in the deformation field. Surprisingly, Motz *et al*. [104] found that the increase in the flow stress caused by the strain gradient plasticity model cannot explain the relative experimentally observed values. Therefore, the strain gradient plasticity approach can be neglected, in order to indicate the observed size effects other restrictions must impose. A number of competing explanations have been discussed in the literature. The three most common theories proposed to explain why the mechanical strength of the metal increases with decreasing sample size are (i) dislocation multiplication, (ii) dislocation source truncation and (iii) dislocation starvation.

Dislocation multiplication is a classical treatment of increase in yield stress caused by an increase of dislocation density, known as Taylor hardening, or work hardening of metals. The trapped dislocations act as obstacles to the movement of mobile dislocations. As a result, dislocation density (ρ) and work hardening increase as dislocations become difficult to move

at increased strain. The flow stress is then the stress required for a dislocation to overcome the stress field caused by the trapped dislocations. Taylor gave the following classical expression:

$$\tau = \frac{\alpha G b}{l}$$

where α (α = 1/8π (1−υ), where υ is Poisson's ratio) is a constant accounting for the fact that dislocations are not impenetrable obstacles, l is the mean distance between the dislocations, G is the shear modulus and b is the Burgers vector.

As a consequence, in large enough samples, where dislocations can interact and multiply before disappearing at the surface, the flow strength is not size dependent, but rather dislocation multiplication-dependent with a bulk-like behaviour.

Dislocation Source Truncation evaluates the effect of sample size on the source lengths, and on their operating strength. Smaller sample volumes have statistically more double-ended sources in operation interacting with the free surfaces and resulting in truncated single arm sources. Consequently, the main source length necessarily has to decrease with sample size, as statistically demonstrated by Parthasarathy *et al*. [105]. Every single dislocation originates an elastic distortion in the lattice. Increasing the line length of a dislocation increases the overall energy of the system. To minimize this elastic lattice distortion, line tension tends to straighten the dislocation. This line tension may be defined as the increase in energy per unit increase in length of a dislocation line. Therefore, according to the line tension theory

previously introduced, the shorter dislocation length between pinned points requires a higher shear stress to operate as a source. Thus, for small enough volumes, where truncated single arm sources begin to represent a significant fraction of the overall active dislocation sources, the flow strength becomes size dependent.

Dislocation starvation One predominant theory for uniaxial compression tests on gold pillars with diameters ranging from 400 to 7450 nm proposed by Greer *et al*. [85] is referred to as 'dislocation starvation'. Once the sample is small enough, the mobile dislocations inside a small micro/nanopillar have a greater probability of annihilating at a free surface than of multiplication via cross-slip or dislocation interaction. As a result, pillars require high stresses in order to nucleate new dislocations and continue deformation.

A number of experiments support the dislocation starvation theory: Greer *et al*. [106] analysed dislocations in a deformed gold pillar using TEM. The results reveal that all the mobile dislocations escaped from the pillar during deformation except for same immobile dislocations which were left due to their lack of resolved shear stress.

A dramatic decrease in dislocation density during the nanocompression test provides direct experimental support for the dislocation starvation mechanism as given by Shan *et al*. [92].

Although the three plastic mechanisms may coexist and interact, each one of them is believed to dominate at a different length scale. For example, dislocation multiplication may dominate

in large enough volumes, where dislocations have the chance to multiply and increase the dislocation density, showing a bulk-like behaviour. On decreasing the sample volume, source truncation by the free surfaces will become more likely, while dislocation multiplication phenomena gradually decrease, giving rise to a regime dominated by the sources' operation strength. Once a critical sample volume is reached, the dislocation annihilation rate will exceed the dislocation multiplication rate leading to a starvation regime where dislocation nucleation may dominate.

So far, no scaling law with one universal power-law exponent has been found. Characterising the plastic response of samples at the micron scale via readily interpretable tests, sample fabrication flexibility and data collection precision are key to understand the complex interaction of these mechanisms and their underlying effects. However, besides sample volume, the behaviour depends in a complex manner on other parameters, i.e. the initial crystal orientation or surface state, which may not be captured in a simple power law.

2.12. Effects of initial dislocations, sample geometry and FIB on micro-compression deformation

2.12.1. Influence of the taper angle, the aspect ratio and misalignment.

In the micropillar compression experiments several errors may occur and influence the mechanical data due to the following reasons.

Firstly, the pillars are produced by FIB milling. Some amount of taper is typically introduced in the sample as also observed by Ref. [92,107]. The taper is defined as the angle between the

wall of the pillar and its axis, i.e. the top of the pillar is smaller then its bottom. The taper shape of the pillar could lead to a comparatively non-homogenous state of stress [8,108,109]. The taper angle will vary with milling conditions but is generally within 2° to 5°. The effect of taper has been studied analytically [92] and numerically by finite element modeling (FEM). These studies showed that the taper geometry results in inhomogeneous deformation, which can lead to inaccuracies in determining the flow stress and also produces an artificial increase in the strain-hardening rate . Although this leads to some variation in axial stress along the column, the taper helps to stabilize the column if there is any misalignment between the microcolumn and the flat punch [95].

Secondly, the aspect ratio (length-to-diameter of the pillar). The issue related to the lateral movement of the top sample surface during a microcompression experiment is plastic instability (buckling). Zhang *et al*. [107] and Raabe *et al*. [110] studied this aspect of testing using isotropic continuum FEM and anisotropic crystal-plasticity FEM, respectively. Both studies show that plastic instabilities occur at lower strain values for samples having either larger length-to-diameter ratios or lower platen-to-sample frictional coefficients. Raabe *et al*. [110] also studied the effect of crystal orientation and showed that crystals near but not exactly parallel to the symmetric [001] orientation display plastic instabilities at smaller strain values compared with more stable multiple-slip orientations. Nevertheless, these studies show that even for the most extreme circumstances (single-slip orientation and zero friction), the flow curves for samples having a 2:1 to 3:1 aspect ratio are not strongly affected by plastic buckling until the engineering strain exceeds a value of 5%.

Thirdly, due to misalignment between pillar‘s upper surface and the indenter tip, stress concentrations may occur on this region of the pillar, which, in turn, lead to its buckling and hence induce a bending component (Kiener *et al*.[109]).

2.12.2.The Ga ion damage

Due to the Ga ions from the FIB milling process, a damaged layer (range of several tens of nm, additional defects and dislocation loops) on the pillar surface is introduced, which may influence the mechanical properties and the observed size effect in the experiments. The extent and thickness of this damage layer are dependent on a number of parameters, including the atomic weight and bonding characteristics of the target material, the angle of the incident beam, the ion energy, and the total dose [8]. Ding *et al.* [2] studied the Ga ion damage from FIB milling process on the Ti-6Al-4V. The Ga content peaked at a depth of ~ 30 nm and dislocation segments were observed within the damaged layer but there was no evidence of significant pile-up of dislocations close to or within the layer. Moreover, Greer *et al*. [106] also selectively studied the effect of ion damage on the sample and showed that the size effect is not linked to a specific fabrication technique. While some minimal Ga+ might be present on the surface of the pillars, it is not a major contributing factor in the strength increase.

2.12.3.The coefficient of thermal expansion

The coefficient of thermal expansion (CTE) is influenced by volume expansion that occurs as a result of the transformation of the alpha HCP structure to the beta BCC structure. As the beta phase fraction increases with temperature the beta becomes progressively less constrained by the alpha phase and its lattice expands progressively up to 1000°C where the transformation is complete. The thermal expansion coefficients of different phases are not the same at the same temperature. This means that during phase transformation an alpha/beta microstructure with different thermal expansion coefficients may lead to higher thermal stresses and results in a different dislocation desity and residual stress in the Ti-6Al-4V polycrystal microstructure.

Chapter Three

3. Experimental

3.1. Introduction

In order to develop a better understanding of the slip systems present in the different phases of titanium and the role played by the alpha/beta phase boundaries, a suitable heat-treatment has been devised. Typically the beta phase has a width of around a couple of hundred nm, making the study of dislocations within the phase difficult. Therefore a series of heat treatments were sought that provided coarse beta lamellae, up to several microns across, that can easily be milled into micropillars either containing solely beta phase or with one boundary between the alpha and beta phases. The sizes of the beta lamellae are restricted by the grain size of the material and thus it follows that grain sizes up to 500 μm are required.

Following this, a variety of characterisation tools have to be used to investigate the formation of specific microstructure features during heat treatment and the subsequent analysis of defects formed during micro-mechanical testing. These include scanning electron microscopy (SEM), energy dispersion x-ray spectroscopy (EDS), electron back-scatter diffraction (EBSD) and dual beam focused ion beam (FIB) which are discussed below. Finally, transmission electron microscopy (TEM) was used to understand the alpha and beta phases and the interfaces between them.

3.2. **Materials Systems**

The alloy used in the present work was Ti-6Al-4V with chemical composition as given in Table 3-1.

Table 3-1 Chemical compositions of the Ti-6Al-4V, weight %.

Grade	**Carbon Max**	**Oxygen Max**	**Nitrogen Max**	**Hydrogen Max**
Ti6Al4V	0.08	0.20	0.05	0.015
	Al	V		
	5.5-6.0	4.0-4.5		

The rationale for choosing Ti-6Al-4V (Ti-64) is that it is by far the most important Ti alloy, accounting for more than 50% of total titanium usage. It is an alpha+beta alloy that is heat treatable to achieve moderate increases in strength. The strength of these alloys can be manipulated and thus maximized by thermo-mechanical processing (TMP) which results in parallel alpha plates separated by beta phase. The microstructural evolution for furnace cooled microstructure is shown in Figure 3-1.

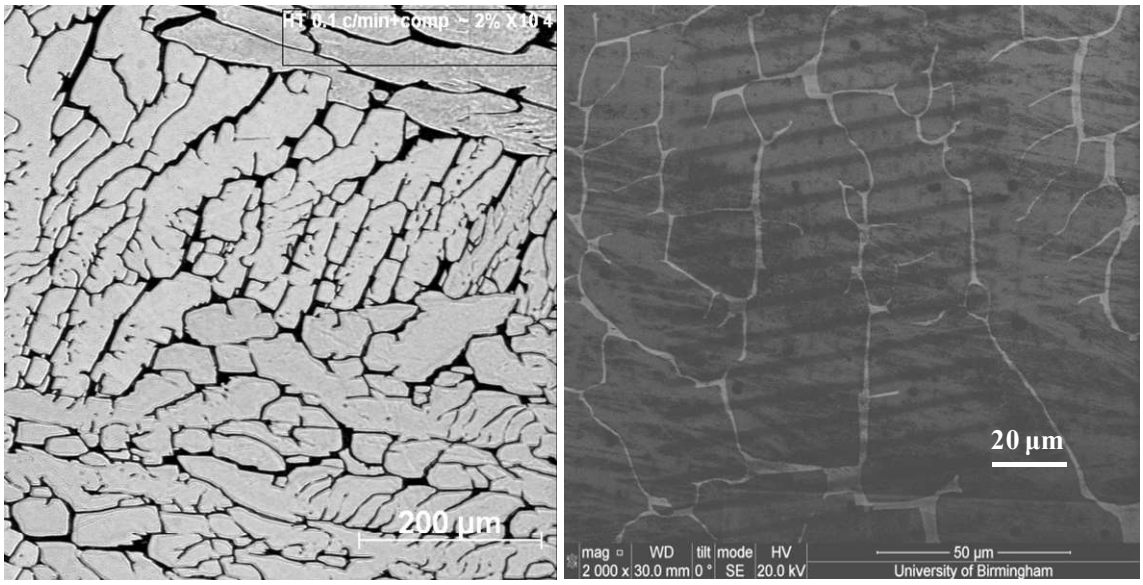

Figure 3-1 Micrograph of Ti6Al4V furnace cooled from 1100°C (a) optical micrograph (b) SEM images through the alloy showing a nearly equiaxed, randomly oriented alpha + beta microstructure.

3.3. **Tube Furnace**

A tube furnace was employed for the heat treatments on Ti64. The furnace consists of an outer box enclosing a series of hard ceramic layers. The ceramic, usually alumina (Al_2O_3), encloses graphite heating coils and provides a cradle for a central alumina tube extending the entire length of the furnace and extending into the open air as shown in Figure 3-2. A specimen is inserted into the central tube and positioned in the centre of the furnace and monitored by a K-type thermocouple to ensure the desired temperature was reached. The ends of the tube are then connected to a vacuum system. The tube was evacuated to 10^{-6} Torr before being backfilled three times with high purity argon to remove any oxygen present.

Figure 3-3 Tube furnace employed for the heat treatments .

3.4. **Sample preparation techniques**

The specimen microstructures were examined after heat treatment using both optical and scanning electron microscopes. In order to reveal the microstructure, the heat treated specimen is first mounted in conductive Bakelite using a combination of 7 minutes heating and 7 minutes water cooling. Then, a smooth surface is achieved by grinding using water-lubricated silicon carbide papers through 200, 400, 600, 800 and 1200 grit respectively with a rotating disc at speeds between 200 and 300 rpm for about 2 to 5 minutes.

The preparation of suitable specimens for EBSD measurements is somewhat challenging requiring very well polished specimens beyond what is achievable by grinding alone. In order

to achieve a 'mirror-like' finish a series of diamond abrasives were used on Struers polishing cloths; the steps are detailed in Table 3-2. This removes any deep scratches in the surface due to the grinding process.

Table 3-2 Types of Struers polishing cloths used at different stages.

Polishing cloths	Polishing	Times
MD-Largo	9 µm	5 Minutes
MD-Dur	6 µm	5 Minutes
MD-Mol	3µm	5 Minutes
MD-Chem	1 µm	15 Minutes
MD-Nap	0.5 µm	45 Minutes

Finally, colloidal silica polishing (i.e OPS) was performed using a combination of colloidal silica emulsion and hydrogen peroxide for one hour. Once the final polish was achieved, the samples were rinsed in warm water before being cleaned by immersion in methanol in an ultrasonic cleaning bath for 10 minutes. EBSD was then used to identify suitable grains for micromechanical testing.

3.5. **Micro-mechanical testing**

Micro-compression is a new method of mechanical testing that allows the measurement of mechanical properties on localized micron-scale volumes of material, in addition to the observation of deformation on a micro-scale. Small scale testing offered a unique opportunity to create single crystal or single colony samples out of material with sufficiently large grains.

Following the micro-compression work of Uchic and Dimiduk on Ni-based alloys [6], a preliminary investigation into the micropillar mechanical properties of alpha and beta phase Ti64 was conducted. To perform homogeneous deformation tests at micron-scale 1 to 6 μm diameters pillars were machined with a focused ion beam (FIB).

Tests were performed *in-situ* in a Tescan Mira XM3 FEG-SEM using a Hysitron PI-85 picoindenter equipped with a 20 μm diameter diamond flat punch tip. A schematic diagram of the micro-compression test is shown in Figure 3-4. It is essential that the top and bottom surfaces of the specimen should be parallel to minimize contact misfit between the sample surface and the compression platen. This was followed by attaching the specimen using silver DAG paint to the special holder for PI-85 as shown in Figure 3-5.

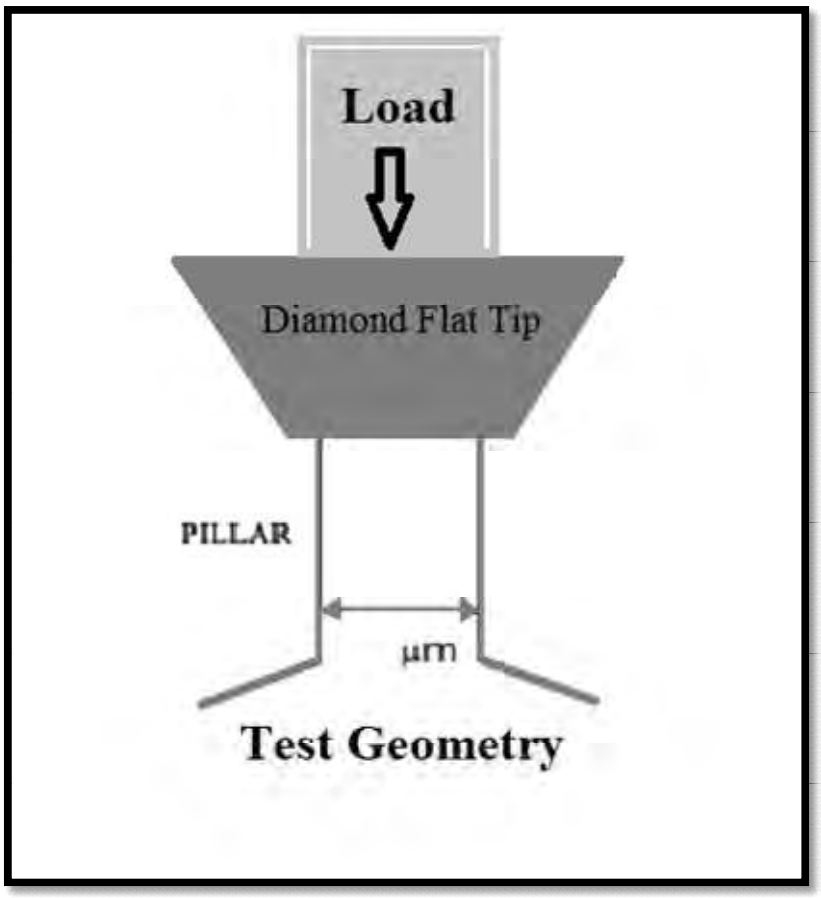
Load
Diamond Flat Tip
PILLAR
µm
Test Geometry

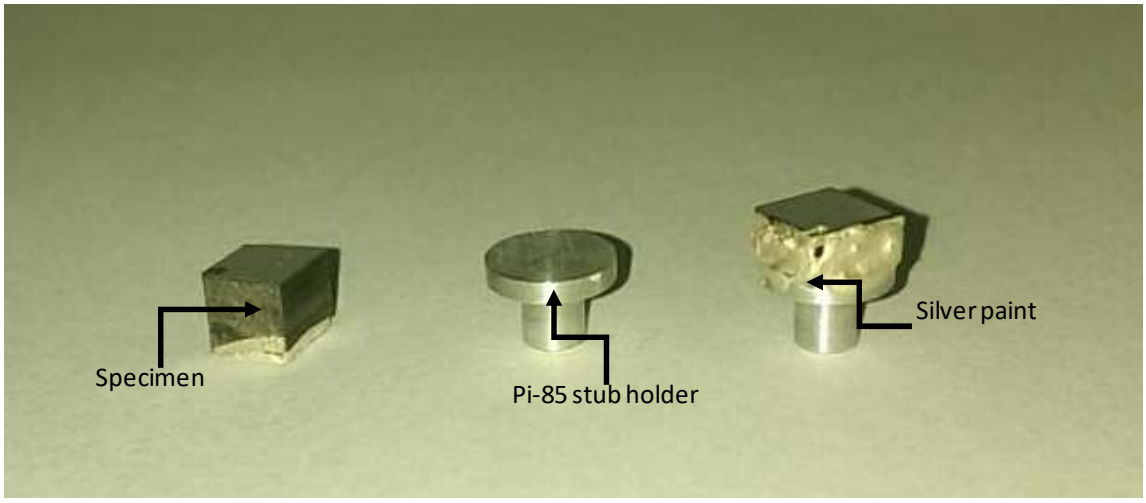
Specimen
Pi-85 stub holder
Silver paint

Micro-pillars were machined using an FEI Quanta 3D FEG dual-beam FIB-SEM to fabricate cylindrical pillars from the alpha, beta and alpha/beta/alpha colonies in a fully lamellar and equiaxed Ti–6Al–4V alloy with extremely large (500 μm) grain size. The pillar diameters ranged from 1 to 6 μm with an aspect ratio between 2:1 and 3:1, as illustrated in Figure 3-6.

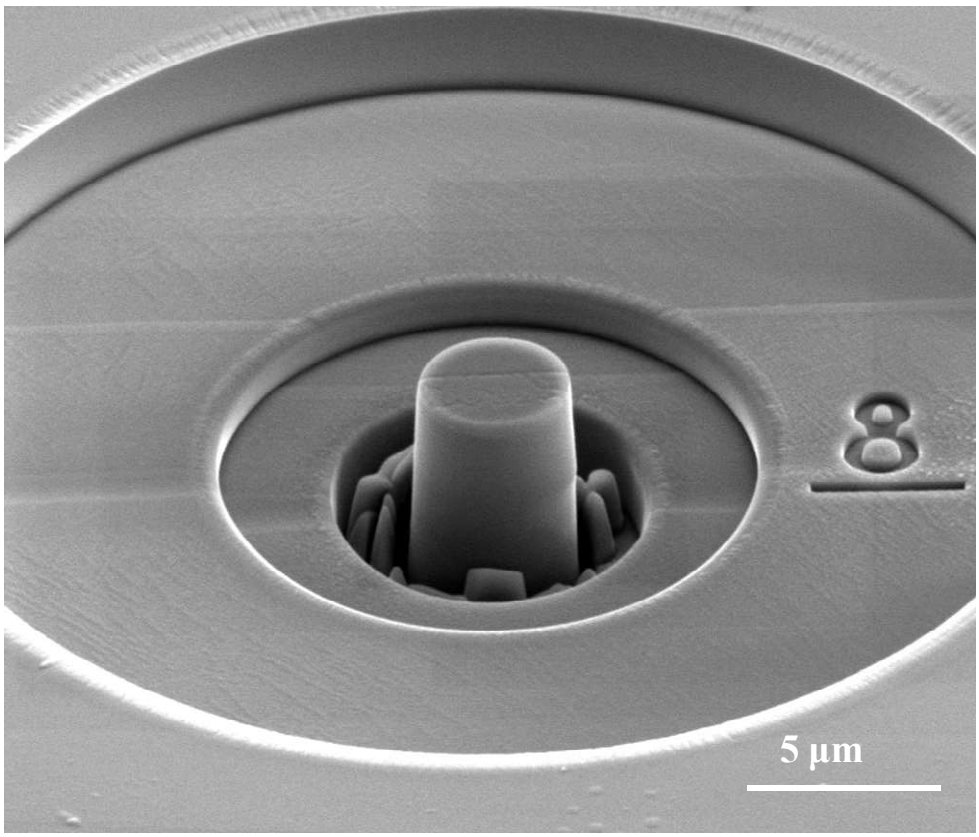

Figure 3-6 Typical SEM image of micro-pillar fabricated by FIB.

Before deforming the micro-pillars, SEM images were taken from a number of angles to ensure uniformity and to measure their dimensions. Several micro-mechanical tests were performed on specimens from each crystal orientation. At least three specimens for each phase (alpha, beta and alpha/beta/alpha), size and crystal orientation were tested to work out

mechanical properties of each individual phases and the strengthening due to the interfaces; these were then correlated with the macroscopic mechanical property measurements. In addition, several additional compression tests were performed, but halted at various strains, in order to identify the planes of the slip bands and to measure the size of the slip steps. The Hysitron software provided data files containing raw Load-Displacement data. These were in addition to the measurements of the original dimensions of the specimen from the SEM images (diameter and height); the true stress and strain of each pillar were then calculated from this information. The relations 3-1 to 3-10 give the different definitions of stress and strain and the relations used to calculate the ones from the others.

Engineering stress-strain and True Stress-strain

$$\text{Engineering stress} \qquad s = \frac{F}{A_\circ} \tag{3-1}$$

$$\text{True Stress} \qquad \sigma = \frac{F}{A} \tag{3-2}$$

$$\sigma = \frac{F}{A} = \frac{F}{A_\circ}\frac{A_\circ}{A} \tag{3-3}$$

$$\text{Engineering strain} \qquad e = \frac{\Delta L}{L_\circ} = \frac{1}{L_\circ}\int_{L_\circ}^{L} dL \tag{3-4}$$

$$\text{True strain} \qquad \varepsilon = \int_{L_\circ}^{L}\frac{dL}{L} = \ln\frac{L}{L_\circ} \tag{3-5}$$

$$e = \frac{\Delta L}{L_\circ} = \frac{L - L_\circ}{L_\circ} = \frac{L}{L_\circ} - 1 \tag{3-6}$$

$$e + 1 = \frac{L}{L_\circ} \tag{3-7}$$

$$\varepsilon = \ln\frac{L}{L_\circ} = \ln\ (e + 1) \tag{3-8}$$

And by the constancy of the volume:

$$\frac{\mathrm{A}_\circ}{\mathrm{A}} = \frac{\mathrm{L}}{\mathrm{L}_\circ} = \mathrm{e} + 1 \tag{3-9}$$

And so,

$$\sigma = \frac{F}{A_\circ}\ (e + 1) = \ s\ (e + 1) \tag{3-10}$$

where L is the instantaneous gauge length,

L_o the initial gauge length,

F the force applied to the sample,

A the instantaneous cross section of the sample,

A_o the initial cross section of the sample.

In the following chapters, micro-mechanical test results will always be presented in the form of true stresses and strains.

3.6. **Compression sample preparation**

Once a suitable grain and colony were identified via EBSD a smaller specimen than the optical and electron microscope samples for the compression testing was carefully cut from the EBSD sample and re-polished from the 6 μm step detailed in Table 3-2. In order to

compress the micro-pillars, the sample needs to be sufficiently small, in this case around 5mm x 5mm x 5mm, to fit in the PI-85 as illustrated in Figure 3-5. Extra care was taken to keep the specimen as parallel as possible to the flat punch tip to reduce the misalignment between them. The Ti6Al4V specimen was then fixed onto a specimen stub with super glue and silver paint. On occasion the specimen can become damaged during handling, especially since conventional tweezers are unsuitable for gripping the sample stub and therefore extra care was taken. The sample and sample stub are shown in Figure 3-7.

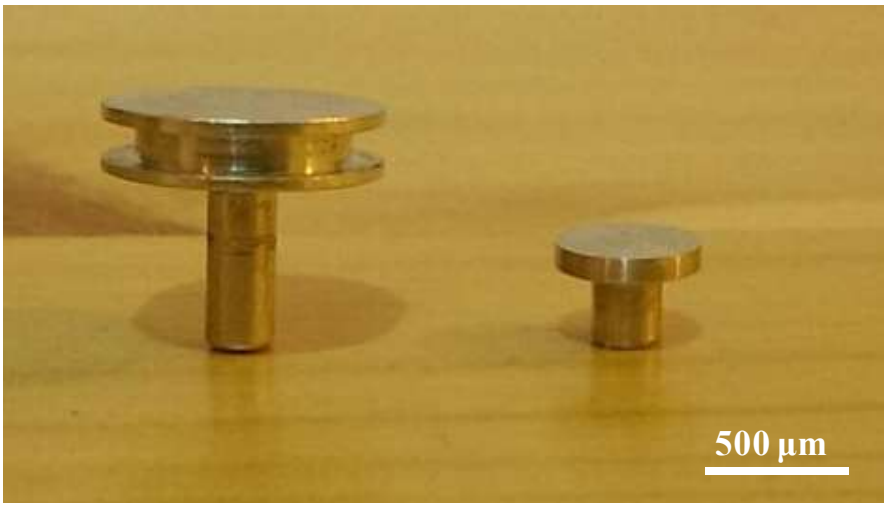

The micro-pillars were fabricated as cylindrical cross-section prisms. The FIB functions by accelerating large gallium ions towards the surface of the samples to remove preferentially material from areas around the centre point of the circle (inner diameter of FIB pattern). Consider the geometry of the FIB stage as displayed in Figure 3-6. For the purpose of machining pillars, the ion beam is aligned normal to the sample surface, which corresponds to a tilt angle of 52º. As material was removed, a cross-sectional taper forms toward the base of the micro-pillar; this is unavoidable in FIB sample preparation.

A high current beam of 20 nA is used to bore a toroidal hole into the surface to create a rough outline of the pillar shape. The milling parameters were then carefully selected in order to reduce the taper angle as much as possible, as listed in Table 3-3.

Figure 3-8 shows the micro-pillar after the final milling where *Di* is the diameter of the inner circle, *Do* is the diameter of the outer circle and *Z* is the milling depth (in this case the height of the pillar). The milling direction should be selected from outer to inner (*Do* to *Di*) rather than inner to outer (*Di* to *Do*) in order to reduce re-deposition on the sides of the pillar.

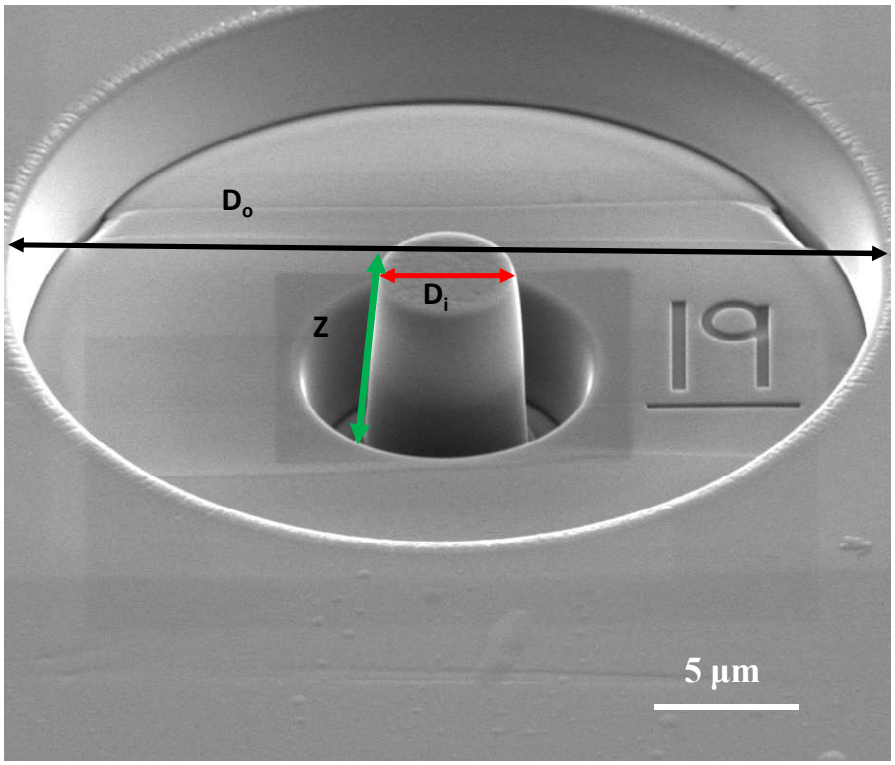

The milling process removes material between the inner and outer circles, the size of which are reduced with each subsequent milling step as detailed in Table 3-3. There are many

advantages of having a relatively large crater size. It is crucial to prevent any contact between the indenter tip and the material surrounding the micro-pillar. It also allows the entire pillar to be inspected prior to and after deformation. Under compression, large craters can help to locate the micropillars on the sample, as they can be seen even in an optical microscope.

Table 3-3 Typical milling conditions for the 1, 2 and 4 µm micropillars at 30 kV. D_o and D_i are the outer and inner diameters at different stages, and Z is the input milling depth. I is the milling current

Pillar Diameters	**1 µm**			**2 µm**			**4 µm**		
I (nA)	D_o (µm)	D_i (µm)	Z (µm)	D_o (µm)	D_i (µm)	Z (µm)	D_o (µm)	D_i (µm)	Z (µm)
20	-	-	-	-	-	-	45	20	2.5
15	45	15	0.75	45	15	1	25	15	1
5	20	6	0.25	20	8	0.5	18	8	1
1	10	2.5	0.25	12	4	0.25	10	6	0.5
0.5	6	2	0.2	6	3	0.25	8	4.3	0.25
0.3	3	1.2	0.1	4	2.2	0.1	5	4.2	0.25
0.1	1.5	1.1	0.1	2.5	2.1	0.1	4.5	4.1	0.1
0.05	1.2	1.1	0.05	2.2	2.1	0.05	4.2	4.1	0.05

3.7. **TEM sample preparation**

Due to the site specific nature of the samples required, the only practical way for TEM sample preparation is to use a FIB to locate precisely the area of interest and to extract the required TEM foils. Twin-jet polishing was not suitable for this research not just because the sample sizes are too small but in the case of the undeformed sample the beta phase dissolves in the chemical solution before the alpha phase achieves the required thickness. TEM foils were extracted from the undeformed pillars as well as the deformed cylindrical pillars. Foils of tri-crystal pillars alpha/beta/alpha were extracted along the plane perpendicular to both the beta phase plane and the top surface, as shown in Figure 3-9. Foils of deformed single crystal pillars were extracted along planes perpendicular to the top surface.

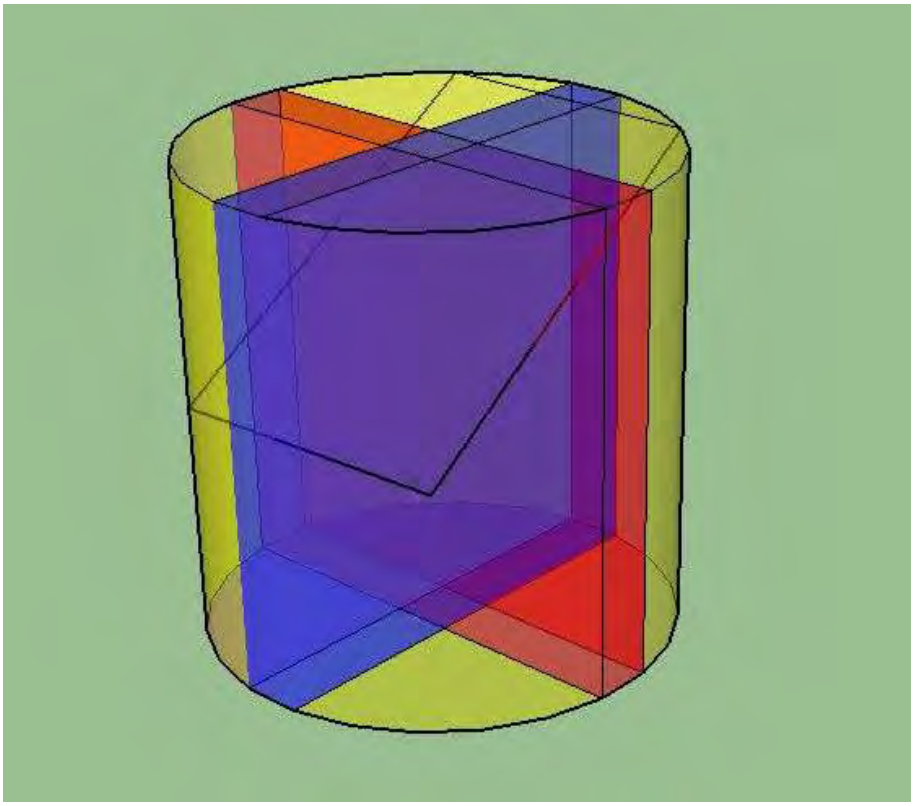

Figure 3-9 Extraction of foils along the plane perpendicular to both the beta phase plane and the top surface.

Caution was taken during the milling to decrease re-deposition and curtaining effects. The steps involved are described below:

1) The surface of the specimen was tilted to 52°(Figure 3-10 (a) and Figure 3-10 (b)), making the top of the pillars normal to the ion milling source. A protective Pt layer was deposited on the top surface of the pillar to protect it from subsequent milling (Figure 3-10 (c). This coating was 4 μm in thickness.

2) Another Pt layer was deposited on the exposed side surfaces after the sample was tilted by 7° and rotated by ± 90° (Figure 3-10 (d) and (e)). These depositions provide additional anchorage for welding the foil to the TEM Cu-grid. As the pillar was very small, a low current (0.1 nA) ion beam was used.

3) Following the Pt deposition, the pillar was tilted back to 52°. A rectangular trench was dug either side of the Pt strip on the pillar (Figure 3-10 (f) and (g)) to thin the pillar to about a 2 μm strip.

4) The strip was tilted to 7° to the horizontal and a U-cut pattern was milled on the strip (h).

5) The strip (at 0°) was attached to the Omniprobe micromanipulator by depositing Pt (Figure 3-10 (i)).

6) This was followed by separating the strip from the bulk sample (Figure 3-10 (j)) and attaching it to the Cu grid with Pt, as shown in (Figure 3-10 (k)). Once attached, the Omniprobe was detached from the strip by milling.

7) More Pt was deposited on the other side of the foil to reinforce the attachment (Figure 3-10(l)).

8) The specimen (strip) was tilted back to 52° and thinned to about 200 nm with the ion beam current set sequentially to 0.3 and 0.1 nA (Figure 3-10 (m)).

9) Finally, the specimen was tilted a further ± 7° and a final polishing (at 44 pA, 5 kV and 16 pA 2 kV) was applied to improve surface quality and to reduce the Ga effect (Figure 3-10 (o)).

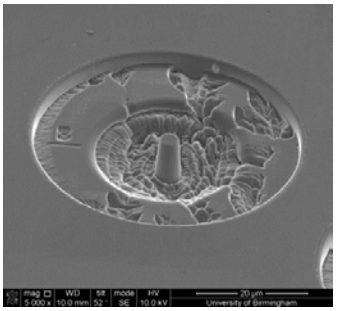

(a)

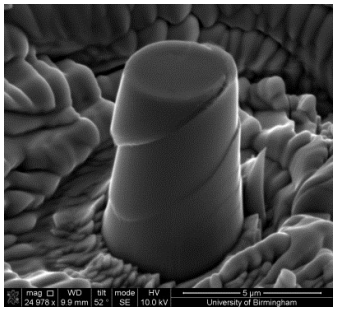

(b)

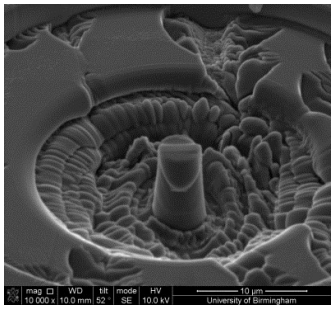

(c)

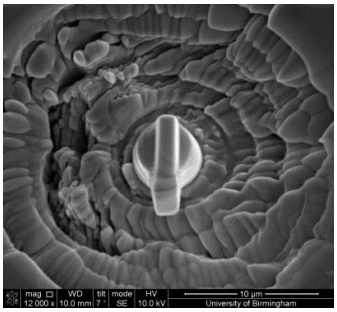

(d)

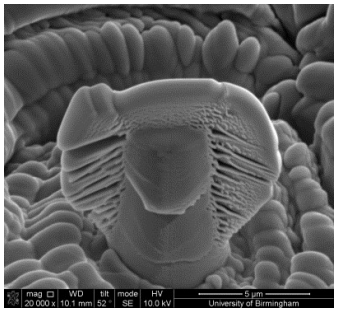

(e)

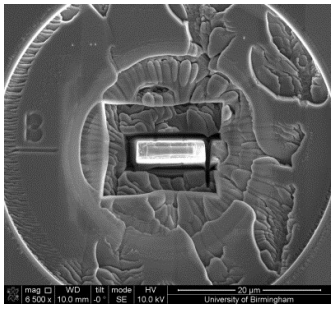

(f)

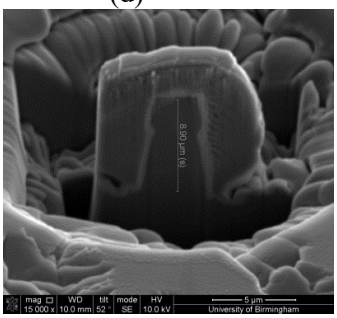

(g)

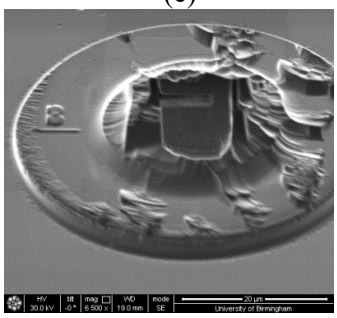

(h)

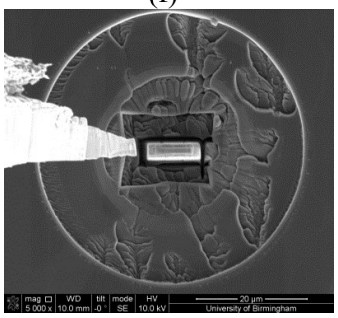

(i)

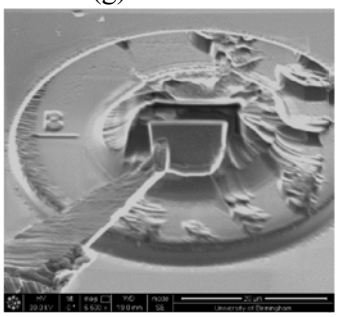

(j)

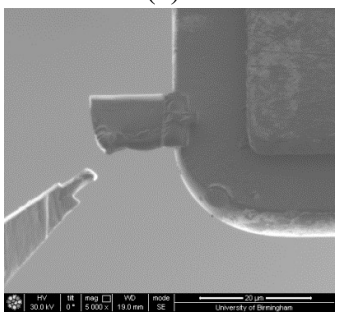

(k)

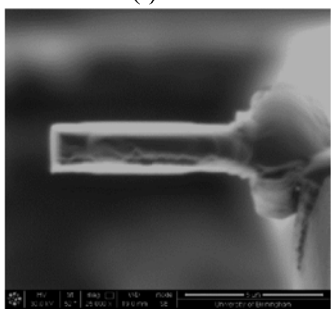

(l)

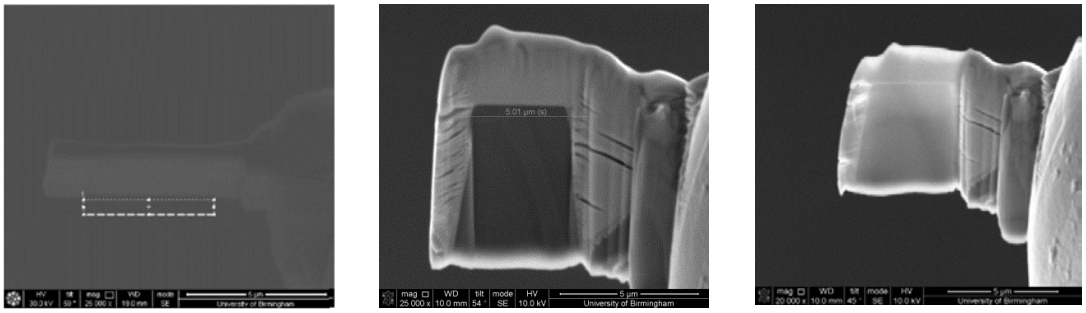

(m) (n) (O)

Figure 3-10 TEM sample preparation: (a) SEM image of a pillar before deformation (b) SEM image of an as-compressed pillar. (c) SEM image of the pillar after Pt-coating on the top. (d) SEM image of Pt-coating applied to the side surface. (e) SEM image of the pillar after coating. (f) SEM image of the rectangle dug around the pillar. (g) SEM image of the pillar strip. (h) Ion beam image of the strip after a U-cut pattern was milled. (i), (j) and (k) SEM images of the strip where the Omniprobe was inserted and adjusted to the strip and then welded. After that the strip was lifted out by the Omniprobe. (l) Ion-beam image of the strip attached to the Cu grid. (m) The back of the strip was welded to the Cu grid to reinforce the attachment. (n) Ion beam image of the thinned TEM specimen. (o) SEM image of the TEM specimen from different viewing directions showing obvious alpha/beta/alpha phases.

3.8. **Measuring plasticity**

Plastic deformation in compression of both the single crystals and polycrystals is straightforward to achieve on an observable scale. Where it is possible for dislocations to pass through the whole width of the sample, slip steps will be formed on the surface. By measuring the angle between the trace of the slip plane and the compression axis where the crystallographic direction is known by EBSD, the slip plane can be identified. Determining the interface strengthening of the single crystals and the polycrystal by this method requires knowledge of the full crystallographic orientation of the sample and the higher Schmid factors.

3.9. **TEM Examination**

TEM examination was adopted to investigate the arrangement and the density of dislocations inside the deformed sample. In this work, bright field images were taken using different g vectors. Burgers vector analysis was used to study the characteristics of the remaining dislocations. Montage images were assembled from individual micrographs. This provides the advantages of capturing the dislocation distribution of a pillar and lowering the errors in estimating the dislocation density.

3.10. **Scanning Electron Microscopy (SEM)**

The various microscopes employed in this work were a JEOL 7000 field emission gun (FEG-SEM), a Tescan Mira XM3 field emission gun (FEG), an FEI Philips XL-30 and the electron column in the FEI-FIB200 Dual Beam. The Scanning Electron Microscopes (SEM) used in this research were equipped with the secondary electron (SE), back scattered electron (BSE) detector, electron back scattered diffraction (EBSD) camera combined with HKL detector (phosphorus screen + Charge Coupled Discharge (CCD) camera). Data collection and analysis software (INCA, Chanel 5 and Aztec) packages were used. The purpose of these was to identify the crystal orientation, determine the dimensions of the samples prior to testing, to visually inspect the samples after testing and in particular to examine the slip trace morphology and the distribution of dislocations. Also, *in-situ* SEM was used to observe and record the beginning of plastic deformation during the straining of the sample.

3.11. Electron Backscatter Diffraction (EBSD)

The electron backscattered diffraction technique was used to acquire a crystal orientation map of the specimen using a Tescan Mira XM3 along with EBSD acquisition software (Aztec), or a Philips XL-30 scanning electron microscope with Flamenco EBSD acquisition software. The electron beam hits the specimen which is tilted 70° from the horizontal axis. Some of the incident electrons will be backscattered by the specimen and then create a Kikuchi pattern which is imaged on a phosphor screen. The bands in the pattern represent the reflecting planes in the diffracting crystal volume. Thus, the geometrical arrangement of the bands depends on the orientation of the diffracting crystal lattice. The working distance was between 15 and 17 mm and the accelerating voltage 20 kV. The step size for a detailed orientation map scan was set to 0.2 μm. Channel 5 software was utilised for the collection and identification of EBSD patterns. The Kikuchi patterns were collected by a sensitive CCD camera. A schematic diagram of a typical EBSD installation in an SEM is provided in Figure 3-11.

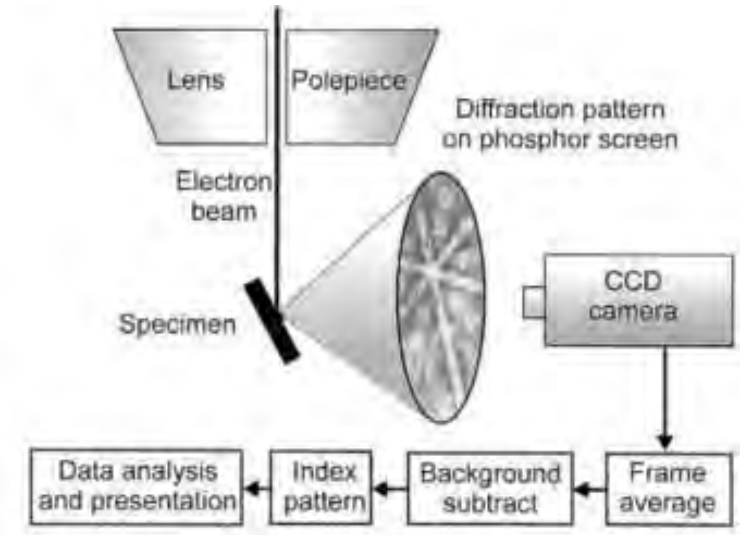

Figure 3-11 Schematic of the electron backscattered diffraction technique.

The loading direction was selected to be as closely as possible 45° to the c-axis for basal slip, 90° for prismatic slip and 0° for c+a pyramidal slip in the alpha phase. The benefit of selecting these orientations is that during deformation Schmid factors on the other slip systems are close to zero.

EBSD data can be presented as an orientation map, as pole figures or inverse pole figures in order to view the crystal orientation and misorientation information.

3.12. Energy dispersive X-ray spectroscopy (EDS)

EDS was used to analyse the chemical composition and to identify the elements present in the samples. The electron beam of the SEM is used to excite the specimen and a scintillation counter is used to collect the x-rays and generate a plot of intensity versus x-ray energy to determine the elements present. In the SEM system, an accelerating voltage of 20 kV was used, and a small spot size was chosen to reduce the probe current. It should be noted that the resolution of the EDS analysis is defined by the size of the interaction volume, not by the spot size.

3.13. The Focused Ion Beam (FIB)

The FIB allows various micro-machining procedures. The FIB can be used to make a series of sections of the microstructure which can be produced as 3D representations. The FIB can also machine specimens from single crystal or polycrystalline pillar structures for micromechanical compression tests. In addition, the FIB is used to fabricate TEM foils from certain regions of interest in a microstructure.

The FIB makes use of a gallium liquid metal ion source (LMIS) to generate an ion beam oriented 52° from the vertical axis to machine the sample surface. A schematic diagram of a typical FIB microscope in an SEM is provided in Figure 3-12. A variety of geometries can be produced such as circles, rectangles and even free form shapes. The ion beam is set to 30 kV

with the beam current ranging between ~1.5 pA to 65,000 pA. Low beam currents are more suited for detailed and fine polishing of samples, whilst high beam currents are best for rapid removal of material.

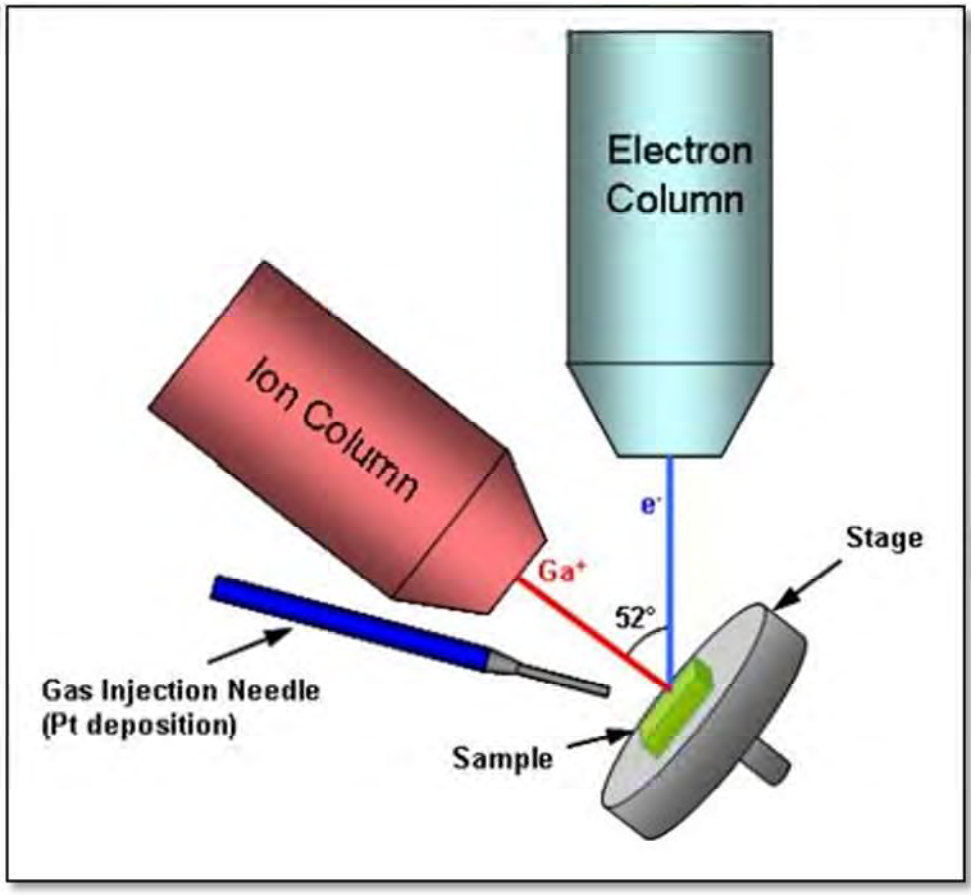

The nano-fabrication capability of the FIB is essential for detailed small scale analyses of metallic specimens. The intricate “slice and view” software capabilities programmed directly into the FIB control algorithms enable the development of a range of techniques for fabrication on the sub micron scale. The ion beam can be accurately positioned with respect to the electron beam to facilitate reproducible serial sectioning of a sample to reveal 3D

morphology in an area of interest. Moreover, the accurate positioning of the ion beam, electron beam and stage enable the fabrication of 200 nm to more than 20 μm cylinders for micro-scale compression testing.

FIB and SEM technologies conjointly enable small scale 3D materials characterisation, analysis, and manipulation. By deposition or removal of material the ion and electron sources allow high-resolution imaging of subsurface structures and sample manipulation for the purpose of patterning, repairing or prototyping. The small stage Dual Beam TM systems are highly suitable for producing thin samples for STEM and TEM analyses.

The FIB allows the fabrication of micro-compression samples from the surface of a bulk crystal with precise control over the size and location of the resulting specimen. Usually, the sample diameter ranges from 200 nm to 20 μm. The benefits of testing at such scales include the ability to measure and probe the sample properties. This can involve measuring the 'single crystal' response of individual grains in a polycrystalline system and to methodically investigate intrinsic size effects created by plastic deformation processes. Figure 3-13 shows the FEI Quanta 3D FEG dual-beam FIB-SEM used in this research.

Figure 3-13 The FEI Quanta 3D FEG dual-beam FIB-SEM

3.14. Nanoindentation

Using nanoindentation, the scale of penetration can be measured to a depth resolution of < 1 Å and a force resolution of several nanonewtons. Nanoindentation involves pressing into the surface of a specimen a sharp indenter with geometry matching those of macroscopic indenter tips. Typically, it is used to determine the Young's modulus and hardness of the specimen from the load and penetration depth, although in this case the nanoindenter was used to carry out uniaxial compression instead of a sharp indentation. A custom-made diamond flat punch indenter tip was prepared using FIB, as demonstrated in Figure 3-14.

Here, an Agilent Nano Indenter PI-85 was used to perform the compression tests. The main components are shown in Figure 3-15. The load is applied by a coil that moves as a result of a magnetic field. The displacement is determined using a capacitance gauge, since it is relatively simple to measure the distance between two parallel plates in an AC bridge circuit if the capacitance is known. This PI-85 nanoindenter has a load resolution of the order of 50 nN and a displacement resolution of 0.1 nm, which makes it ideal for probing very small spaces.

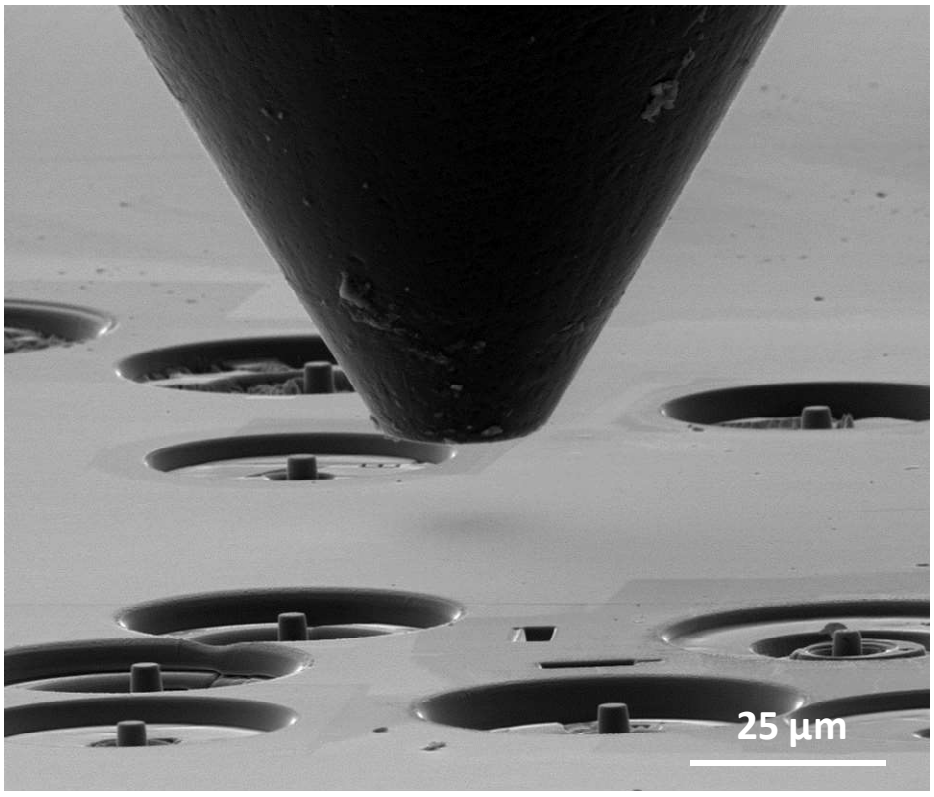

Figure 3-14 Diamond flat punch indenter tip for PI-85.

The samples are loaded into the nanoindenter and separate samples (alpha, beta, alpha/beta/alpha phases) were selected for testing. The flat punch tip is brought into contact with the top surface of the micropilllars to perform the micro-compression test. Before testing, the sample cross-sectional area and gauge length are measured, since these are required to convert the load- displacement data into a stress-strain curve using the standard formulae for compression tests. These dimensions are typically obtained from SEM images. Examples in the literature can be found of both load controlled and displacement controlled testing, but a majority of experiments concentrate on performing constant displacement rate tests where the initial strain rate is ~ $2.5 \times 10^{-4} s^{-1}$.

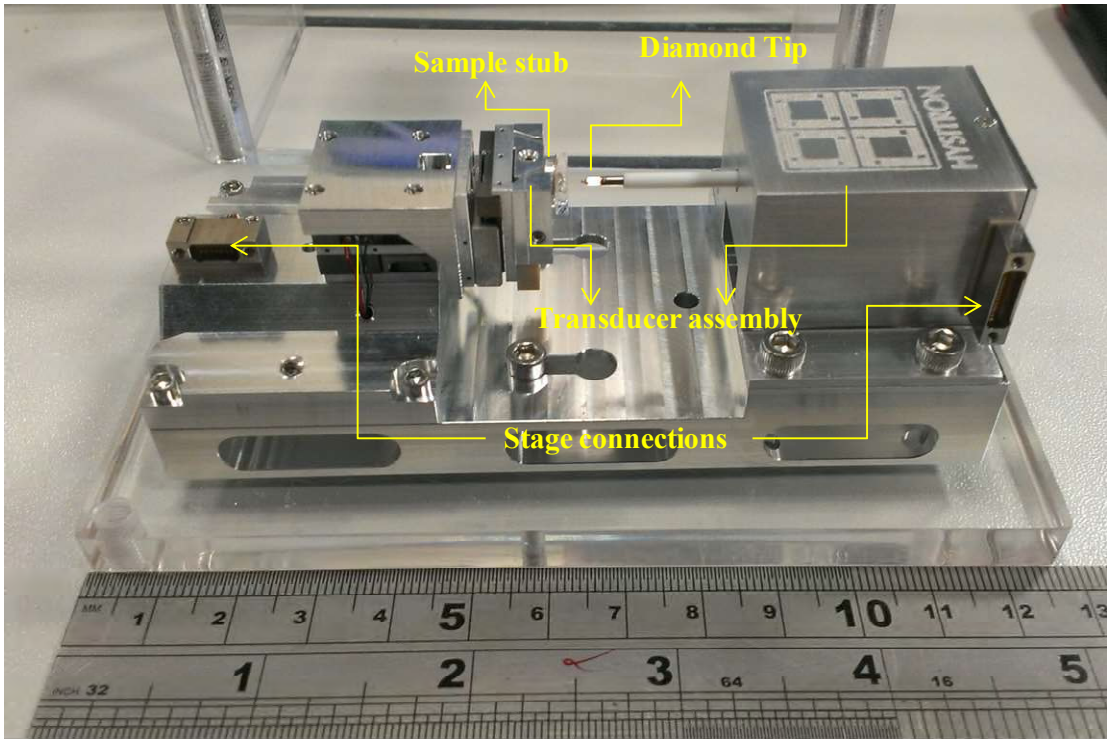

Figure 3-15 The SEM PicoIndenter PI-85.

3.15. Transmission Electron Microscopy (TEM)

Transmission Electron Microscopy (TEM) was carried out in JEOL 2100 and Philips Tecnai F20 microscopes operating at 200 kV. The JEOL 2100 instrument was utilised primarily for bright field (BF TEM), dark field (DF TEM) and diffraction (ED) imaging when a large tilt range was necessary for microstructural analysis. The Tecnai instrument, fitted with high angle annular dark field (HAADF STEM) imaging as well as for energy dispersive spectroscopic (EDS) analysis was primarily utilised for scanning transmission electron microscopy (STEM) in bright field (BF STEM) or dark field (DF STEM) as well as for energy dispersive spectroscopic (EDS) analysis.

TEM transmits very high energy electrons which have a very small wavelength (0.025 Å) through a thin sample (electron transparent) to image and analyse the microstructure of the materials with high resolution. This small wavelength of the electrons allows the observation of planar and line defects, grain boundaries, interfaces, morphologies, crystal phases and defects present in the material. In order to understand the whole dislocation distribution in the pillar, montages of the whole sample were constructed from smaller images. Sample preparation for TEM generally requires more time compared to other characterisation techniques.

Diffraction according to Bragg's law occurs whenever the Ewald sphere (sphere of radius: 1/wavelength) touches a point on the reciprocal lattice. In many/multi-beam conditions,

diffraction occurs for all the reciprocal lattice points (diffraction directions) lying close to the Ewald sphere.

For two-beam conditions, the reciprocal lattice is rotated by appropriate double tilts (X and Y) so that a particular g (hkil) satisfying the Weiss zone law is brought exactly to the Ewald sphere. It is known as two-beam since only the (0000) and (hkil) (i.e. only two directions) are on the Ewald sphere.

In this work, two-beam conditions were used to observe the dislocation distributions in the specimens, and bright field images were taken at different diffraction conditions.

Bright field (BF) TEM observations were made by tilting the sample to obtain a two beam condition and then inserting the objective aperture over the transmitted spot. Weak beam imaging was accomplished by using the dark field tilts to move the +g diffraction vector onto the optic axis and by inserting the objective aperture over the +g diffraction vector.

g.b analysis was performed to identify the nature of the dislocations present in the alpha and the beta phase and in some cases line direction analysis was also performed to identify the line direction of the dislocations and help determine the slip plane of the dislocations.

Chapter Four

4. Micro-mechanical properties

4.1. Introduction

This chapter is concerned with the deformation of Ti64 alpha, beta single phase crystals and alpha/beta/alpha tri-crystals all in the form of cylindrical pillars of different orientations and with diameters varying from 1 to 6 μm. The focus was on working out the strengthening due to the interfaces and (inevitably) any size effect. To the best of our knowledge, no systematic investigation of the effect of orientation on the strengthening or the size effect of Ti-6Al4V micropillars has been published so far. The micro-mechanical tests were performed using nano-indentation interpreted using scanning electron microscopy (SEM) in subsequent chapters.

The original material was heat treated at 1100°C for 3 hours to produce an equiaxed α/β lamellar microstructure with beta phase between the α grains as shown in Figure 4-1a. The alpha phase lamellae have an orientation that is related to the beta phase according to the Burgers orientation relationship, while the beta phase remains from the original large beta grains as shown in Figure 4-1b.

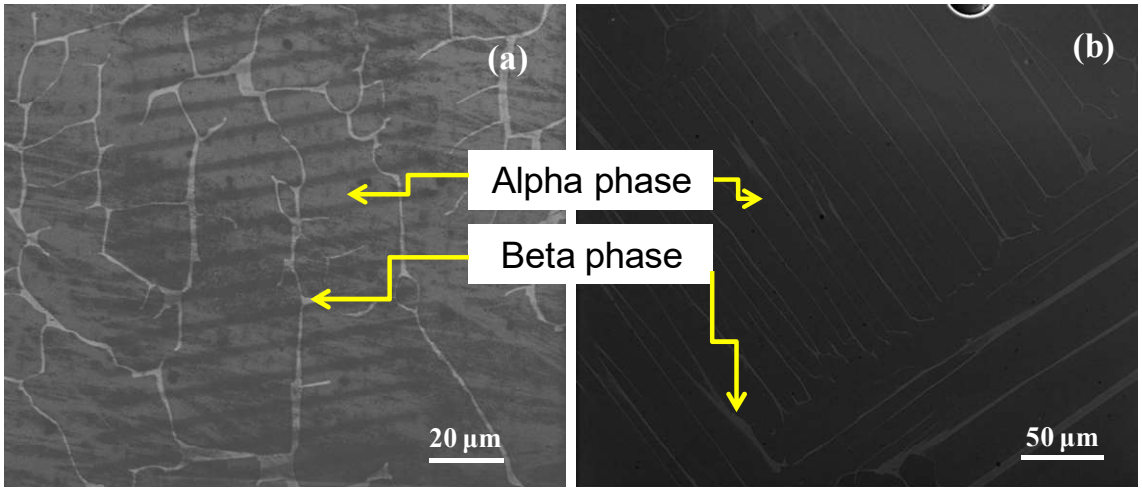

Figure 4-1 SEM of Ti6Al4V furnace cooled from 1100°C. Two different microstructures occur: (a) equiaxed microstructure (the common situation) and, more rarely, the (b) lamellar microstructure (basal plane parallel to polishing surface). The bright phase in both micrographs is beta and the dominant phase alpha. Both (a) and (b) have been used in what follows.

The selected orientations were identified using electron backscatter diffraction (EBSD). The alpha phase has been chosen to define the loading direction as it is the dominant phase. The remanent beta grains are very narrow compared to the alpha grains and therefore using an EBSD step size of 6 µm it was very difficult to obtain accurate data from the beta phase in

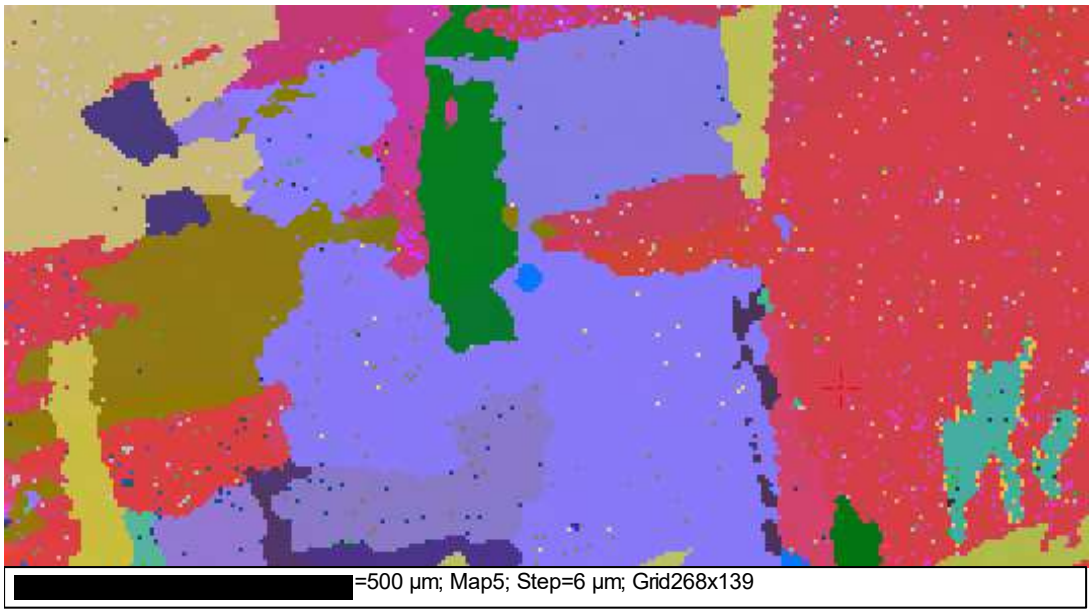

Figure 4-2 Microstructure orientation maps for alpha phase from EBSD data. Beta phase is not obvious due to its narrowaess and the 6 µm step size (see Figure 4-1).

this microstructure, as illustrated in Figure 4-2. Slip systems were selectively activated by choosing appropriate grains with a high Schmid factor for those systems.

Cylindrical micro-pillars (alpha/beta/alpha) with different diameters were manufactured using a focused ion beam (FIB), and an example is shown in Figure 4-3-b. Each group of specimens was cut from the same colony of alpha grains, in order to keep the crystal orientation constant. The SEM micrographs in Figure 4-3 (a-b) show a typical 4 μm diameter micro-pillar fabricated by FIB, prior to deformation (Figure 4-3-c).

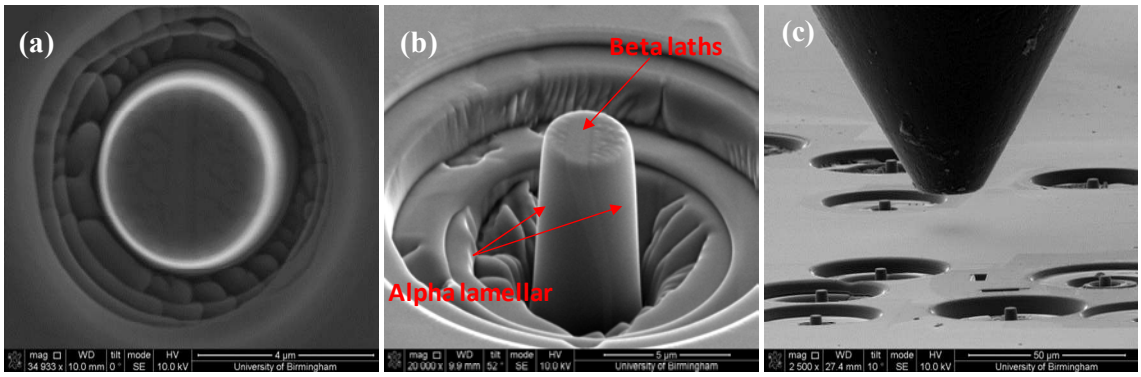

Figure 4-3 SEM micrographs of a typical micro-pillar fabricated by FIB prior to deformation (a) photographed normal to the pillar (b) with the pillar tilted 52° to measure its height and (c) flat punch and pillars, prior to deformation.

Single phase cylindrical micro-pillars with small diameters were produced in order to investigate the mechanical properties of the individual alpha and beta phases. The SEM micrograph in Figure 4-4 shows a typical 2 μm diameter micro-pillar fabricated by FIB prior to deformation (a) α-phase and (b) beta phase.

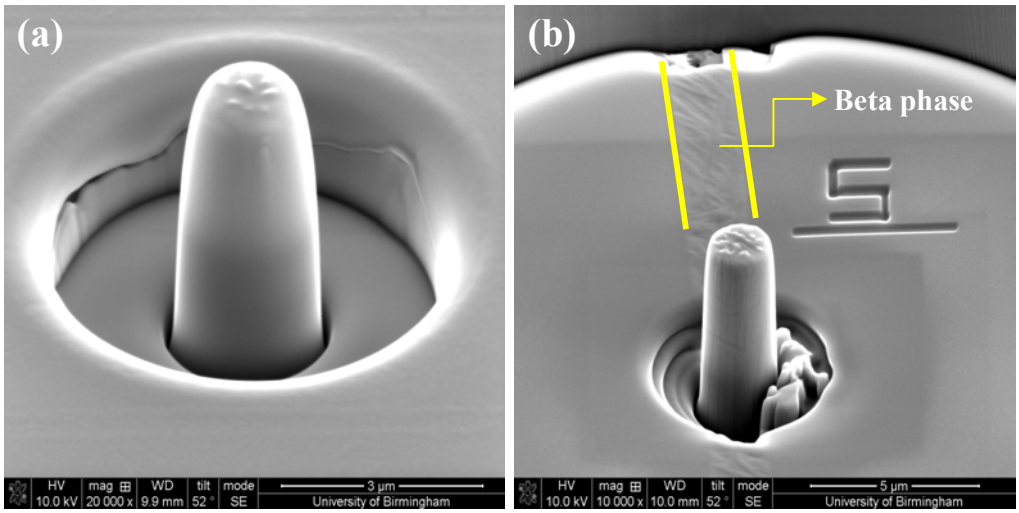

Figure 4-4 SEM micrographs of a single phase 2 µm micro-pillar fabricated by FIB prior to deformation (a) alpha phase pillar; (b) beta phase pillar. Pillars are tilted by 52°.

The crystallographic orientation of the loading axis determines the initial slip system. The Schmid factors for the three a-type $\langle 1\bar{2}10 \rangle$ slip directions $(a_1, a_2 \, or \, a_3)$ on basal and prismatic planes and for <c+a> on pyramidal planes are presented in Table 4-1. Table 4-2 lists the Schmid factors for $< 111 >$ slip on $\{101\}$ and $\{112\}$ planes in the corresponding β phase for each orientation. The loading direction had been chosen as mentioned in Chapter Three (see section 3.10). The pillars are numbered in order of their preparation.

The micropillars were compressed at a constant strain rate of $2.5 \times 10^{-4} \, s^{-1}$ at room temperature (25° C). The specimens were oriented to activate basal, prismatic and pyramidal slip systems respectively, in the alpha phase. Attempts were made to ensure a 1:2 aspect ratio of mid-plane diameter to height and to minimize the column taper.

The three different orientations were chosen as they lead to single phase (alpha and beta) or tri-phase (alpha/beta/alpha) micropillars during compression test as shown in Figure 4-5.

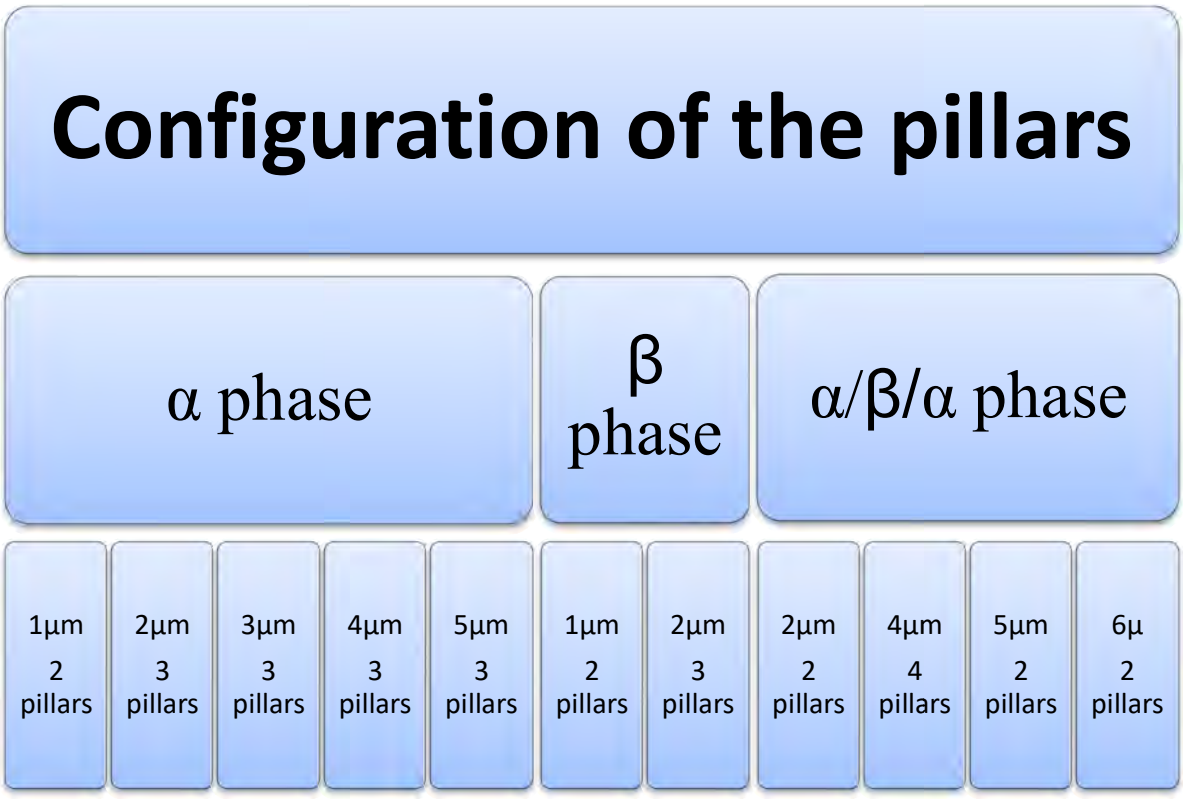

Figure 4-5 Overview of the configuration of the samples.

The uniaxial compression tests on micropillars with different diameters 2 µm to 6 µm, in the alpha/beta/alpha and 1 µm to 5 µm for (basal and prismatic plane) and 2 µm to 4 µm for pyramidal <c+a> slip in the alpha phase and 1 µm to 2 µm for the beta phase at room temperature and constant strain rate for each loading direction are presented in Figure 4-5.

Table 4-1 Alpha phase Schmid factors for loading directions used. Bold signifies operative slip system.

Slip plane type	Slip systems	Loading directions		
		$[\mathbf{0001}]$	$[\mathbf{\bar{1}5\bar{4}6}]$	$[\mathbf{01\bar{1}0}]$
Basal	$(a/3)[\bar{2}110](0001)$	0	0.1	0
	$(a/3)[1\bar{2}10](0001)$	0	**0.47**	0
	$(a/3)[11\bar{2}0](0001)$	0	0.37	0
Prismatic	$(a/3)[\bar{2}110](01\bar{1}0)$	0	0.08	0
	$(a/3)[1\bar{2}10](\bar{1}010)$	0	0.13	**0.43**
	$(a/3)[11\bar{2}0](\bar{1}100)$	0	0.2	**0.43**
<c+a> Pyramidal	$(a/3)[\bar{2}113](1\bar{1}01)$	**0.451**	-	-
	$(a/3)[\bar{2}113](10\bar{1}1)$	**0.451**	-	-
	$(a/3)[1\bar{2}13](01\bar{1}1)$	**0.451**	-	-
	$(a/3)[1\bar{2}13](\bar{1}101)$	**0.451**	-	-
	$(a/3)[11\bar{2}3](\bar{1}011)$	**0.451**	-	-
	$(a/3)[11\bar{2}3](0\bar{1}11)$	**0.451**	-	-

Table 4-2 Beta phase Schmid factors for loading directions used. Bold signifies operative slip system. The three directions shown are parallel to those in Table 4-1 (see Appendix A).

Burgers vectors	Slip systems	[101]	[124]	$[\mathbf{1\bar{2}\bar{1}}]$
$\boldsymbol{b_1}$ $\frac{\boldsymbol{a}}{\boldsymbol{2}}[\mathbf{11\bar{1}}]$	$[\mathbf{11\bar{1}}](\mathbf{101})$	0	0.09	0
	$[\mathbf{11\bar{1}}](\mathbf{011})$	0	0.11	0
	$[\mathbf{11\bar{1}}](\mathbf{\bar{1}10})$	0	0	0
	$[\mathbf{11\bar{1}}](\mathbf{112})$	0	0.12	0
	$[\mathbf{11\bar{1}}](\mathbf{\bar{1}21})$	0	0.08	0
	$[\mathbf{11\bar{1}}](\mathbf{\bar{2}1\bar{1}})$	0	0.04	0
$\boldsymbol{b_2}$ $\frac{\boldsymbol{a}}{\boldsymbol{2}}[\mathbf{\bar{1}11}]$	$[\mathbf{\bar{1}11}](\mathbf{101})$	0	**0.49**	0
	$[\mathbf{\bar{1}11}](\mathbf{110})$	0	0.29	0.27
	$[\mathbf{\bar{1}11}](\mathbf{01\bar{1}})$	0	0.19	0.27
	$[\mathbf{\bar{1}11}](\mathbf{211})$	0	0.45	0.15
	$[\mathbf{\bar{1}11}](\mathbf{\bar{1}2\bar{1}})$	0	0.06	0.32
	$[\mathbf{\bar{1}11}](\mathbf{\bar{1}1\bar{2}})$	0	0.39	0.16

$\boldsymbol{b_3}$ $\frac{\boldsymbol{a}}{\boldsymbol{2}}[\mathbf{111}]$	$[\mathbf{111}](\bar{\mathbf{1}}\mathbf{10})$	-0.5	0.14	0.14
	$[\mathbf{111}](\mathbf{01}\bar{\mathbf{1}})$	-0.5	0.27	0.14
	$[\mathbf{111}](\bar{\mathbf{1}}\mathbf{01})$	0	0.40	**0.44**
	$[\mathbf{111}](\bar{\mathbf{2}}\mathbf{11})$	-0.24	0.31	0.40
	$[\mathbf{111}](\bar{\mathbf{1}}\mathbf{2}\bar{\mathbf{1}})$	**-0.47**	0.08	0.32
	$[\mathbf{111}](\bar{\mathbf{1}}\bar{\mathbf{1}}\mathbf{2})$	0.24	0.39	0.1
$\boldsymbol{b_4}$ $\frac{\boldsymbol{a}}{\boldsymbol{2}}[\mathbf{1}\bar{\mathbf{1}}\mathbf{1}]$	$[\mathbf{1}\bar{\mathbf{1}}\mathbf{1}](\mathbf{011})$	0.41	0.35	0.40
	$[\mathbf{1}\bar{\mathbf{1}}\mathbf{1}](\mathbf{110})$	0.41	0.18	0.14
	$[\mathbf{1}\bar{\mathbf{1}}\mathbf{1}](\bar{\mathbf{1}}\mathbf{01})$	0	0.18	0.27
	$[\mathbf{1}\bar{\mathbf{1}}\mathbf{1}](\bar{\mathbf{1}}\mathbf{12})$	0.24	0.30	0.39
	$[\mathbf{1}\bar{\mathbf{1}}\mathbf{1}](\mathbf{121})$	**0.47**	0.30	0.31
	$[\mathbf{1}\bar{\mathbf{1}}\mathbf{1}](\bar{\mathbf{2}}\bar{\mathbf{1}}\mathbf{1})$	-0.24	0	0.1

4.2. **Basal slip**

The first group of cylindrical micro-pillars was prepared to study <a> slip on the basal plane of the alpha phase.

4.2.1. Basal slip: alpha/beta/alpha phase

Each micro-pillar contained two alpha lamellae separated by a thin fillet of beta phase. The long axis of the pillar was selected to be as closely as possible at 45° to the basal slip plane in the alpha phase. An inspection of Table 4-1 shows that the $[\bar{1}5\bar{4}6]$ loading direction should ensure basal slip, provided the CRSS for prismatic slip is not too far below that for basal slip. The <c+a> CRSS will certainly be much greater. The angle between $[\bar{1}5\bar{4}6]$ and [0001] is 40°. The indices of the x, y, and z axes in the sample coordinate system after the EBSD acquisition were imported via the HKL (Channel 5) software as shown in Figure 4-6. From Figure 4-7 the crystal normal to the top of the pillar (z direction) is $[\bar{1}5\bar{4}6]$ while the y

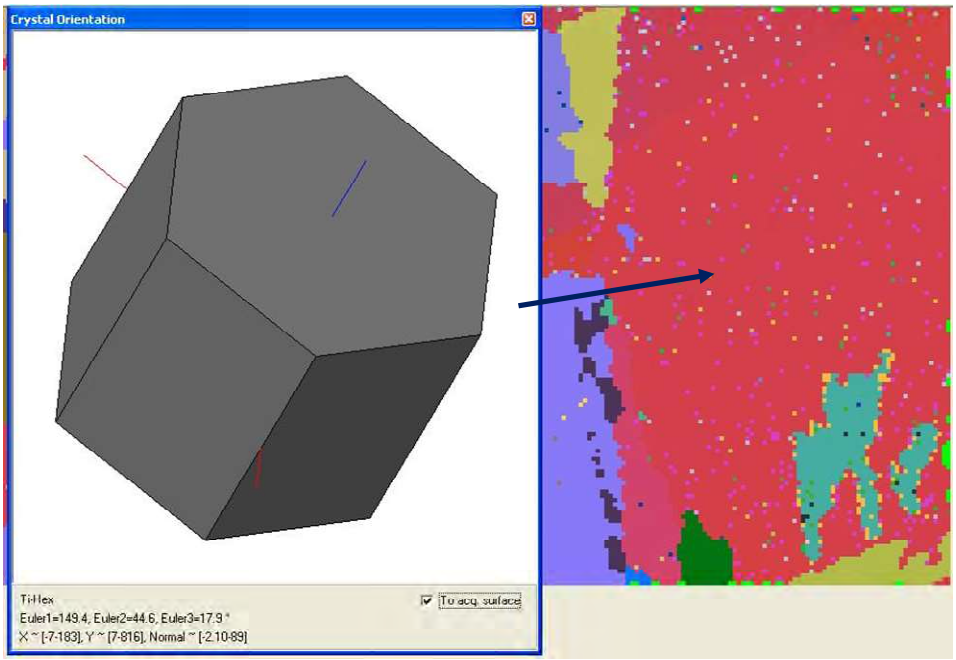

Figure 4-6 The 4-indices of the x $[\bar{4}\bar{1}53]$, y $[4\bar{5}13]$, and z $[\bar{1}5\bar{4}6]$ axes at the pillar extraction location as given by the HKL Channel 5 software.

direction corresponding to the eventual TEM foil normal orientation was $[4\bar{5}13]$.

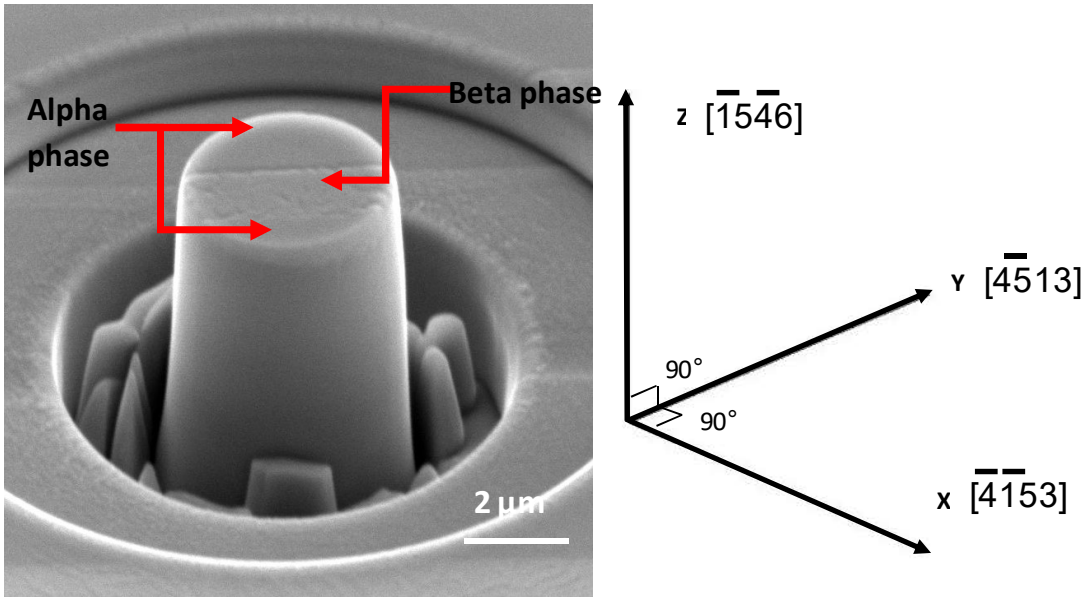

A nano-indenter was then used to conduct micro-compression tests. Room temperature compression tests were performed to strains between 2 % to 7 %. The force displacement data were recorded and then true stress-strain curves were calculated, assuming that volume is conserved during plastic deformation. Typical SEM micrographs of two alpha/beta/alpha micro-pillars 4 µm in diameter, before and after deformation, are shown in Figure 4-8. 2 to 6 µm pillars for alpha/beta/alpha have been chosen for this microstructure because they are a suitable size for micro-compression test using the equipment available (Hysitron PI-85) which is limited to a load of 48 mN. Generally slip bands are formed on two (parallel) planes in 4 µm pillars, while in a very few cases deformation occurs preferentially on only one slip band. The slip plane analysis will be discussed in more detail in the chapter six.

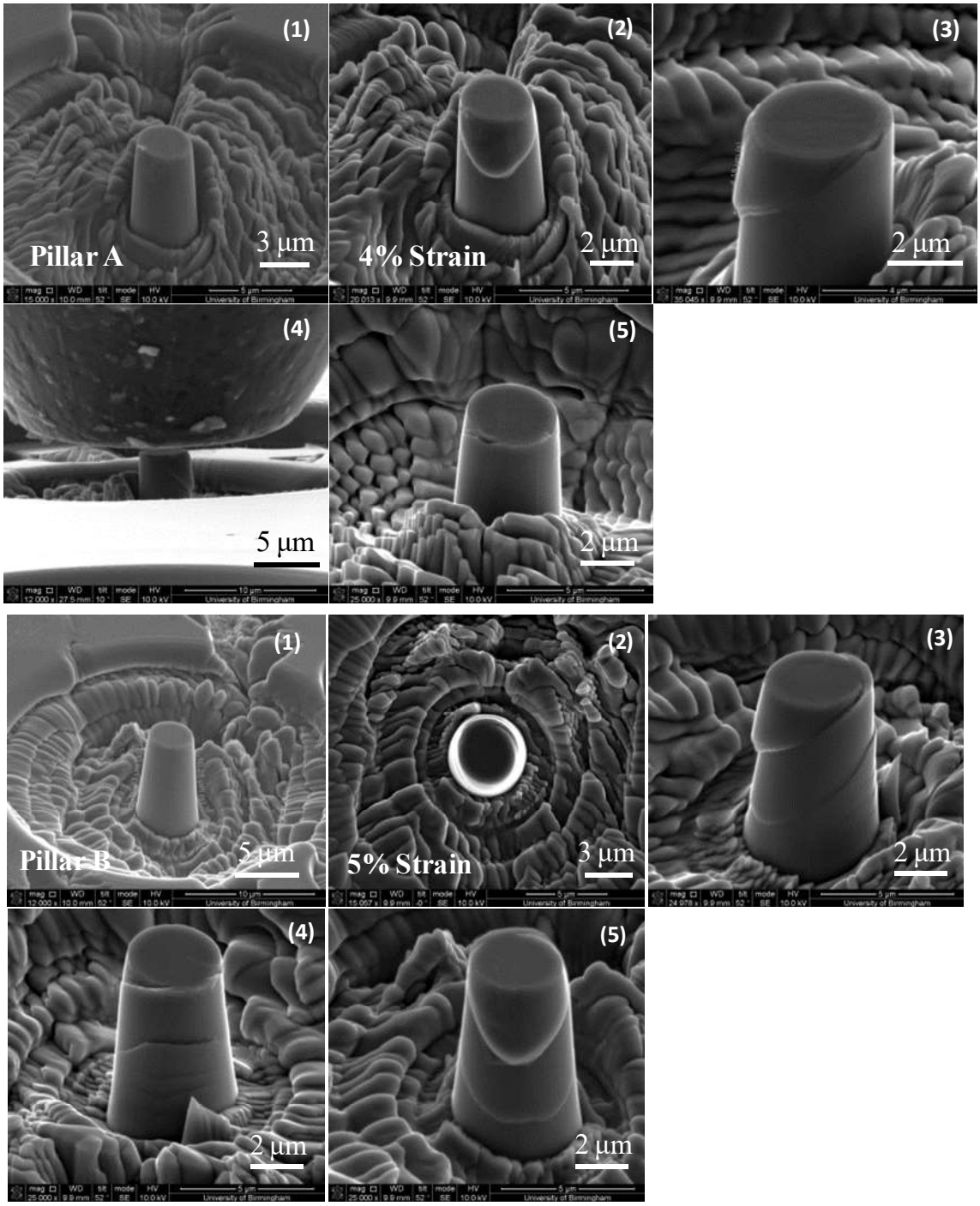

Figure 4-8 Typical SEM micrographs of (alpha/beta/alpha) micro-pillars with a nominal diameter of 4 μm before and after deformation. Pillars A and B are 2 different specimens (1) undeformed (2) - (5) after deformation (photographs from different directions). Pillar A was strained 4% and pillar B to 5%.

True stress-strain curves for micro-pillars with different diameters (2 to 6) μm are shown in Figure 4-9. It is widely observed in both macro and micro-scale compression testing that the early stages of loading produce a non-linear section of the stress-strain curve. This is commonly attributed to a small misalignment between the flat punch indenter and the pillar, causing uneven compression. In fact, for basal slip, the stress increased initially almost linearly with strain until the appearance of a gradient change about 1.5% strain and at a stress level of nearly ~ 700 MPa. From the definition of yield stress, yield points are selected from the point where there is a clear distinction between elastic and plastic deformation. In many cases, the distinction (Elastic region) is not so straightforward.

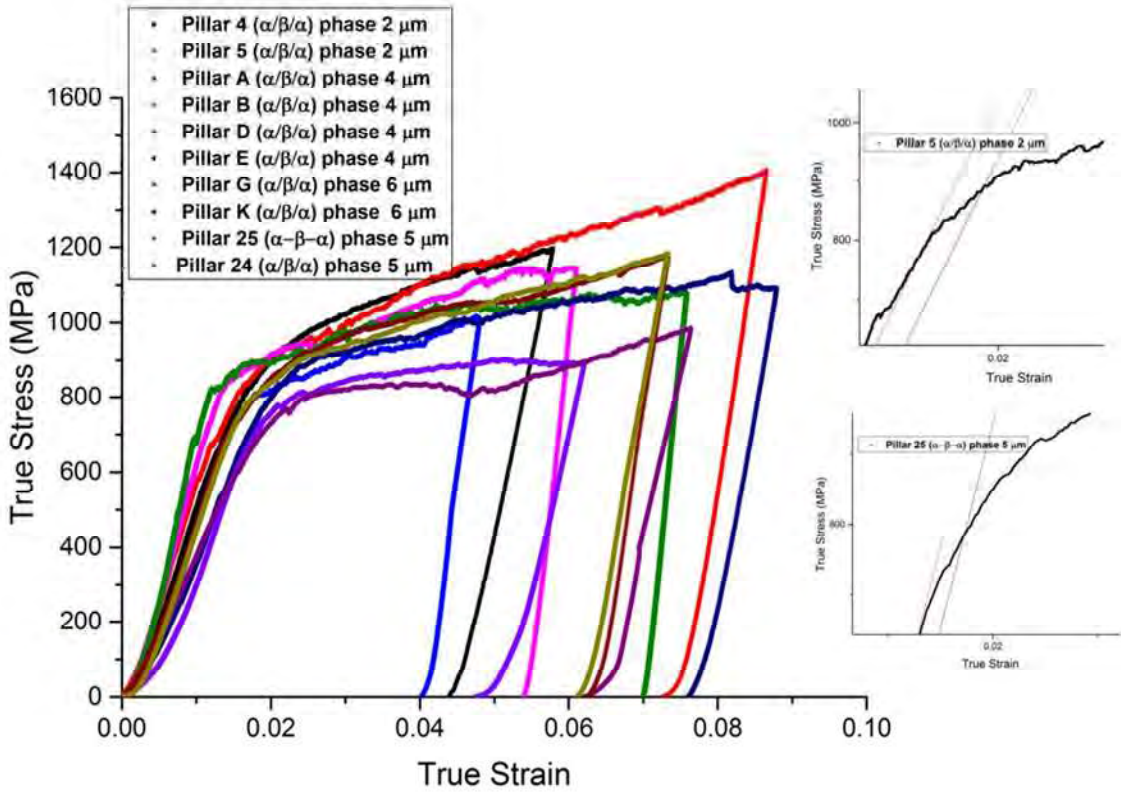

An alternative is to attempt to define an initial linear slope on the stress-strain curve and then to draw a line parallel to this which is offset by a specific strain (0.2%). The intercept of this line with the stress-strain curve defines the 0.2% proof stress, as illustrated in Figure 4-10. From now on, all the yield stresses are determined like that in Figure 4-10.

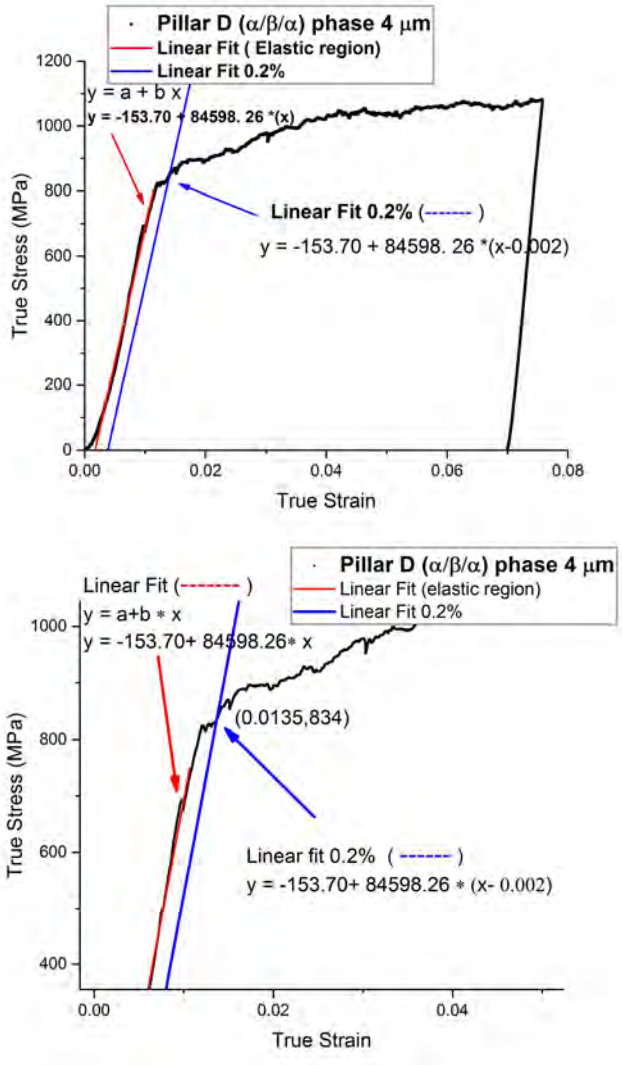

Figure 4-10 The yield stress defined as the intercept of the blue line (Linear fit and 0.2% strain) with the curve which is 834 MPa for pillar D.

The stress corresponding to this first change from linearity is regarded as the yield strength because it indicates the beginning of detectable plasticity. In order to compare α/β/α proof stresses with single phase, 2 μm cylindrical micro-pillars were fabricated. This was because it was impossible, given the microstructure, to make single phase β pillars of more than 2 μm diameter. The specimens were examined using secondary electrons (SE) in the SEM before and after mechanical testing as shown in Figure 4-11. Generally, there is one slip band formed in 2 μm pillars.

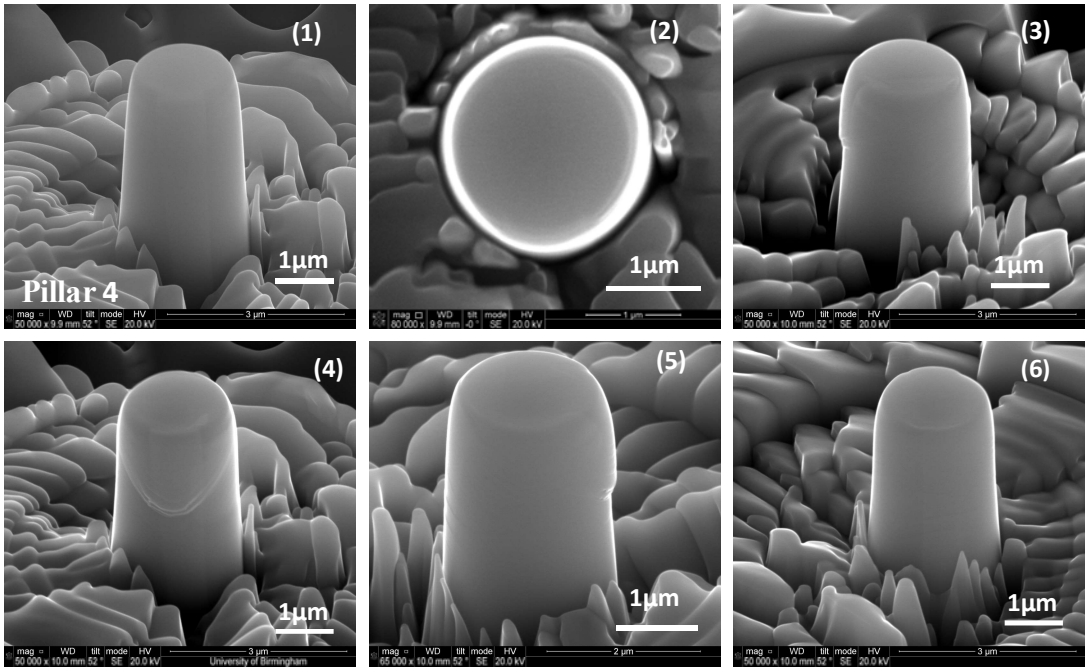

Figure 4-11 SEM micrographs for (alpha/beta/alpha) micro-pillar 4 with a nominal diameter of 2 μm before and after deformation. (1) undeformed (2) - (6) after deformation, photographs from different directions. Pillar 4 was strained 4% to activate basal slip.

Sometimes continuous slip lines can be observed through the α/β/α grain boundaries or through the α/β interfaces between lamellae. This was observed between two α lamellae, between parallel laths of the α+β colonies (see Figure 4-11-4) . In the micrograph presented in

Figure 4-11, slip transmission is allowed in spite of the presence of β interfaces between α lamellae.

The true stress-strain curve for an (alpha/beta/alpha) micro-pillar with a diameter of 2 μm is shown in Figure 4-12. Despite the difference in size between the 4 μm and 2 μm pillars the stress-strain curve both show a classic linear elastic deformation followed by plastic deformation. Beyond the linear part of the stress-strain curve, a further increase in load produces very large increases in strain.

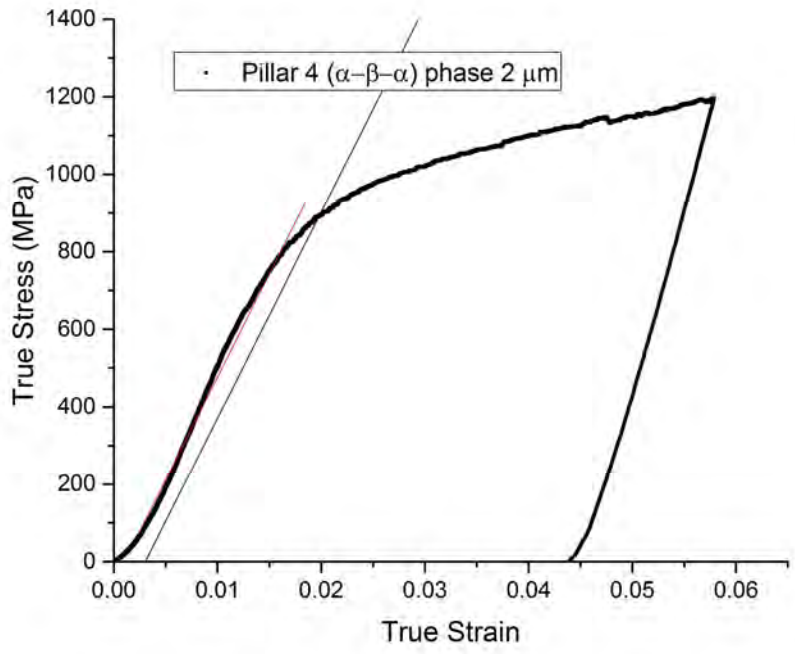

The exact dimensions of each cylindrical pillar tested are listed in Table 4-3, which summarizes the initial dimensions, yield stress, the 0.2% offset yield strength and CRSS deduced from the highest Schmid factor. Hereafter, dislocations on slip systems having the highest Schmid factor are referred to as primary dislocations and the others as secondary.

Table 4-3 Summary of constant strain rate data acquired for selected alpha/beta/alpha 2 µm to 6 µm diameter micro-pillars in compression.

Planes	Pillars	Diameter (µm)	Height (µm)	Yield Stress (MPa)	0.2% Strength (MPa)	CRSS for basal slip (MPa)
Basal Plane	Pillar 3	2	4.2	773	905	422 ± 5
	Pillar 4	2	4	790	895	
	Pillar 5	2.1	4.3	813	891	
	Pillar A	4	8.7	724	807	396 ± 15
	Pillar B	4	10.3	733	861	
	Pillar D	4	9.7	692	834	
	Pillar E	4	7.9	773	871	
	Pillar 24	5	10.36	744	812	375 ± 10
	Pillar 25	5.1	12.17	685	791	
	Pillar G	6	13.5	671	771	360 ± 5
	Pillar K	6	11.6	680	763	

Referring back to Figure 4-8 the different numbers of slip traces in the two micro-pillars with a nominal diameter of 4 μm indicate that there were clear differences in the volume of the beta phase separating the alpha lamellae and that potentially the beta phase size plays an important role in plastic deformation [111]. Due to present of the beta phase through the whole of pillar D, while it is just showing in the top of pillar E and, also the deformation in the BCC (beta phase) is symmetry so it is softer than the hexagonal crystal structure (alpha phase). Therefore, it was necessary to measure the mechanical properties of each phase in order to quantify how these microstructural changes contributed to the overall strength of the material.

4.2.2. Basal slip systems: Alpha phase

It is useful as a comparator to study the flow stress in the alpha phase alone. Cylindrical single phase (α-phase) micro pillars were prepared with diameters 1 to 5 μm. They were prepared from the same colony as the alpha/beta/alpha phase specimens. SEM images of the deformed single alpha phase $[\bar{1}5\bar{4}6]$ micro-pillars before and after deformation are shown in Figure 4-13. The secondary electron SEM images of the sample surface were taken from different directions to help study the slip lines on the sample surface.

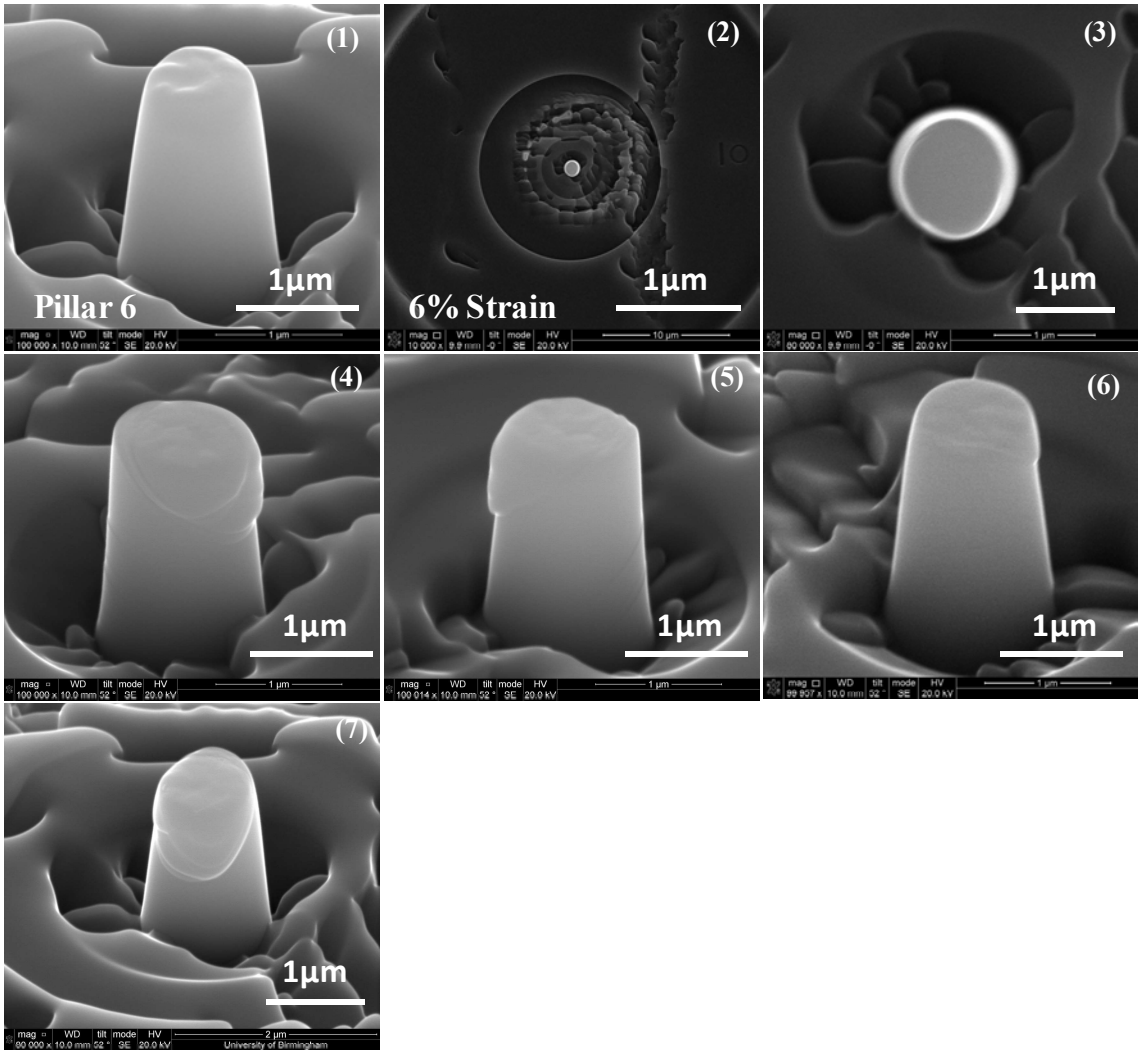

(Continued)

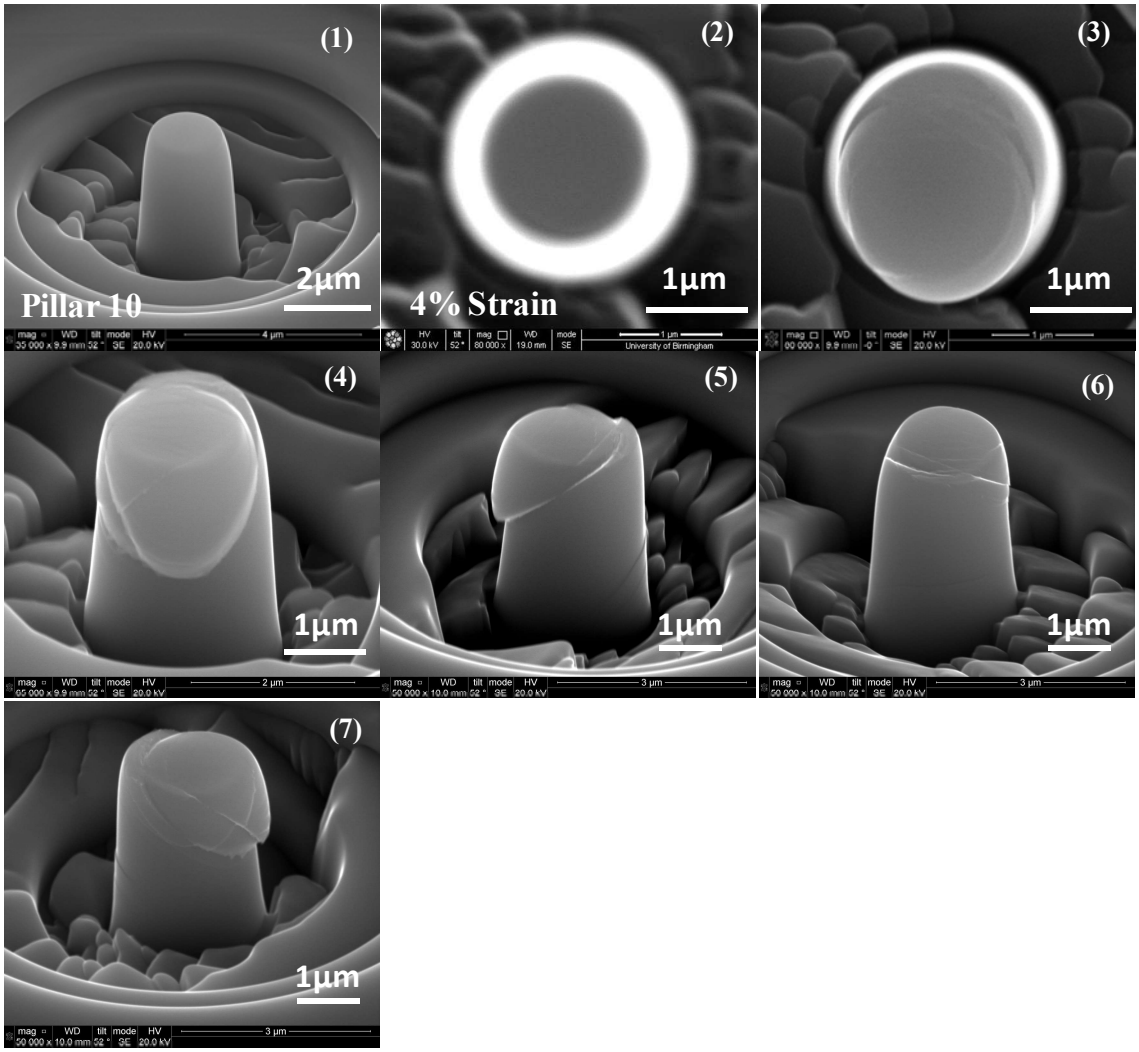

Figure 4-13 Typical SEM micrographs before and after deformation of single α phase cylindrical micro-pillars fabricated by FIB. Pillars 6, 1 µm in diameter, and 10, 2 µm in diameter, (1) and (2) undeformed (3) - (7) after deformation, photographs from different directions. Pillar 6 was strained 4% and pillar 10 6%.

Comparing Figure 4-11 and Figure 4-13, we can see that both pillars exhibit slip traces. However, in the single crystal α pillar, the magnitude of this slip is far greater as shown in Figure 4-13 (5). On the other hand, while a slip step is present in Figure 4-11 (5), it is far smaller despite the same loading, demonstrating the effectiveness of the beta laths in restricting slip motion.

In this study, α-phase has the largest grain size, after heat treatment and a very slow cooling rate, and the β-phase has the smallest size (width 600 nm to ≤ 2 μm). Larger grain sizes will have a greater density of dislocation sources and, hence, should deform at a higher rate. Further, alpha phase provides bigger lengths for pile-up formation than beta phase, leading to higher stress concentrations at the α/β interface. Greater stress concentrations at beta boundaries will lead to higher slip and the alloy will accumulate bigger strains.

True stress-strain curves for $[\bar{1}5\bar{4}6]$ single crystal alpha phase cylindrical micro-pillars with five different sizes are shown in Figure 4-14. The flow stresses show more fluctuation than for the alpha/beta/alpha specimens. The mechanical data are analysed in Table 4-4.

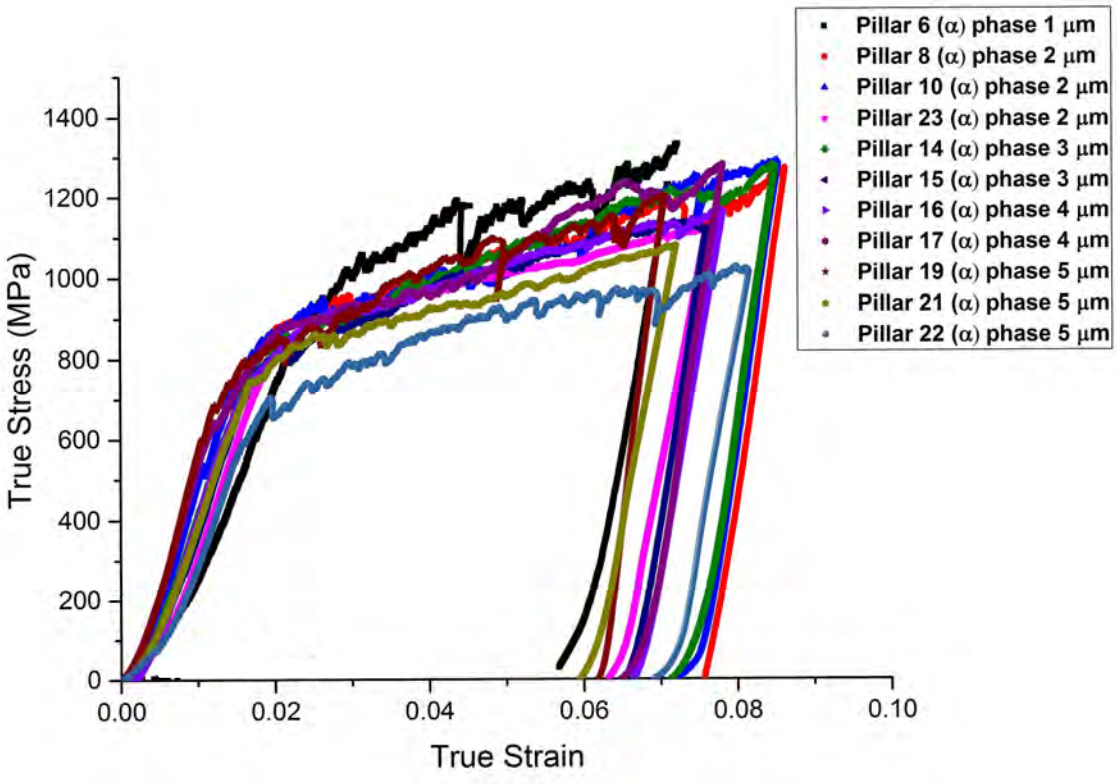

Table 4-4 Mechanical indentation data for compression of 1 and 5 µm single α-phase micropillars.

Planes	Pillars	Diameter (µm)	Height (µm)	Yield Stress (MPa)	0.2%Strength (MPa)	CRSS (MPa)
Basal Plane	Pillar 6	1.1	2.2	794	928	433 ± 10
	Pillar 9	1.1	2.0	773	918	
	Pillar 8	2.15	4	794	872	407 ± 10
	Pillar 10	2.1	4	720	854	
	Pillar 23	2.15	4.2	751	869	
	Pillar 14	3.2	6.45	732	828	385 ± 5
	Pillar 15	3.2	8.0	755	811	
	Pillar 16	4.2	8.22	694	783	366 ± 10
	Pillar 17	4.2	8.85	652	775	
	Pillar 19	5	13	683	745	353 ± 10
	Pillar 21	5.1	10.2	616	749	
	Pillar 22	5.2	9.65	595	762	

4.2.3. Single beta phase

SEM images of two deformed [124] $_{\beta}$ micro-pillars before and after deformation are shown in Figure 4-15. Although, there was no obvious slip band across the whole surface of sample 3 (diameter 1 µm), the deformation on the top of the pillar is clear as illustrated below (Figure 4-15, pillar 3 after deformation (3)). The slip plane in pillar 7 is very obvious as shown in Figure 4-15 after deformation (3 to 7).

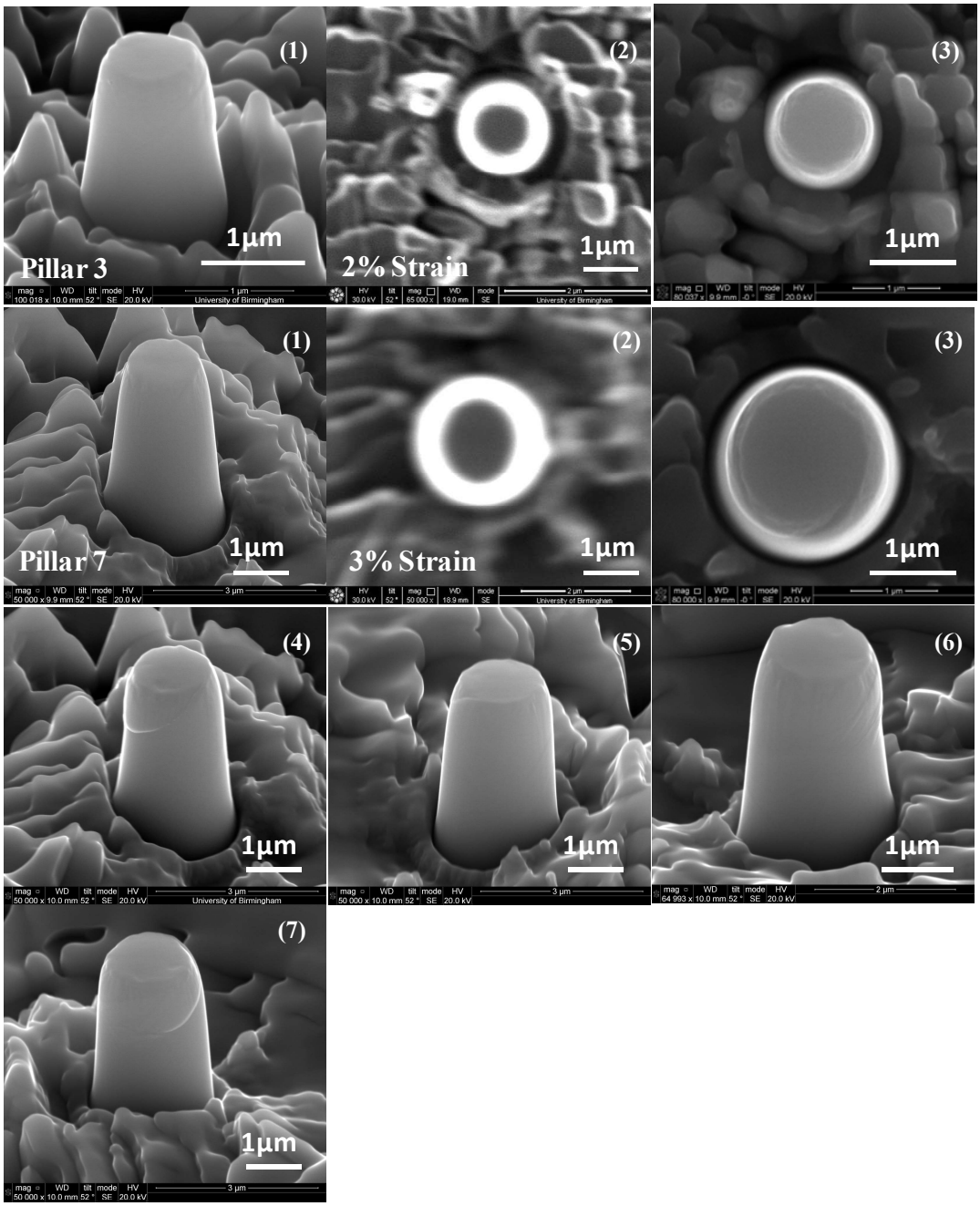
(1)
1µm
Pillar 3
(2)
1µm
2% Strain
(3)
1µm
(1)
1µm
Pillar 7
(2)
1µm
3% Strain
(3)
1µm
(4)
1µm
(5)
1µm
(6)
1µm
(7)
1µm

Representative true stress-strain curves are shown in Figure 4-16.

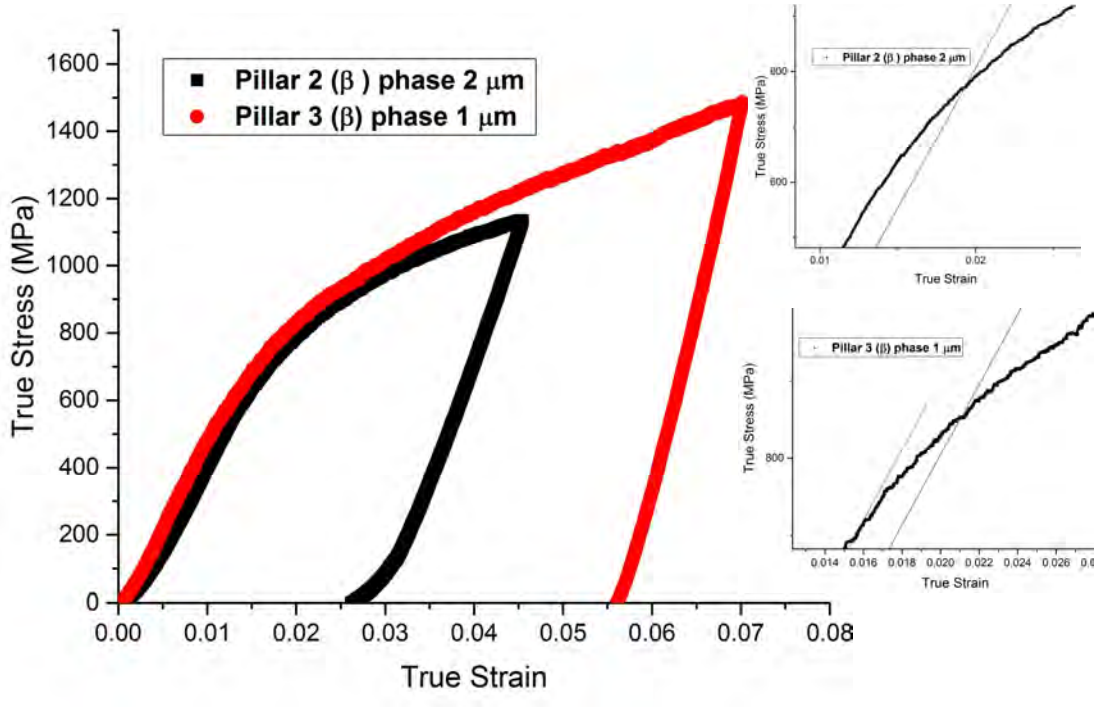

Summaries of the mechanical properties of the 1 μm and 2 μm single beta phase micro-pillars are shown in Table 4-5. From now on, the CRSSs for beta phase were worked out assuming that the slip system with the highest Schmid factor in Table 4-2 was activated.

Table 4-5 Summary of constant strain rate data for compression of single β-phase micro-pillars.

Planes	Pillars	Diameter (μm)	Height (μm)	Yield Stress (MPa)	0.2%Strength (MPa)	CRSS (MPa)
{101}	Pillar 3	1.1	2	723	854	418
	Pillar 2	2.2	4	649	767	372 ± 8
	Pillar 7	1.85	4	668	752	

4.3. **Prismatic slip systems**

The second type of slip investigated was <a> slip on the prismatic plane of the alpha phase (i.e.$< 11\bar{2}0 > \{10\bar{1}0\}$).

4.3.1. Prismatic slip systems: alpha/beta/alpha phase

Referring back to Table 4-1 shows that the $[01\bar{1}0]$ loading direction should ensure prismatic slip provided the CRSS for <a> slip has higher Schmid factor. From the EBSD data shown in Figure 4-17 the crystal direction normal to the top of the pillar (z direction) was $[01\bar{1}0]$ while the y direction corresponding to the foil normal orientation was $[2\bar{1}\bar{1}0]$.

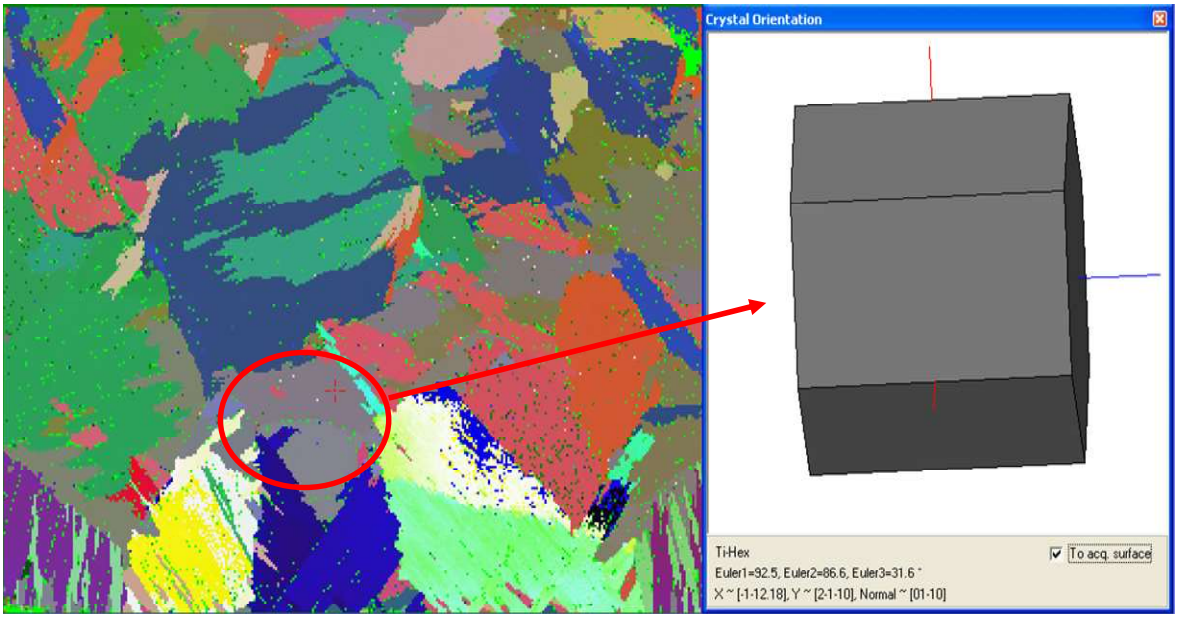

Figure 4-17 The 4-indices of the x $[\bar{1}\bar{1}28]$, y $[2\bar{1}\bar{1}0]$, and z $[01\bar{1}0]$axes at the pillar extraction location given by the HKL Channel 5 software.

SEM micrographs of pillars before and after deformation are shown in Figure 4-18. The slip traces are consistent with the primary slip system as the angle between the loading direction and possible slip plane was ~ 60°, which was oriented for the maximum resolved shear stress. That will be discussed in more detail in the next chapter. In order to confirm the activation of the desired slip system and to observe the interaction of slip lines with the β-lath the samples were examined in the SEM before and after mechanical testing as shown in Figure 4-18. Figure 4-18 (pillars 17 and 19) (3 to 6) shows the slip lines on the micro pillar surface.

Typical true stress-strain behaviour for micropillars with sizes 2 μm to 6 μm is presented in Figure 4-19.

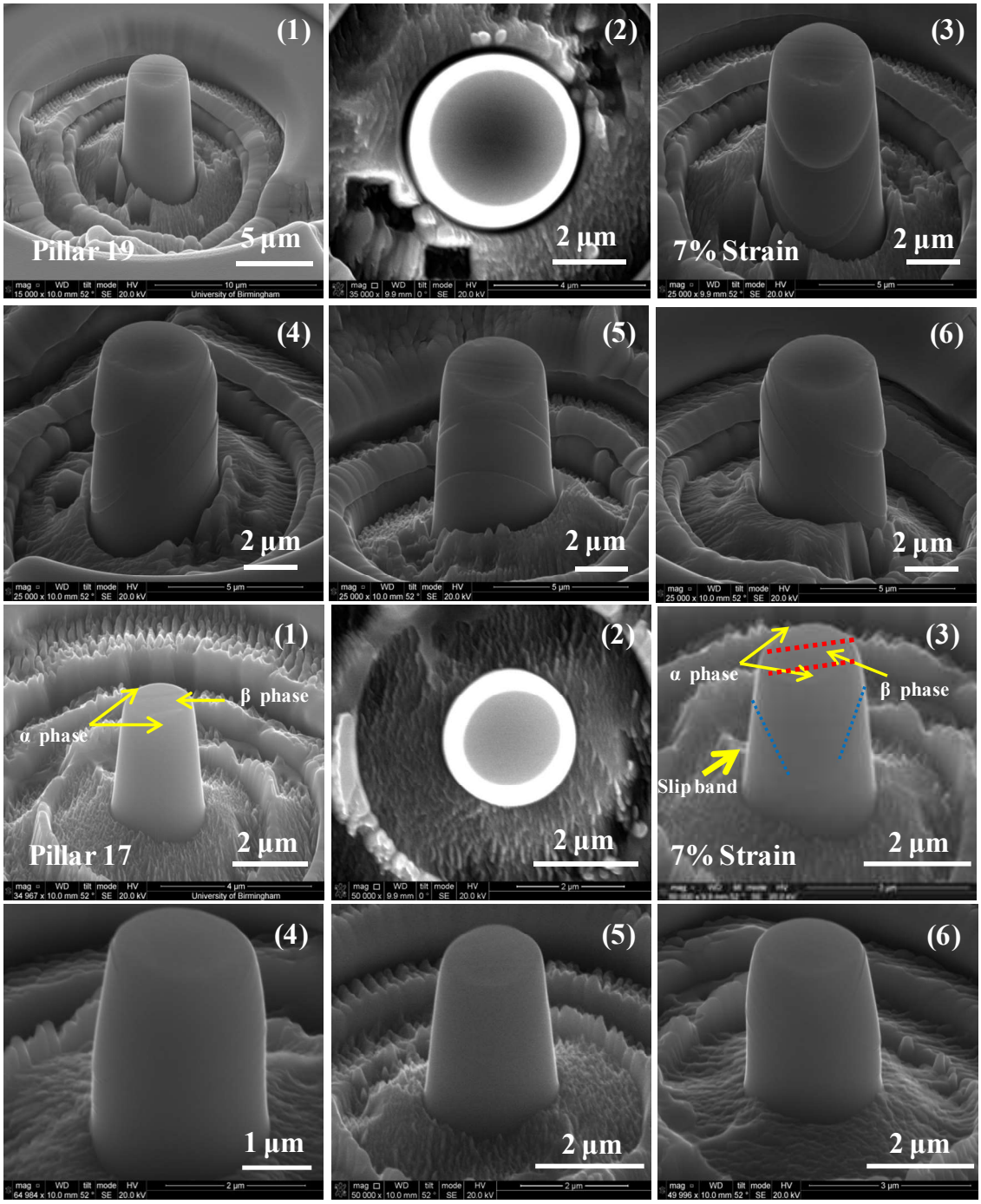
(1)
Pillar 19
5 µm
(2)
2 µm
(3)
7% Strain
2 µm
(4)
2 µm
(5)
2 µm
(6)
2 µm
(1)
β phase
α phase
Pillar 17
2 µm
(2)
2 µm
(3)
α phase
β phase
Slip band
7% Strain
2 µm
(4)
1 µm
(5)
2 µm
(6)
2 µm

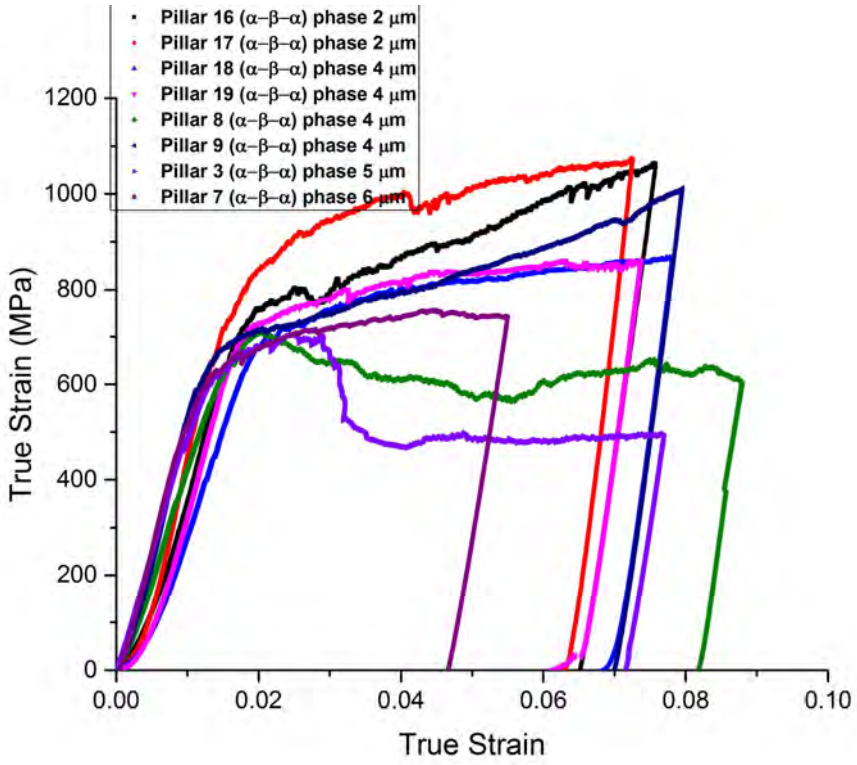

As shown in Figure 4-19, the applied stresses increased almost linearly up to 1% strain at a stress level of 600 MPa to 650 MPa with subsequently the appearance of a small change of stress which is regarded as the beginning of the plastic yield. Therefore, a slip step forms on the surface of the pillar; deviations in the stress-strain curves are associated with the formation of discrete slip bands in the pillars. At room temperature the 0.2% flow stresses are found to be 702 MPa (pillar 18), 725 MPa (pillar 19) (both 4 μm) and 802 MPa (pillar 17) (2 μm). It was found too difficult to FIB pillars of 1 μm diameter containing a beta boundary between alpha laths.

The general features of the curves are similar in specimens of different diameter (2 μm to 4 μm) and strain. Typical SEM micrographs show slip in the cylindrical micro pillars which were loaded above the critical point, such as in Figure 4-20.

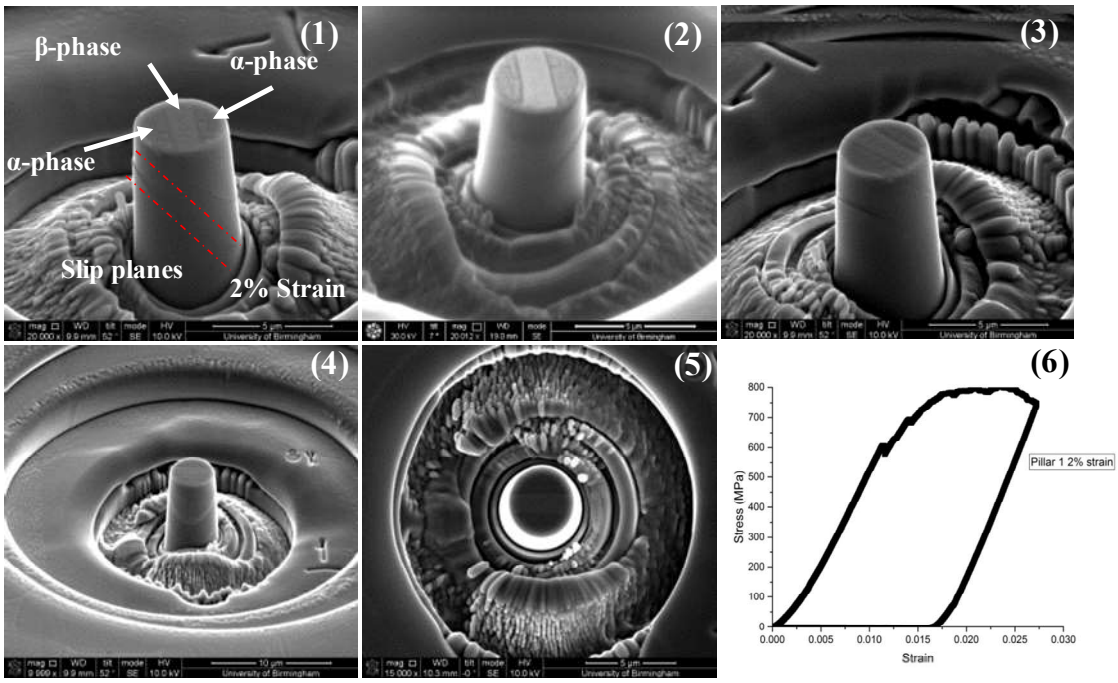

Figure 4-20 shows SEM micrographs for a deformed micro-pillar at different orientations to provide a more detailed picture of the deformation morphology typical of prismatic slip systems. The true stress-strain curve for the same pillar deformed 2% at constant strain rate and room temperature is also shown.

The mechanical data analysis for compression of different diameter from 2 to 6 μm alpha/beta/alpha pillars is shown in Table 4-6.

Table 4-6 Summary of constant strain rate data acquired using micro-pillar compression via <a> prismatic slip for 2 µm and 6 µm alpha/beta/alpha tri-crystal pillars in Ti-6Al-4V.

Slip planes type	Pillars	Diameter (µm)	Height (µm)	Yield Stress (MPa)	0.2% Strength (MPa)	CRSS for prismatic slip (MPa)
Prismatic plane	Pillar 16	2.1	4.15	625	762	336 ± 20
	Pillar 17	2.15	4.85	647	802	
	Pillar 8	4.08	9	612	685	301 ± 15
	Pillar 9	4.1	10	591	687	
	Pillar 18	4.15	10.15	628	702	
	Pillar 19	4.15	9.45	663	725	
	Pillar 3	5.1	12	545	645	278 ± 5
	Pillar 4	5.2	12	538	661	
	Pillar 6	6.2	15	564	630	269 ± 5
	Pillar 7	6.1	12.3	519	624	

4.3.2. Prismatic slip systems: Alpha phase

To examine single alpha phase in compression, 1 μm and 5 μm pillars were fabricated. They were prepared from the same colony as the alpha/beta/alpha specimens. SEM images of the deformed $[01\bar{1}0]$ pillars with the two diameters are shown in Figure 4-21. In most cases two slip bands formed on two sets of planes in the 2 μm pillars, while for the 1 μm pillars deformation occurs normally via one slip band only (Figure 4-21).

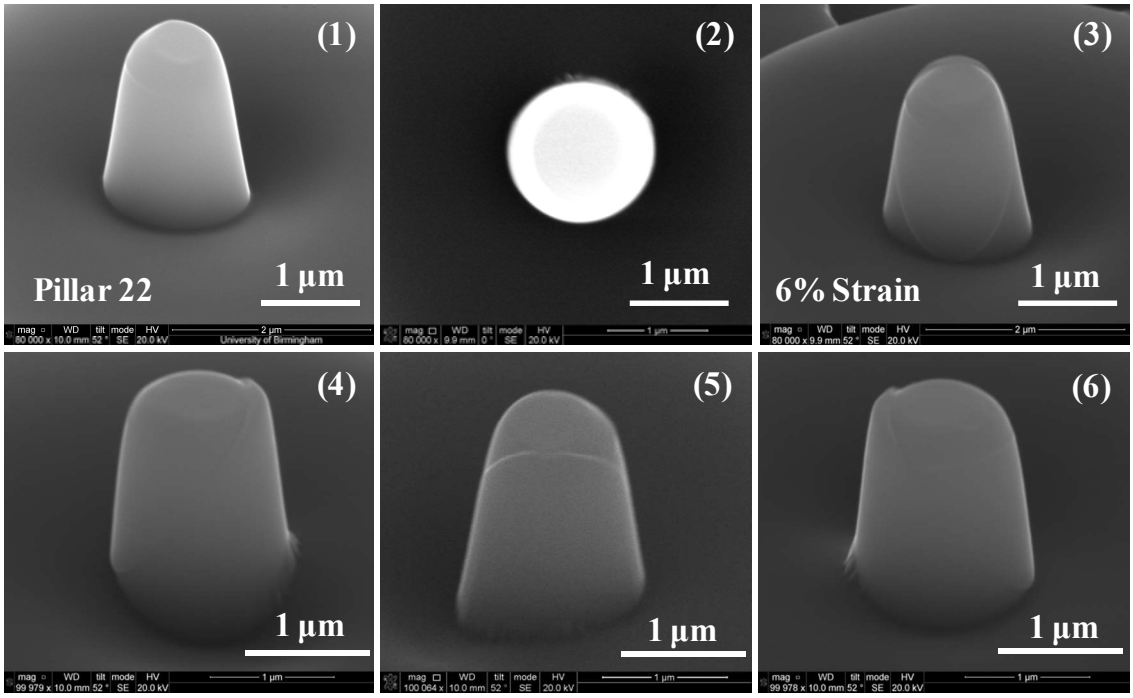

(Continued)

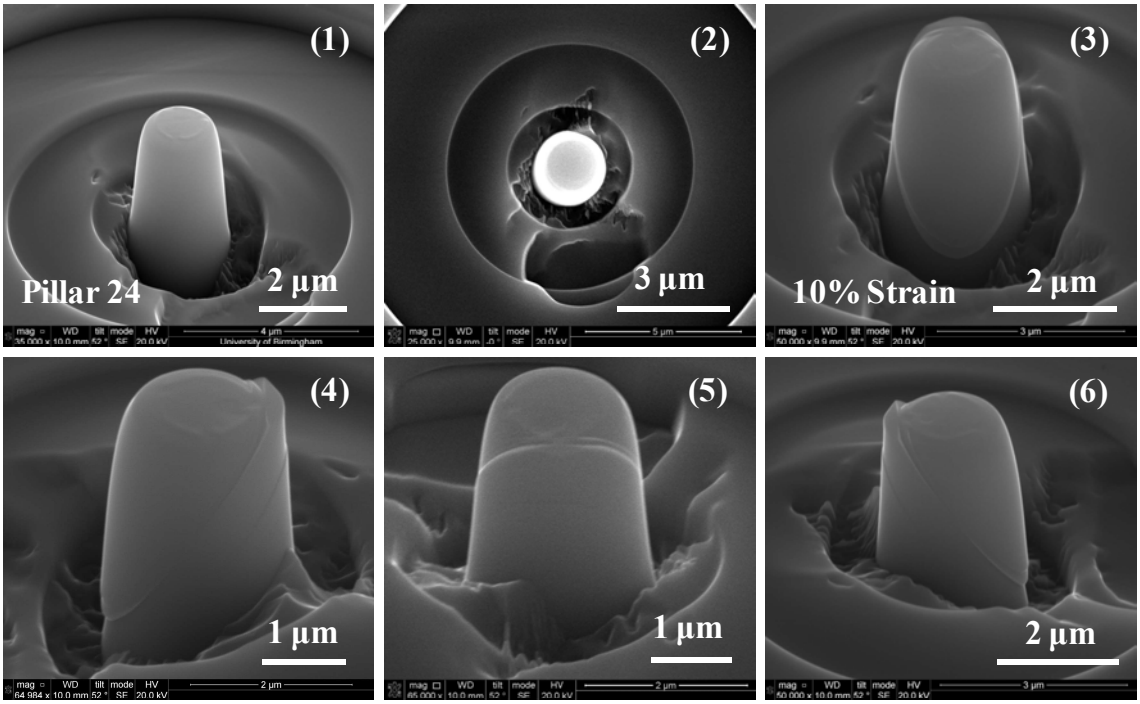

As seen before (section 4.3.1) a higher stress was needed for plastic deformation of the α/β/α pillars which makes the α/β/α pillars far less susceptible to slip than the single phase ones as seen in Figure 4-18 (pillar 17 (6)). To compare, Figure 4-21 shows the α pillar loaded in the same direction, under the same condition. We therefore conclude that the α/β interface is effective in impeding slip movement regardless of slip direction. Typical true strain-stress curves are shown in Figure 4-22.

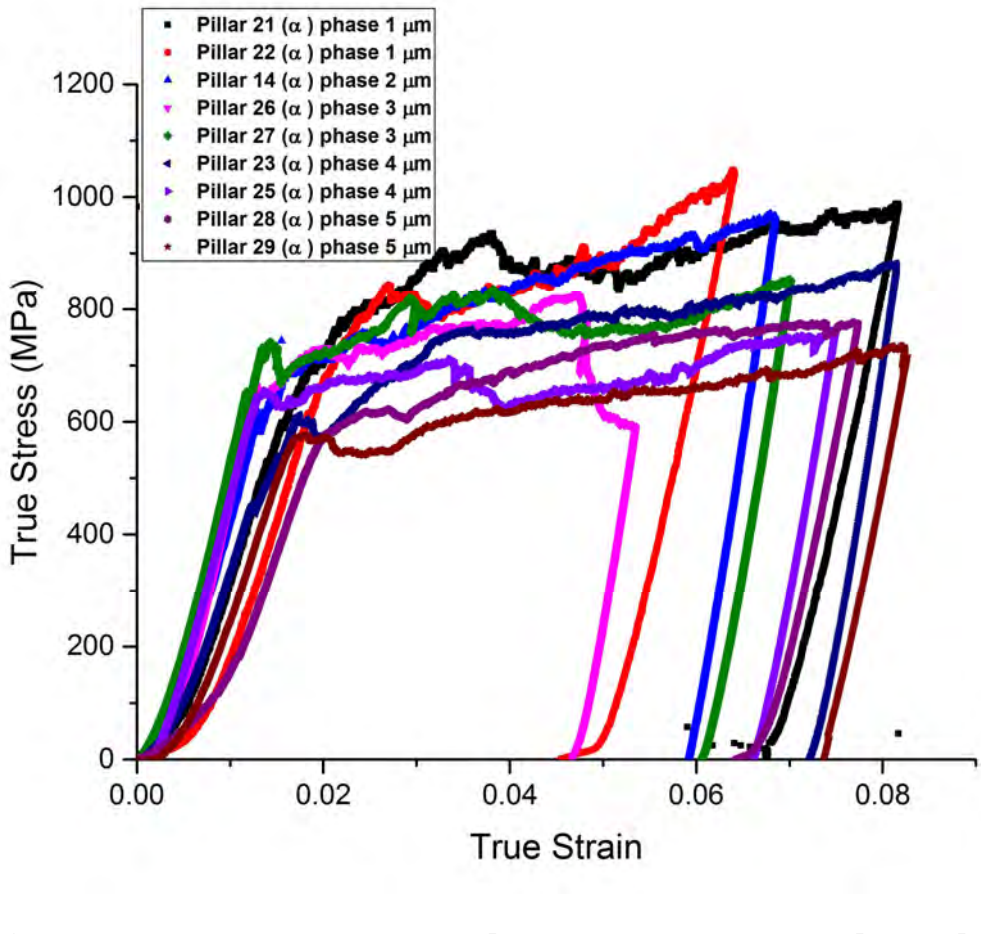

It is observed in 1 μm micro-pillars during compression that the early stage of loading produces a non-linear section of the stress-strain curve until ~ 1%. After that the applied stresses increase almost linearly up to 2% strain at a stress level of nearly 700 MPa, followed by hardening until a maximum stress is reached around 970 MPa. A slip line was seen to form on the surface of the pillar during deformation.

The flow stress for the 2 μm micropillar is smaller than those for the smaller diameter. However, for the others micropillars (diameter larger than 2 μm), the stress-strain curves increased almost linearly up to the yield point where a change of strain caused a very obvious

slip line to form on the surface of the pillar (using *in-situ* SEM) , followed by hardening up to a maximum stress.

The mechanical measurements on the comparator single crystal alpha pillar with prismatic slip are analysed in Table 4-7.

Table 4-7 Summary of constant strain rate data for compression via <a> prismatic slip for the 1 µm and 5 µm single crystal α phase micro-pillars.

Slip plane type	Pillars	Diameter (µm)	Height (µm)	Yield Stress (MPa)	0.2%Strength (MPa)	CRSS for prismatic slip (MPa)
Prism plane	Pillar 21	1.05	2	599	792	340 ± 5
	Pillar 22	1.25	2.05	612	787	
	Pillar 14	2.1	4.0	615	711	312 ± 15
	Pillar 24	2.1	4.2	674	742	
	Pillar 26	3.2	10.1	526	661	282 ± 5
	Pillar 27	3.15	7.85	554	652	
	Pillar 23	4.2	7.8	543	610	268 ± 10
	Pillar 25	4.2	10.6	604	641	
	Pillar 28	5.1	9.35	536	577	247 ± 3
	Pillar 29	5.1	9.45	506	572	

4.3.3. Single Beta phase

The beta phase is very narrow in this microstructure; therefore it was very difficult to get an accurate beam signal for EBSD from it. The beta phase crystal direction was therefore deduced from the Burgers orientation relationship (BOR) between the alpha and beta phases. Figure 4-23 shows SEM micrographs of single crystal beta phase columns with diameter 2 µm (Figure 4-23).

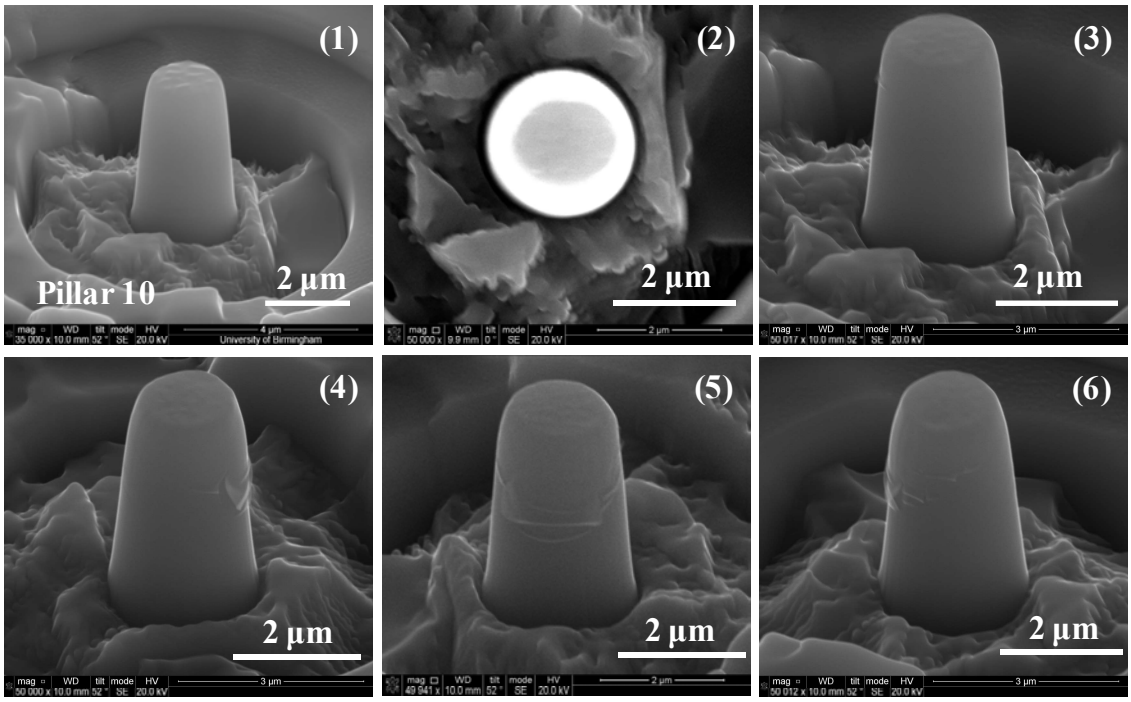

(Continued)

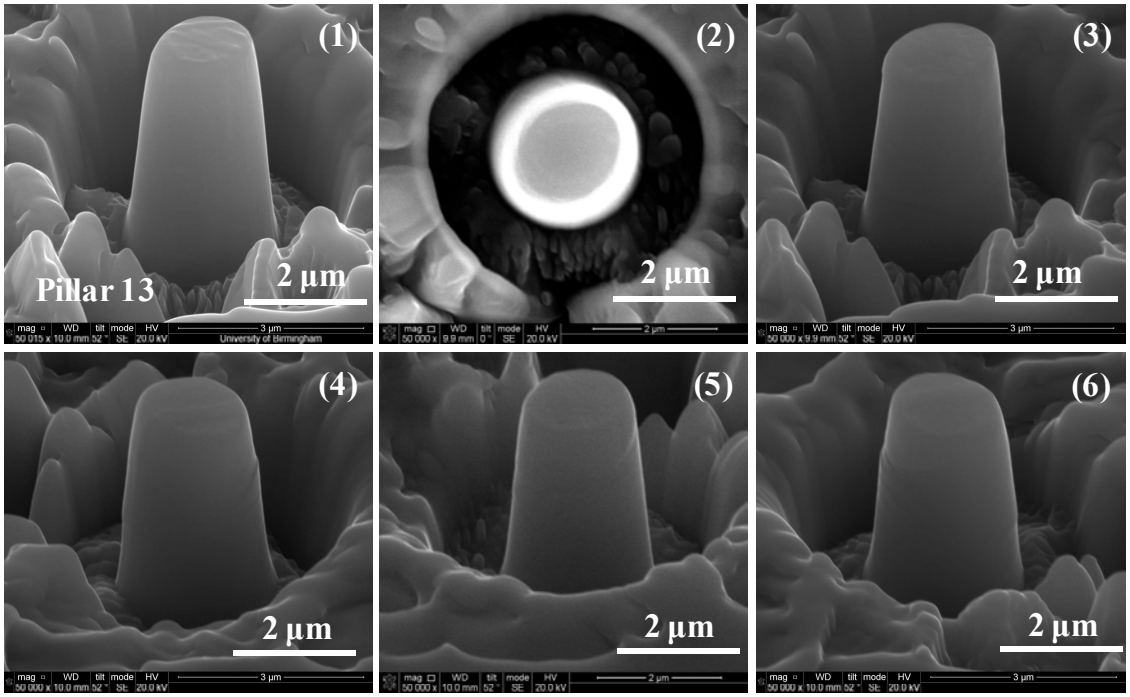

Figure 4-23 SEM micrographs of single β-phase cylindrical micro-pillars before and after deformation. Pillars (10) and (13) are 2 different specimens with the same diameter, 2.1 µm (1) and (2) undeformed (3) - (6) after deformation, photographs at different orientations. Pillar 10 was strained 4.5% and pillar 13 5.5%.

Comparing Figure 4-23 with Figure 4-18 and Figure 4-21 the slip lines are far less obvious. A typical true stress versus true strain curve for the single crystal beta pillar is presented in Figure 4-24. The stress-strain curves show a linear increase from 0.7% strain until ~ 2.3% strain, followed by hardening. There are no distinct load drops and there is a monotonic rise of the true stress with true strain up to ~ 5%. Figure 4-25 demonstrates the effectiveness of the beta laths in restricting slip motion compared to single phase.

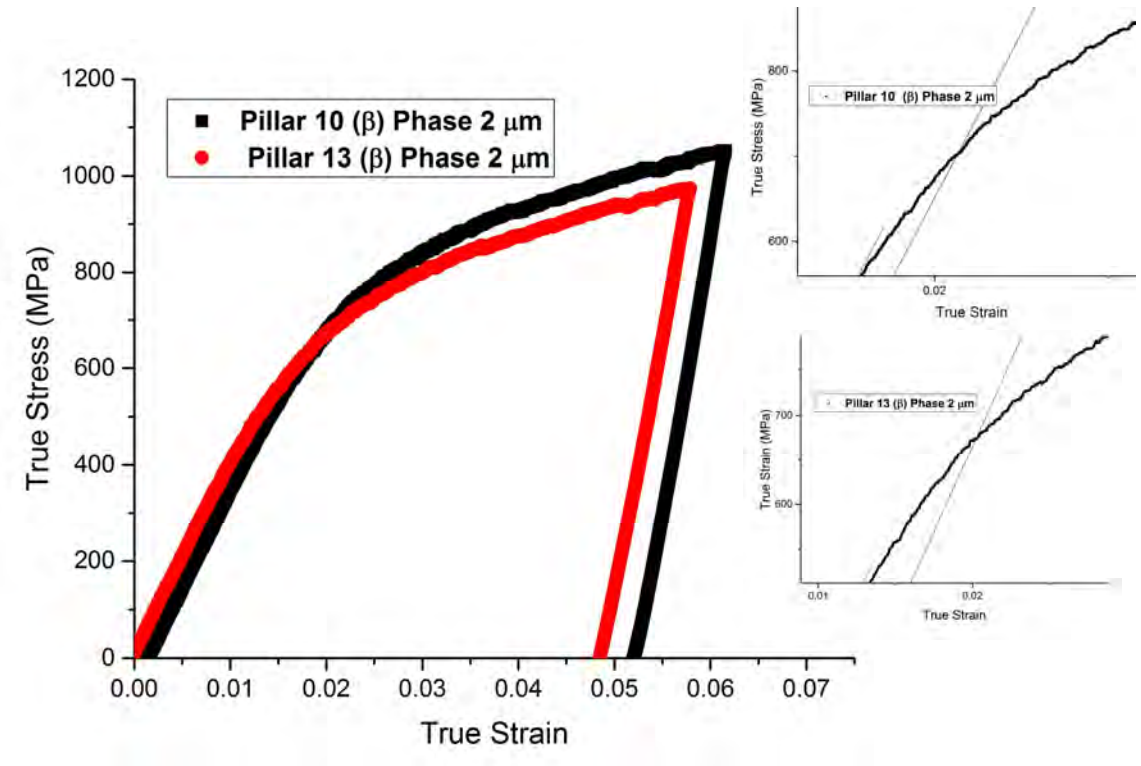

The resulting mechanical data for compression of single beta phase pillars are provided in Table 4-8.

Table 4-8 Mechanical measurements for the 2 μm single crystal β phase in micro-pillar.

Slip planes type	Pillars	Diameter (μm)	Height (μm)	Yield Stress (MPa)	0.2%Strength (MPa)	CRSS (MPa)
Beta plane	Pillar 10	2.15	4.15	579	702	302 ± 10
	Pillar 13	2.1	4.4	524	672	

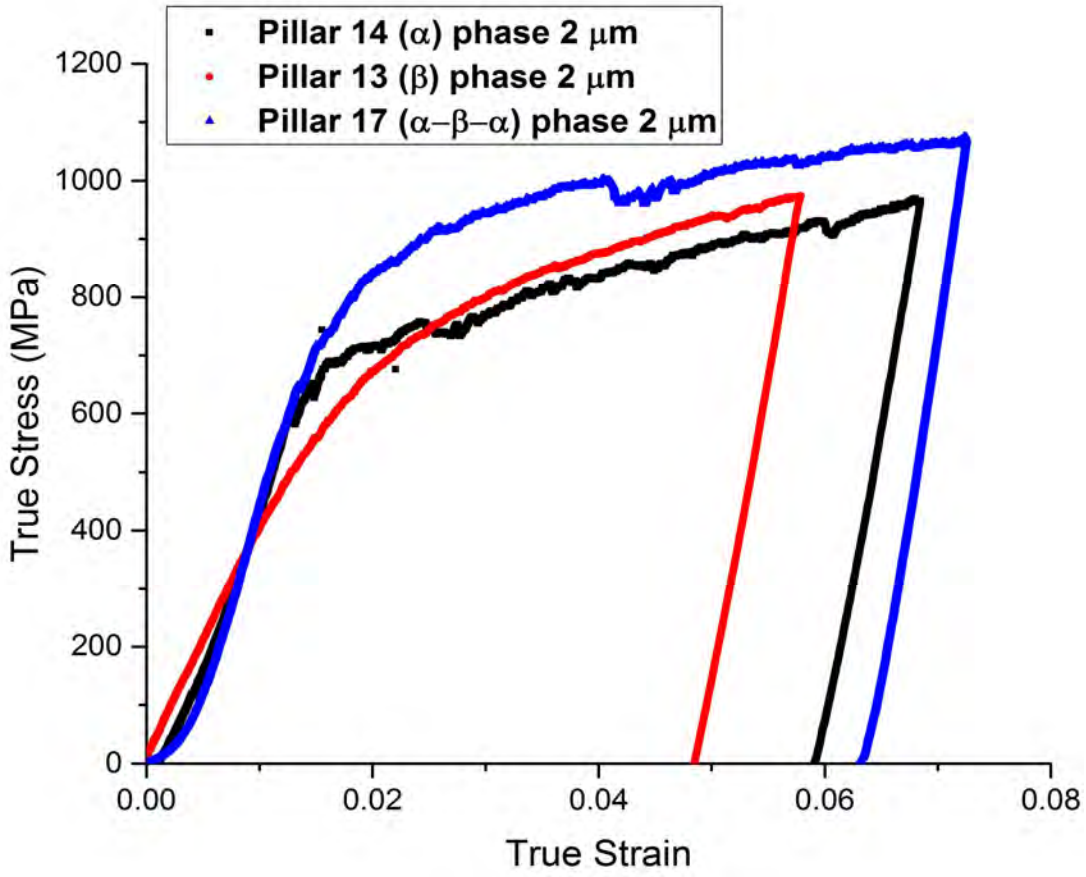

Figure 4-25 True stress-strain curve for single crystal alpha and beta pillars, for tri-crystal (alpha/beta/alpha) pillar with diameter 2 μm and strained between ~ 4% to 6%.

4.4. Pyramidal <c+a> slip

The last type of cylindrical micro pillar was prepared from grains with the prism planes parallel to the loading direction and the top surfaces of the pillars perpendicular to the c-axis.

4.4.1. Pyramidal slip systems: alpha/beta/alpha pillars

Two samples (grains) were oriented for pyramidal slip: with the first grain, as the EBSD data shows, the crystal direction normal to the top of the pillar (z direction) is [0001] while the y direction corresponds to the eventual foil normal orientation $[1\bar{1}00]$ as shown in Figure 4-26. In the second grain the crystal orientation of the top of the pillar z direction again corresponds to [0001] while the y direction corresponds to the foil normal orientation $[11\bar{2}0]$ as shown in Figure 4-27. The foil normals for the first and second grains are identified in the stereographic projection in Figure 4-28.

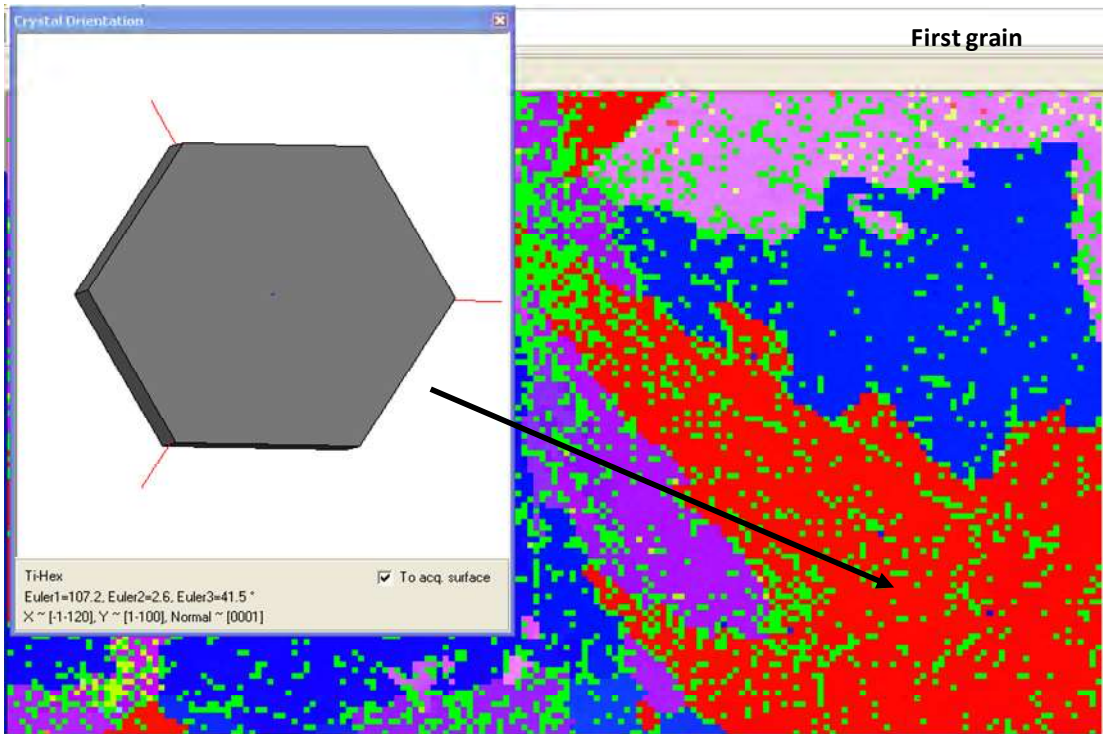

Figure 4-26 The 4-indices of the $x\,[\bar{1}\bar{1}20]$, $y\,[1\bar{1}00]$, and $z\,[0001]$ axes at the pillars extraction location given by the HKL Channel 5 software.

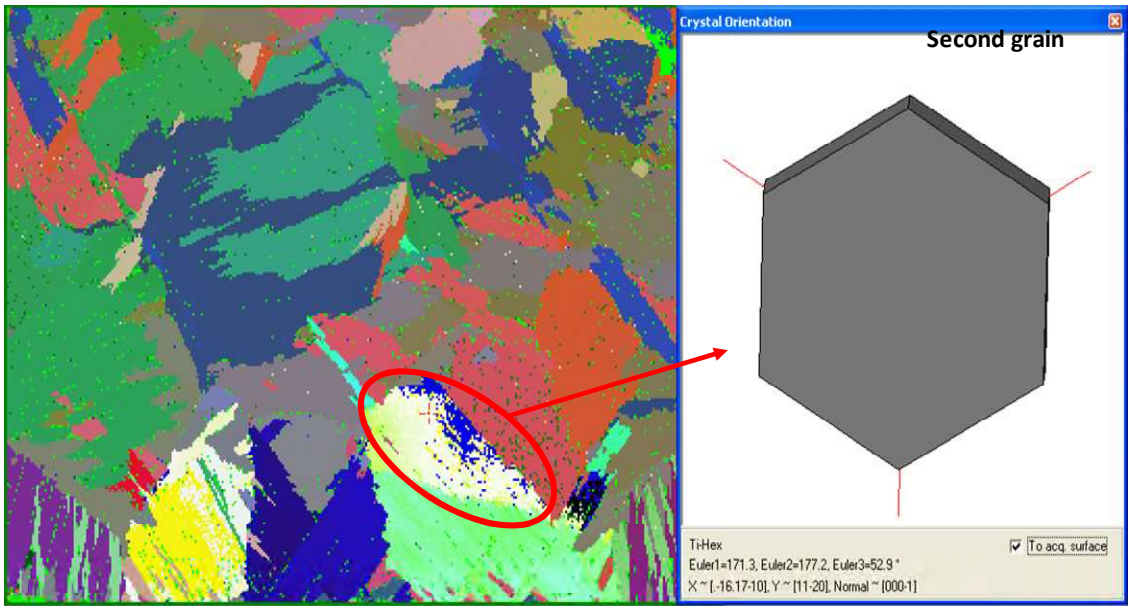

Figure 4-27 The 4-indices of the x~ $[\bar{1}100]$, y $[11\bar{2}0]$, and z $[000\bar{1}]$ axes at the pillar extraction location given by the HKL Channel 5 software (second grain).

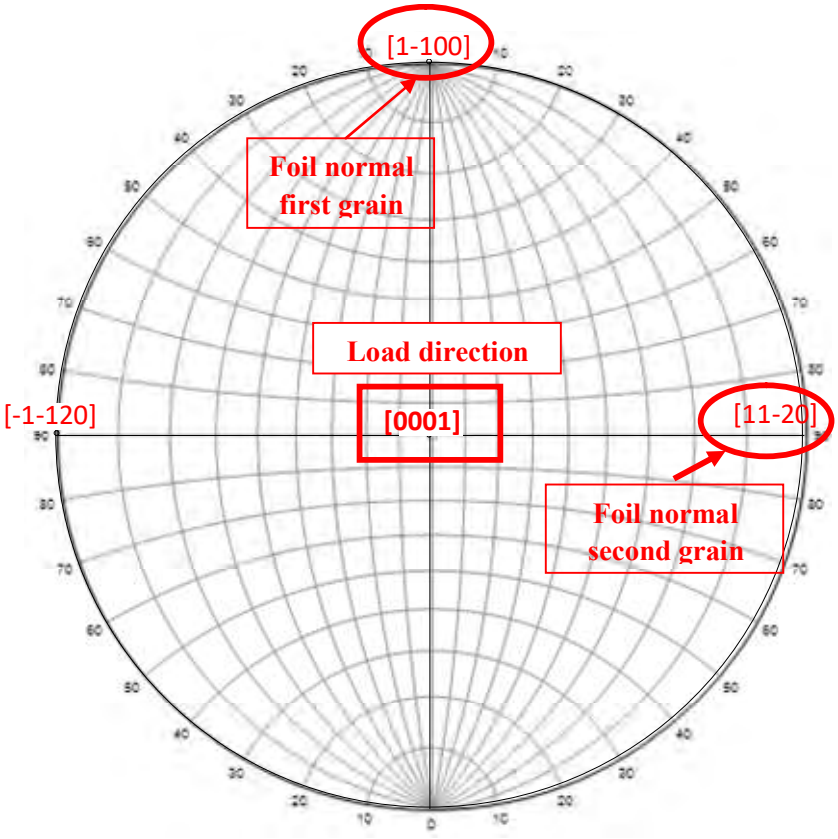

Figure 4-28 Stereographic projection for the first and second grains showing the loading directions in the α phase and the foil normals $[1\bar{1}00]$ and $[11\bar{2}0]$.

At this orientation, <a> slip on both basal and prismatic planes is suppressed as shown schematically in Figure 4-29. The target slip system is <c+a> on the pyramidal planes. Consequently, the Schmid factors on other slip systems, such as <a> on the basal and prismatic planes, are zero. It is therefore expected that the plastic deformation must be accommodated by pyramidal slip as shown in Figure 4-30. There are 6 slip systems that can accommodate the deformation with the possibility of cross-slip of <c+a> dislocations between $\{10\bar{1}1\}$ planes. This in turn would lead to very strong hardening due to the intersection of these slip planes.

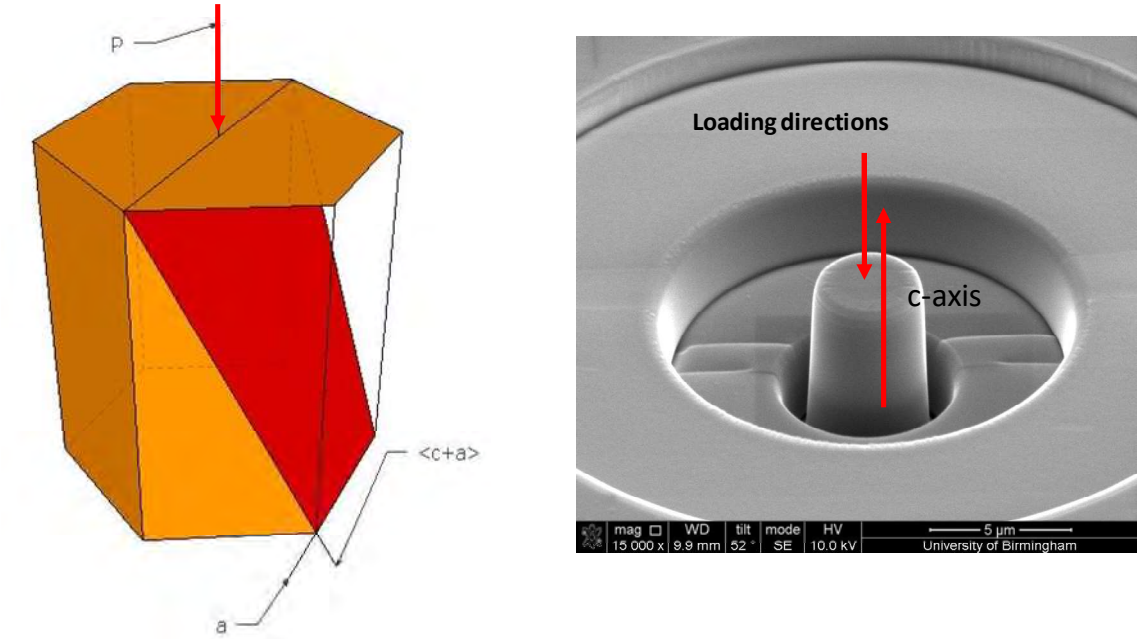

Figure 4-29 The crystal orientation of the micro-pillars and operation of a pyramidal <c+a> slip system.

An example of SEM micrographs of a single colony sample is shown in Figure 4-30. The slip lines are visible on the sample surface from different directions.

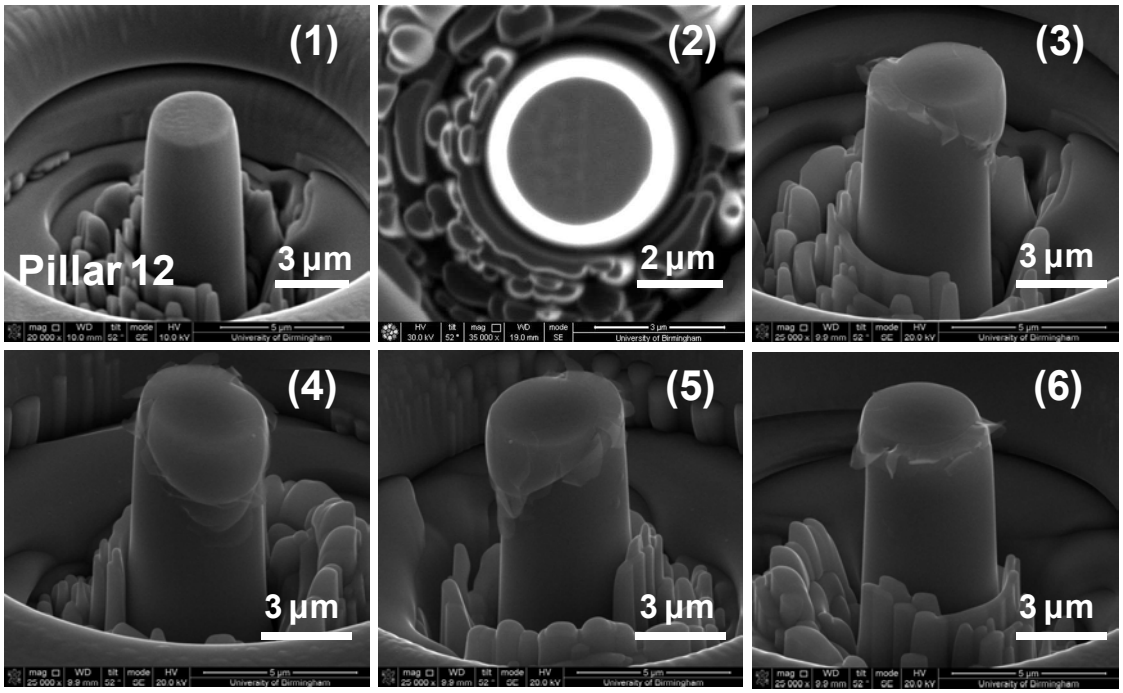

Figure 4-30 SEM micrographs of a typical micro-pillar fabricated by FIB and deformed; there is obvious slip. Pillar 12 (1) and (2) undeformed, (3) to (6) after deformation photographed from different directions. Pillar 12 was strained 7%.

Figure 4-30 corresponds to a small change in slope in the stress-strain curve. A slip step forms on the surface of the cylindrical micro-pillar (*in-situ* SEM deformation); change in the stress-strain curves are associated with discrete slip bands in the micro-pillars.

The crystallographic orientation of the pyramidal slip systems in the (alpha/beta/alpha) cylindrical micro pillar is shown schematically in Figure 4-31. The pillar is oriented favourably for pyramidal slip, with the compression axis aligned along the [0001] direction, allowing massive pyramidal slip to occur at a critical stress. Therefore, if the sample is well aligned the buckling direction and massive shear directions (for highly stressed columns) should show no single preferred direction amongst the compressed columns, as the various

pyramidal slip systems have the same Schmid factors relative to the [0001] loading direction (see Table 4-1). In practice usually only few slip system is activated per pillar, through some pillars exhibit three slip systems. It is interesting to note that, despite being from the same grain, the slip direction varies between pillars as shown in Figure 4-30 and Figure 4-31 . This is probably due to minor misalignments between the tip and pillar.

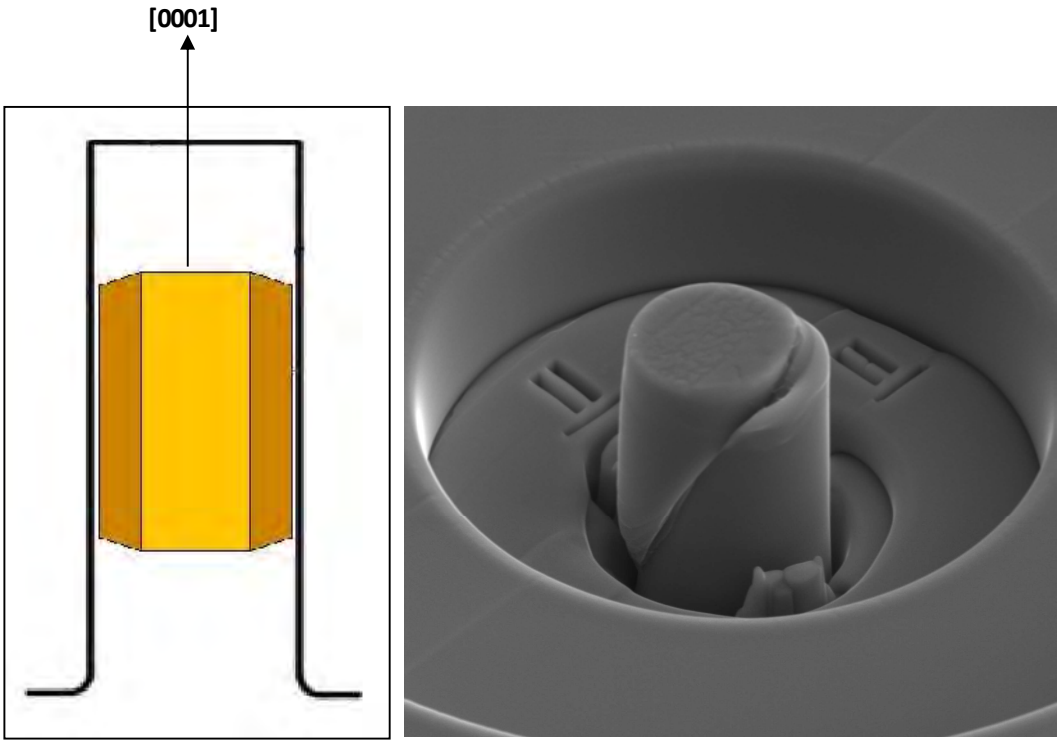

Figure 4-31 The crystallographic orientation of the pyramidal slip systems in a cylindrical micro-pillar.

The *exact* plastic strain applied to the micro-pillars during compression is determined from the stress-strain curve and will be discussed in more detail in the next chapter.

Typical stress strain curves of micro-pillars with different diameter (2 to 6 μm) oriented to activate pyramidal slip in tri-crystal alpha/beta/alpha pillars are shown in Figure 4-32. Figure

4-33 shows SEM micrographs of one deformed tri-crystal (alpha/beta/alpha) pillar with a nominal diameter of 4 μm, photographed from different orientations.

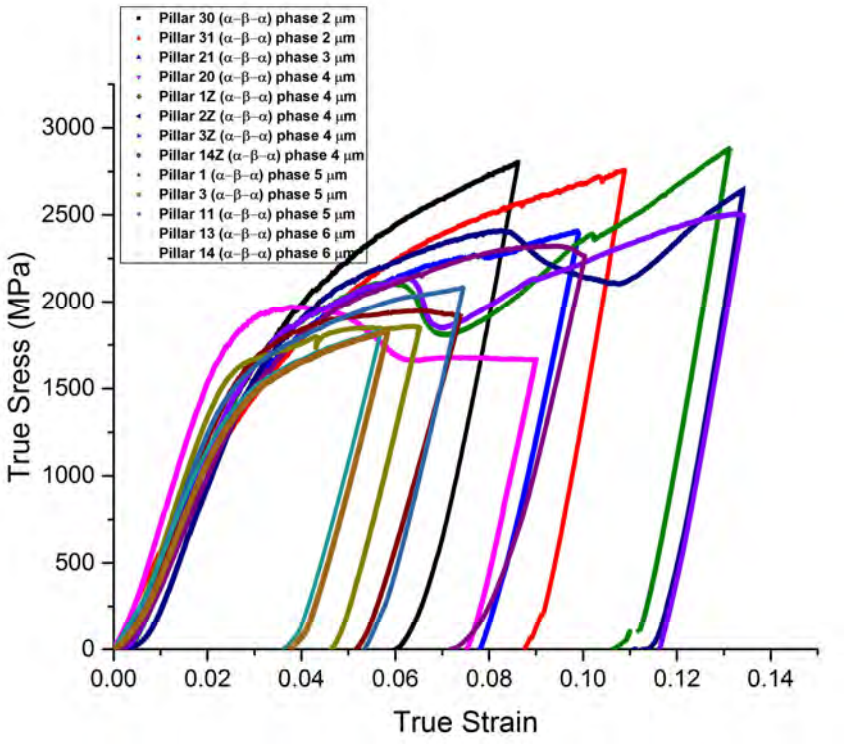

The samples follow linear elastic loading up to a stress of 1550 MPa, as shown in Figure 4-32. Figure 4-33 shows SEM micrographs of a tri-crystal (alpha/beta/alpha) pillar with a nominal diameter of 4 μm. The slip traces are consistent with the primary slip system, $\frac{1}{3}[1\bar{2}13]\{10\bar{1}1\}$, which was oriented for the maximum resolved shear stress by considering the angle between the alpha and beta phase as shown in Figure 4-33

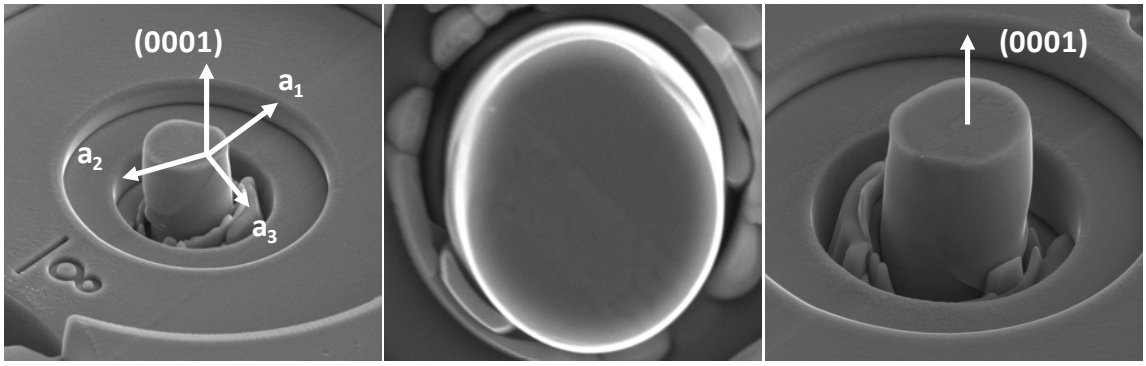

Figure 4-33 SEM micrographs for (alpha/beta/alpha) micro-pillar from different points of view with a nominal diameter of 4 µm for grain oriented to activate <c+a> pyramidal slip. Pillar 8 was strained ~ 6%.

The pillar 8 surface from Figure 4-33 shows small offsets both in the α phase and at the α/β interfaces as indicated by the yellow arrow. However, as seen in the secondary electron (SE) micrograph (Figure 4-33(b)), the offsets near the α/β interface are due to the presence of shear traces near the interfaces at the top of pillar 8. The shear traces are continuous and were observed to run throughout the sample.

The true stress-strain curve for (alpha/beta/alpha) micro-pillars with a diameter of 2 µm is presented in Figure 4-32, in order to compare with single (alpha and beta) phases for the same size. Table 4-9 presents the mechanical data.

Table 4-9 Summary of constant strain rate data acquired from the typical alpha/beta/alpha 2 µm to 6 µm diameter micro-pillars in compression set to activate <c+a> pyramidal slip.

Planes	Pillars	Diameter (µm)	Height (µm)	Yield Stress (MPa)	0.2%Strength (MPa)	CRSS (MPa)
Pyramidal plane	Pillar 30	2.06	4.3	1794	1950	888 ± 10
	Pillar 31	2	4.0	1815	1988	
	Pillar 21	3.15	6.2	1715	1815	821 ± 20
	Pillar 19	3.1	8.9	1641	1824	
	Pillar 20	4.15	8.65	1566	1736	770 ± 20
	Pillar 1Z	4.2	8.1	1632	1715	
	Pillar 2Z	4.2	8.5	1561	1720	
	Pillar 3Z	4.2	8.5	1534	1665	
	Pillar 14Z	4.2	8.1	1414	1583	
	Pillar 1	5.2	11	1383	1590	702 ± 10
	Pillar 3	5.15	11.5	1405	1574	
	Pillar 11	5.2	10.1	1378	1511	
	Pillar 13	6.03	14.2	1245	1420	630 ± 10
	Pillar 14	6.18	12	1174	1375	

4.4.2. Pyramidal slip systems: Alpha phase

SEM images of deformed [0001] single α-phase cylindrical micro-pillars with 2 μm diameter before and after deformation are shown in Figure 4-34. The slip lines are visible on the sample surface at different orientations.

True stress-strain curve representative of micro-compression experiments conducted at room temperature (25°C) on single alpha crystals with different diameters (2 to 4) μm oriented to activate <c+a> pyramidal slip are shown in Figure 4-35.

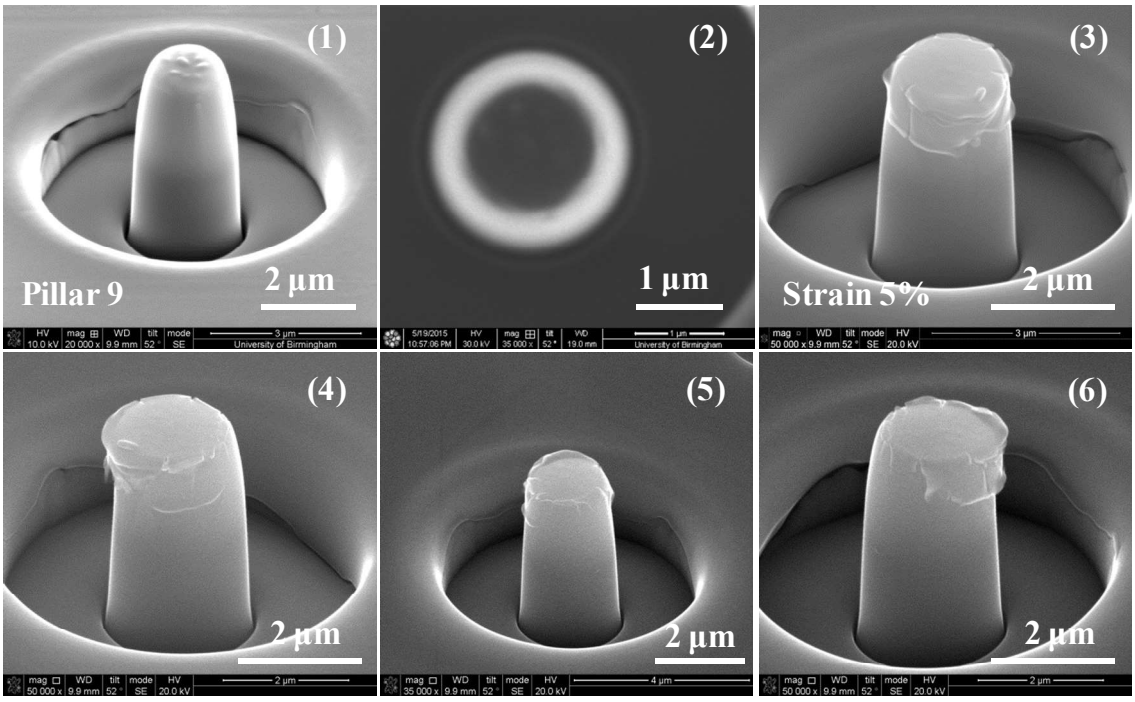

Figure 4-34 SEM micrographs of typical α micro-pillar fabricated by FIB. Obvious slip band on the micro pillar photographed at different orientations. Pillar (9) 2 μm diameter, (1) and (2) undeformed, (3) to (6) after deformation. Specimen was strained ~ 4%.

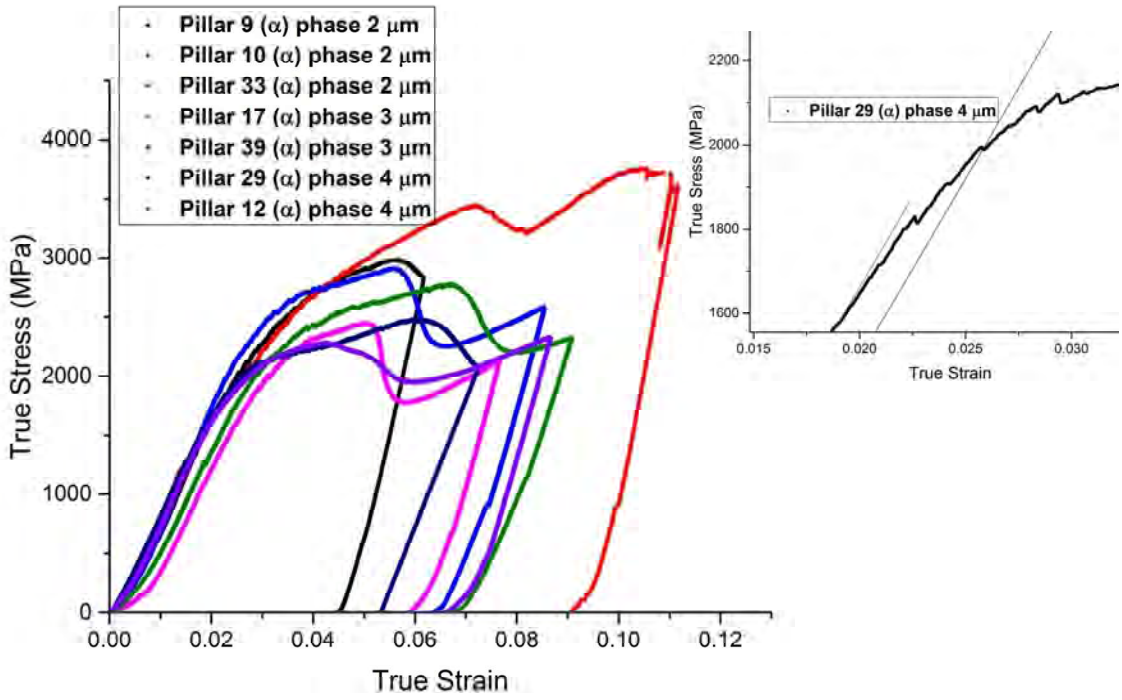

From Figure 4-35, for pyramidal slip in the alpha phase, the stress initially increased almost linearly with strain until the appearance of a small strain change around 2.5 % (as shown in the inset to Figure 4-35) strain and at a stress level of nearly 1900 MPa. The results of the mechanical analysis are shown in Table 4-10.

Table 4-10 Mechanical data for compression of single crystal oriented to activate pyramidal slip in alpha phase.

Planes	Pillars	Diameter (μm)	Height (μm)	Yield Stress (MPa)	0.2% Strength (MPa)	CRSS (MPa)
<c+a> pyramidal planes	Pillar 9	2.08	6	1855	2293	1057 ± 15
	Pillar 10	2.14	6	1979	2337	
	Pillar 33	2.1	6.08	1985	2407	
	Pillar 17	3.1	9.5	1801	2079	938 ± 15
	Pillar 39	3.08	6.1	1877	2172	
	Pillar 40	3.02	8.0	1763	1994	
	Pillar 12	4.12	10.2	1696	1972	880 ± 20
	Pillar 29	4.15	10.8	1720	1962	
	Pillar 42	4.06	8.3	1766	1925	

4.4.3. Beta phase

The cylindrical micro pillars were prepared from the same grain and colony as the alpha phase, where the crystal orientation of the top of the pillar z direction corresponds to $[0001]_{\alpha}$ or $[101]_{\beta}$. SEM images before and after deformation are shown in Figure 4-36.

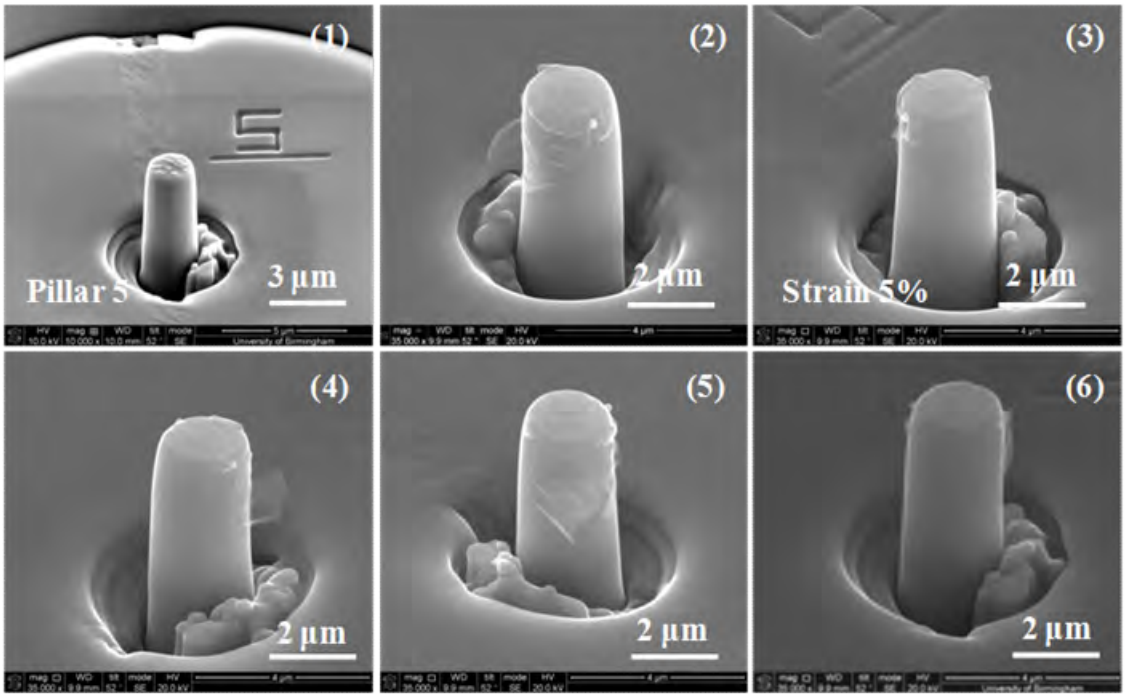

(Continued)

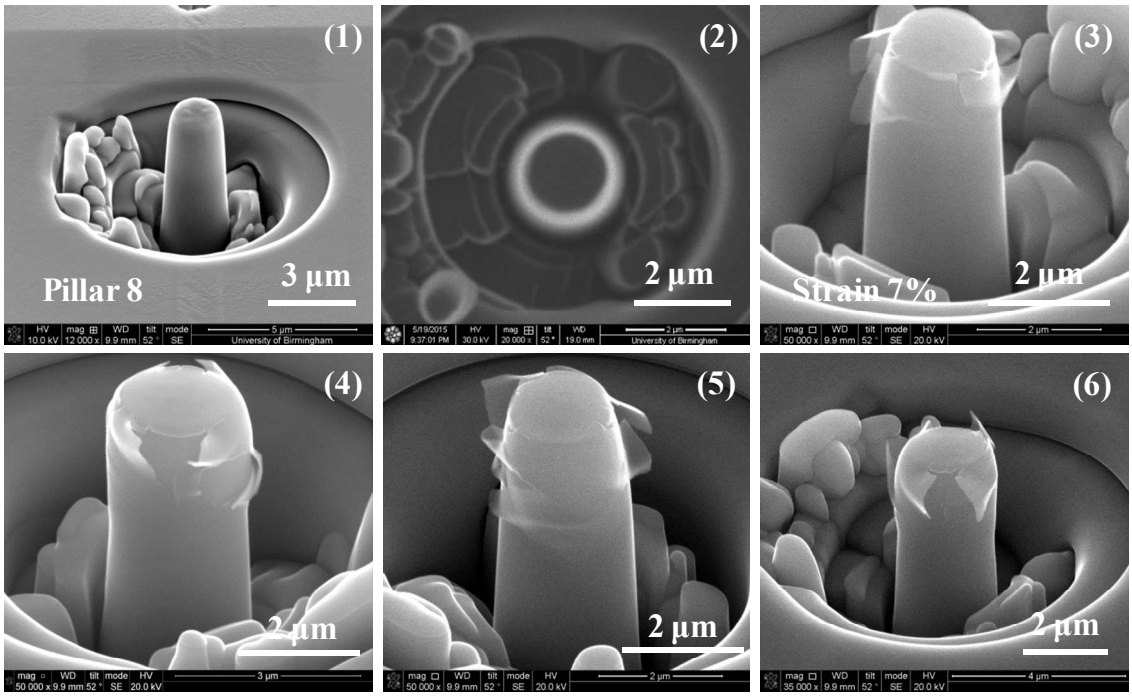

Figure 4-36 SEM micrographs of typical micro-pillars fabricated by FIB from beta phase. Obvious deformation on the micropillars at different orientation. Pillars (5 and 8) are 2 specimens (1) undeformed (2) to (6) after deformation, different orientations.

The true stress-strain curves for micro-pillars of single beta phase with two diameters 1 and 2 µm are shown in Figure 4-37. The diameters measured at the mid-height of the micro-pillars were 1 and 2 µm. The exact dimensions of each cylindrical pillar are listed in Table 4-11.

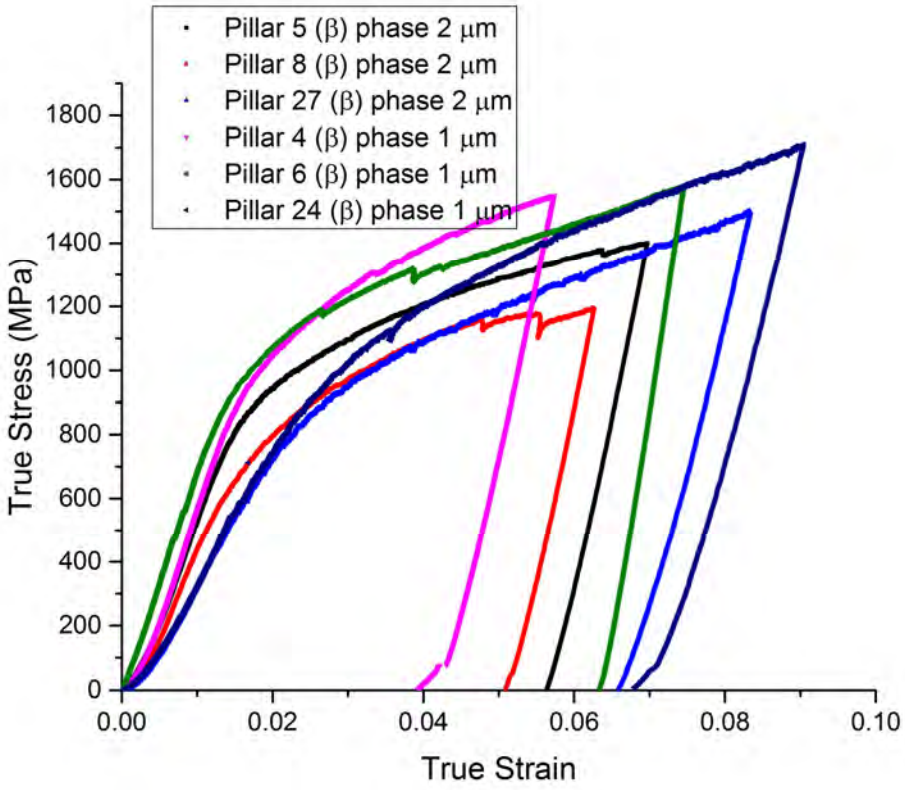

Figure 4-37 True stress-strain curves for β micro-pillars parallel to $[0001]_{\alpha}$.

As shown in Figure 4-37, the applied stress increased almost linearly up to 2% strain at a stress level of nearly 900 MPa, followed by further but slower hardening. The results obtained from the mechanical analysis are shown in Table 4-11.

Table 4-11 Summary of constant strain rate data acquired from micro-pillar compression for 1 and 2 µm single phase β pillars.

Slip phase type	Pillars	Diameter (µm)	Height (µm)	Yield Stress (MPa)	0.2% Strength (MPa)	CRSS (MPa)
{101} plane	Pillar 4	1.05	2.4	810	1015	446 ± 10
	Pillar 6	1.1	2.8	847	996	
	Pillar 24	1.06	2	791	956	
	Pillar 5	2.08	6.0	820	907	391 ± 15
	Pillar 8	2.12	7.4	714	835	
	Pillar 27	2.0	4.6	743	860	

4.5. **Orientation-size effects**

The micropillar compression test was originally conceived of as a means of studying the size dependence of plasticity. It has been used this way extensively in metals, where there is much evidence that strength increases as the sample size decreases. If micropillar compression is to be used to measure bulk yield stresses and critical resolved shear stresses, it is vital to understand the effect of size on the values obtained.

Observation of size effects in Ti-64, tri-crystal alpha/beta/alpha pillars, single crystalline alpha pillars and beta pillars and their dependence on orientation are presented in this section.

Alpha and (alpha/beta/alpha) phase pillars with [0001], $[\bar{1}5\bar{4}6]$ and $[01\bar{1}0]$ compression axes and with different diameters have been examined. In single and tri-crystal cases, we investigated the size effect of dislocation plasticity, but in the case of the tri-crystal [0001], $[\bar{1}5\bar{4}6]$ and $[01\bar{1}0]$ orientations, we must also consider the beta phase strengthening.

To minimize the strengthening from the β phase as well as to simplify defect evolution and hardening mechanisms, a single phase is also oriented for maximum shear stress along the <a> direction $[1\bar{2}10]$ on the basal plane (0001), $\langle\bar{2}110\rangle$ on the prismatic plane $\{\bar{1}010\}$ and <c+a> directions on the pyramidal planes. True stress–strain curves for basal slip versus sample diameter in α/β/α pillars and in single alpha pillars are shown in Figure 4-9 and Figure 4-14. These figures clearly show the overall change in flow behaviour as a function of sample size.

The flow stresses for (α/β/α) basal slip are plotted versus sample diameter in Figure 4-38. It is apparent from this plot that an increase in strength with decreasing sample size is observed.

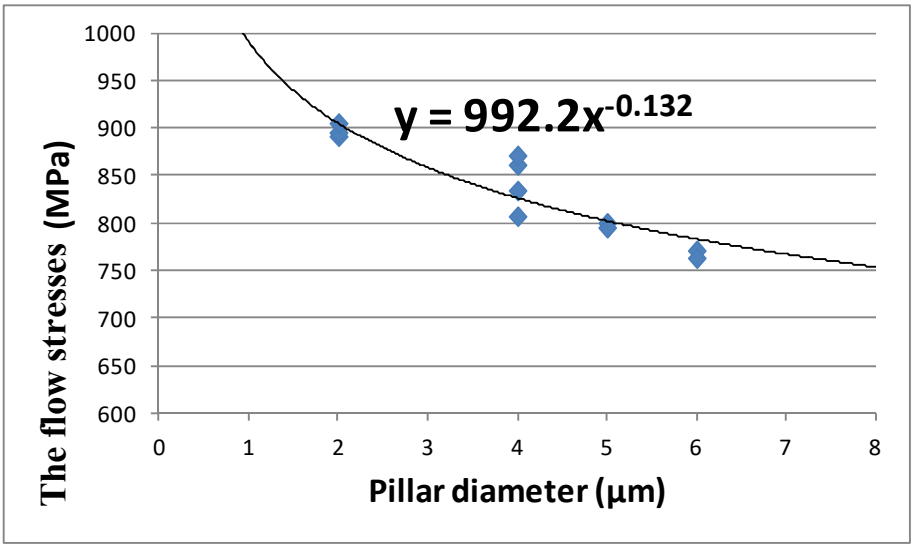

The strength versus pillar diameter for the alpha phase micropillar for basal <a> slip is shown in Figure 4-39.

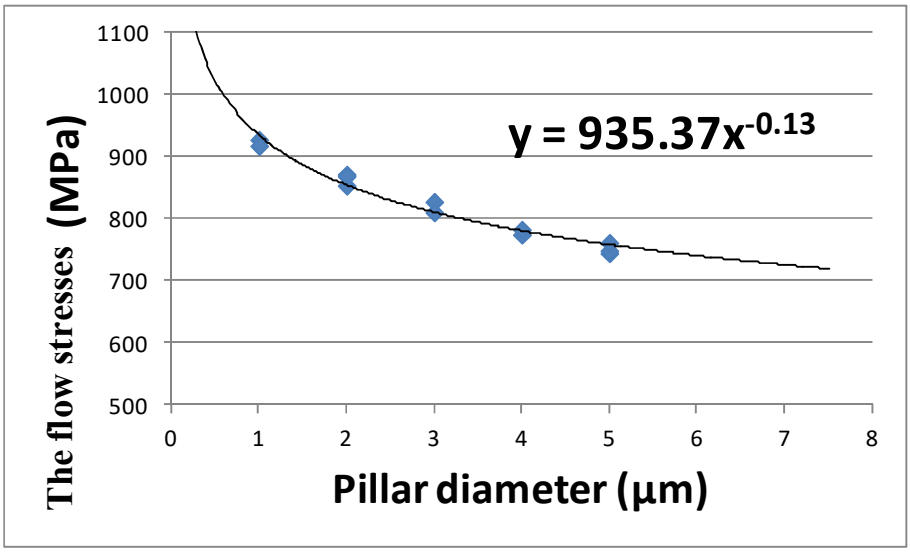

Strength versus pillar diameter for the alpha/beta/alpha and alpha columns for prismatic <a> and pyramidal <c+a> slip are shown in Figure 4-40 to Figure 4-43.

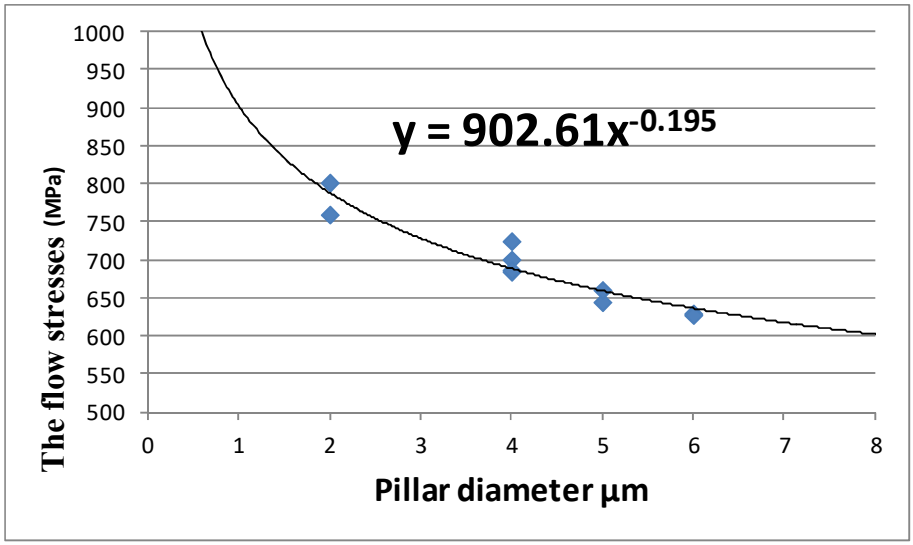

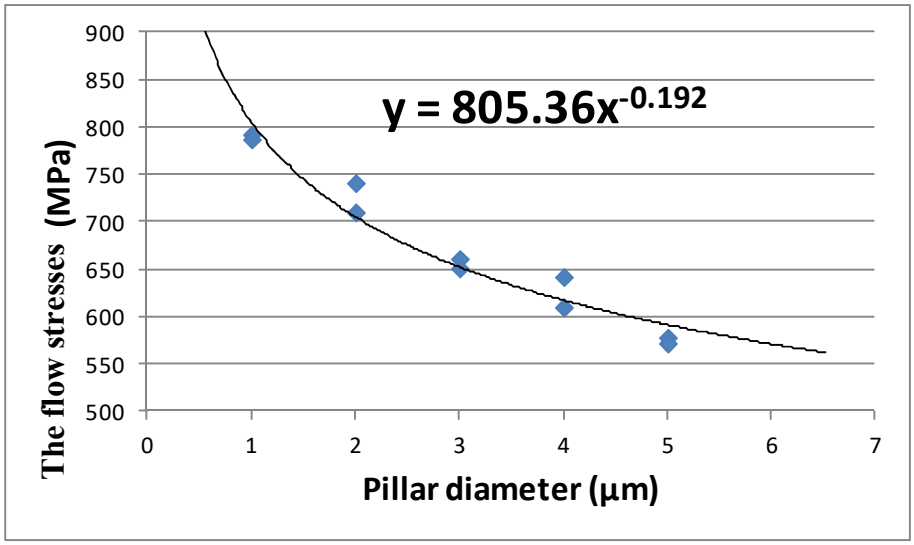

Figure 4-41 Strength versus pillar diameter for alpha columns prismatic slip (the line is fitted). Strength is taken as the flow stress at 0.2% plastic strain.

The strength for α/β/α pyramidal slip versus sample diameter (Figure 4-42and Figure 4-43).

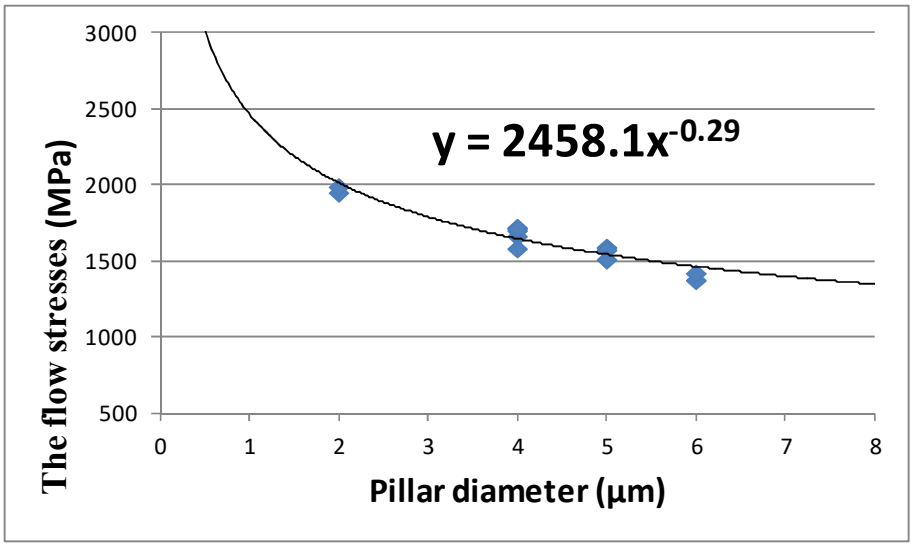

Figure 4-42 Strength versus pillar diameter for alpha/beta/alpha pillars c+a pyramidal slip (linear power fit of measured data). Strength is taken as the flow stress at 0.2% plastic strain.

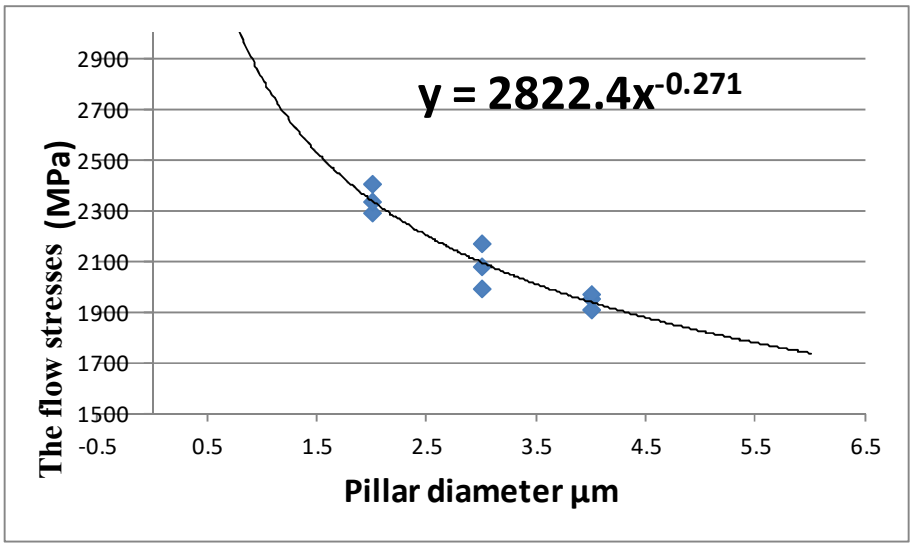

Figure 4-43 Strength versus pillar diameter for alpha columns c+a pyramidal slip (linear power fit of measured data). Strength is taken as the flow stress at 0.2% plastic strain

In comparing these curves (from Figure 4-38 to Figure 4-43) the most obvious difference is the pronounced influence of the pillar diameter. The exponents m from a power law

expression describing the size effect vary from -0.29 for Pyramidal <c+a> slip, exhibiting the largest size effect, through -0.194 for prismatic <a> slip to -0.132 for basal <a> slip. When the pillar diameter is 6 μm and above (Figure 4-32), the stress-strain behaviour is different from that when deformed at 5 μm and below, as the microcompression machine cannot reach a sufficiently large force to show load drops for a pillar or to activate pyramidal <c+a> slip for pillars wider than 6 μm. For this strain, after reaching the yield strength, the flow stress increases with strain with different work hardening rates.

Sample size is strongly affected by orientation as shown in Figure 4-44 and Figure 4-45, in contrast to the fcc crystal structure, for which the sample size effect does not show orientation dependence [11].

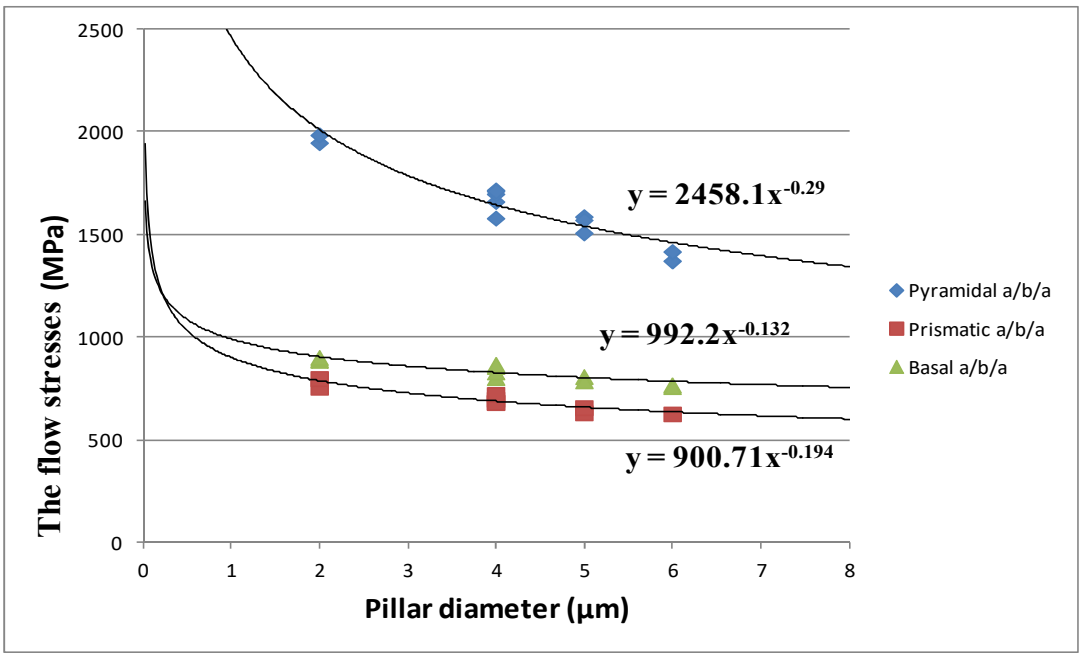

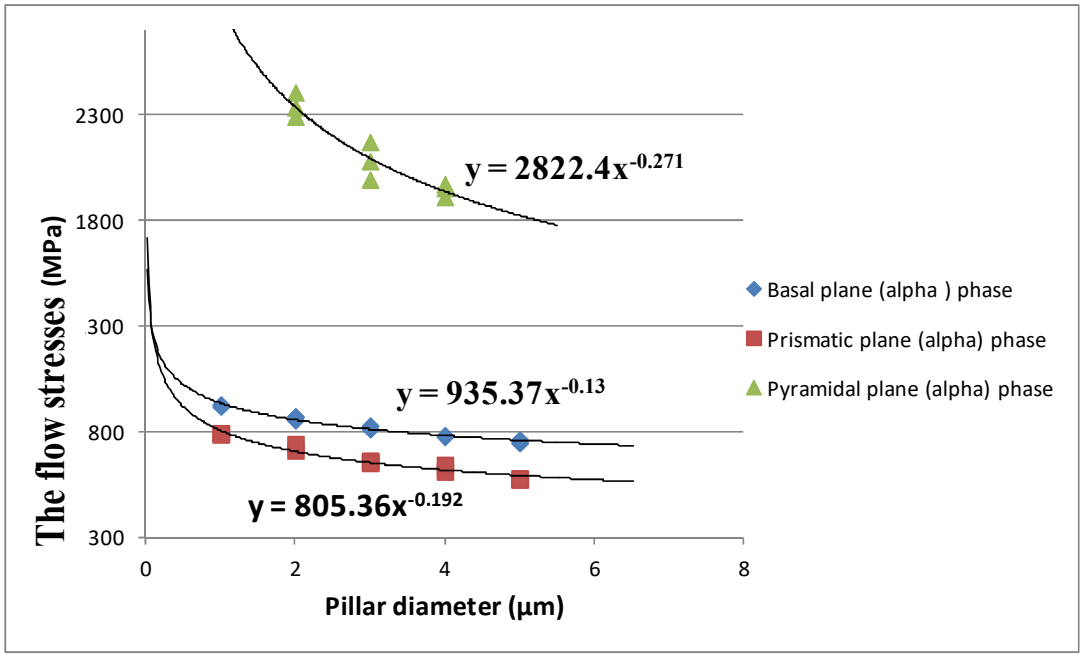

It is accepted that the α/β interface will lead to an increase in the rate of hardening: it is a sessile defect acting as an obstacle to dislocation motion. Both group of micropillars (single and tri-crystal types) show a pronounced rise of the flow stress with decreasing sample dimension.

4.6. **Strain hardening**

Traditionally, strain hardening is associated with strong interactions between dislocations and an increase in dislocation density throughout an experiment. Strain hardening has been inconsistently observed in other micro-pillar studies, is found to be a function of both diameter and orientation. Although the precise mechanism for hardening is unknown,

transmission electron microscopy reveals dislocations throughout the pillar and into the base material suggesting that dislocation interactions and deformation below the pillar play a role in the observed strain hardening [112]. Frick *et al*. [112] suggests that the strain hardening rate for small-scale Ni pillars is inherently dependent on both orientation and diameter regardless of aspect ratio [112].

A closer inspection of the true stress-strain figures shows that with smaller micropillar exhibiting higher strain-hardening rates (ignoring the fluctuations and measured from yield point and proof stress to 0.5% strain). The underlying physical mechanism can be understood in terms of a competition between the dislocation nucleation/activation rate and the (mobile) dislocation annihilation rate. If there are enough mobile dislocations or a productive enough dislocation source to accommodate the imposed deformation a stress/load drop will occur. However, if there are not enough active sources or dislocations to accommodate the imposed deformation the stress/load will increase. This phenomenon may contribute to the increasingly high strain hardening values as a function of decreasing diameter observed in the true stress-strain figures.

The observed increase in SHR as a function of the diameter for the Ti-64 micropillars ($SHR \propto d^{-0.45}$ to $d^{-1.15}$) is very similar to that reported by Volkert and Lilleodden [87] for Au pillars ($SHR \propto d^{-1.07}$).

4.7. **Summary**

1. The stress-strain curves for alpha/beta/alpha micro-pillars oriented in the $[\bar{1}5\bar{4}6]$ direction to activate basal slip show that the stress increased initially almost linearly with strain until the appearance of a gradient change about 1.5% strain and at a stress level of nearly ~ 700 MPa.

2. The stress-strain curves for alpha single crystal have a lower CRSS than the alpha/beta/alpha tri-crystal. Thus, the effectiveness of the α/β interface in restricting slip motion is very obvious and thereby the strengthening in the pillar.

3. The 2 μm cylindrical pillars have been compared for alpha and beta single crystals and alpha/beta/alpha samples for both basal and prismatic planes. The alpha/beta/alpha ones have a much higher CRSS and flow stress in both cases the alpha/beta interfaces within these colonies was considered to provide hindrance to slip and therefore add interface strengthen to the pillar strengthen. The single beta phase has lower CRSS values than the single alpha and alpha/beta/alpha crystal structures.

4. The difference in the exponents from a power law expression relates to the additional strengthening from the beta phase, which are considered to provide hindrance to slip movement.

5. Both basal and prismatic slip were compared. Generally speaking, the CRSS value for <a> slip on the basal plane for the Ti alloys is higher by 25% than for <a> slip on prismatic planes.

6. The effectiveness of the α/β interface in restricting slip motion in basal and prismatic planes is obvious from the mechanical indentation data for compression, alpha/beta/alpha and single alpha phase micro-pillars.

7. The single alpha phase CRSS for <c+a> pyramidal slip is higher than for the alpha/beta/alpha pillars, but the alpha/beta/alpha pillars are harder than a single beta pillar for pyramidal alpha slip.

8. The observed values for critical resolved shear stress (CRSS) for the basal and prismatic slip orientations were lower than those observed for the pyramidal orientations. Significant anisotropy in the values of CRSS for the three different slip systems in Ti-6Al-4V has been observed.

9. In general, the effect of the beta lath causing a difference between the exponents m from a power law expression is clear for the three different slip systems.

10. It is apparent from the mechanical analyses that an increase in strength with decreasing sample size is observed. The size effect is substantially stronger for the <c+a> pyramidal orientation than for the <a> basal and prismatic orientations.

11. Micropillar Ti-64 shows increase in strain hardening with decreasing diameter. This 'enhanced' strain hardening behaviour is size-scale dependent, with smaller samples exhibiting higher strain-hardening rates.

Chapter Five

5. Scanning Electron Microscopy Results

5.1. Introduction

In this chapter will be reported SEM observations of the micropillar compression tests. The mechanical results were reported in the last chapter and the TEM results will be reported in the next. The focus here was to identify the number of slip bands, the slip planes, the slip directions, to measure the sizes of the slip steps, thus determining the number of dislocations corresponding to each slip step and finally to determine how the dislocations interact with the β laths, all of these based on the SEM data.

5.2. Alpha/beta: crystallography and orientation relationship

Previous studies on a near-alpha Ti alloy (Ti–15V–3Cr–3Sn–3A) [17] and a β-Ti alloy containing alpha precipitates (Ti-7.15Cr) [50] confirmed that the Burgers OR (shown in Figure 5-1) between alpha and beta phases, $(0001)_\alpha \,//\, (101)_\beta$; $[2\bar{1}\bar{1}0]_\alpha \,//\, [11\bar{1}]_\beta$, is generally but not exactly followed. $[\bar{1}11]_\beta$ is not precisely parallel to $[1\bar{2}10]_\alpha$.

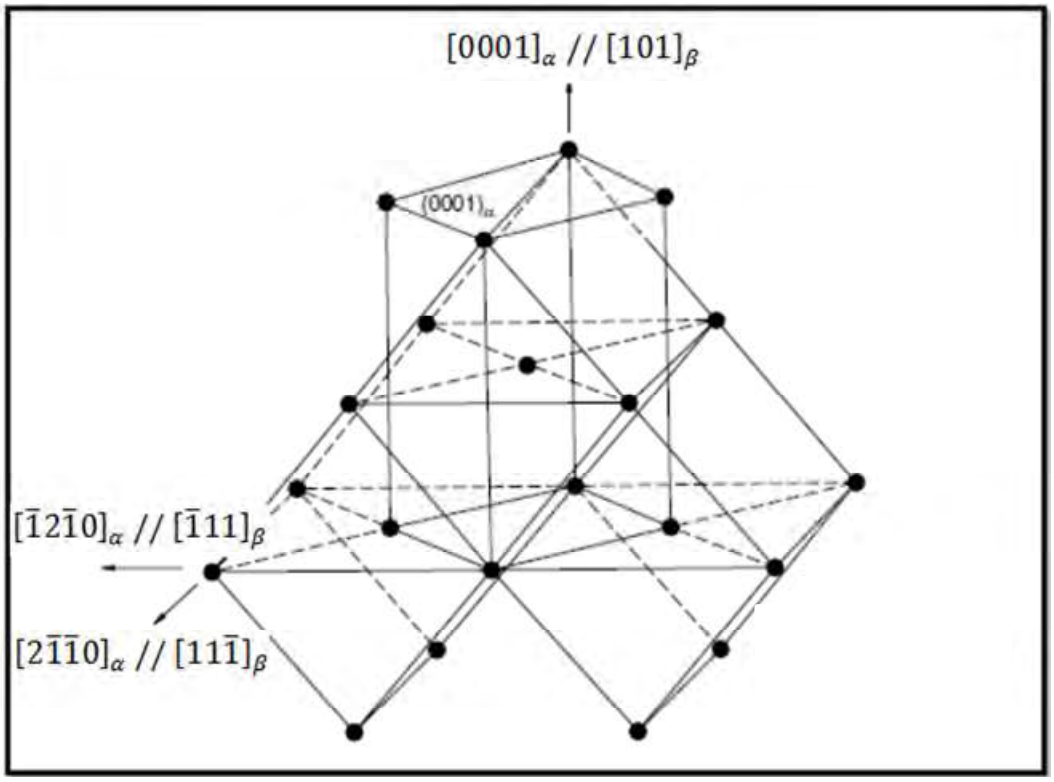

Figure 5-2 shows selected-area diffraction patterns taken from the alpha–beta interface along the $[1\bar{2}10]_\alpha$// $[\bar{1}11]_\beta$ direction. The β phase is exactly at the $[101]_\beta$ zone axis; the $[0002]_\alpha$ zone is slightly off (see Figure 5-2 c). The misorientation is a rotation of 0.57° about $[\bar{1}11]_\beta$ (or $[1\bar{2}10]_\alpha$).

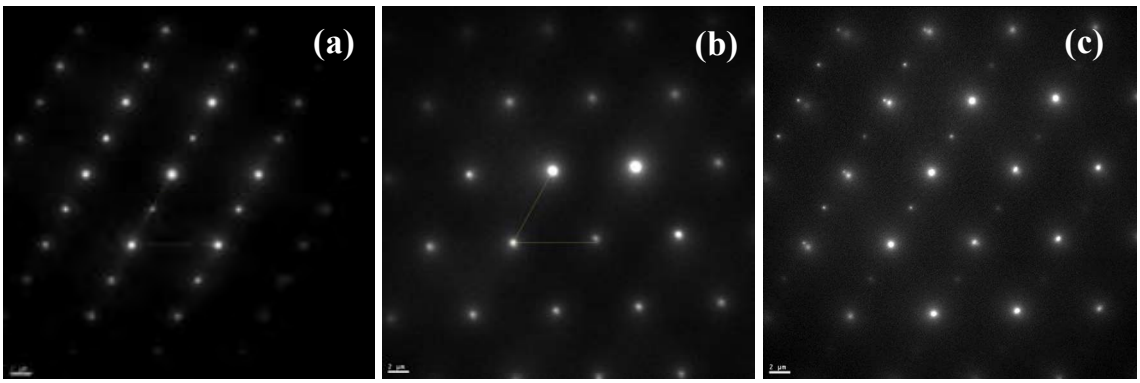

A selected area diffraction (SAD) pattern obtained from an alpha/beta interface along the $[0001]_{\alpha}$ // $[101]_{\beta}$ directions is shown in Figure 5-3.

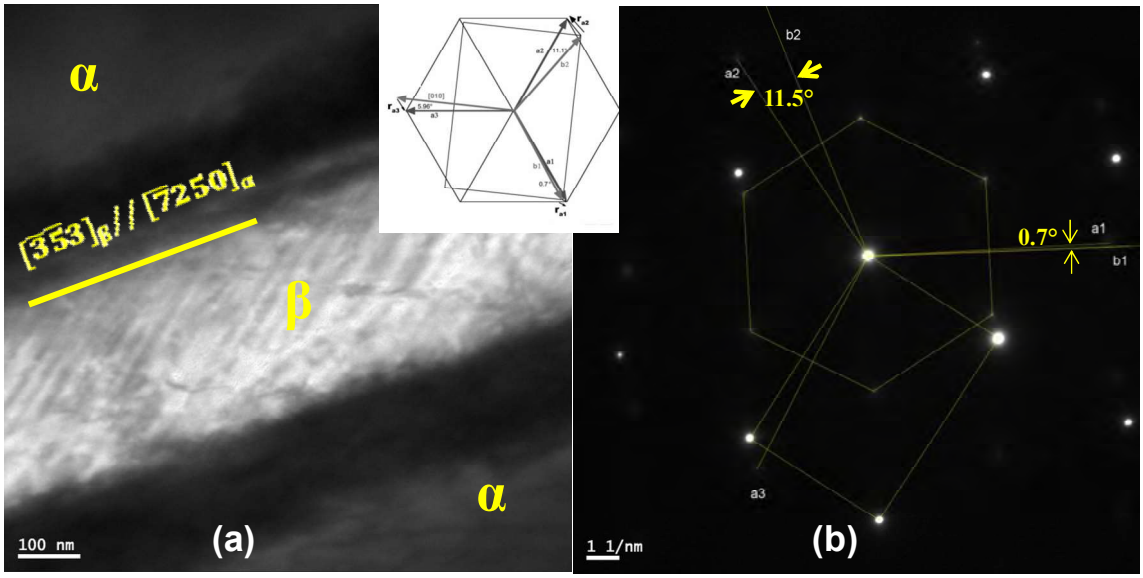

Figure 5-3 (a) TEM micrograph of the alpha/beta interface along the [0001]α// [101]β direction, (b) selected area diffraction (SAD) pattern taken at the alpha/beta interface along the [0001]α//[101]$_\beta$ directions showing the alignment of the (a_1, a_2 and a_3) alpha phase directions with (b_1 and b_2) beta phase directions arising from the near-BOR. Note inset figure is a schematic of the observed near-BOR in Ti64 single colony.

A careful examination of the SAD patterns reveals a misalignment of 0.7° between the a_1 slip direction in the alpha phase and the $[1\bar{1}\bar{1}]_\beta$ slip direction in the β phase (thus resulting in easy slip transmission across the alpha/beta interface). Previous studies have defined (a_1, a_2 and a_3) for alpha phase as being nearly aligned with (b_1 and b_2) in beta phase [51] (for details see [113]). In contrast, a rotation of about ~11.5° is required between the a_2 type slip direction in the alpha phase and the closest matching $[\bar{1}11]_\beta$ slip direction in the beta phase, therefore resulting in more difficult slip transmission and a measurably higher critical resolved shear stress, while for the a_3 type slip direction, there is no correspondence between the slip vectors of the two phases for which, therefore significant hardening might be anticipated. The obstruction to slip may cause higher CRSS values for these slip systems, leading to activation of unexpected slip systems and invalidating the Schmid factor calculation.

The angle of rotation about the $[0001]$ || $[101]$ directions to obtain an invariant line direction depends upon the principal distortions (and through that on the ratio of the lattice parameters). Figure 5-4 (a), taken from the work by Dahmen [51] shows the dependence of the angular rotation on the ratio of the lattice parameters. For Ti64, the ratio of the lattice parameters between the two phases is determined from the SADP's as $\sqrt{2}\ a_\alpha/a_\beta = 1.27$ and $(c/a)_\alpha = 1.587$. Thus the rotation angle (θ) (see Figure 5-4 (a) for details) predicted by the invariant line analysis is 5.8°. This rotation is 0.54° more than 5.26°, which is the "crystallographic" rotation which will allow $[2\bar{1}\bar{1}0]\alpha$ to be exactly parallel to $[11\bar{1}]_\beta$. [Note that the "crystallographic" rotation is that associated with the Burgers OR relative to the Pitsch-Schrader OR.] The extra rotation of 0.54° is close to our experimental finding of 0.57° although not precisely the same as the prediction of the invariant line analysis [51]. The additional rotation beyond the Burgers OR suggests that this orientation relationship is reached before the invariant line direction is produced. It was proposed by Dahmen [51] that any additional disorientation should be accommodated by rotating about $[11\bar{1}]_\beta$ || $[2\bar{1}\bar{1}0]_\alpha$. Figure 5-4 (b) shows the dependence of the angular rotation as a function of the ratio of lattice parameters for different c/a ratios for a Potter OR. This predicted rotation θ about the $[2\bar{1}\bar{1}0]_\alpha$ || $[11\bar{1}]_\beta$ axis is predicted to be 1.38° (as seen in Figure 5-4 (b)). However, this rotation is significantly larger than our experimental result of 0.74°. It seems that for this particular bcc/hcp system, it is difficult to explain completely the experimental observations using the invariant line analysis.

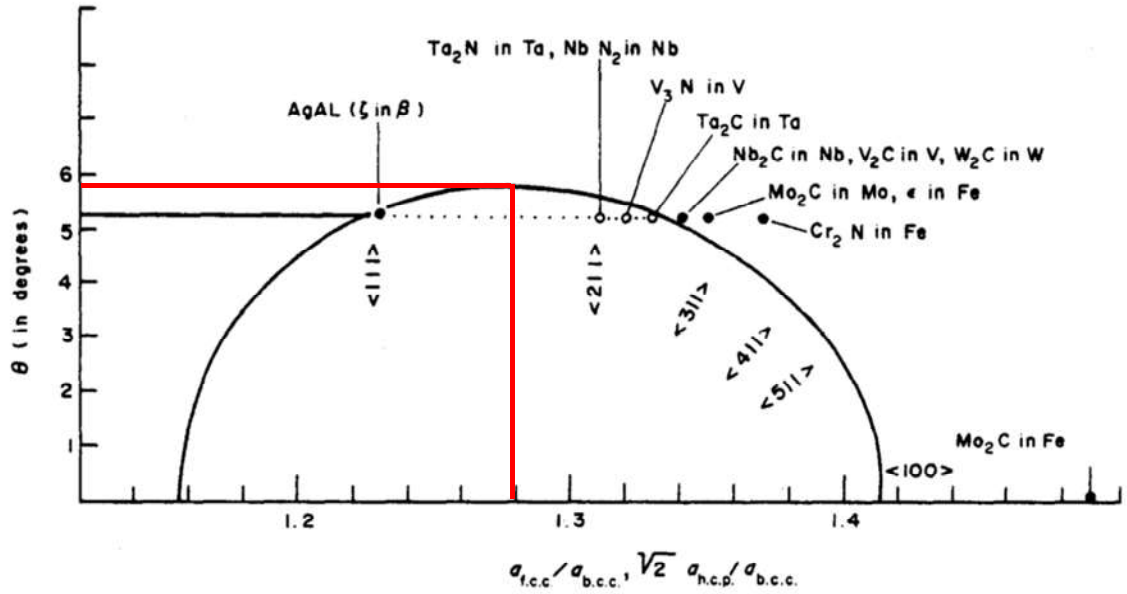

(a)

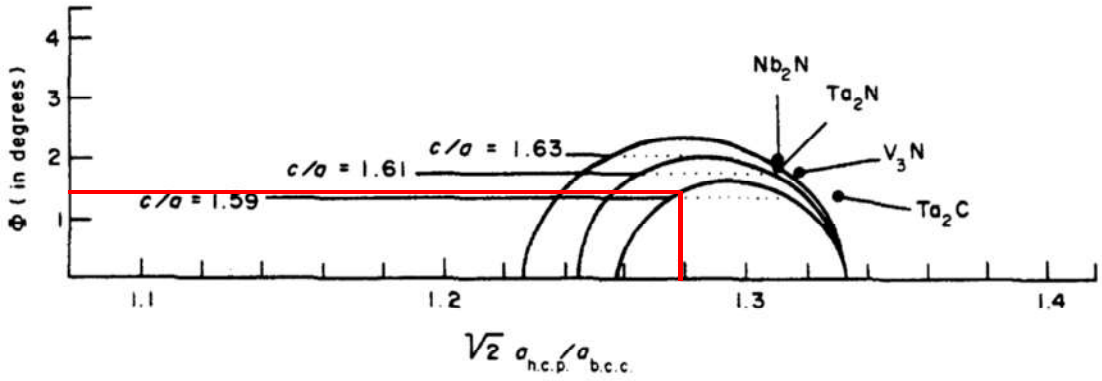

(b)

Figure 5-4 (a) Rotation angle θ necessary to produce an invariant line by rotation around the normal to the close packed planes of the bcc/hcp phases, namely the (101) || (0001). A ratio of 5.26° results in the Burgers OR. (b) Invariant line rotation β for bcc/hcp systems in the range of Potter's OR, the rotation axis being parallel to close packed directions, namely $[2\bar{1}\bar{1}0]_\alpha$ || $[11\bar{1}]_\beta$ [51].

It is appropriate, then, to examine the relative inclination of the invariant lines. By definition an invariant line is a direction that remains straight during the transformation, as would be

expected from the different slip directions at the alpha/beta interface by overlapping the SAD patterns with the BF TEM image as shown in Figure 5-5. The measured inclinations of the a_1, a_2 and a_3 slip directions to the invariant line were 14.5°, 75° and 45.5°, respectively.

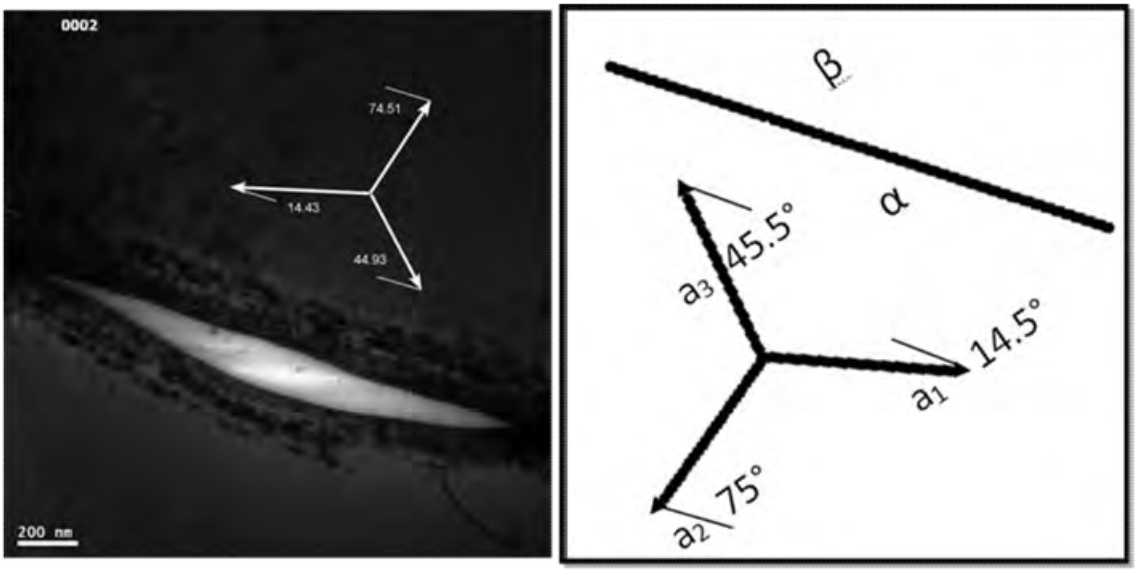

On one side of the lath, the interface is seen to be relatively straight, while facets are clearly observed on the other side. In both cases, the long facets of the interface are parallel to the invariant line direction. These long facets that run into the plane of the paper are termed the 'broad faces' of the β laths (for details see [17]) .

The invariant line construction was proposed by Dahmen [51]. In order to describe a method to determine the invariant line direction for the alloy used in the current study, we start with a Burgers orientation relationship (see Appendix A):

$$(0001)_\alpha \,//\, (101)_\beta \quad \textbf{5-1}$$

$$[2\bar{1}\bar{1}0]_\alpha \,//\, [11\bar{1}]_\beta \quad \textbf{5-2}$$

For a basal plane of the hcp lattice superimposed on a {101} plane of a bcc lattice (see ref. [51] for details), the deformation matrix is given by

$$A = \begin{pmatrix} \frac{c_\alpha}{\sqrt{2}a_\beta} & 0 & 0 \\ 0 & \sqrt{\frac{3}{2}}\,\frac{a_\alpha}{a_\beta} & 0 \\ 0 & 0 & \frac{a_\alpha}{a_\beta} \end{pmatrix} \quad \textbf{5-3}$$

where a_α and a_β are the lattice parameters for the respective phases. Table 5-1 the lattice parameters measured by electron diffraction for the alpha and the beta phases for the alloy in this study.

Table 5-1 the lattice parameters measured by electron diffraction for the alpha and the beta phases for the Ti 64 and Burgers vectors.

	Beta phase (β)	Alpha phase (α)
a	**0.327 nm**	**0.295 nm**
c	/	**0.468 nm**
b	**0.284 nm**	**0.295 nm**
c/a	/	**1.586**

In addition to the deformation, a rotation θ is required such that.

$$\hat{R} = \begin{pmatrix} 1 & 0 & 0 \\ 0 & \cos\theta & \sin\theta \\ 0 & -\sin\theta & \cos\theta \end{pmatrix} \quad \textbf{5-4}$$

The invariant line, by definition is a direction that remains undeformed and non-rotated during the transformation. Mathematically, this can be expressed as

$$\hat{u} = \hat{R}\, A\, \hat{u} \quad \textbf{5-5}$$

which implies that

$$\left|\hat{R}A\right| = 1 \quad \textbf{5-6}$$

or

$$\cos\theta = \frac{1 + \frac{\sqrt{3}}{\sqrt{2}}\frac{a_\alpha^2}{a_\beta^2}}{\sqrt{\frac{3}{2}}\frac{a_\alpha}{a_\beta} + \frac{a_\alpha}{a_\beta}} \quad \textbf{5-7}$$

Substituting the values of a_α and a_β into Equation 5-7, one gets a value of θ equal to 5.797°. Substituting the value of θ into Equation 5-4, one gets the invariant line direction in the Cartesian coordinates to be close to $[\bar{3}\bar{5}3]_\beta$.

In order to accommodate the misfit at the α/β interface with only structural ledges, an extra small rotation from θ = 5.26° is needed to make the structural ledge follow the invariant line (i.e. $[\bar{3}\bar{5}3]_\beta$ or $[\bar{7}250]_\alpha$).

5.3. Propagation of <a> dislocations: Basal <a> slip

5.3.1. Summary of mechanical properties

Pillars D and E were examined in detail by SEM. Their mechanical properties, abstracted from Figure 4.10, are shown in Figure 5-6.

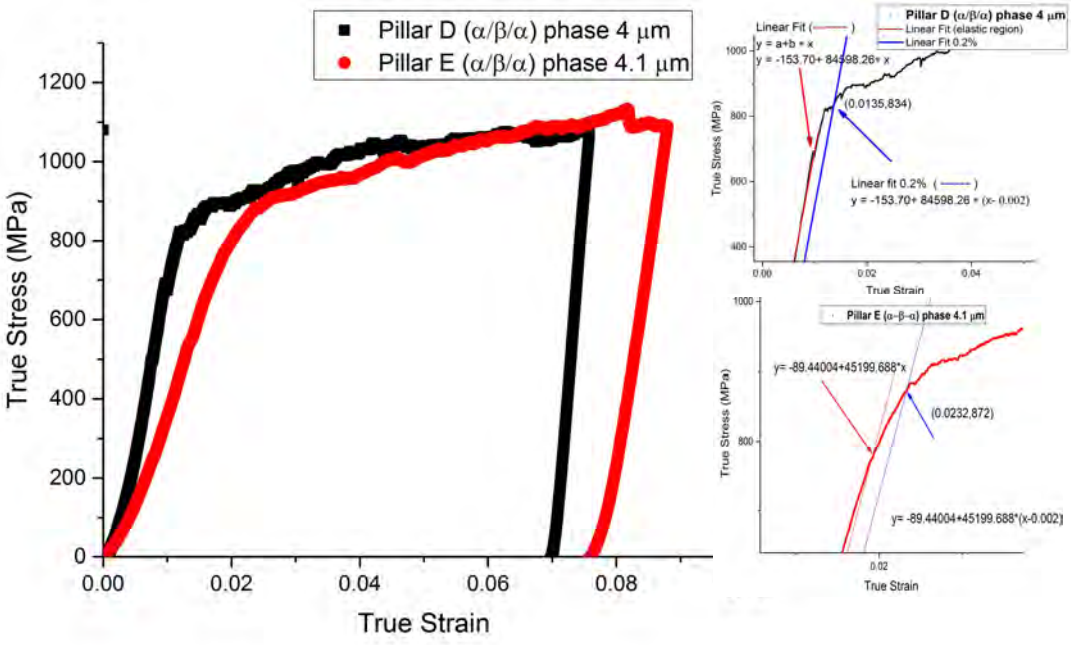

Figure 5-6 Typical true stress-strain curves of micropillars (alpha/beta/alpha) with a nominal diameter of ~ 4 μm oriented to activate basal slip in the alpha phase. Pillars D and E were strained ~ 6.5 %.

The critical resolved shear stress for activation of the <a> basal slip system is calculated based on the highest Schmid factors in the alpha phase (see Table 4.1) and from stress-strain

curves at 0.2% strain, for each plane. The correlation between the micromechanical properties and the evolution of the slip traces will be described in the next sections.

5.3.2. How many slip bands?

As seen from the SEM micrographs already shown in the previous chapter, basal slip shows a tendency for slip traces in the upper half of the crystal only, whereas the prismatic slip bands were distributed throughout the whole pillar.

For micropillars selected to activate basal slip in the alpha colony, most of the time two parallel slip bands are formed for a strain between 6% and 7%, while in a few cases deformation occurs preferentially on only one slip band.

Figure 5-7 shows pillar D after 6.5% strain. The slip trace is roughly planar.

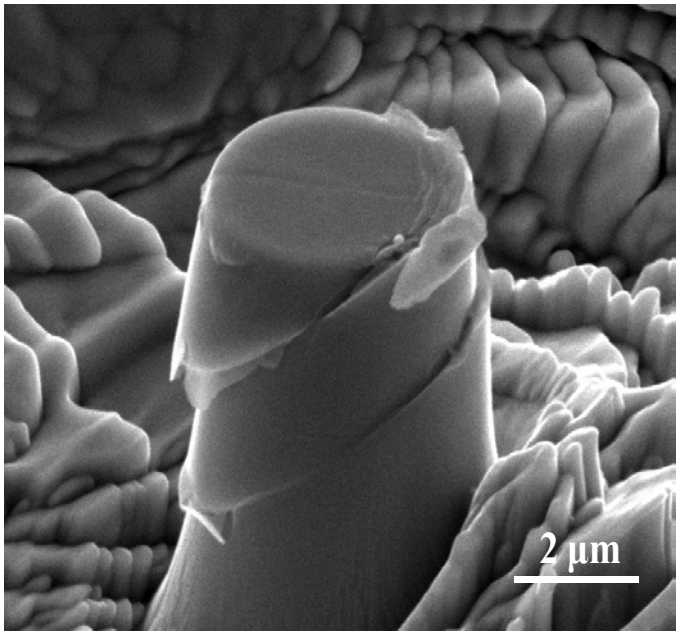

Figure 5-7 SEM image of deformed alpha/beta/alpha micropillar D, basal slip, 4 µm diameter and strain 6.5% .

Figure 5-8 shows that Ledges in the top of the column are related to the slip traces.

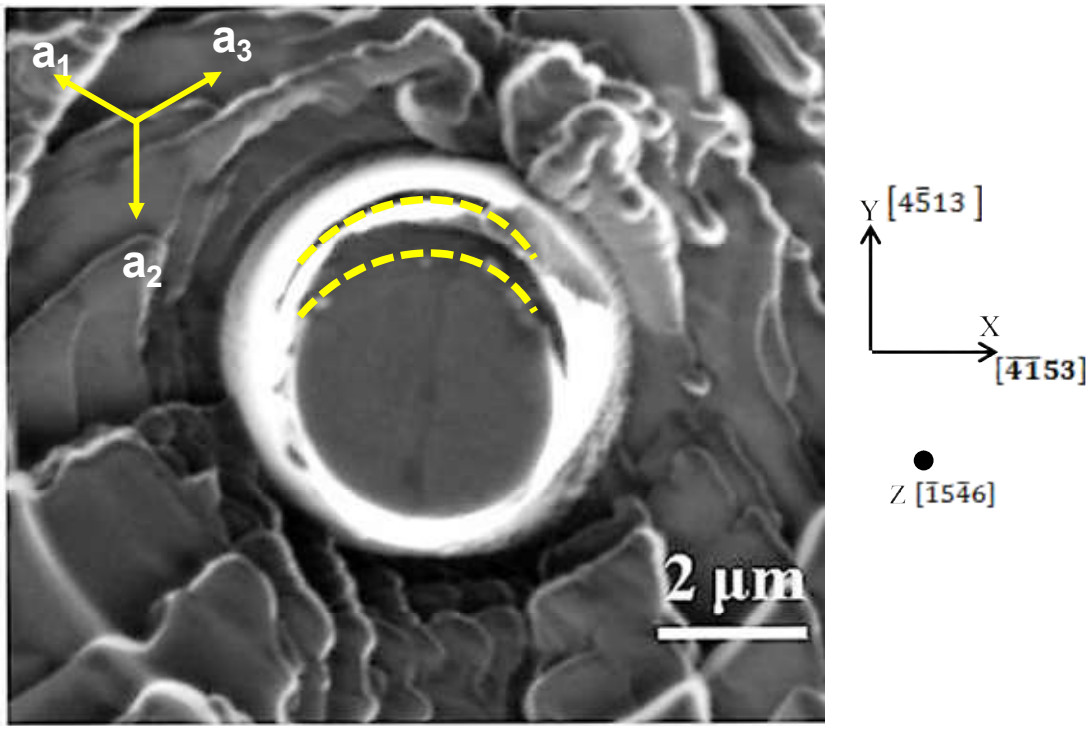

Figure 5-8 SEM photograph of the two slip bands from Figure 5-7, at the top of pillar D, with EBSD data indicating the x and y axes from the top of the pillar.

The average slip line spacing was determined to be ~ 2 µm. The appearance of pillar D (Figure 5-9 (a)) is typical of many tests.

There are similarities between the characteristics expressed by single alpha phase and those described in (alpha/beta/alpha) pillars. However, the slip bands in the single beta phase pillar taken from the same grain as the (alpha/beta/alpha) pillars did not appear due to the small size of the pillar and does not has enough size for dislocation.

5.3.3. Determination of slip plane

Alpha/beta/alpha pillars

The crystal orientation of the micropillar was measured using EBSD and is shown in Figure 5-9 (b) together with an SEM micrograph (Figure 5-9 (a)). Compressed pillars can easily be manipulated inside the SEM to make the Burgers vector parallel to the SEM screen, as in Figure 5-9. The pillar has been tilted 52° about the slip direction/Burgers vector. Moreover, a line has been drawn from the middle of the top of the shear slip band of the pillar (right hand of Figure 5-9 (a)) to the end point of the slip band on the left hand of Figure 5-9 (a). The active slip plane was identified by measuring the angle between the line of intersection with the loading axis. The slip plane normal (SP) is shown in Figure 5-9 (a).

Figure 5-9 (a) and (b) show that the apparent inclination angle (φ) between the load axis and the slip plane normal for the basal slip colonies is ~32.5°, when the sample is tilted to 52° for imaging. The correlation between the apparent inclination angle (φ) and the actual inclination angle (ϕ) between the load axis and the slip direction is: (see Appendix B)

$$\emptyset = tan^{-1}\left(\frac{\tan 32.5°}{\sin 52°}\right)$$

$$= 39°$$

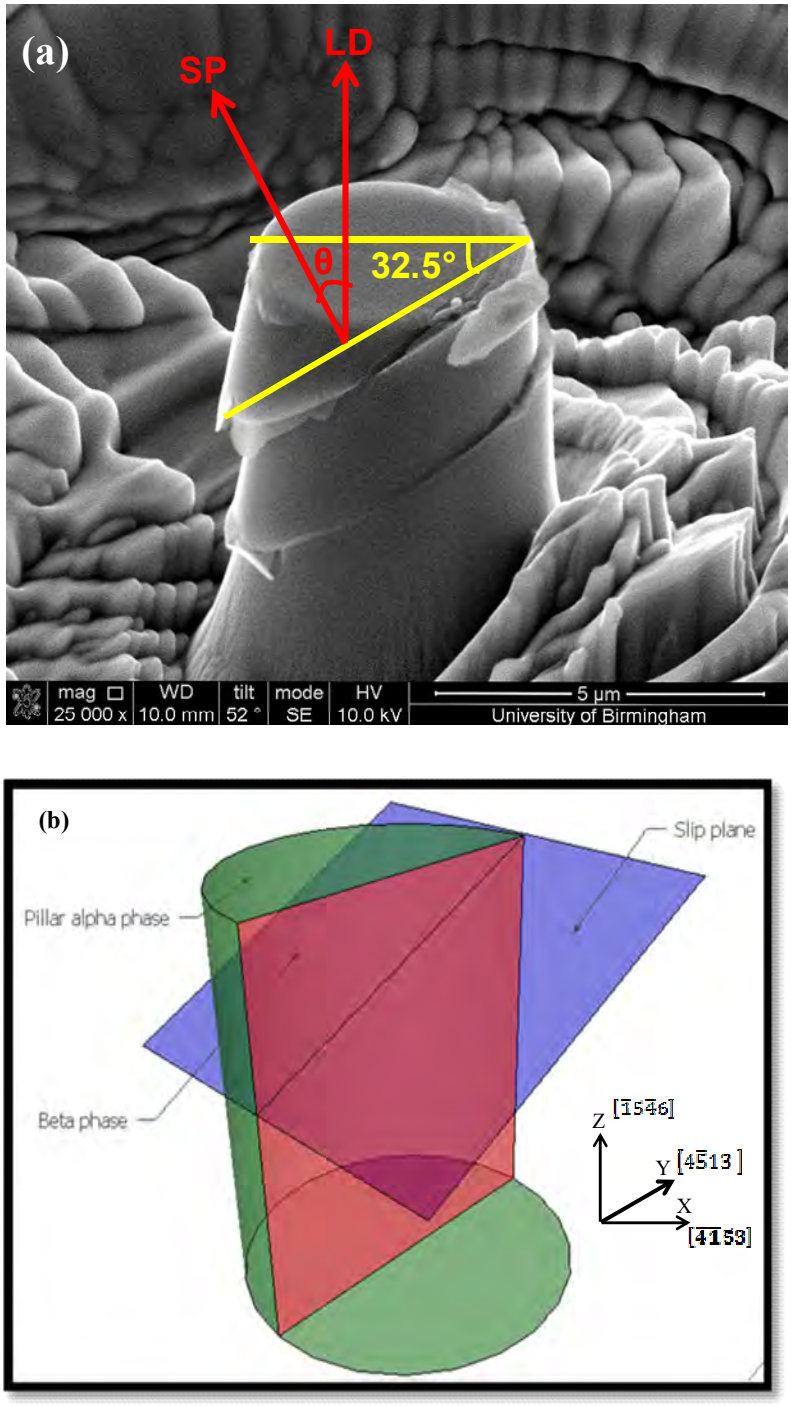

Figure 5-9 SEM images of deformed sample with a tilt of 52° for imaging (alpha/beta/alpha phase): (a) pillar D basal slip showing the slip band at 32.5° to the loading axis, (b) schematic showing the crystal orientation of a column with the basal slip plane and the alpha and beta phases.

Thus the angle between $[\bar{1}5\bar{4}6]$ and [0001] is 40°. This confirms basal slip. Also the angle between the normal to the slip plane (0001) and the x-axis $[\bar{4}\bar{1}53\ ]$ is measured to be to 57.5°; 63.3° after tilt correction. The calculated angle is 63°, again confirming basal slip.

Alpha pillar

The typical slip line morphology of a single alpha crystal oriented for <a> basal slip is shown in the SEM image in Figure 5-10.

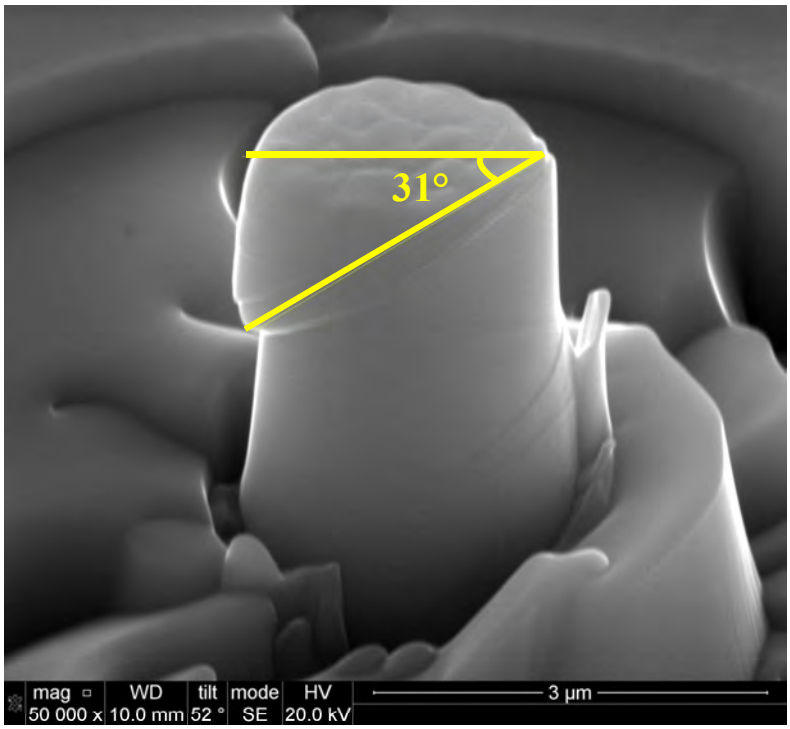

The actual corrected inclination angles (ϕ) are ~39° and ~63° for the angles between $[\bar{1}5\bar{4}6]$ and [0001] and between the normal to the slip plane (0001) and the x-axis $[\bar{4}\bar{1}53\ ]$,

respectively. These inclinations match the theoretical values 40° and 63° for (0001), again proving basal slip.

As mentioned earlier, due to the small size of the pillar for single beta phase I could not find a slip band. Thus, there is no determination of a slip plane for the beta phase.

5.3.4. Slip direction

From the EBSD data, for basal slip, slip directions have been determined as will be described. EBSD allows the orientation of the pillar to be determined in 3D space and the slip plane identified as illustrated in Figure 5-11. The crystallographic directions corresponding to the vectors x, y and z; which form an orthonormal basis with z along the pillar axis and the slip plane normal contained in the x-z plane, are found.

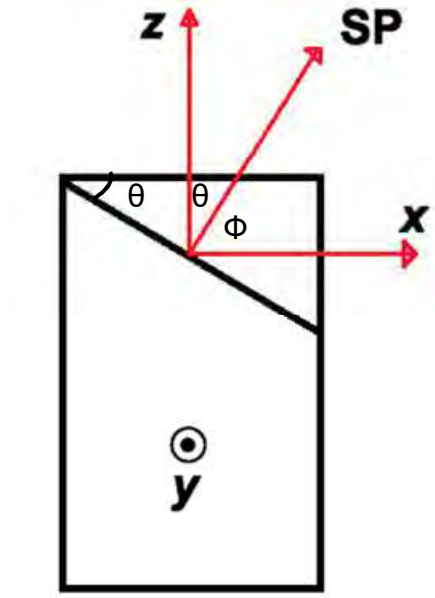

The angles between the loading direction (z vector), x vector and the slip plane normal (SP), defined in Figure 5-11, were measured from SEM micrographs, taking care to account for the viewing angle, as the specimen were oriented in the microscope until the Burgers vector was parallel to the screen. The slip plane normal, SP, can be located as shown on the stereogram Figure 5-12 contained in the y-z plane.

By plotting a stereogram with both the loading direction (z direction) and the x and y axes, we can plot two circles which define the slip plane given a knowledge of the angles between (y axis + slip plane), and (loading direction + slip plane), based on Figure 5-10. The point at which the two circles intersect is thus the activated slip plane as shown in Figure 5-12. We can plot a slip trace 90° from the slip plane: any slip directions that fall on this great circle are thus possible.

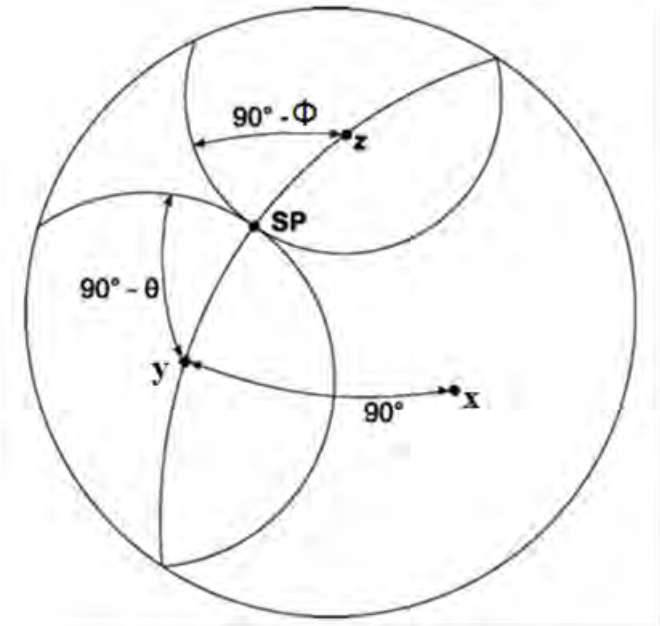

Figure 5-12 Stereogram describing the identification of the slip plane using EBSD.

By measuring the angle between each of the possibilities (a_1, a_2 and a_3) and the known directions (i.e. y axis, loading direction and slip plane) the possible slip direction can be found. For instance the angle between a_2 and the z axis is 127° , thus 127° is equal to (θ + Φ) as shown in Figure 5-13.

The results indicate that $a_2 = {}^{1}/_{3}\,[1\bar{2}10]\,(0001)$ is the slip direction as shown in bold in Table 5-2.

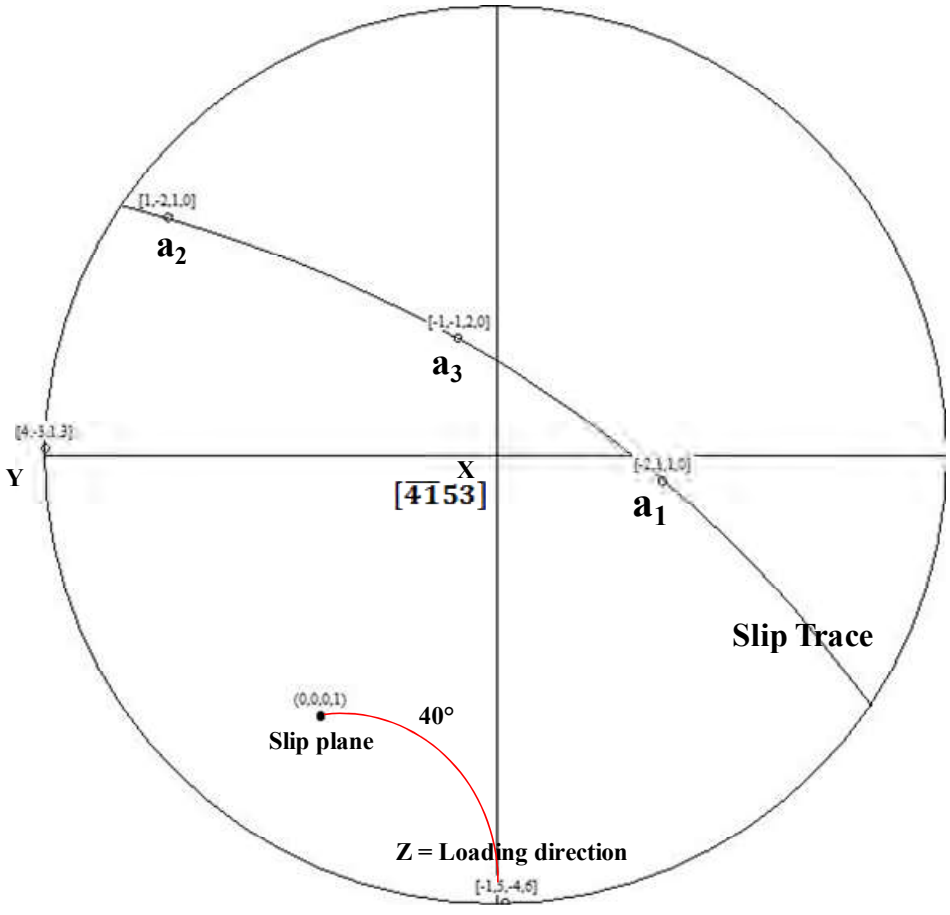

Figure 5-13 Stereogram with EBSD data, slip plane and dislocation direction in basal plane.

Table 5-2 Angle between z loading direction, y axis and x axis with possible dislocation directions in basal plane.

Dislocation directions	Z = Loading Direction $[\bar{1}5\bar{4}6]$	Y axis $[4\bar{5}13]$	X = $[\bar{4}\bar{1}53]$	Schmid factors
$a_1 = {}^1/_3\ [\bar{2}110]$	83°	130.4°	49.5°	0.1
$a_2 = {}^1/_3\ [1\bar{2}10]$	**127°**	**36°**	**81°**	**0.47**
$a_3 = {}^1/_3\ [11\bar{2}0]$	61°	99.3°	35.85°	0.37

The slip lines attributed to basal slip correspond to the slip system with the highest Schmid factor (see Table 4-1).

5.3.5. The relationship between the beta lath and the basal slip plane

Figure 5-14 shows SEM images of the micropillars compressed by 6.5% strain (pillar D) (Figure 5-14 (1)) and 6.25% strain (pillar E) (Figure 5-14 (2)). The micropillar samples were tilted by 52° about the x axis of the micropillars to reveal both the top and side surfaces. The SEM image of the 6.5% strain pillar shows very clear slip traces at the top (Figure 5-14 (1-d)) and also the side surfaces of the pillars. The slip traces pass straight through the alpha/beta boundary, as shown in Figure 5-14 (1-d). There are two clear slip traces (arrowed) on the surface of the right side of the pillar with a large slip step (Figure 5-14 (1-b)); there are two (arrowed) on the visible left side of the pillar with a slip step smaller than on the right side as will be shown in the following section.

For the pillar E, compressed by 6.25%, one slip trace was observed on both the top and side surfaces with a larger slip step than for pillar D, as shown in Figure 5-14 (2). This may be due to the fact that the beta phase in pillar E does not extend from top to bottom of the pillar. There is also a slip trace (arrowed) in the top of pillar E and the alpha/beta boundary is sheared (Figure 5-14 (2-e)). It is interesting to point out that the side face of the β laths is perpendicular to the primary slip plane in the α phase for basal slip.

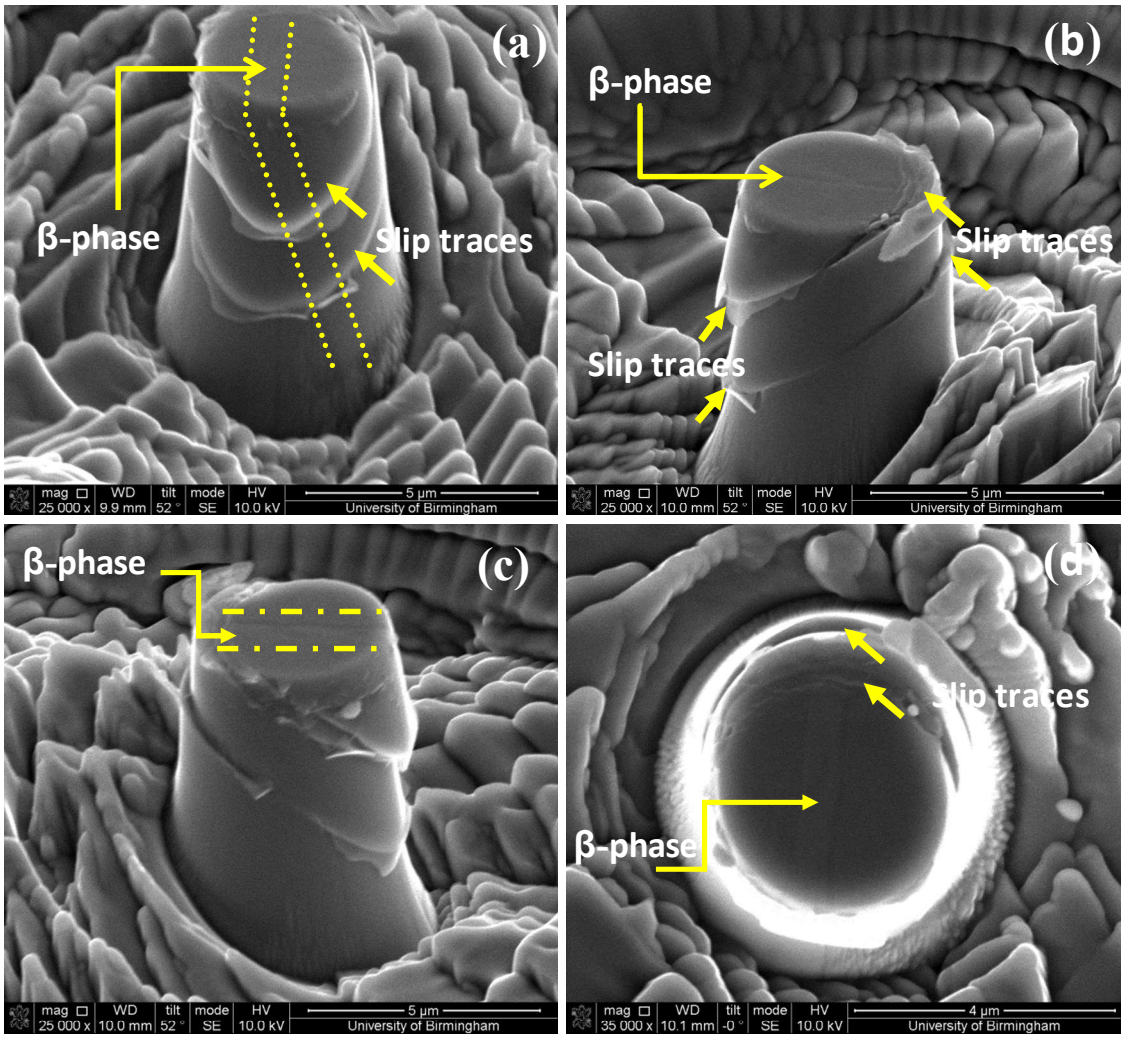

(1)

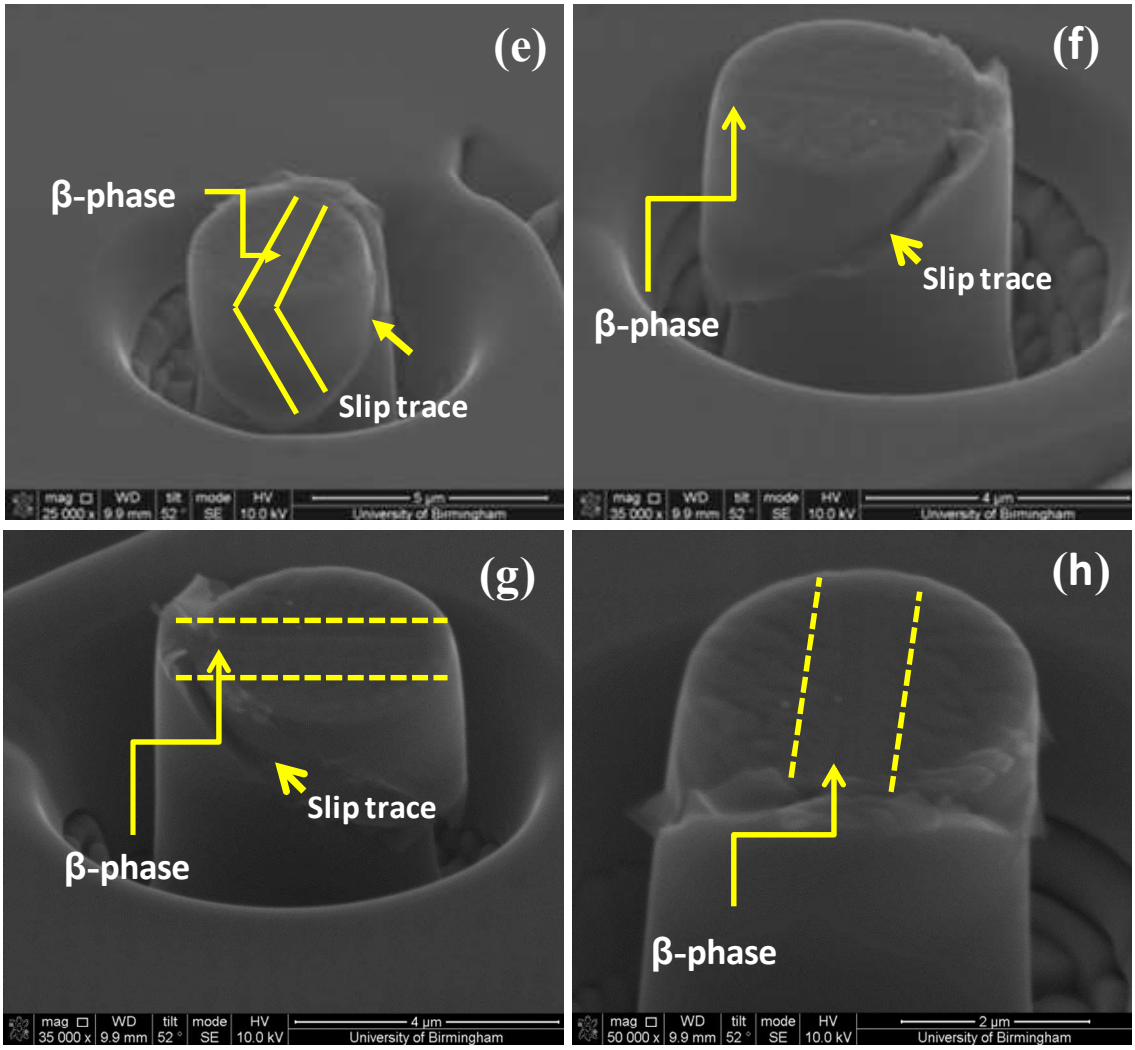

(2)

Figure 5-14 (1) SEM images of the pillar D compressed by 6.5%: (a-d) showing two clear slip traces (arrowed) on the side and top of the micropillar. Slip starts close to the alpha/beta boundary and then moves through the pillar (as shown in (1-d)), (2) SEM image of the pillar E compressed by 6.25% strain (e-h) showing a slip trace (arrowed) on the side and the top pillar; Figure 5-14 (2-h) shows there is a slip trace (arrowed) at the top of the micropillar E and the ledge regards to the alpha/beta boundaries then moves through pillar.

5.3.6. Correlating strains in SEM micrographs with micromechanical curves

Micropillars were compressed by various strains causing a decrease in the specimen length; an example is shown in Figure 5-15. The slip band on the surface showed clear offsets along the column.

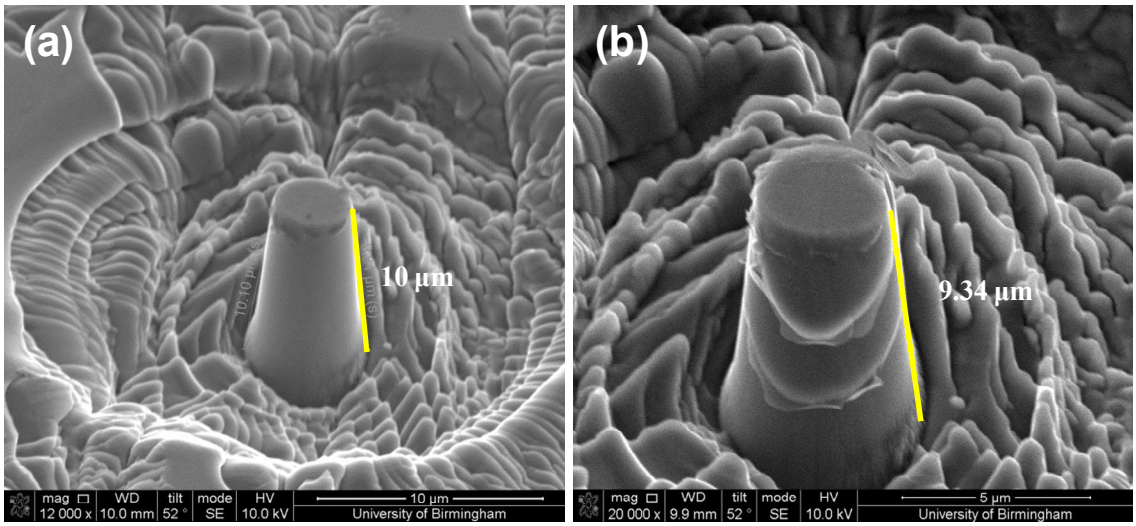

The percentage of the strain (ε) which contributed to compress the micropillars has been calculated from the measurements of the initial length of the pillars and the pillars' lengths after deformation on the specimen, according to the following formula:

$$strain\ percentage\ (\varepsilon) = \frac{\Delta L}{L_{\circ}}$$

where ΔL is the decrease in the sample length; $L_\circ$ is the initial length of the micropillars. For instance, the initial length ($L_\circ$) for pillar D was 10 μm. The *exact* plastic strain applied to the micropillars during compression is determined from the stress-strain curve and is compared with the SEM measurements in Table 5-3.

Table 5-3 Correlation between SEM and plastic strain applied to the micropillars.

Pillars	Phases	Initial length ($L_\circ$) μm	Length after deformation (L) μm	The decrease of the sample length (ΔL) μm	The strain (ε)	The strain (ε) Percentage from SEM ± 0.3 %	The strain (ε) Percentage from stress-strain curves
Basal slip colony							
Pillar D	(α/β/α)	10	9.34	0.66	0.066	6.6%	6.5%
Pillar E	(α/β/α)	8	7.38	0.62	0.062	6.2%	6.25%
Pillar 4	(α)	4	3.82	0.18	0.045	4.5%	4.3%
Pillar 6	(α)	4	3.75	0.25	0.062	6.2%	6.0%
Pillar 2	(β)	4	3.9	0.1	0.025	2.5%	2.7%
Pillar 7	(β)	4	3.84	0.13	0.033	3.3%	3.5%

5.3.7. Slip steps and the corresponding <a> dislocation numbers

The slip steps on the top and in the middle of the pillar D and pillar E surfaces were observed after plastic deformation. These steps are parallel to the basal plane for both pillars D and E. Moreover, those features of the plastic deformation which are produced at both strains and at different places on the same alpha lath are shown schematically in Figure 5-16. For pillar D compressed to 6.5% strain, the sizes of the steps at the top of the pillar are 660 nm (top right) and 300 nm (middle left) for instance the distance between the two yellow lines on pillar D as shown in Figure 5-17. These correspond roughly to 2237 and 1016 dislocations for a Burgers vector of 0.295 nm.

$$\text{Numbers of dislocations} = \frac{\text{Slip Step (nm)}}{\text{size of Burgers vector}}$$

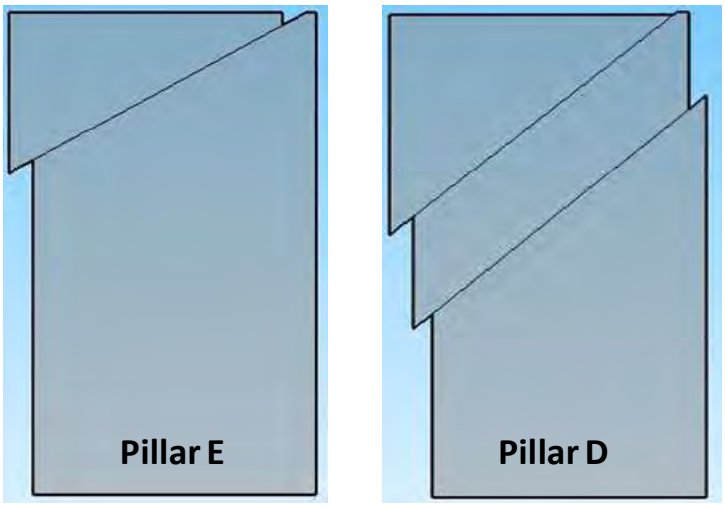

For the first slip band, for example, there appear to be at least 339 dislocations remaining in the pillar on the slip plane (see Table 5-4).

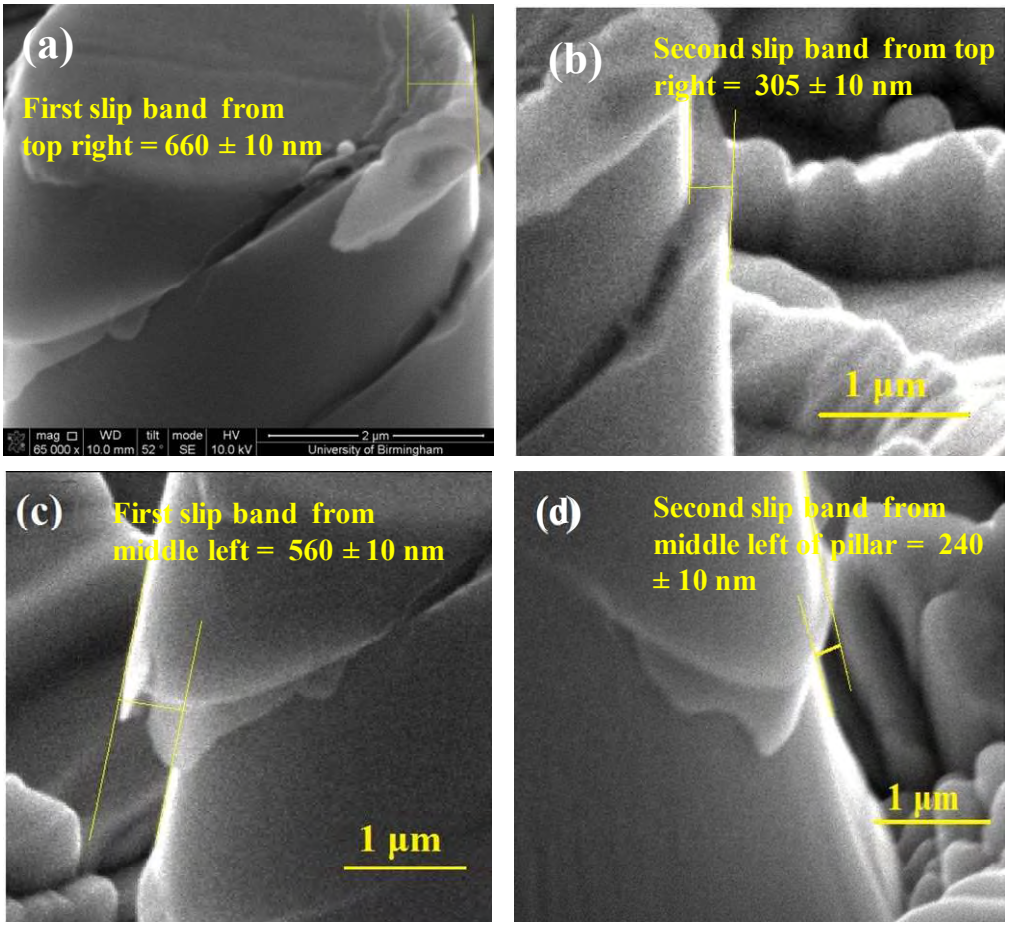

Table 5-4 Dimensions of slip steps and the corresponding dislocation numbers for basal slip.

	Pillar D - Slip band (from top)		Pillar E - Slip band (from top)
Ledges in top right micropillar surface	First slip band	Second slip band	First slip band
Slip step (nm)	660 ± 10	305 ± 10	720 ± 10
Numbers of dislocations	2237 ± 34	1033 ± 34	2441 ± 34
Strain applied into the top right of the pillar	6.2%		5.8%
Ledges in middle left micropillar surface	First slip band	Second slip band	First slip band
Length (nm)	560 ± 10	240 ± 10	560 ± 10
Numbers of dislocations	1898 ± 34	814 ± 34	1898 ± 34
Strain applied into the middle of the pillar	5.2%		4.5%

The lateral size of the slip steps can also be used to calculate the strain along z and should agree with the strain worked out previously. The strain worked out accordingly are 6.2% (pillar D) and 5.8% (pillar E) which agree with in the error with the values in Table 5-3

The analysis of slip step heights and numbers of dislocations of Burgers vectors remaining in the foil afforded by the micro-pillar structure allows a quantitative geometric analysis of the plastic strain at the specimens. This level of quantification for micropillar sliding is an attractive feature of this approach.

5.4. **Prismatic <a> slip**

For prismatic slip, the slip plane and direction were determined using the same procedure as for the basal plane.

5.4.1. Summary of mechanical properties

Figure 5-18 shows the mechanical properties for pillar 18 and pillar 19 abstracted from Figure 4.19.

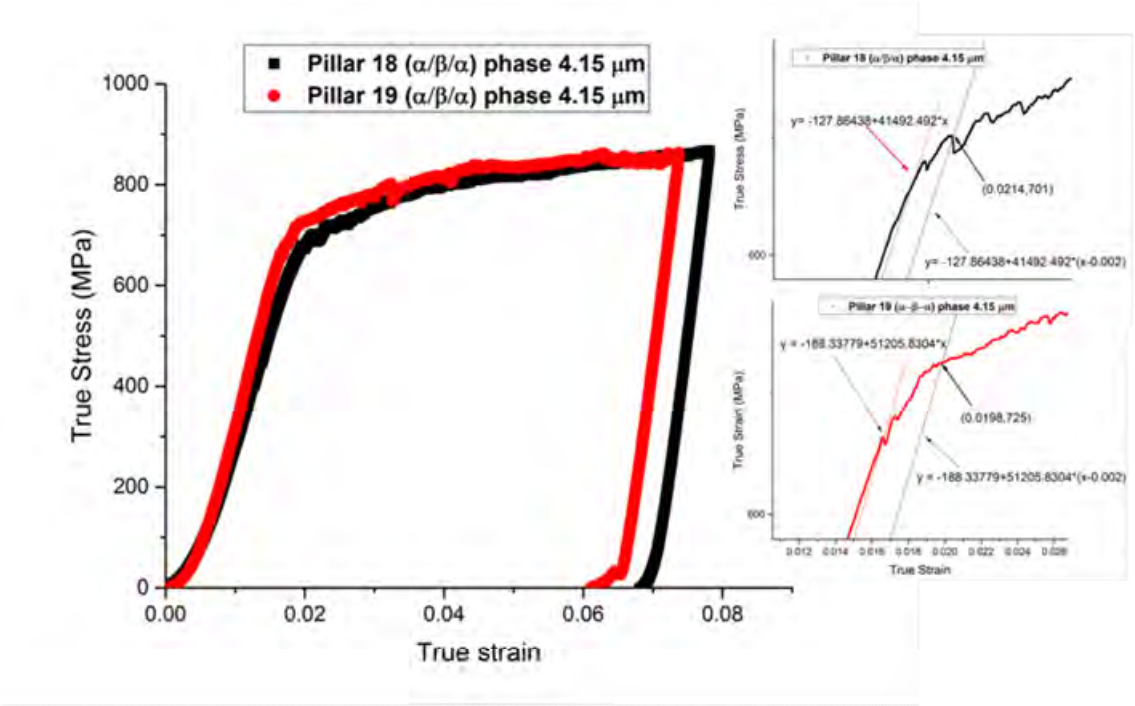

Figure 5-18 Typical true stress-strain curves of micro-pillars (alpha/beta/alpha) with a nominal diameter of 4 μm oriented to activate prismatic slip in the alpha phase. Pillars 18 and 19 were strained ~ 6%.

5.4.2. How many slip bands?

Figure 5-19 shows an SEM picture of the slip bands for (alpha/beta/alpha) microcompression samples oriented for prismatic slip (in the alpha phase). The SEM image illustrates more than five slip bands with different slip steps on parallel planes for pillar 19.

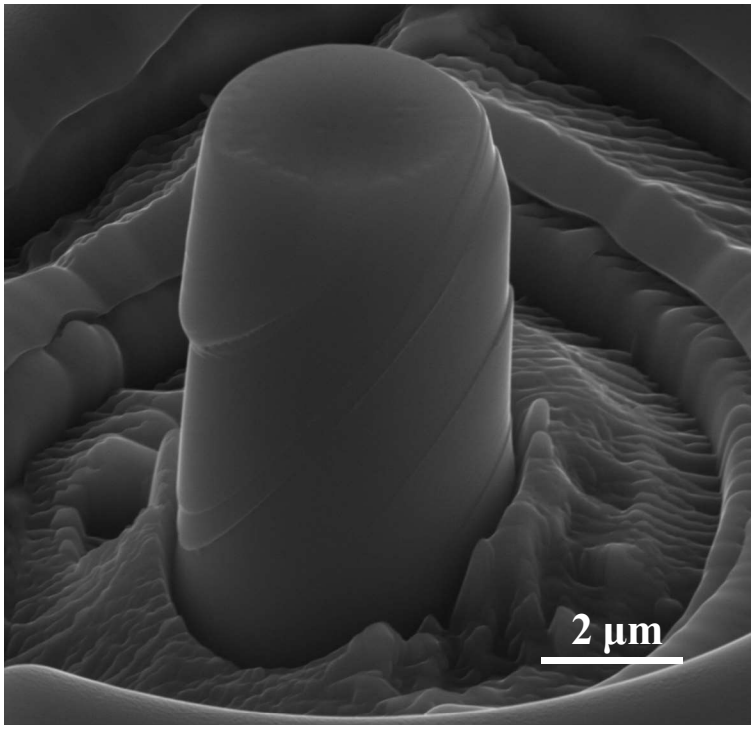

Figure 5-19 SEM images of deformed alpha/beta/alpha micropillar 19 prismatic slip 4 µm and strain 5.7%.

The slip line spacing was determined to be roughly 1 to 2 μm for prismatic slip. The EBSD data for pillar 19 prismatic slip is shown in Figure 5-20.

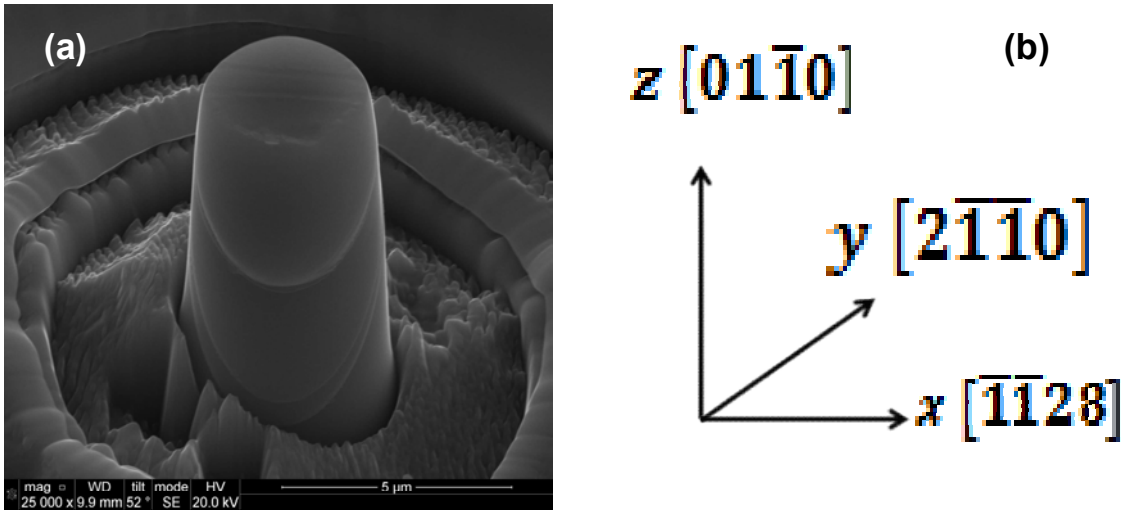

Figure 5-20 (a) SEM micrograph of a compressed micropillar (pillar 19) prismatic slip, (b) show the crystal orientation of the micropillar was measured using EBSD.

5.4.3. Determination of slip plane

The line of intersection along the slip planes in pillar 19 is displayed in Figure 5-21.

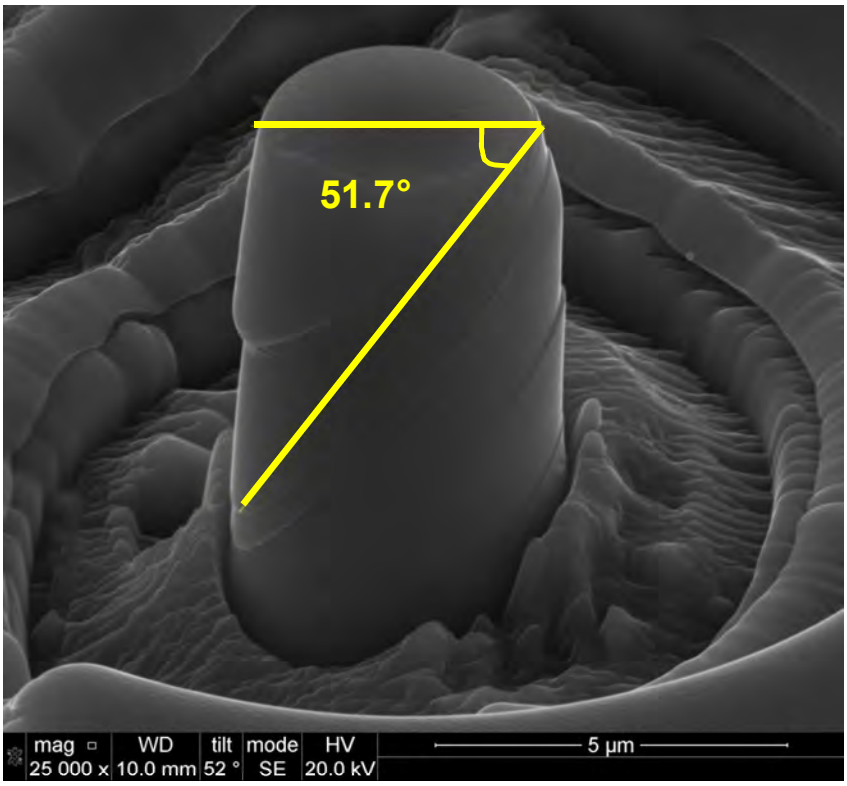

Figure 5-21 SEM image of deformed pillar 19; prismatic slip showing the slip bands at 51.7° to the loading axis.

From Figure 5-21 the angle between the slip plane normal (SP) and the loading direction (LD) is ~ 52°. The actual inclination angle (ϕ) between the load axis and the normal to the slip plane for pillar 19 prismatic slip is 58°, which confirms prismatic slip on $(10\bar{1}0)$.

The typical slip line morphology of a single alpha crystal oriented for <a> prismatic slip is shown in the SEM images in Figure 5-22.

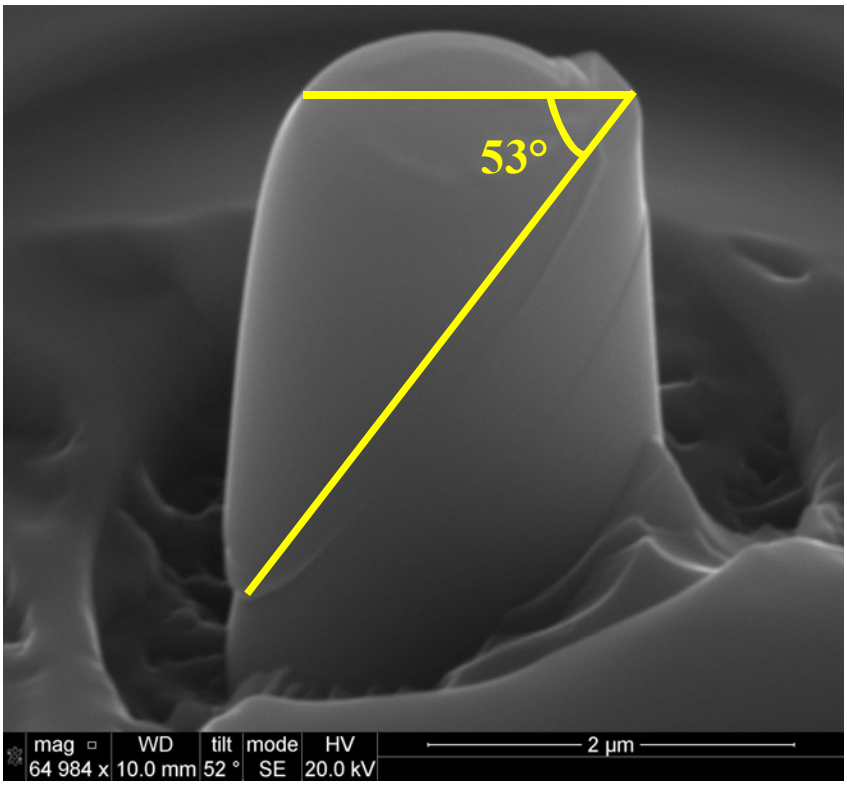

From the EBSD data for prismatic slip and the corrected inclination angle (ϕ) the slip plane matches the magnitude of 60° for $(10\bar{1}0)$ plane. Morever, the activation of <a> dislocations on this slip system agrees with the maximum resolved shear stress (see Table 4-1).

5.4.4. Slip direction

The slip direction was determined using the same procedure as for the basal plane. The results of determining the angle indicate that $a_2 = {}^{1}/_{3}\ [\bar{1}2\bar{1}0]$ is the only possible Burgers vector as the angle between the loading direction and a_3 alone crossponds to the angle determined from the SEM as summarised in Table 5-5.

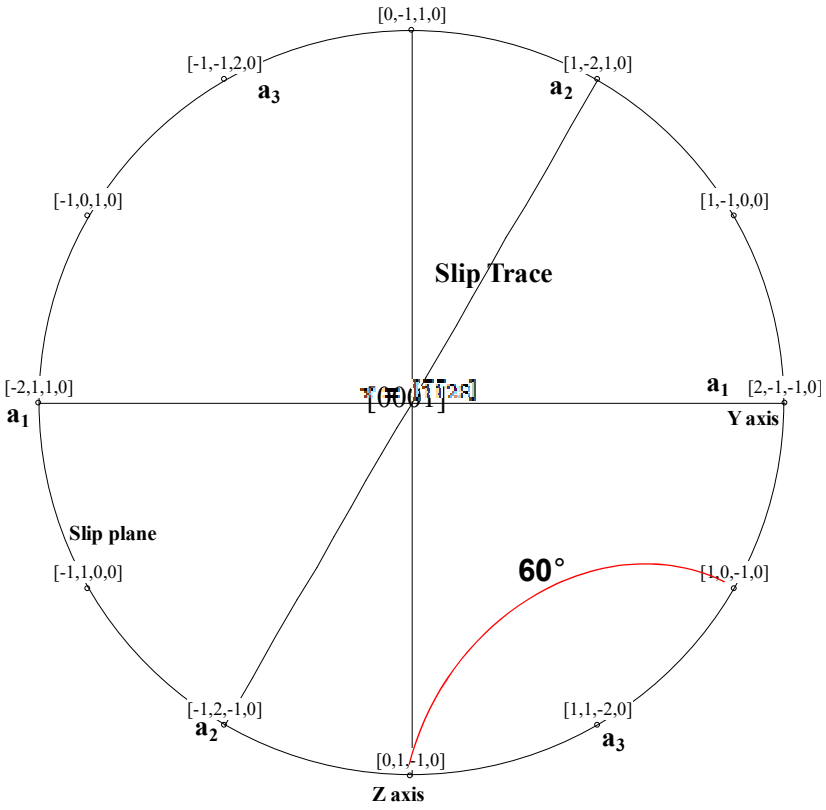

The activation of $a_2 = {}^{1}/_{3}\ [\bar{1}2\bar{1}0](10\bar{1}0)$ corresponds to the maximum Schmid factor (see Table 4-1).

Table 5-5 Angle between z axis (loading direction), y axis and x axis with possible dislocation directions in the prismatic plane.

Dislocation directions	Z axis = Loading Direction $[01\bar{1}0]$	Y axis $[2\bar{1}\bar{1}0]$	X aixis $[\bar{1}\bar{1}28]$	Schmid factor
$a_1 = {}^1/_3\ [2\bar{1}\bar{1}0]$	90°	0°	~ 90°	0
$a_2 = {}^1/_3\ [\bar{1}2\bar{1}0]$	**30°**	**120°**	**~ 90°**	**0.43**
$a_3 = {}^1/_3\ [\bar{1}\bar{1}20]$	150°	120°	~ 90°	0.43

5.4.5. Prismatic slip: the process of slip propagation through an α/β boundary

Figure 5-24 shows the slip traces on the side face of a micropillar deformed to activate <a> type dislocations on prismatic planes in the alpha phase. The micropillar was tilted by 52° about the loading axis of the micropillar to reveal both the top and side surfaces. Although all the basal and prismatic slip pillars have been deformed to similar strain levels, the slip traces for the micropillars oriented to activate prismatic slip has much smaller CRSS value than the basal slip. An example of slip traces on the surface of a pillar is shown in Figure 5-24 (b), and they are indicated by the yellow arrows. It is interesting to note that the slip traces initiate in single alpha phase, then moving through the side face of the beta lath and splitting from the interface (indicated by the yellow lines in Figure 5-24 (b) and (d)), unlike pillars D and E (for basal slip) where the Burgers vector subtends a smaller angle with the alpha/beta interface due to the crystallographic orientation of the pillar.

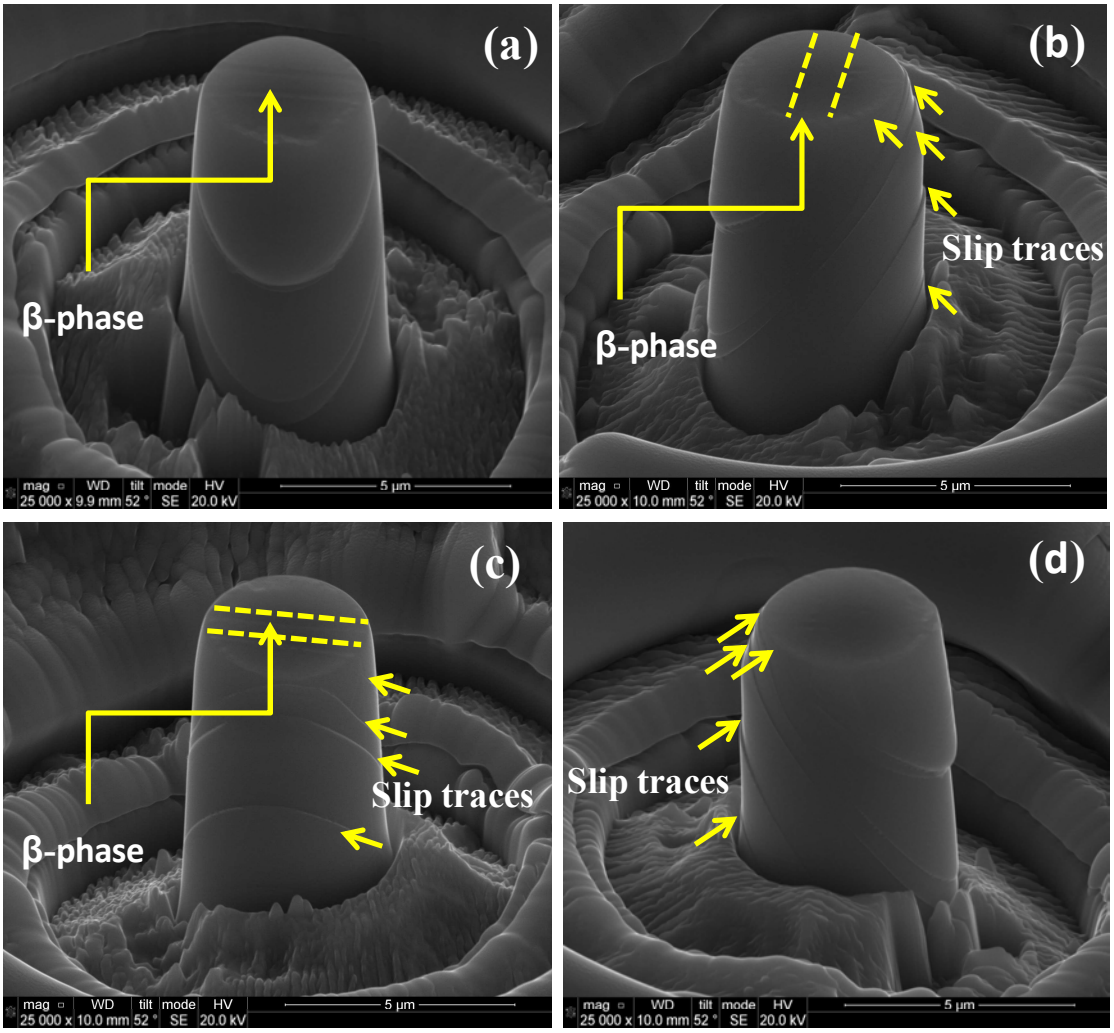

Similar to the basal slip the characteristics expressed by single alpha phase and those described in (alpha/beta/alpha) pillars have the same slip plane and slip direction and therefore only the alpha/beta/alpha pillars have been presented in this chapter. Also, the slip bands in single beta phase could not be found due to the same reasons mentioned in section 5.3.4.

5.4.6. Correlating strains in SEM micrographs with micromechanical curves

A straightforward correlation between the mechanical stress-strain curves and the scanning electron microscope images is presented in Table 5-6. Agreement is seen to be good.

Table 5-6 Correlation between SEM and plastic strain applied to the micropillars.

Pillars	Phases	Initial length ($L_\circ$) µm	Length after deformation (L) µm	The decrease in the sample length (ΔL) µm	The strain (ε)	The strain (ε) Percentage from SEM ± 0.3 %	The strain (ε) Percentage from stress-strain curves
Prismatic slip colony							
Pillar19	(α/β/α)	9.45	8.9	0.55	0.058	5.8%	5.7%
Pillar18	(α/β/α)	10.15	9.55	0.6	0.059	5.9%	5.8%
Pillar24	(α)	4.2	3.775	0.425	0.102	10.2%	10.4%
Pillar14	(α)	4.0	3.74	0.26	0.065	6.5%	6.4%
Pillar10	(β)	4.17	3.98	0.19	0.046	4.6%	4.5%
Pillar13	(β)	4.4	4.15	0.25	0.057	5.7%	5.5%

5.4.7. Slip steps and the corresponding <a> dislocation numbers

The results of determining the corresponding dislocation numbers for a typical prismatic slip in pillar 19 are listed in Table 5-7.

Table 5-7 Dimensions of slip steps and the corresponding dislocation numbers for prismatic slip.

	Pillar 19 - Slip band (from top)					
Ledges in top right micropillar surface	First slip band	Second slip band	Third slip band	Fourth slip band	Fifth slip band	Sixth slip band
Slip step (nm)	-	70	30	100	120	50
Numbers of dislocations	-	237	102	339	406	169
Strain applied to the top the pillar		3.5 %				
Ledges in middle left micropillar surface	First slip band	Second slip band	Third slip band	Fourth slip band	Fifth slip band	Sixth slip band
Length (nm)	205	65	27	-	-	-
Numbers of dislocations	695	220	91	-	-	-
Strain applied to the middle the pillar		2.75 %				

Using entrance and exit slip steps to determine applied strain on the prismatic pillar 19 was not so useful in this analysis, for the reason that the start and finish slip steps were not very obvious on the pillar 19 as shown in Figure 5-24 (b) first slip band.

5.5. **Pyramidal <c+a> slip**

<a> slip on the basal, prismatic, and pyramidal π1 (first order) planes does not bring about any dimensional change along the c-axis, for example, when the stress is applied along the c-axis as shown in Figure 5-25. Additional deformation modes involving <c+a> slip (Burgers vector $1/3 < 11\bar{2}3 >$) are therefore necessary. The slips systems are symmetrically distributed relative to the c-axis. Due to the relatively high stresses needed to activate <c+a> glide, these dislocations are most commonly observed in grains lacking suitable <a> slip systems and the dislocations of the pyramidal $\{10\bar{1}1\}$ slip system experience a greater Schmid factor than the other slip systems.

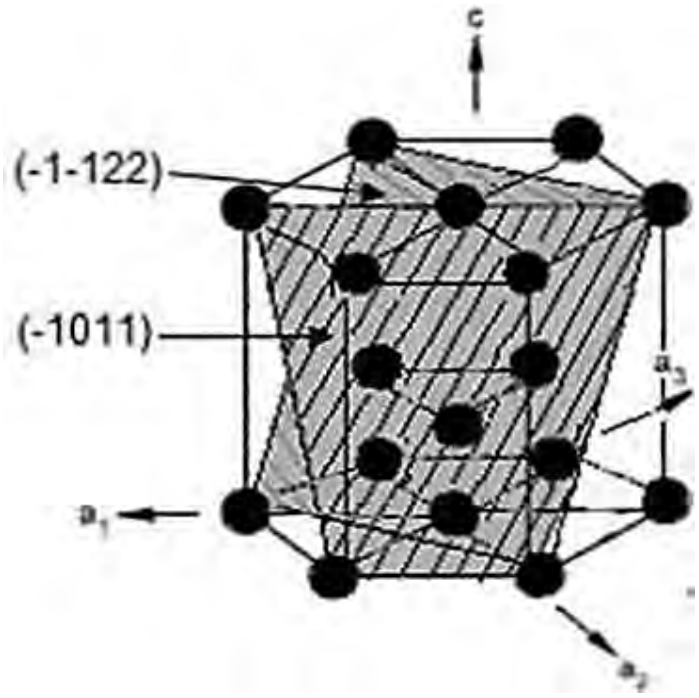

5.5.1. Summary of <c+a> micro-mechanical properties

Typical true stress-strain curves for (alpha/beta/alpha) micro-pillars oriented along the c-axis with a nominal diameter of 4 μm are shown in Figure 5-26.

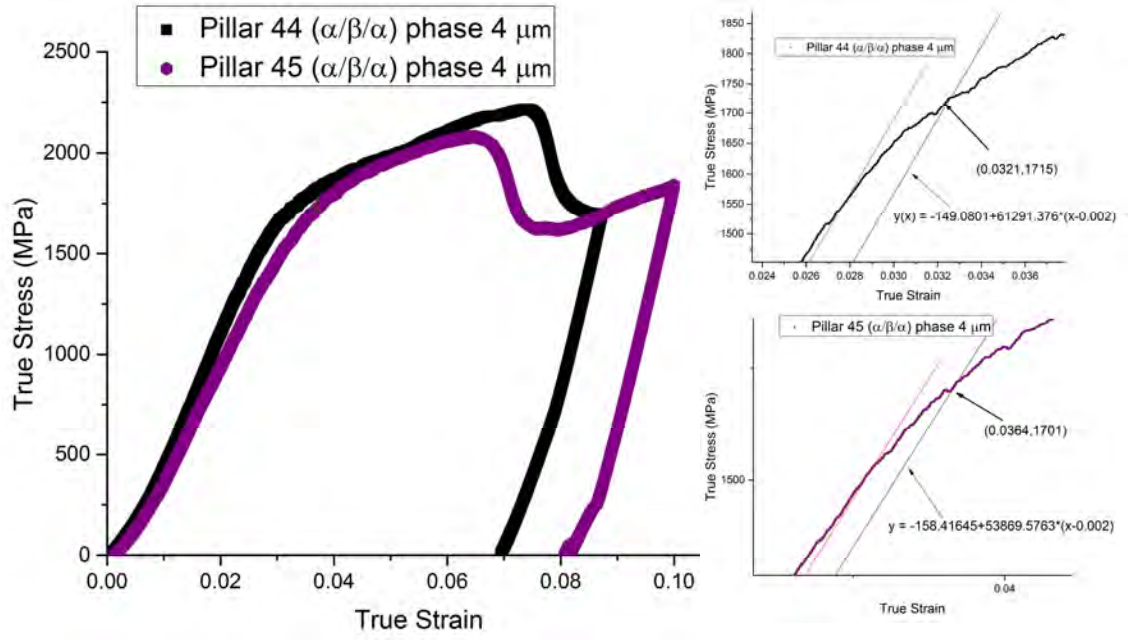

Figure 5-26 Typical true stress-strain curve of a micro-pillar (alpha/beta/alpha) with a nominal diameter of 4 μm oriented to activate pyramidal <c+a> slip in the alpha phase. Pillar 44 was strained 6% and pillar 45 by 7%.

The CRSS values for the <c+a> slip are considerably larger than for the <a> slip systems. The CRSS value for the activation of <c+a> dislocations on the pyramidal slip system was determined using the same mechanism as for <a> dislocations (see insert Figure 5-26). It is expected that the deformation is accommodated by the 6 slip systems. If there is cross-slip of

the <c+a> dislocations onto other $\{10\bar{1}1\}$ planes, this would lead to very strong work hardening.

5.5.2. Characteristics of slip bands

The SEM micrographs show that the pillars in the <c+a> pyramidal slip colonies were more likely to exhibit observable slip deformation closer to the pillar top. Typically only two of the six possible $\{10\bar{1}1\}$ slip plane traces are observed on the surfaces of the micropillars, as shown in Figure 5-27 (a), while in some cases, deformation occurs preferentially on only one shear slip band, as illustrated in Figure 5-27 (b). In addition, the number of slip bands on this slip plane are not measurable accurately, but they are more than the basal and prismatic plane, i.e. more than five slip bands.

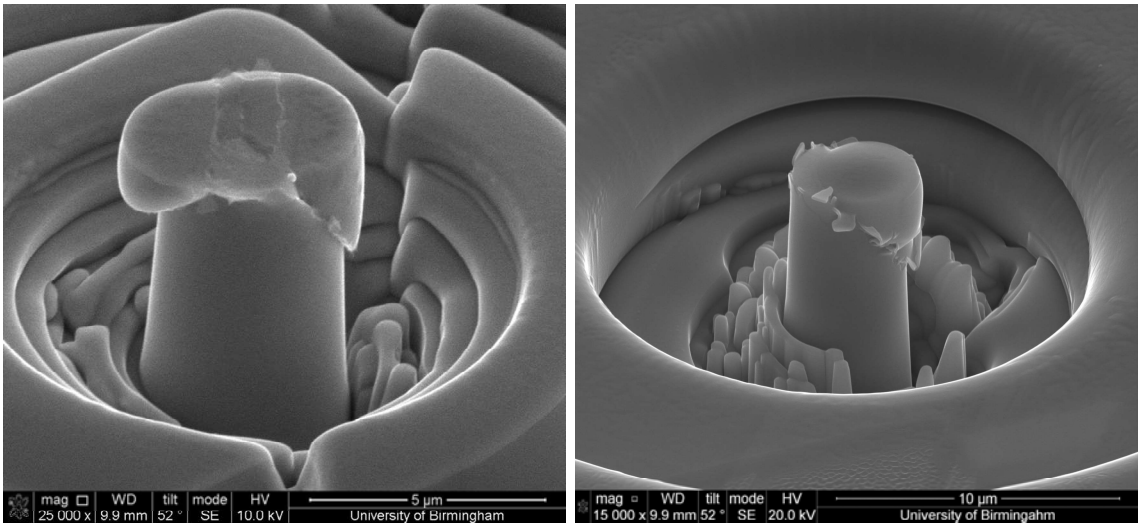

Figure 5-27 SEM micrographs of the pillars deformed to activate <c+a> dislocations in a pyramidal slip colony; (a) two slip plane traces are observed on the surface of the micropillar 1; (b) only one slip plane trace is observed on the surface of the micropillars.

When the micropillar is oriented to activate <c+a> dislocations, most of the slip traces pass completely through the pillars. However, it is not known decisively whether the slip traces are due to the interaction of the dislocation arrays in the bands with the alpha/beta boundary, or due to individual dislocation arrays; although common observation of the latter in TEM studies would favour this conclusion.

5.5.3. Slip plane

Figure 5-28 shows that there are only two slip systems, which is obvious on the micropillars by using SEM when deformed to ~ 6% strain. Measurement of the incident angle of these slip lines with respect to the loading axis and broad face of the α/β interface will confirm for us the activation of the <c+a> dislocation in the alpha lath (many slip bands are activated). The apparent inclination angles (φ) between the plane of the loading direction and slip traces are 38.75° and 40 °, for the first slip band from the top of the pillar and the second slip band, which is below the first slip band, respectively. The actual inclination angles (ϕ) are 45.53° and 46.8°, respectively. These inclination angles are very close to the theoretical angle between [0001] and $\{10\bar{1}1\}$ which is 47.5° as shown in Figure 5-29. Figure 5-30 shows an SEM photograph of the top of pillar 44 and EBSD data, which indicate the Burgers vector relashinship with the beta phase, also a schematic diagram for the activation of dislocations on pillar 44.

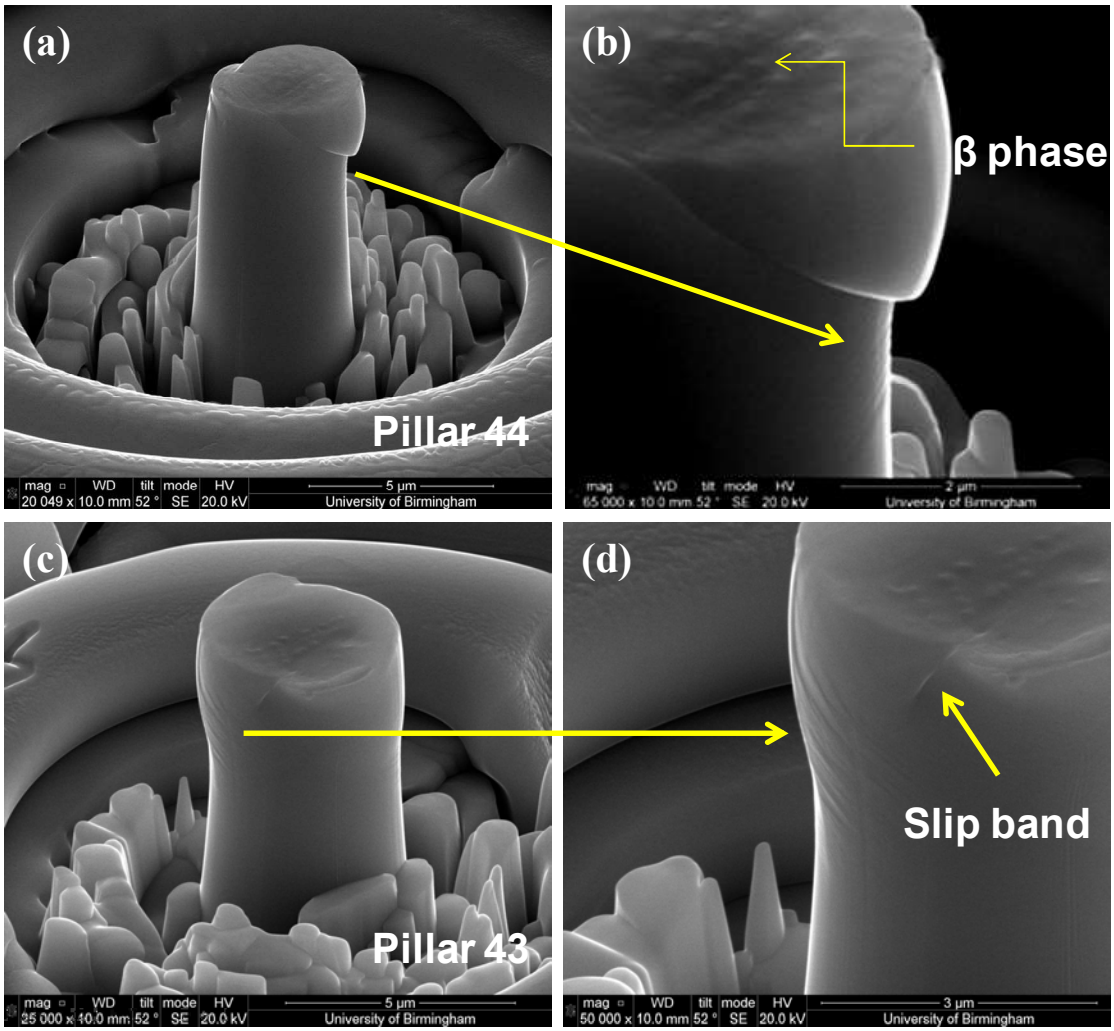

Figure 5-28 SEM micrographs of pillars 44 and 43 compressed by ~ 6% strain to activate <c+a> dislocations; (a) and (c) showing a clear slip band on the side of the micropillar and its shear across the alpha/beta/alpha phases; (b) and (d) showing slip traces in addition to the obvious slip bands which are on a different plane.

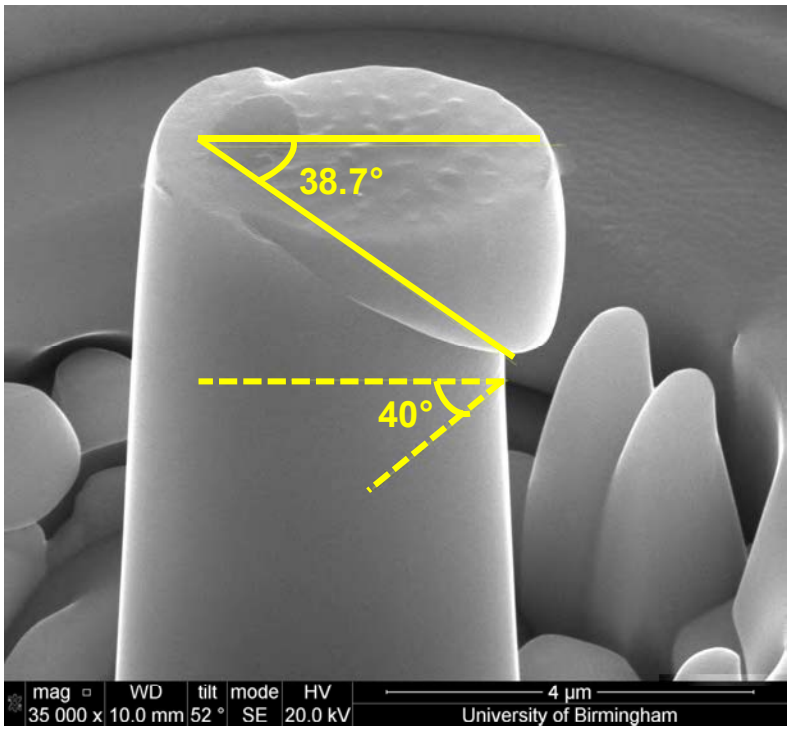

Figure 5-29 SEM images of a deformed sample with a tilting angle of 52° for imaging (alpha/beta/alpha phase) pillar 44 pyramidal slip showing the slip bands at 38.75° and 40° to the loading axis.

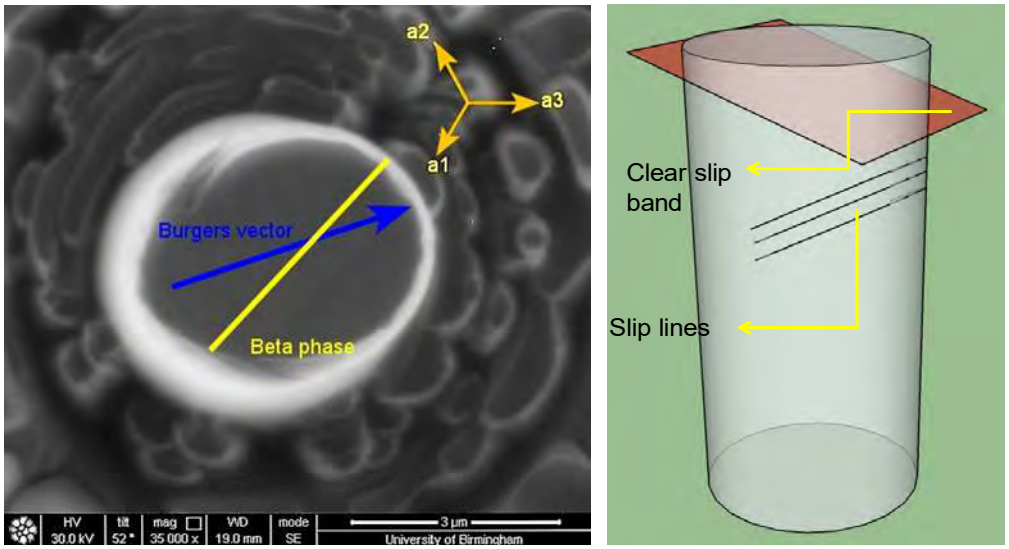

Figure 5-30 (a) SEM photograph of the top part of the pillar 44 and the slip band from Figure 5-29, with EBSD data indicate the Burgers vector from the top of pillar, (b) schematic of the micropillar showing the area of activated dislocations on pillar 44.

From Figure 5-29 and Figure 5-30 the results of determining the angles indicate that $(1\bar{1}01)$ and $(10\bar{1}1)$ are activiated in the compression along $[0001]$.

5.5.4. Slip direction

In order to find the *exact* slip directions for <c+a> dislocations, stereogram, EBSD data and SEM micrographs have been used as has been described in section 5.3.4 (see Figure 5-31).

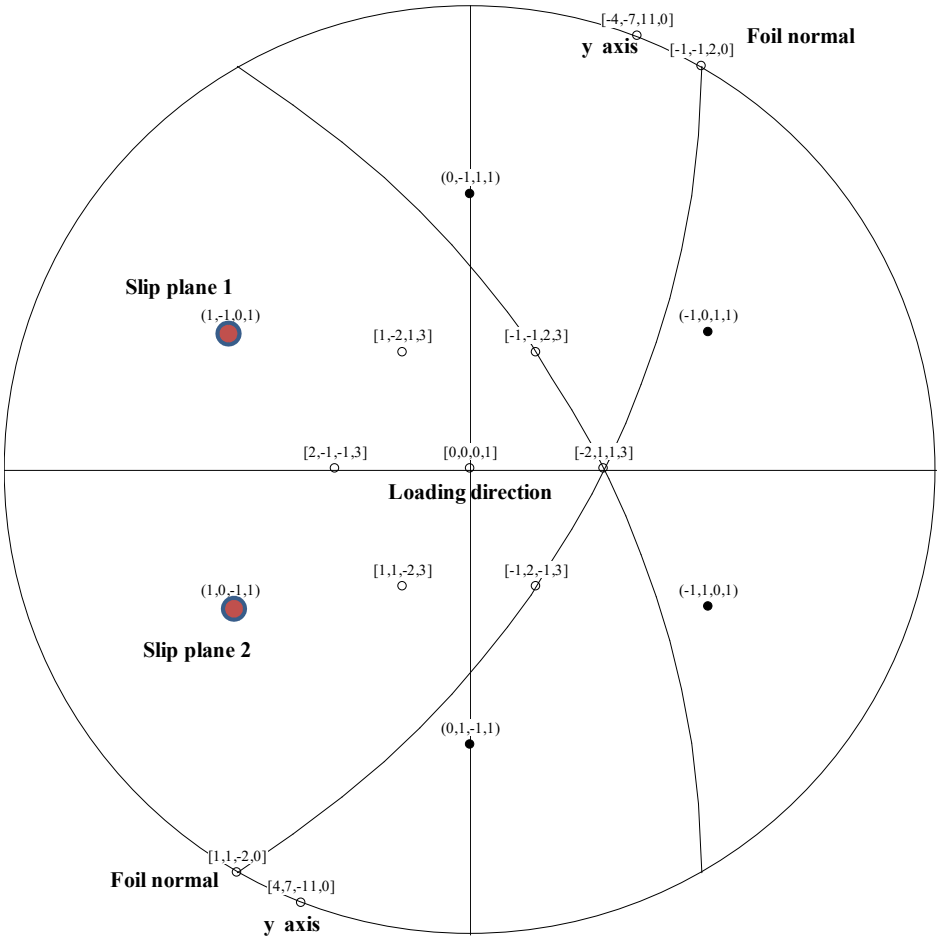

Table 5-8 Angle between loading direction, y axis and broad face show the possible dislocation directions in the pyramidal planes in the pillar 44.

Dislocation directions	Loading Direction $[0001]$	Y axis $[11\bar{2}0]$	Foil Normal ~ $[13\bar{4}0]$
$^1/_3\ [\bar{2}113]$	**32.2° for slip plane $(1\bar{1}01)$and $(10\bar{1}1)$**	105.5°	97.35°
$^1/_3\ [2\bar{1}\bar{1}\bar{3}]$	32.2°	74.5°	82.65°
$^1/_3\ [1\bar{2}1\bar{3}]$	32.2°	105.5°	116°
$^1/_3\ [\bar{1}2\bar{1}3]$	**32.2° for slip plane $(1\bar{1}01)$**	74.5°	64°
$^1/_3\ [\bar{1}\bar{1}23]$	**32.2° for slip plane $(10\bar{1}1)$**	122.2°	118.82°
$^1/_3\ [11\bar{2}\bar{3}]$	32.2°	57.8°	61.2

This is similar to the behaviour of the basal and prismatic alpha laths which was discussed previously. Even though all the <c+a> slip planes are equally stressed, there are, in Figure 5-29, only two slip planes obviously present in the SEM micrograph.

5.5.5. The process of slip propagation through an α/β boundary

Figure 5-32 illustrates an SEM image of a pillar compressed by 7% strain to activate <c+a> dislocations in the alpha phase which then move through the alpha/beta boundary, indicated by fine slip lines on the surface and top of the micropillar. These <c+a> dislocations in the alpha phase usually appear to have passed through the thin beta phase fillets as shown in Figure 5-32.

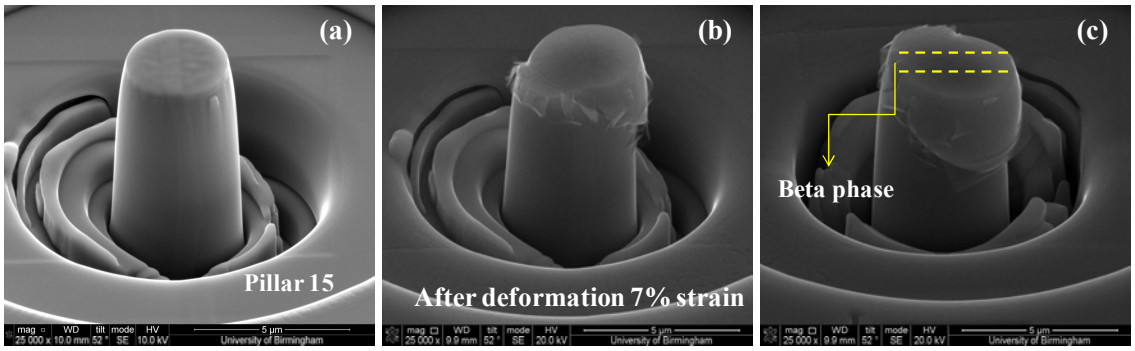

Figure 5-32 SEM images of pillar 15 compressed by 7%; (a) before deformation (b) showing only one clear slip trace on the side and top of the micropillar; slip band, probably starts from the alpha phase then moves through the alpha/beta boundaries as shown in (c).

The angle between the slip directions and the alpha/beta interface is the same for all the <c+a> slip systems, which are equally stressed; they have the same Schmid factors as they are symmetrical with regard to the loading direction [0001].

5.5.6. Correlation between strain measured by SEM with micromechanical data

The strain percentage can be calculated from the difference between the micropillar's initial length and the decrease in the specimen's length. This correlates with the measured stress-strain curves. The same equation has been used as earlier to find the strain (ε) (see section 2.5.5). Table 5-9 summarises the *exact* plastic strain applied to the pillars during compression corresponding to the SEM measurements.

Table 5-9 Correlation between strain measured by SEM and mechanical data.

Pillars	Phases	Initial length ($L_\circ$) µm	Length after deformation (L) µm	The decline of the sample length (ΔL) µm	The strain (ε)	The strain (ε) Percentage from SEM ± 0.3 %	The strain (ε) Percentage from stress-strain curves
Pyramidal slips colony							
Pillar12	(α/β/α)	10.2	9.5	0.7	0.068	6.8%	6.6%
Pillar15	(α/β/α)	9.57	8.91	0.66	0.069	6.9%	7.2%
Pillar44	(α/β/α)	8.23	7.75	0.48	0.058	5.8%	6.0%
Pillar45	(α/β/α)	8	7.47	0.53	0.066	6.6%	6.8%
Pillar29	(α)	10.8	10.25	0.55	0.051	5.1%	5.0%
Pillar42	(α)	8	7.5	0.5	0.062	6.2%	6.1%
Pillar 5	(β)	6	5.73	0.27	0.045	4.5%	4.3%
Pillar 8	(β)	7.4	6.95	0.45	0.061	6.1%	6.0%

5.5.7. Slip steps and the corresponding <c+a> dislocation numbers

The slip steps on the top of the pillar surface to the middle were observed after plastic deformation of alpha/beta pillars. As mentioned previously, the slip step is parallel to the pyramidal planes and usually the plastic deformation is near the top of the pillar (see Figure 5-32). Micropillars oriented to activate <c+a> dislocations have a slip system $\left[\frac{1}{3}\langle 11\bar{2}3\rangle\{10\bar{1}1\}\right]$. The magnitude of the Burgers vector of the <c+a> dislocations is $\left(\sqrt{(a)^2+(c)^2}\right)$. For instance, with pillar 44 compressed at 7% strain the sizes of the steps at the top surface are 650 and 265 nm (top to middle of the upper half of the pillar), respectively as shown in Figure 5-33. These correspond roughly to 1175 and 479 dislocations for a Burgers vector of 0.5535 nm. Table 5-10 contains the corresponding dislocation numbers for pyramidal slip systems in micropillars with a nominal diameter of 4 μm.

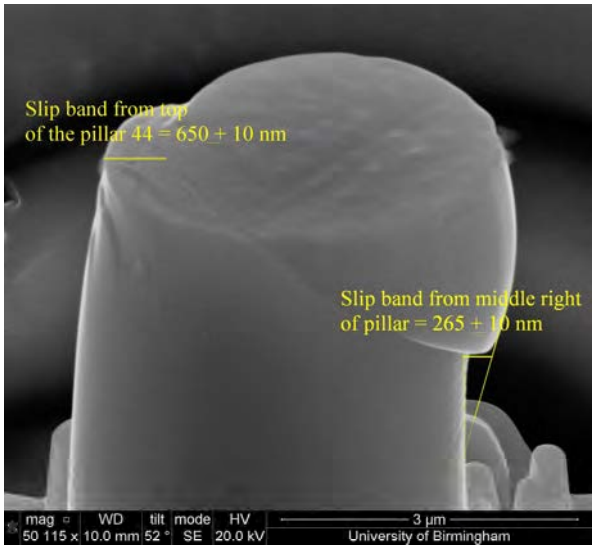

Figure 5-33 SEM images for pillar 44 of pyramidal planes, slip bands from top left and slip bands from middle right.

Table 5-10 Dimensions of slip steps and the corresponding dislocation numbers for <c+a> pyramidal slip.

	Pillar 12	Pillar 15	Pillar 44	Pillar 45
Ledges in top right micropillar surface	First slip band	First slip band	First slip band	First slip band
Slip step (nm)	820	708	650	770
Numbers of dislocations	1482	1279	1174	1391
Strain applied to the top of the pillar	6.0%	5.5%	5.8%	7.0%
Ledges in middle left micropillar surface	First slip band	Second slip band	First slip band	First slip band
Length (nm)	455	405	265	422
Numbers of dislocations	822	732	479	763
Strain at the middle of the pillar	3.3%	3.15%	2.4%	3.9%

5.6. **Summary**

1. SEM examination of the micropillars (alpha/beta/alpha and single alpha phase) shows that localised two slip bands are developed parallel to each other and confined to the upper half of the pillar.
2. The number of visible slip traces is equal in the alpha single crystal and alpha/beta/alpha tri-crystals, indicating that the extent of deformation is the same on both crystals with different amounts of beta lath strengthening between them.
3. The basal slip plane of the micro compression samples (alpha/beta/alpha and single alpha phase) was confirmed in detail in the SEM. Also, the slip line spacing was determined to be ~ 2 μm or more for basal slip Figure 5-9.
4. It is clear that the observed a_2 basal slip direction corresponds to the maximum Schmid factor. Therefore, the most highly stressed <a> type dislocation on the microscopically observed slip plane is activated Figure 5-13.
5. The strain measured by SEM agreed well with the micromechanical data.
6. The slip bands on the prismatic plane were more homogeneously distributed through the pillar than were the basal slip bands. The SEM micrographs show the prismatic slip bands distributed throughout the whole pillar Figure 5-19.
7. The slip system on the prismatic plane was determined to correspond to the maximum Schmid factor.
8. The SEM examination shows more than five slip bands with different slip steps on parallel planes for prismatic slip. Moreover, the slip line spacing was determined to be roughly 1 to 2 μm for prismatic slip Figure 5-19.

9. The slip traces of prismatic planes initiate in the alpha phase, then moving through the side face of the beta lath and splitting at the interface.
10. The uniaxial strain measured by SEM agrees well with the micromechanical data for the prismatic planes.
11. Although all the <c+a> slip planes are equally stressed, only a limited number is activated more likely due to the misalignment between tip and pillar.
12. Commonly there are only one or two shear slip bands near the top of the pillar and many other slip bands do not shear through the whole pillar which they are located in the upper half of the pillar (see Figure 5-28).
13. The slip systems on the <c+a> pyramidal planes were confirmed to correspond to the maximum Schmid factor in the SEM.
14. The slip line spacing of the pyramidal planes is very small compared to the <a> slip systems: in the nano range ~ 200 nm, because the probability of generating cross slip on c+a is more compared to a type.
15. The sums of the magnitudes of the entrance slip steps agree well with the strains measured by the micromechanical data and SEM (thus three independent measurements of strain).
16. The slip steps either end of each slip band have different sizes. From the taper of the column one would expect slip to initiate nearer the top of the column. On this basis the entrance slip steps are larger than the exit ones, implying that many dislocations remain in the pillar.

Chapter Six

6. Transmission Electron Microscope (TEM)

6.1. Introduction

TEM specimens were prepared from some of the microcompression specimens described in Chapters Four and Five and examined in order to analyse the dislocation microstructure.

6.2. TEM Examination

Three TEM specimens were extracted from the basal slip colony (see for example Figure 6-1). TEM foils were also prepared from an undeformed sample in order to study the initial dislocation density. The foil normal for all of them was $[4\bar{5}13]$; they were from the same alpha colony as shown in Figure 6-2.

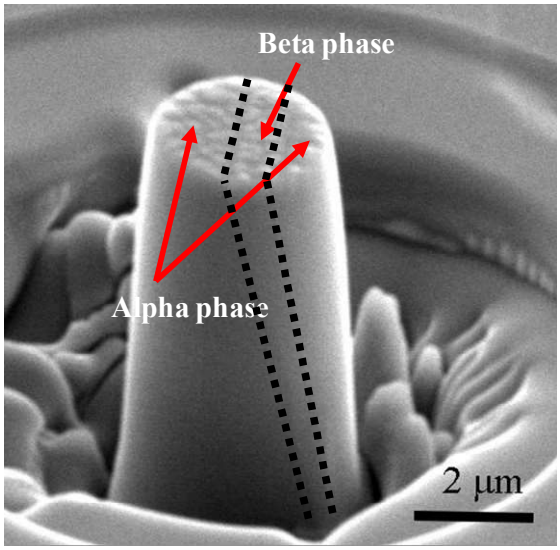

Figure 6-1 SEM micrograph of a typical 4 μm diameter micro-pillar fabricated by FIB which itself had a FIB-TEM sample extracted from it.

Table 6-1 Summary of the TEM specimens from the basal and pyramidal slip colony.

Number of pillars	Pillar labelled		Strain	Dimensions of Pillar (Diameter × Height) (μm)
1	Pillar N	Undeformed pillar	0	4 × 8.5
2	Pillar D	Basal <a> slip	6 %	4 × 10
3	Pillar E	Basal <a> slip	6 %	4 × 8
4	Pillar 12	Pyramidal <c+a> slip	7 %	4 × 10

The bright field TEM micrographs are presented such that the upper part of the TEM image is the top of the pillar and the lower part of the image is the pillar base.

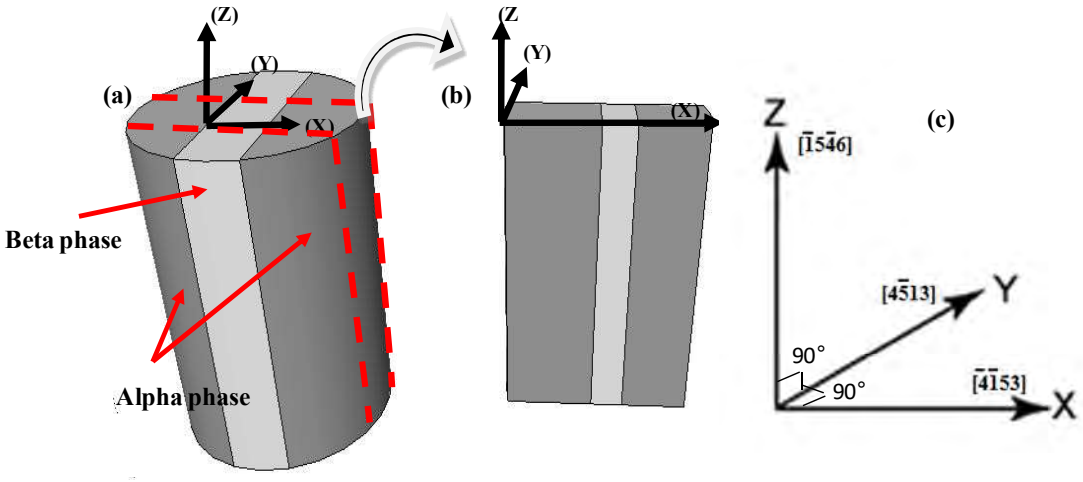

Figure 6-2 Schematic diagrams showing a TEM foil extracted along the loading axis according to EBSD data. The long dimension of the pillar was parallel to the Z-axis which corresponds to the $[\bar{1}5\bar{4}6]$ direction while the foil normal corresponds to the Y direction $[4\bar{5}13]$. It should be noted that the angles between (Z and Y) and (Y and X) are (~ 90°). (a) Cylindrical shape corresponding to the pillar, (b) rectangaloid corresponding to the TEM foil extracted from the pillar. The dark grey colour and light grey colour in the pillar and TEM foil correspond to the alpha phase and beta phase, respectively; (c) X, Y and Z directions indexed.

6.2.1. Undeformed Specimen: initial dislocation densities in the alpha and beta phases.

A TEM foil was extracted from an undeformed 4 μm cylindrical micropillar and was then observed by TEM. The dislocation density for the alpha and beta phases were calculated using the following equation [114]:

where L is the total length of the dislocation lines divided by V which is the volume of the specimen. A is the surface area and t is the foil thickness.

This was achieved using Image J software to trace the dislocations manually. The total length of dislocation was obtained via measuring each dislocation line in the specimen. The TEM foil thickness was measured via an SEM micrograph taken inside the FIB during specimen preparation. Also the TEM Convergent Beam Electron Diffraction (CBED) technique was adopted to determine the precise thickness of the alpha phases. The CBED technique is based on the observation of Kossel-Mollenstedt fringes in the TEM, which occur in the {000} and {hkl} discs under two-beam conditions. Knowing the extinction distance and the spacing of these intensity oscillations, the specimen thickness can be deduced (see [115] for details). Using a CCD camera, the distance between the fringes on the CBED pattern was measured by using the Digital Gatan software. Figure 6-3 shows a representative pixel averaged CBED pattern. Thickness measurements having an accuracy of ± 2% or better are routinely determined using the CBED technique. Because the foil thickness can be measured at precisely the point of the diffraction and analysis, and because the method is very amenable to computerisation, it has become more popular.

Figure 6-4 shows a montage of bright field TEM micrographs taken with g = $0\bar{1}11$ near the $[01\bar{1}2]$ zone axis for the alpha crystal. The dislocation density of the alpha phase is lower than in the beta lath region of this foil as shown in Figure 6-4. The dislocation density for the beta phase has been measured here and is $\sim 10^3$ times higher than alpha phase , as is very obvious from Figure 6-4.

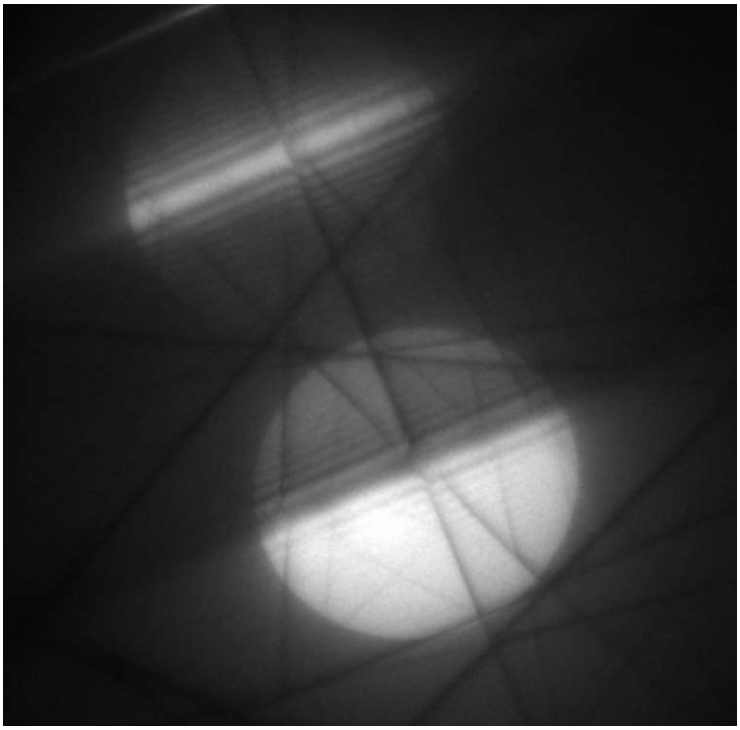

Figure 6-3 Convergent beam electron diffraction pattern from the alpha phase in the pillar, acquired on a CCD camera, at 200 keV.

The initial dislocation density measurements determined using this formula, which relies crucially upon measurement of the foil thickness, is estimated to be $\sim 1.2 \times 10^{13}\ m^{-2}$ in the alpha phase and from Figure 6-4.

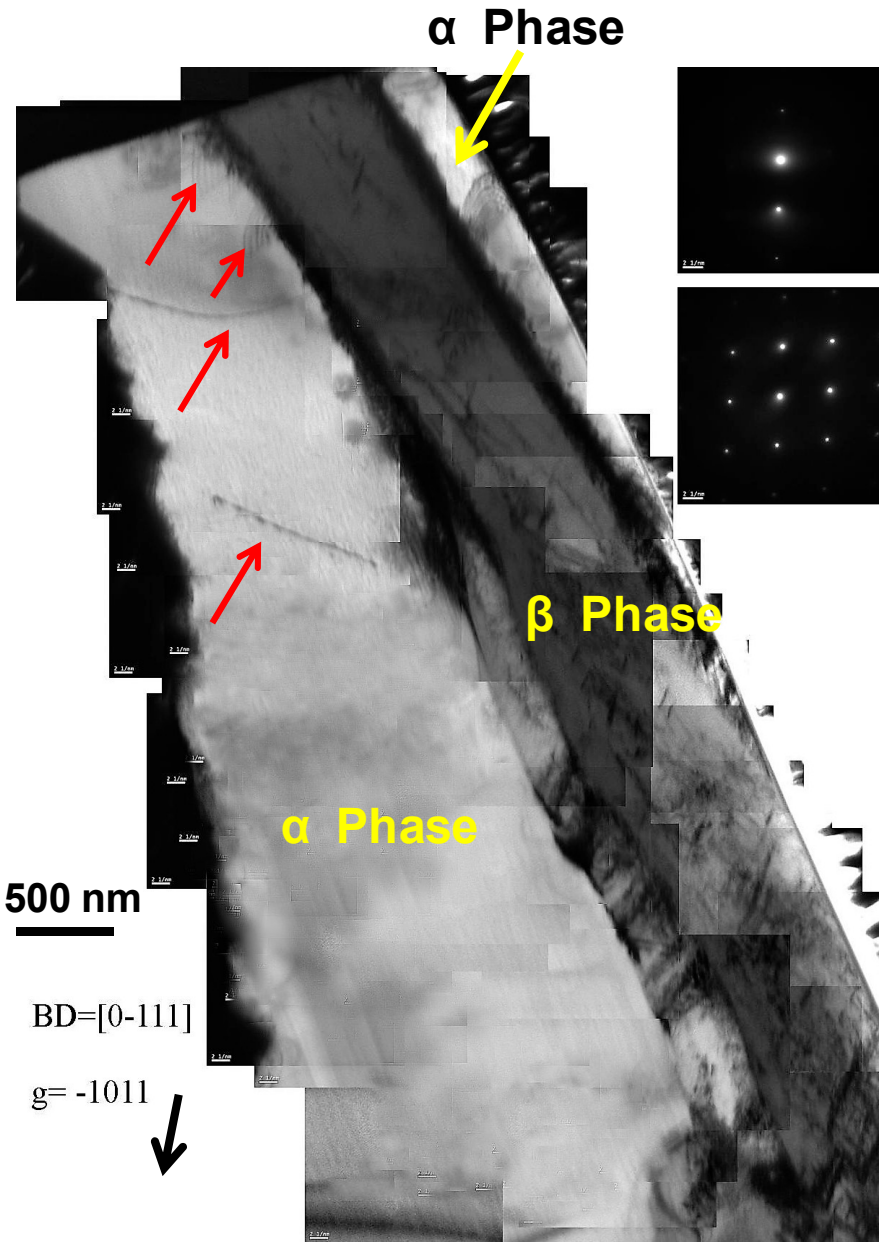
α Phase
β Phase
α Phase
500 nm
BD=[0-111]
g= -1011

The initial dislocation density for the beta phase is higher than the alpha phase that due to the coefficient of thermal expansion (CTE). Coefficient of thermal expansion (CTE) is also an important parameter among the physical properties. Such properties are mainly determined by the inter-atomic bonding character and therefore by the chemistry. True stress-strain table (Chapter Four) shows that the proof stress of the beta phase is lower in comparison to a conventional alpha phase and alpha/beta/alpha phase assemblage. Investigation of the different strengths in the different phases indicates that an increasing aluminium content causes higher CTE values, while increasing the content of high melting point elements, e.g. vanadium, decreases the coefficient of thermal expansion. Therefore, hexagonal titanium exhibit a lower coefficient of thermal expansion than conventional titanium alloys and especially beta Ti. During the phase transformation and considering the effect of thermal expansion (CTE), initial dislocation density of the beta phase is much higher than in the alpha phase as shown in the undeformed pillar by TEM. The preexisting dislocations in the beta phase progressively left the pillar and were accompanied by intermittent bursts of new dislocations which correspondingly caused the load to fluctuate.

Most solid materials expand upon heating and contract when cooled. The change in length with temperature for a solid material can be expressed as:

$$\frac{(l_f - l_\circ)}{l_\circ} = \alpha_1 (T_f - T_\circ)$$

$$\Delta l / l_\circ = \alpha_1 \Delta T \quad , \quad \alpha_{1=1} / l(\frac{dl}{dT})$$

where $l_\circ$ and l_f represent, respectively, the original and final lengths with the temperature change from $T_\circ$ to T_f The parameter α_1 CTE and has units of reciprocal temperature (K^{-1}) such as μm/m · K or 10^{-6}/K.

6.2.2. Deformed specimens: Basal slip

6.2.2.1. Overall description of dislocation content

TEM foils were extracted in the way shown in Figure 6-2. Figure 6-5 shows the zone axes close to the foil normal (FN). The closest major zone axis is $[1\bar{1}01]$. A Kikuchi map is sketched in Figure 6-6.

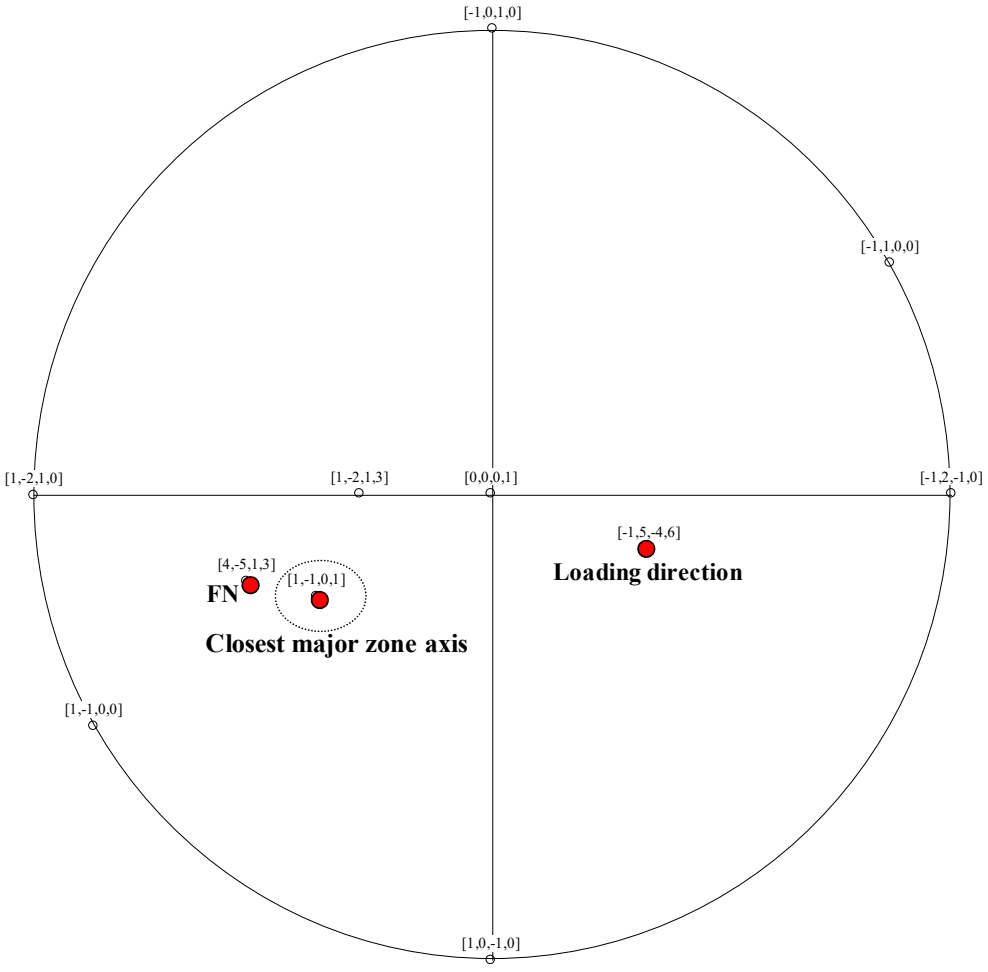

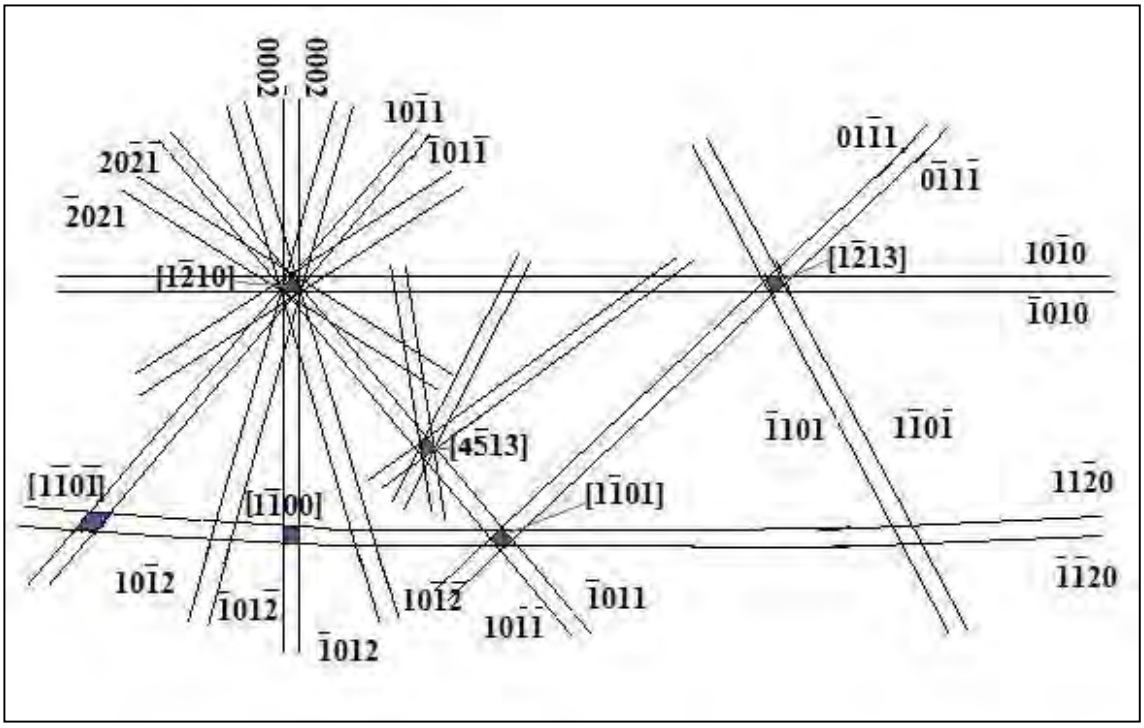

Figure 6-6 Accessible beam directions.

To ensure that the TEM foil contained an active slip trace and beta phase between alpha phase laths, Pt deposituion was used to define the plane of the active slip band as will be discussed further below for pillar (D) and illustrated in Figure 6-7. The procedure consisted of covering the entire micro-pillar with a platinum film to protect the sample during FIB thinning. During thinning, the micropillar initially appears on the cross-sectional surface as two distinct points along the outer edge of the microsample which indicate the intersections of the slip bands with the edges of the pillar.

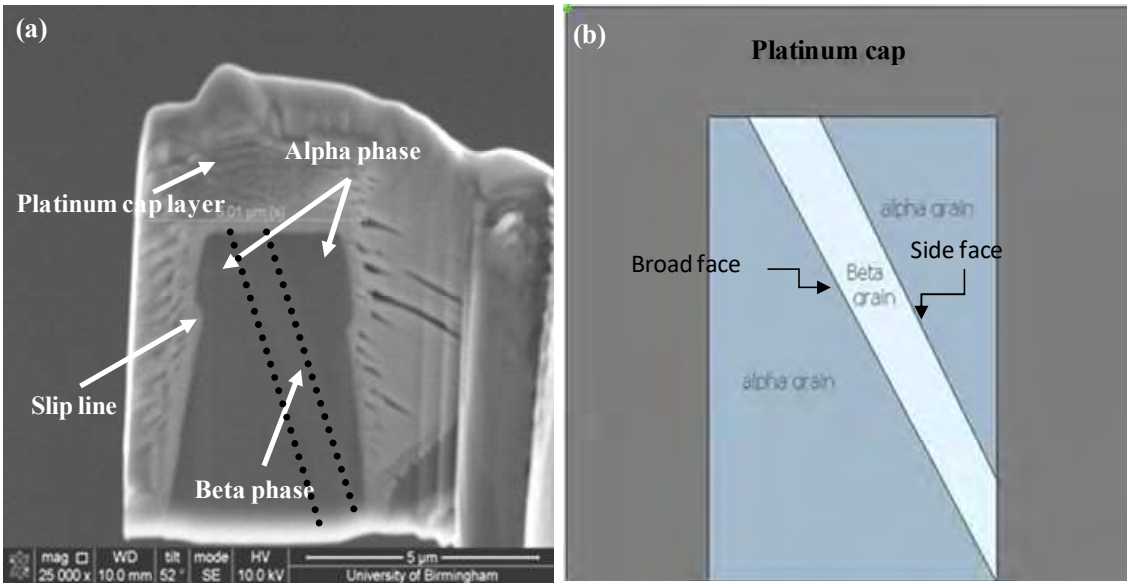

Figure 6-7 (a) SEM micrograph of a cross section through the deformed pillar (D); (b) schematic of the TEM foil showing alpha and beta phases, platinum coating and the broad and side faces.

Figure 6-8 shows a TEM overview through the pillar D.

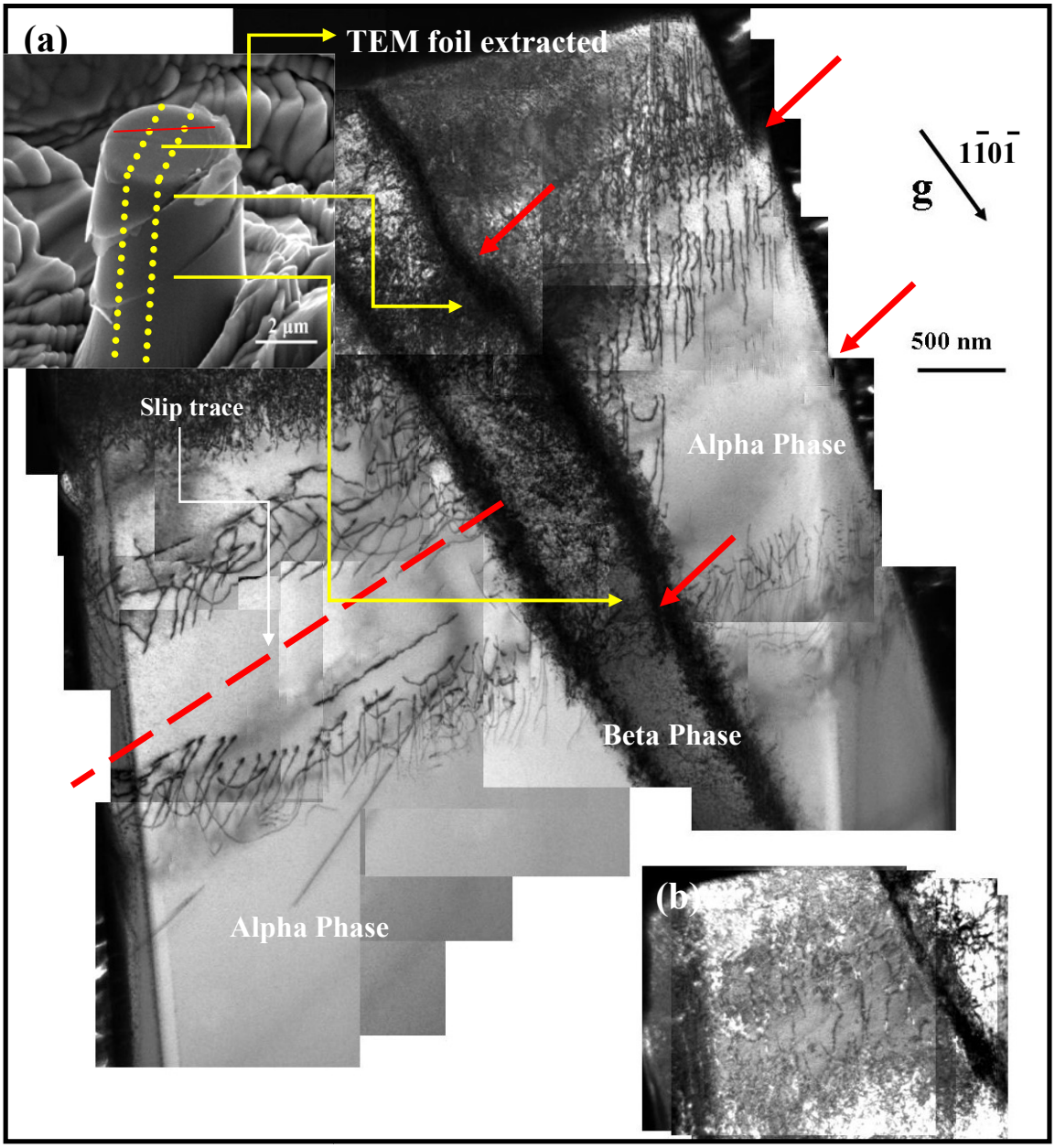

Figure 6-8 (a) A montage of bright field TEM micrographs taken with $g = 1\bar{1}0\bar{1}$ near the $[1\bar{2}13]$ zone axis for pillar (D), (b) Left top corner of pillar shown more brightly at same magnification to facilitate analysis of dislocations.

The TEM foil from pillar (E) is shown in Figure 6-9. The cylindrical compression specimen came from the same alpha colony as pillar (D).

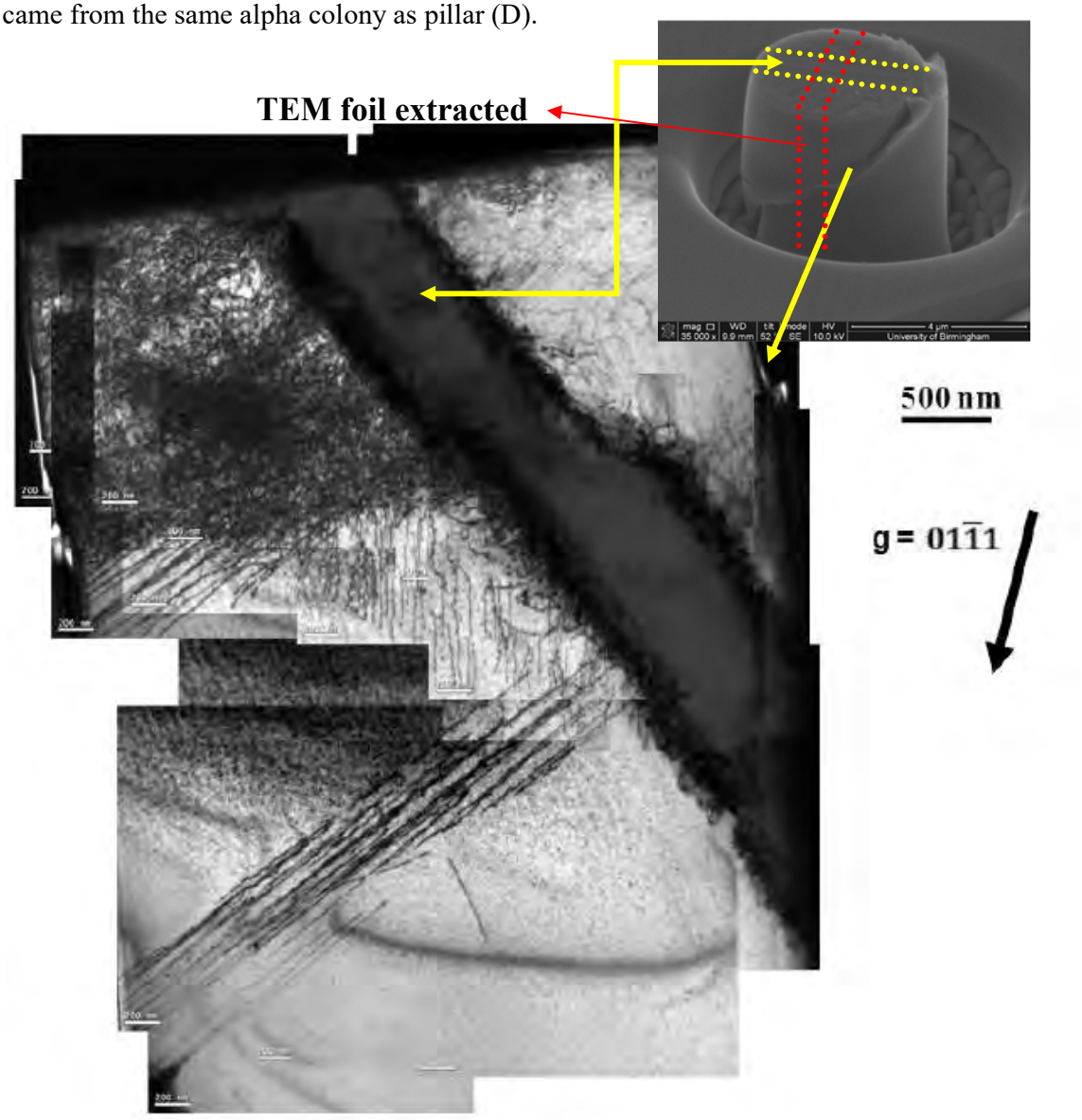

Figure 6-9 An overview of pillar (E) compressed 6%, taken with g = 01$\bar{1}$1 near the [1$\bar{1}$01] zone axis.

To summarise observations through the pillar D, Figure 6-10 includes a colour code for the dislocations in the alpha phases.

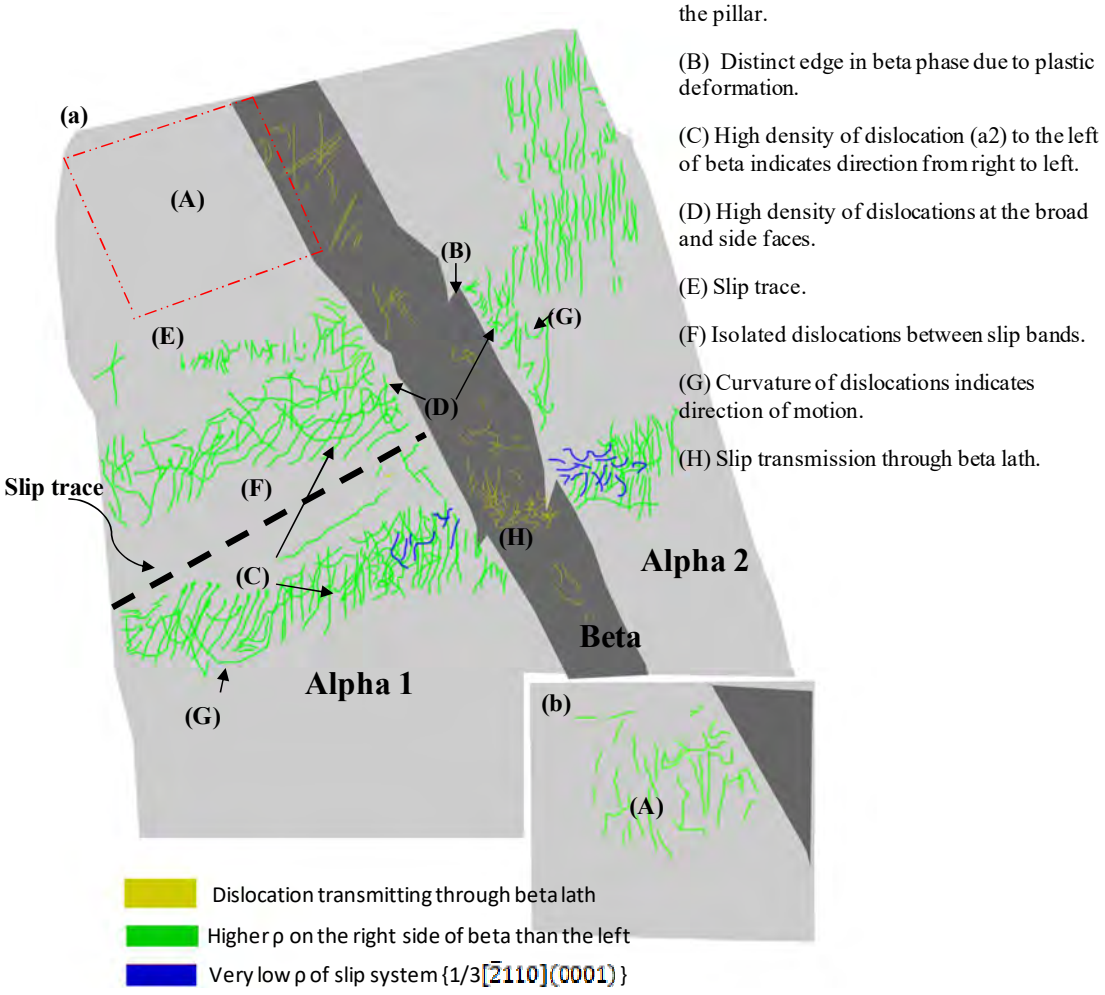

(A) High density of dislocations at the top of the pillar.

(B) Distinct edge in beta phase due to plastic deformation.

(C) High density of dislocation (a2) to the left of beta indicates direction from right to left.

(D) High density of dislocations at the broad and side faces.

(E) Slip trace.

(F) Isolated dislocations between slip bands.

(G) Curvature of dislocations indicates direction of motion.

(H) Slip transmission through beta lath.

In Figure 6-8, closely spaced dislocations occurred as two distinct slip bands, which extended across the entire specimen (alpha/beta/alpha phase). Both slip bands are parallel, thus both slip bands have the same slip plane. The bands have resulted in a shearing of the β lath, as indicated by red arrows in Figure 6-8 and region B in Figure 6-10. In Figure 6-9 (pillar E) there is only one slip band that crosses the beta phase inside the pillar, indicated by the yellow arrow on the right hand of the pillar.

There is a much greater dislocation density at the top of the pillar D and E than anywhere else. Slip commonly occurs in the upper half of the cylindrical micro-pillars (as mentioned in Chapter Five) and as exemplified by Figure 6-8. This is because the top diameter is smaller than the base diameter of each pillar and therefore the pillars deform earlier at the top than at the bottom (see Figure 6-8).

It is also clear from Figure 6-8 and Figure 6-11 that the lower regions of the alpha phase in pillar D are free from dislocations whereas large numbers of dislocations are present along the total length of the beta phase as will be described in more detail over the next few pages. The dislocations in the alpha phase were traced manually using Image J software, as shown in Figure 6-11, from which the density was deduced to be $2.2 \times 10^{15}\ m^{-2}$. In a similar manner to the alpha phase, the dislocations in the beta phase have been measured; the beta phase has a higher dislocation density by $\sim 10^4$ times than the alpha phase due to the sysmetrical crystal structure and easer deformation than alpha phase.

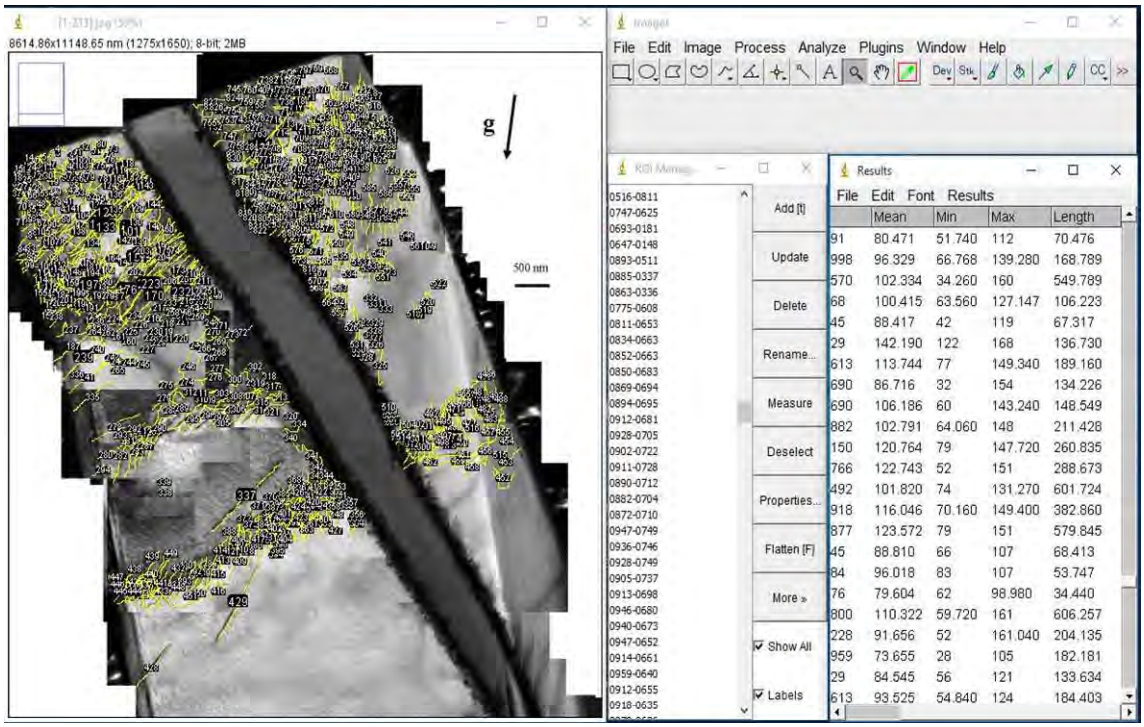

Figure 6-11 Dislocation lines for pillar (D) traced using Image J.

6.2.2.2. Identification of slip plane

In order to verify that the dislocations are in the basal plane two approaches have been used. Firstly, a stereogram is used to define the line direction of the dislocations. The slip plane contains the line direction and the Burgers vector. When appropriate crystallographic information is available it is straightforward to relate line directions of defects or directions in surfaces to the orientation of the crystal axes. For unambiguous analysis, it is clear that information is required in more than one projection so that true directions can be extracted from projected directions. Thus, in the case of the projected line direction $[\boldsymbol{h_1 k_1 l_1}]_p$ of a dislocation viewed in a direction B_1 all that can be said is that the true direction lies in the plane defined by $[\boldsymbol{h_1 k_1 l_1}]_p$ and by B_1. Micrographs taken in any other beam direction B_2

result in a second projected direction $[\boldsymbol{h_2 k_2 l_2}]_{\boldsymbol{p}}$ and hence a plane defined by $[\boldsymbol{h_2 k_2 l_2}]_{\boldsymbol{p}}$ and by B_2.The zone axis for these two planes defines the true direction of the dislocation. This is illustrated in Figure 6-12 [116].

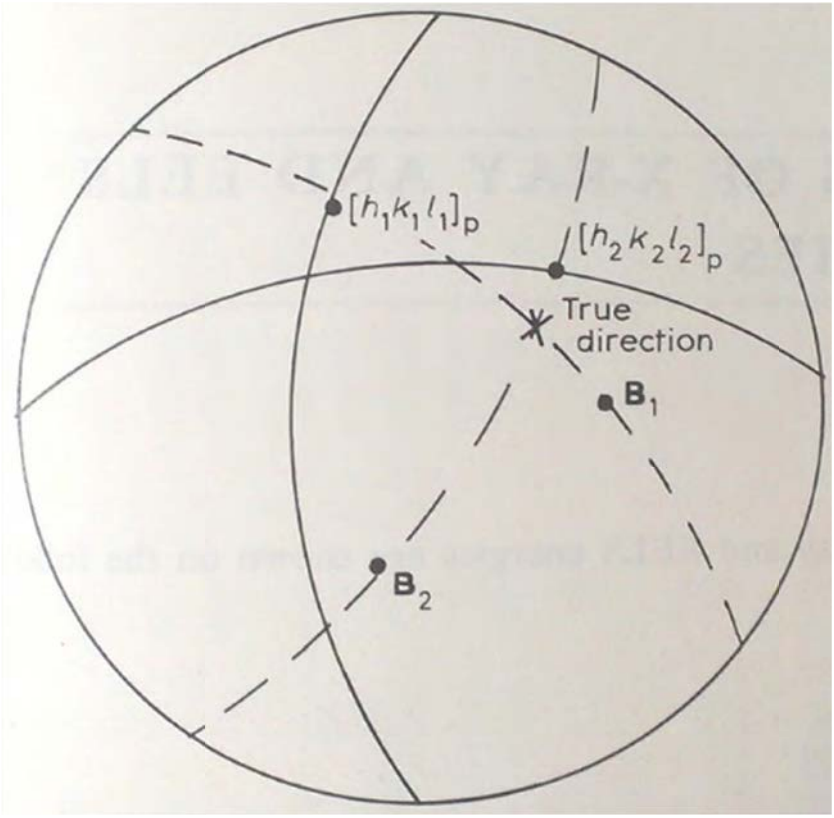

Figure 6-12 Schematic stereogram illustrating trace analysis to determine the true direction of a line which when viewed in B1 and B2 project along $[\boldsymbol{h_1 k_1 l_1}]_{\boldsymbol{p}}$ and $[\boldsymbol{h_2 k_2 l_2}]_{\boldsymbol{p}}$respectively [118]**.**

All the alpha phase dislocations were out of contrast with $g = 0002$ (Figure 6-13). This indicates that the dislocations on both sides of the beta fillet (in the alpha phase) were <a> type.

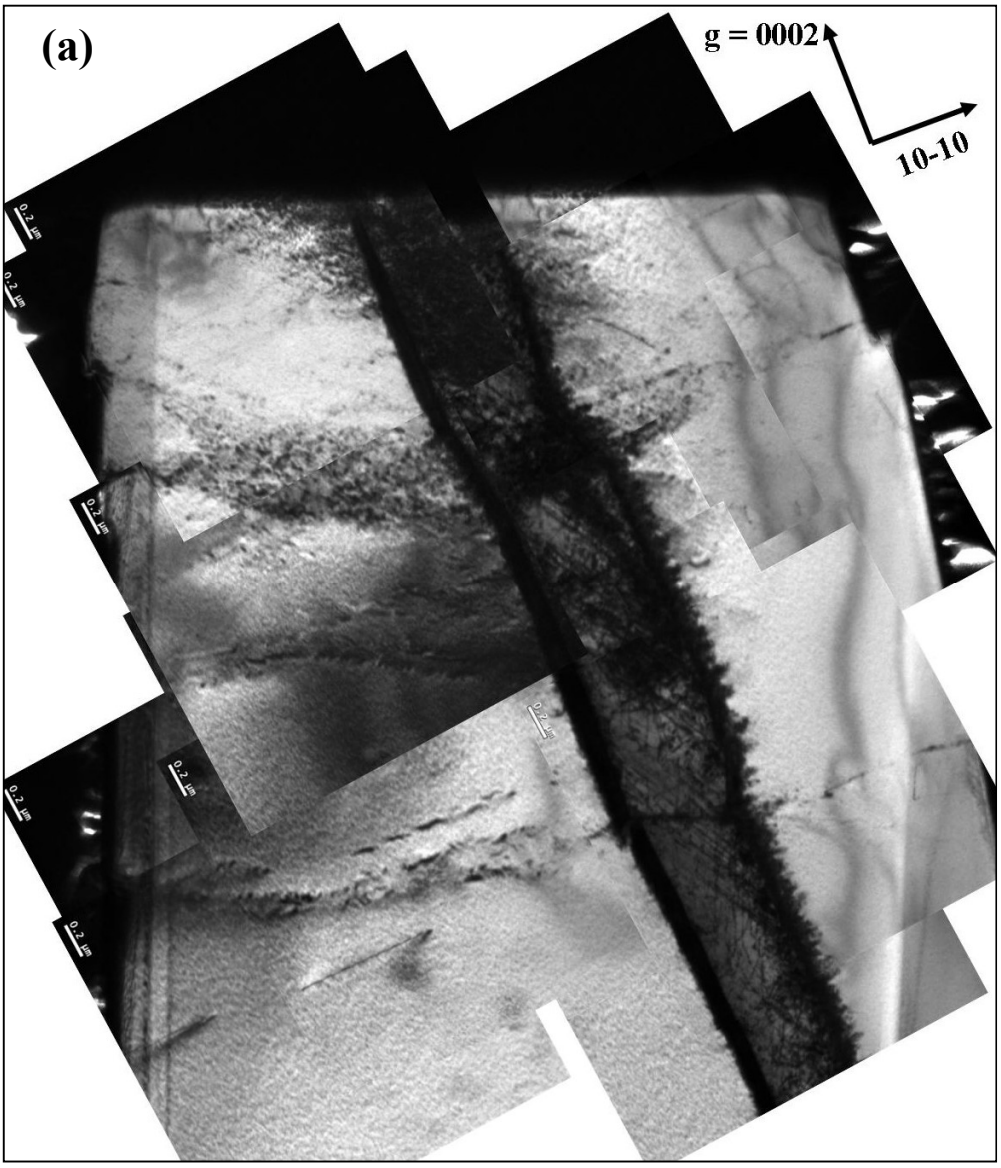

(Continued)

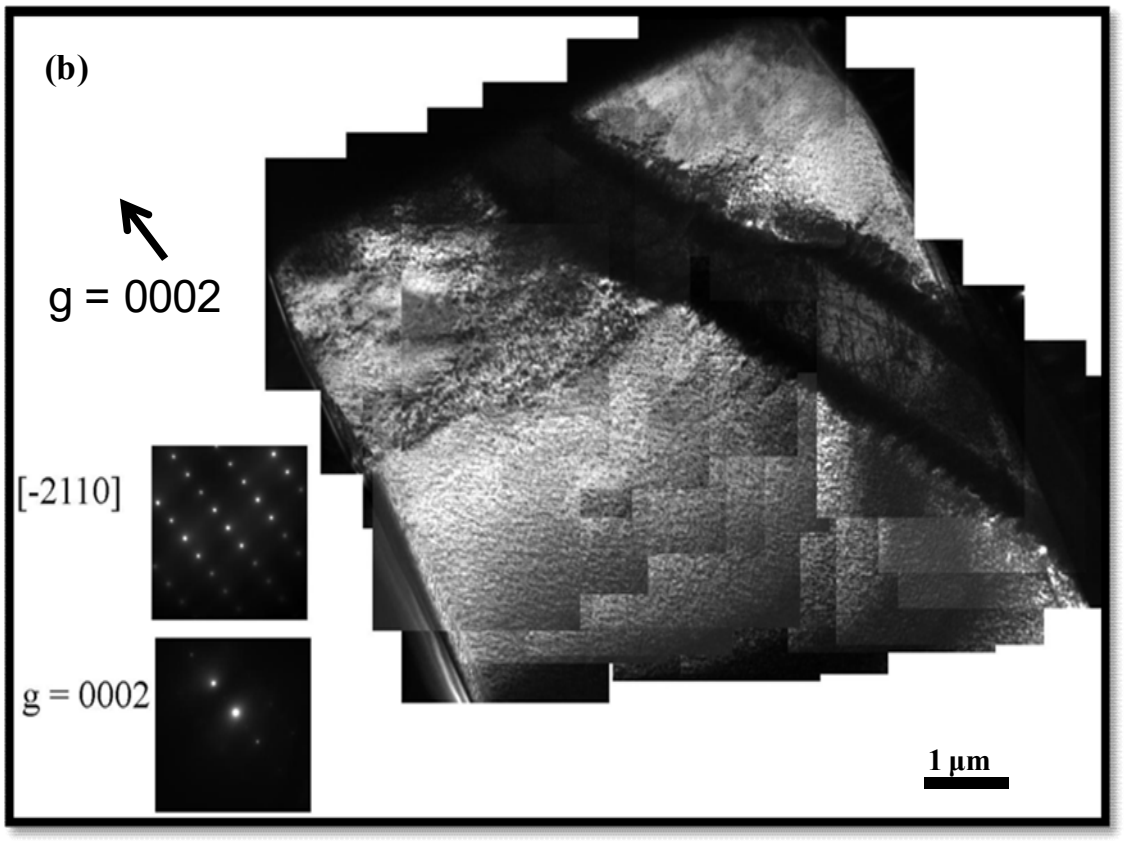

Figure 6-13 Bright Field TEM micrographs with dislocations invisible taken with g = 0002 near the $[\bar{2}110]$ zone axis (a) pillar D, (b) pillar E.

The observations made with beam direction and diffraction condition are summarised in the stereogram in Figure 6-14. The dislocations in regions (A, C and G) based on Figure 6-10 are in the basal plane.

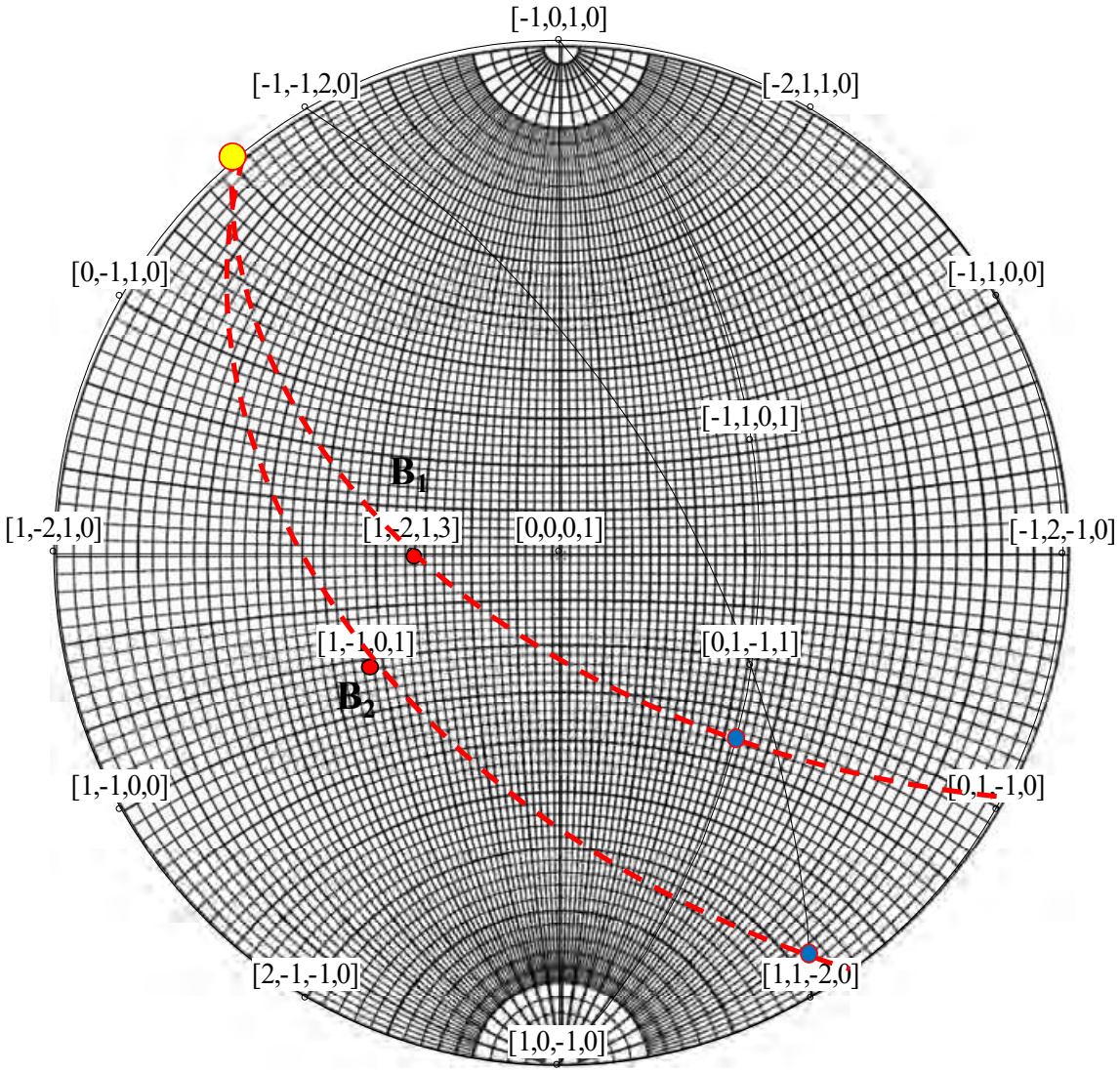

To summarise Figure 6-14, the true directions of the dislocations are in the basal plane.

The second approach, a line is drawn parallel to the dislocation. This line is superimposed on a diffraction pattern from the closest zone axis and the corresponding projected direction for the line defines the plane which contains the dislocation line. The same feature is imaged in another electron beam direction, and then the true direction can be obtained as the cross product between the two lines (two traced lines on the dislocations) in the different beam directions. Finally, the plane which contains the Burgers vector and normal to both lines by cross product again. Thus, the basal plane is the slip plane. The observations made for dislocations in different electron beam direction are summarised in Figure 6-15.

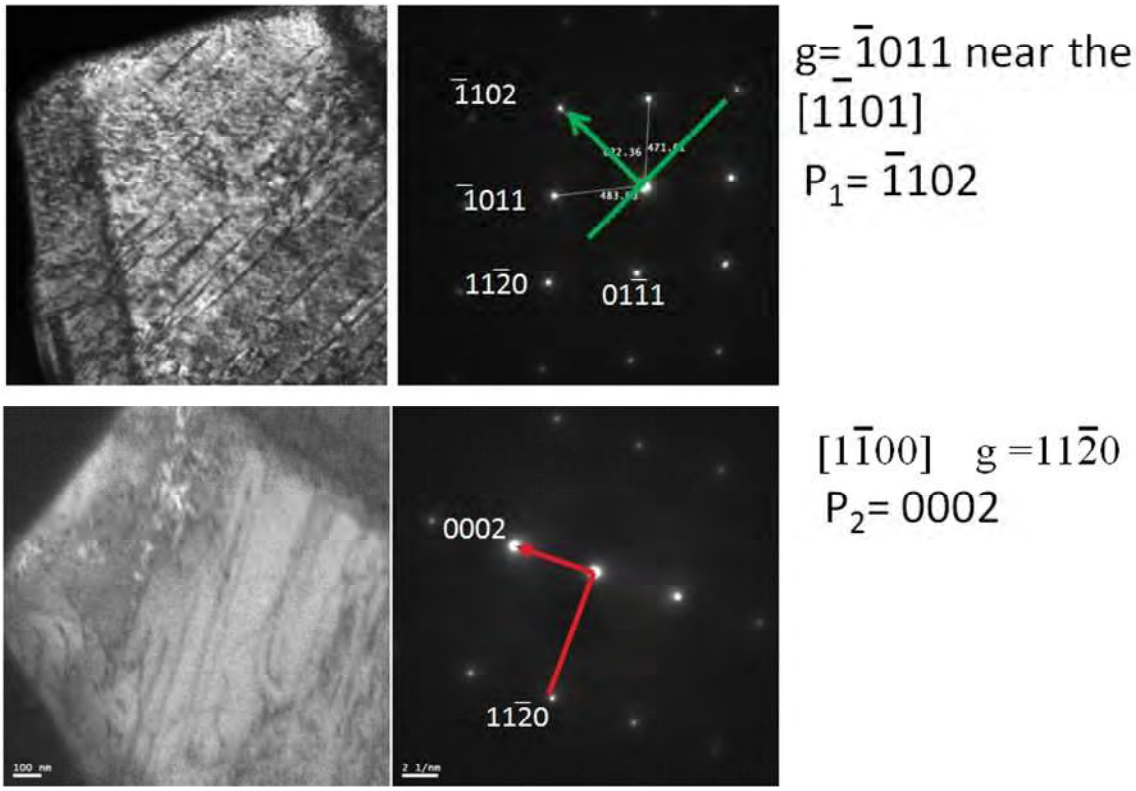

(a)

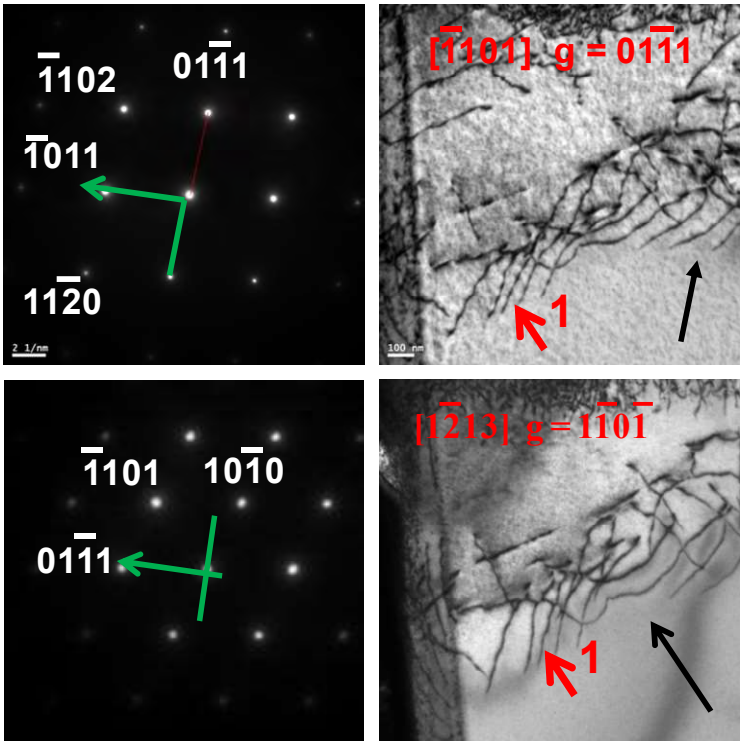

(b)

The second approach in the pillar D is summarise in Table 6-2 based on Figure 6-15.

Table 6-2 Summary of the results obtained from the dislocation analysis in the alpha phase based on Figure 6-15

Figure 6-15	$P_1 \times P_2 = u$	$u \times b = Slip\ plane$
(a)	$1\bar{1}00$	0002
(b)	$11\bar{2}0$	0002

6.2.2.3. Burgers vector analysis

g.b analysis was performed to identify the nature of the dislocations present in the α and the β phase and help to analyse the characteristic of the dislocations. The foil normal was also determined for the sample analysed. This was done using diffraction pattern mode. The zone axis was within 1 to 2 degrees from the actual foil normal and was designated as the foil normal for the grain (see Figure 6-16).

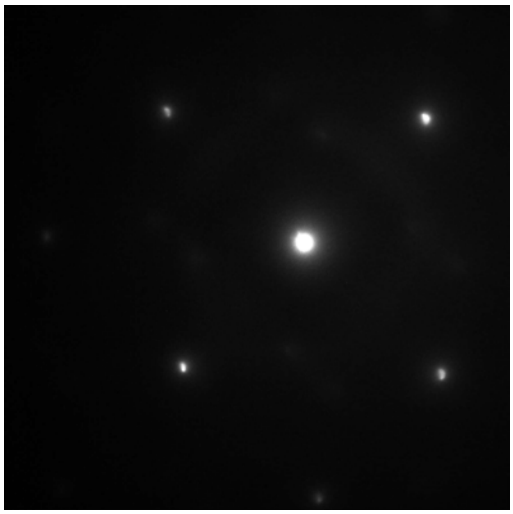

Figure 6-16 Selected-area diffraction pattern taken from the alpha phase illustrating the foil normal zone axis $[4\bar{5}13]$which is within 2 degrees of the actual foil normal.

A g·b analysis was carried out on these well separated dislocations, which were then classified into three different sets for alpha phase and four sets for beta phase, then labelled individually in the images. The dislocations in the pillar will be analysed except for the dislocations in the top of the pillar (which we believe come from the free surface) due to their high density.

6.2.2.3.1. Burgers vector analysis for <a> dislocations in the alpha slip colony

There follow four micrographs (Figure 6-17 - Figure 6-20), using different reflections, of the TEM specimen taken from pillar D.

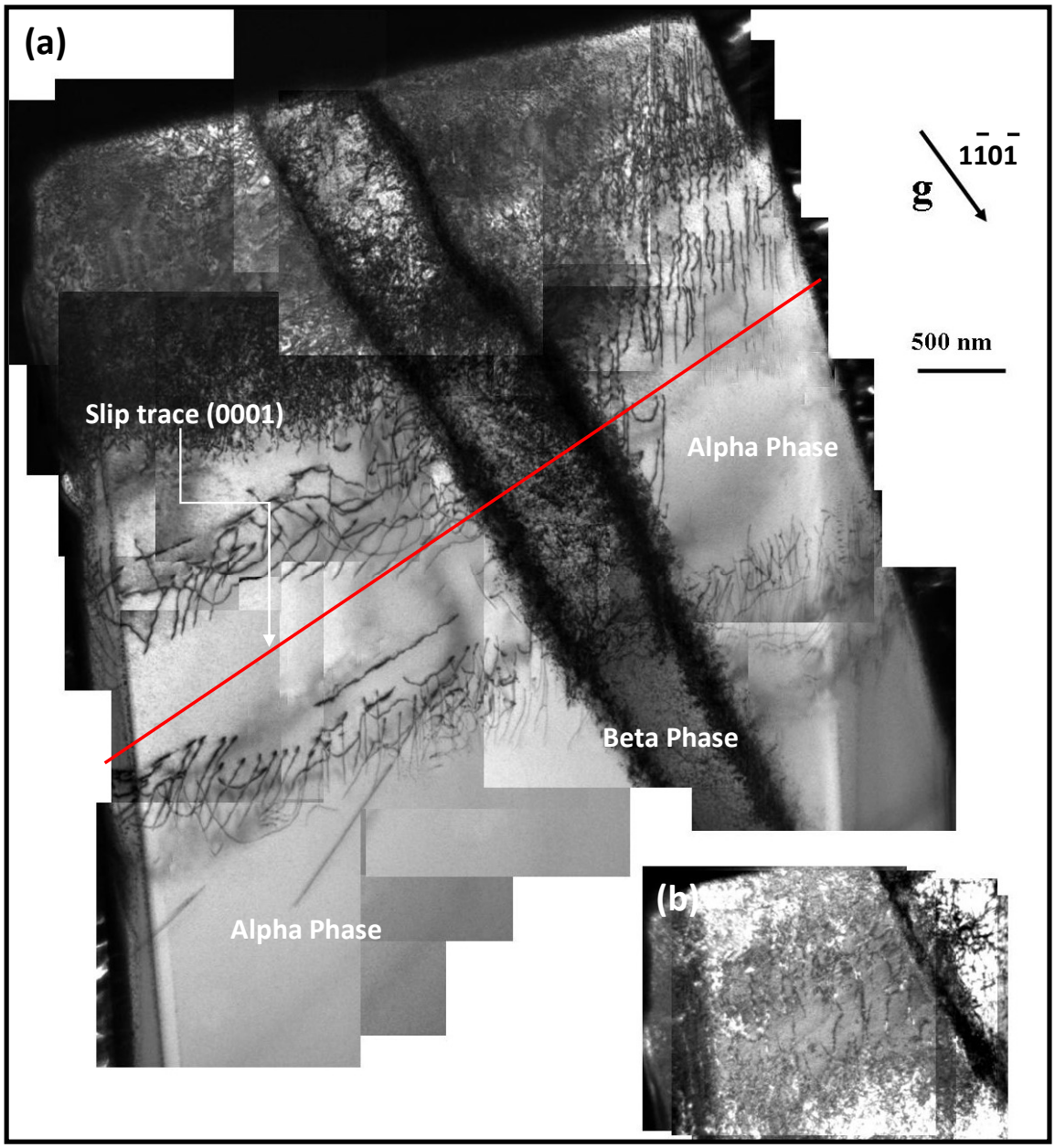

Figure 6-17 (a) A montage of bright field TEM micrographs taken with $g = 1\bar{1}0\bar{1}$ near the $[1\bar{2}13]$ zone axis for pillar (D), (b) Left top corner of pillar shown more brightly to facilitate analysis of the dislocations.

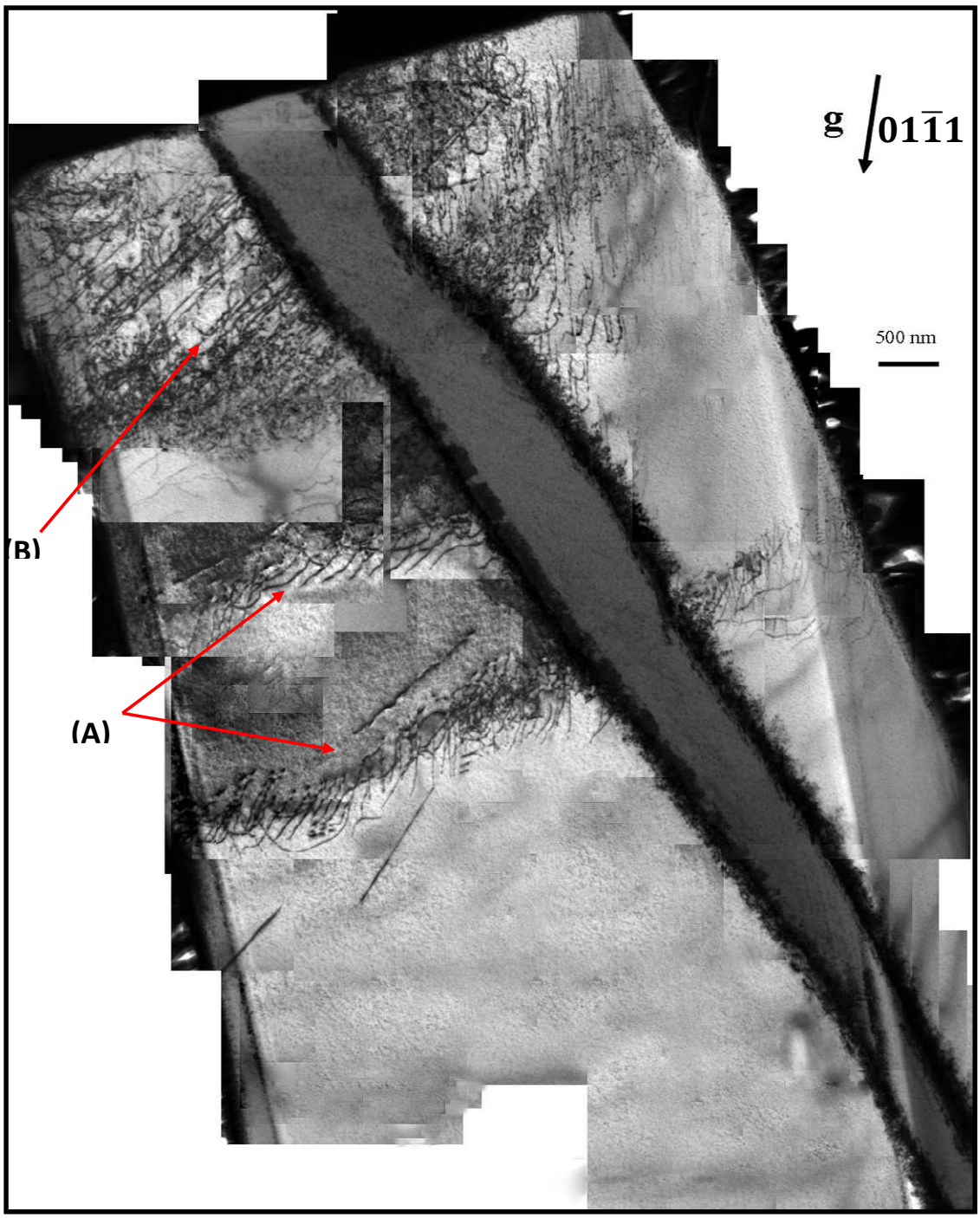

Figure 6-18 Bright field TEM micrographs with $g = 01\bar{1}1$ near the $[1\bar{1}01]$ zone axis in pillar (D).

Figure 6-19 BF- TEM micrographs with $g = \bar{1}011$ near the $[1\bar{1}01]$ zone axis in pillar (D).

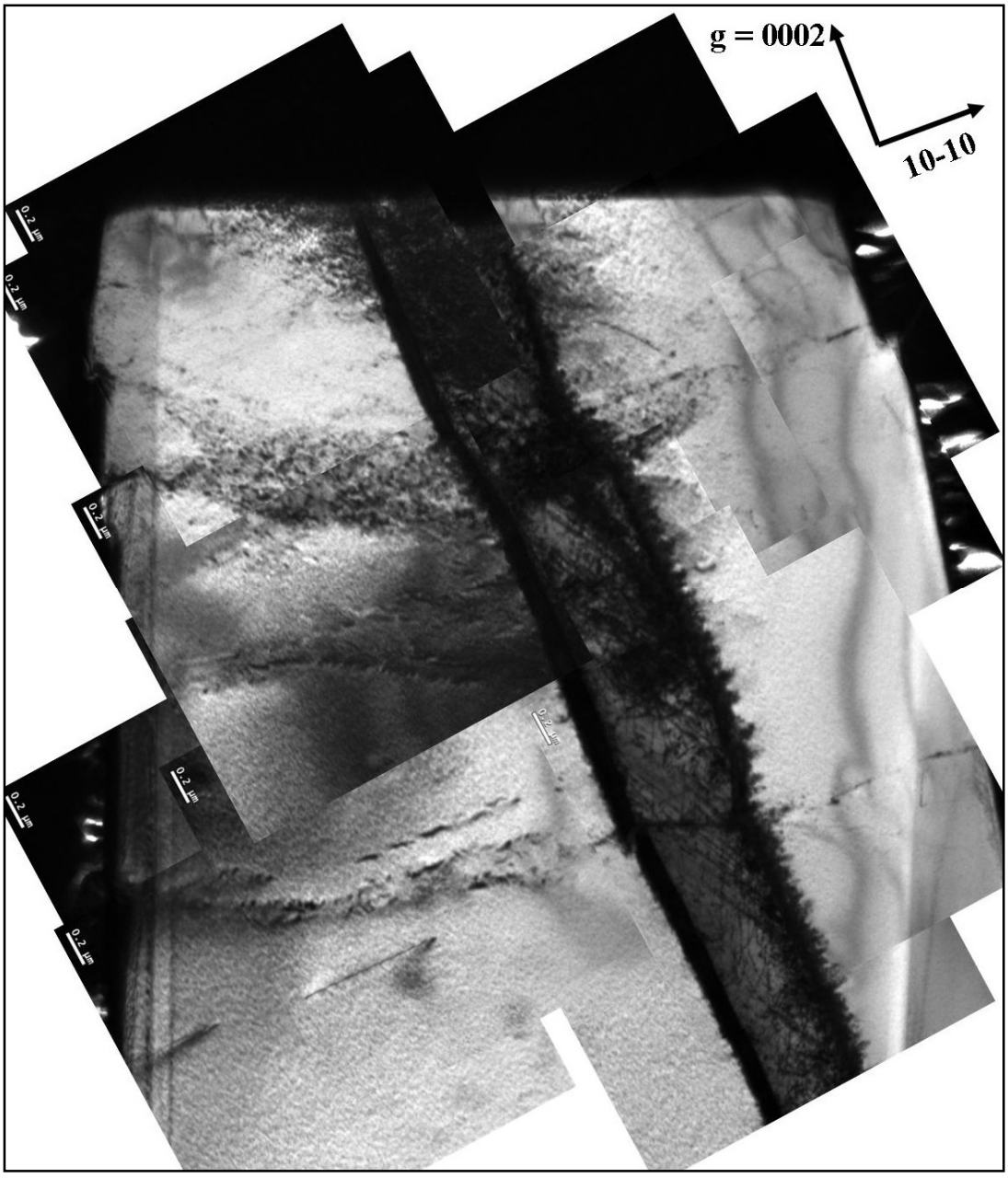

Figure 6-20 Bright Field TEM micrographs with dislocations invisible taken with g= 0002 near the $[1\bar{2}10]$ zone axis for the pillar D.

Most of the dislocations shown in Figure 6-17 have been identified as a_2 dislocations (using g.b analysis). A very few other dislocations are observed near the β lath which were analysed as a_1 (see Figure 6-19). Figure 6-19 provides an example of the invisibility of the a_2 dislocations shown in Figure 6-17. Figure 6-19 shows a bright field TEM micrograph taken with g= $\bar{1}011$ near the $[1\bar{1}01]$ zone axis. With this particular vector, dislocations with Burgers vectors $b = \frac{1}{3}[11\bar{2}0]$ and $b = \frac{1}{3}[\bar{2}110]$ are both visible. Figure 6-20 shows micrographs with g vectors parallel to (0002) taken close to the $[1\bar{2}10]$ zone. Figure 6-20 shows <a> type dislocations in pillar D.

The operative slip systems in the samples that were analysed are presented in Table 6-3.

Table 6-3 Summary of the results obtained from the dislocation analysis in the alpha phase using different diffraction conditions (see Figure 6-17 to Figure 6-20).

Beam direction	g vector	Slip system $1/3[\bar{2}110](0001)$	Slip system $1/3[1\bar{2}10](0001)$	Slip system $1/3[11\bar{2}0](0001)$	Figures
$[1\bar{2}13]$	$g_1 = 1\bar{1}0\bar{1}$	V	V	I	Figure 6-17
$[1\bar{1}01]$	$g_2 = 01\bar{1}1$	I	V	V	Figure 6-18
	$g_3 = \bar{1}011$	V	I	V	Figure 6-19
$[1\bar{2}10]$	g = 0002	I	I	I	Figure 6-20

The dislocations were colour coded using Photoshop. Table 6-4 lists the colour chosen for each system.

Table 6-4 The possible slip systems in the alpha phase for the pillar (D) with a loading direction of $[\bar{1}5\bar{4}6]$.

No. of slip systems	Slip system	Colour coding
1	$1/3(0001)[\bar{2}110]$	Blue
2	$1/3(0001)[1\bar{2}10]$	Green
3	$1/3(0001)[11\bar{2}0]$	Red
4	$1/3(10\bar{1}1)[1\bar{2}10]$	Purple

There is a high density of dislocations at the top of the specimen as seen in Figure 6-17, most of which are out of contrast when viewed in the $01\bar{1}1$ condition near the $[1\bar{1}01]$ zone axis (Figure 6-18). This would suggest that they are a_1. The slip system (1) $1/3[\bar{2}110](0001)$ is indicated by a red circle (A) in Figure 6-19 taken with g= $\bar{1}011$ near the $[1\bar{1}01]$ zone axis in the pillar (D). The a_1 dislocations appear on both sides of the beta phase. Figure 6-21 shows all the results merged into one picture.

Figure 6-21 Colour coding for the dislocations in the alpha phases for the pillar D. The green and red dislocations are traced from Figure 6-17 and Figure 6-18, the blue from Figure 6-19. The yellow colour shows dislocations across the beta phase.

The slip system on the pillar D is only a qualitative ranking based on the amount of activity of a particular slip system in the analysed grain. One can observe from Figure 6-21 that basal (a_2) $1/3[1\bar{2}10](0001)$ slip was by far the most frequently observed primary slip system. Basal (a_3) slip was also observed and was the most common secondary slip system. Pyramidal <a> slip was active in a few cases, which we believe is due to a back stress from the interface. In Table 6-4, data for <a> type slip systems only are present. It should be noted that <c+a> pyramidal slip was not observed in any of the grains (see Figure 6-20). In fact, along the entire length of this particular β lath, additional dislocations in the α phase were observed. A schematic diagram of the activation of <a> dislocations on basal and pyramidal planes is shown in Figure 6-22.

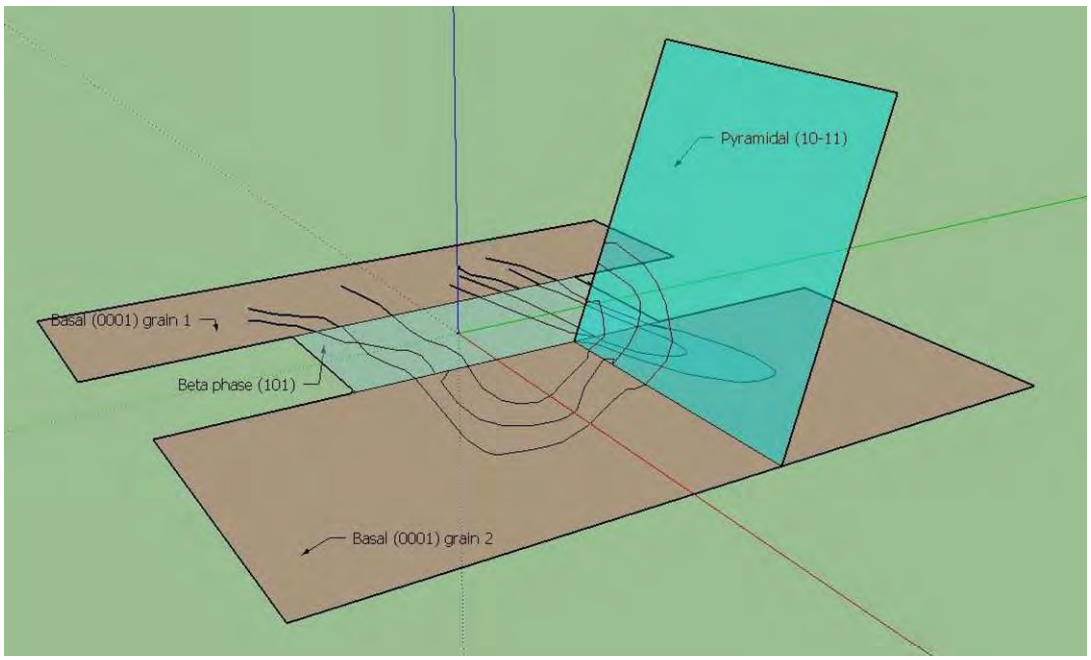

6.2.2.3.2. Character of the dislocations

To evaluate the character (edge or screw) of the dislocations, the Burgers vector orientations are projected next to the TEM images in Figure 6-23 and Figure 6-24. The projections of the three (a) Burgers vectors have been drawn by the side of the BF-TEM image. If the Burgers vector is perpendicular to the dislocation line, it is an edge dislocation, while when the dislocation is a screw dislocation the Burgers vector is parallel to the dislocation line.

From Figure 6-23 and Figure 6-24 we can conclude that the dislocations for slip system (2) $1/3[1\bar{2}10](0001)$ are almost screw with some mixed type dislocations. Also, the dislocations in slip system (1) $1/3[\bar{2}110](0001)$ are mixed type dislocations as shown in Figure 6-24.The dislocations coloured red for slip systems (3) $1/3[11\bar{2}0](0001)$ are screw as shown in Figure 6-24 since their line vectors are close to the $[11\bar{2}0]$ direction (Burgers vector direction). Finally, the purple colour dislocations in Figure 6-23 represent slip system (4) $1/3[1\bar{2}10](10\bar{1}1)$ and are pretty much screw dislocations. Figure 6-25 shows all the dislocation characters merged into one picture.

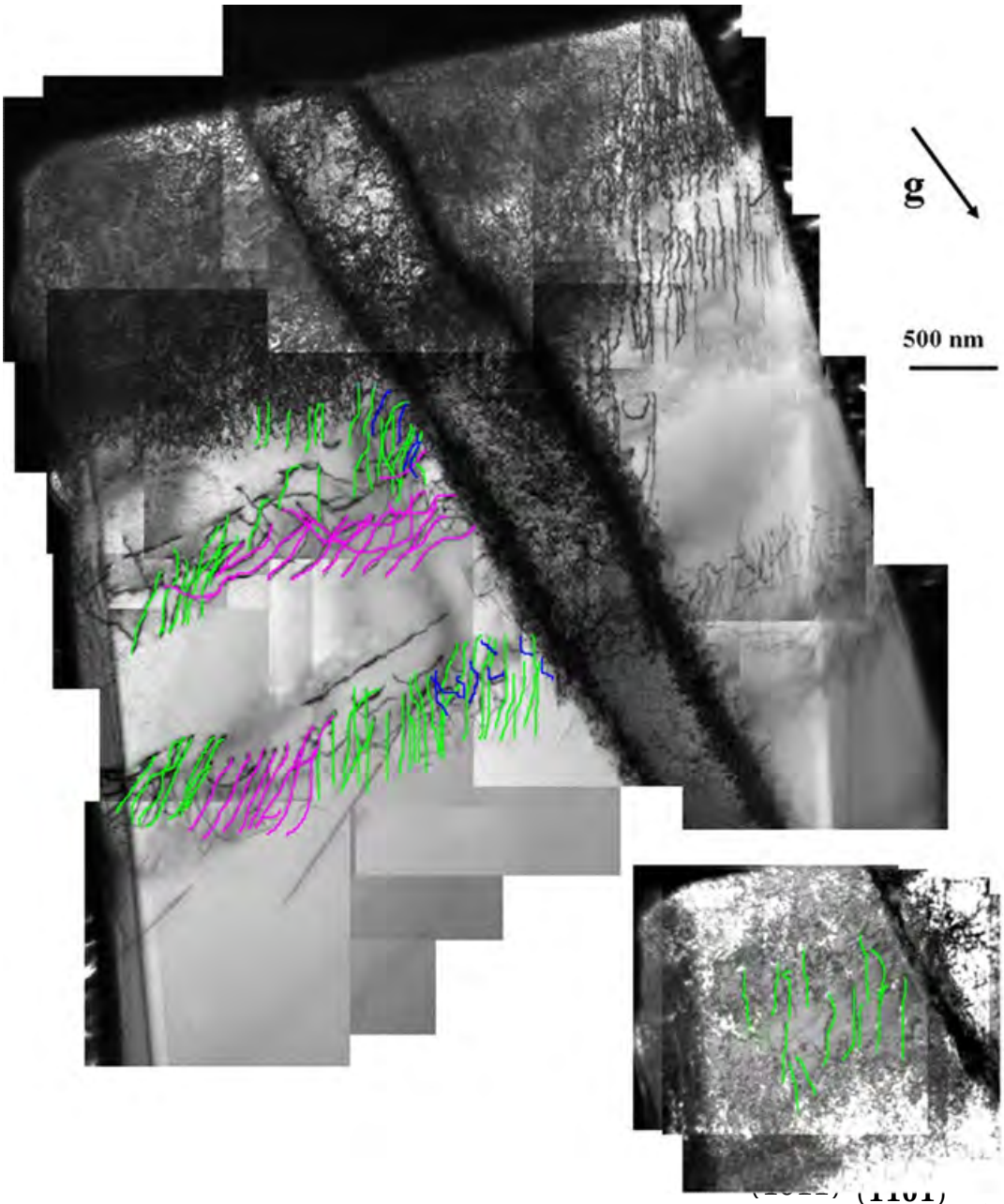

Figure 6-23 BF-TEM images taken with $g = 1\bar{1}0\bar{1}$ near the $[1\bar{2}13]$ zone axis for the pillar (D). Slip system /3 $[1\bar{2}10]$ (0001) .

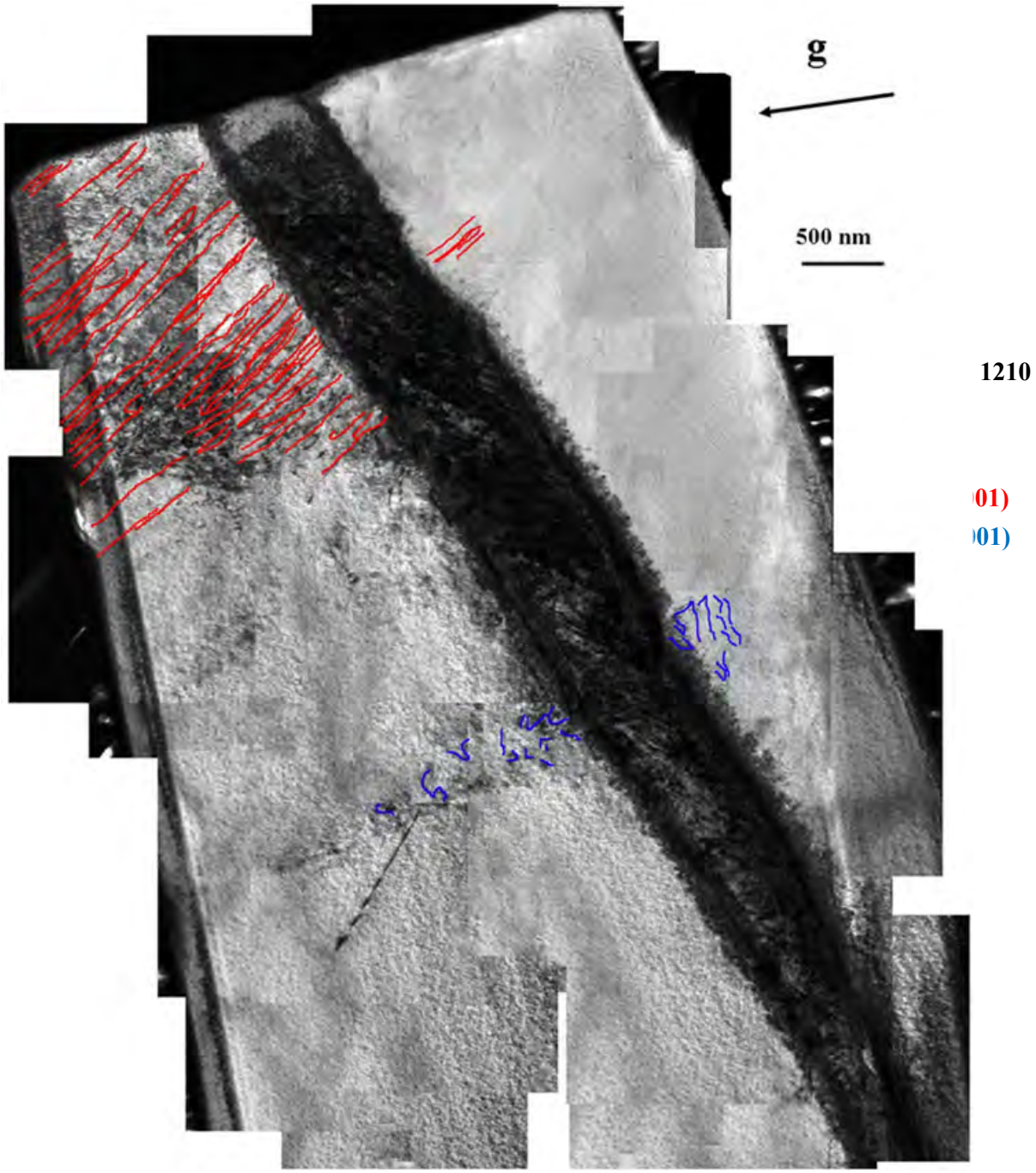

Figure 6-24 BF-TEM images taken with $g = \bar{1}011$ near the $[1\bar{1}01]$ zone axis for pillar (D). Blue is slip system $1/3\ [\bar{2}110]\ (0001)$ and red is slip system $1/3\ [11\bar{2}0]\ (0001)$.

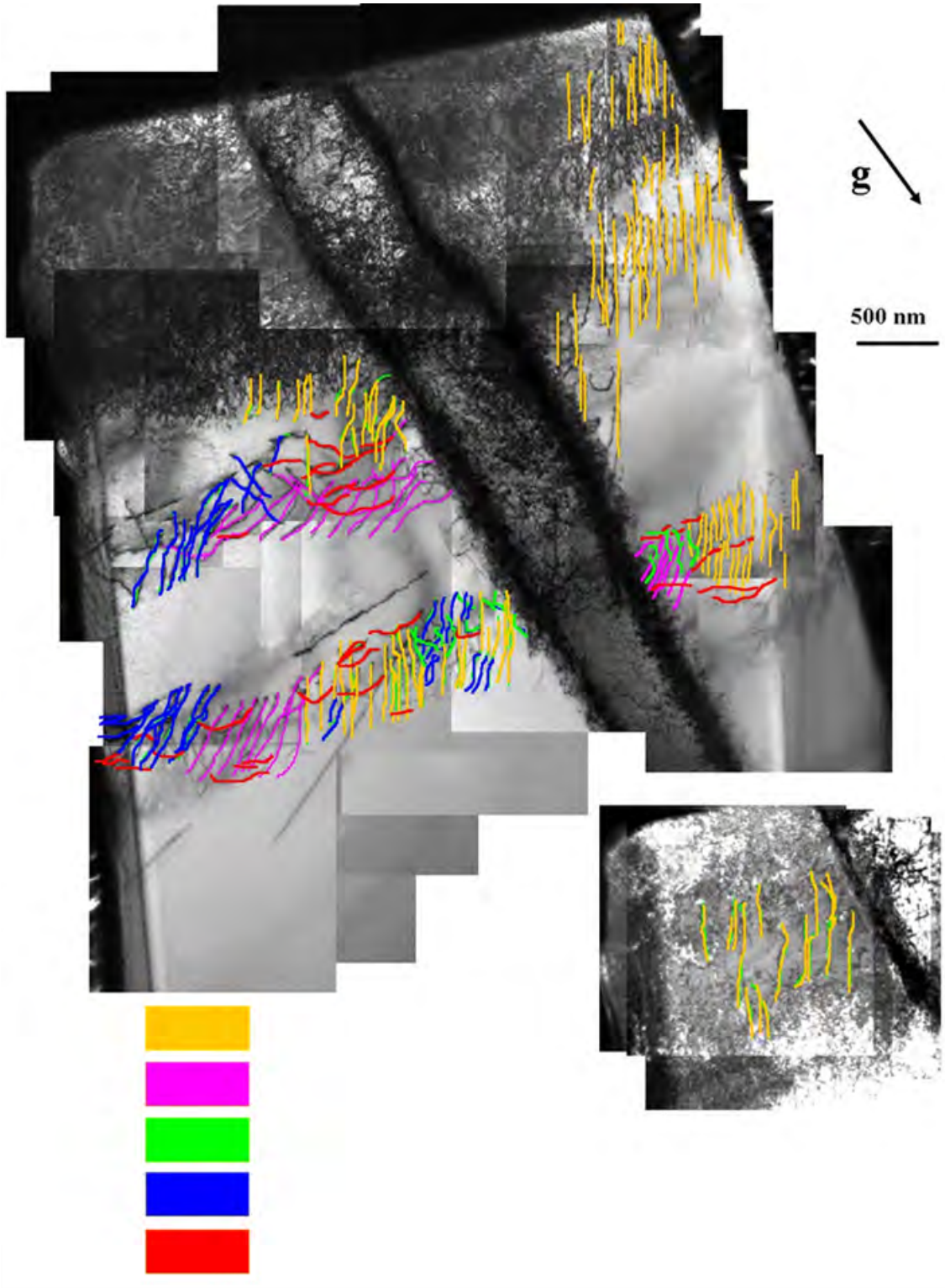

Figure 6-25 BF-TEM images taken with g = $1\bar{1}0\bar{1}$ near the [$1\bar{2}13$] zone axis for the pillar (D).

6.2.2.3.3. Dislocation direction

In Figure 6-26 shows that the dislocations are obviously coming from the entry side as indicated by the orange arrow in Figure 6-26 (c,e and f) and going through the beta phase, and then the exit side as indicated by the yellow arrow in Figure 6-26 (d to f). Thus agrees with researchers such as Kacher and Robertson [117].

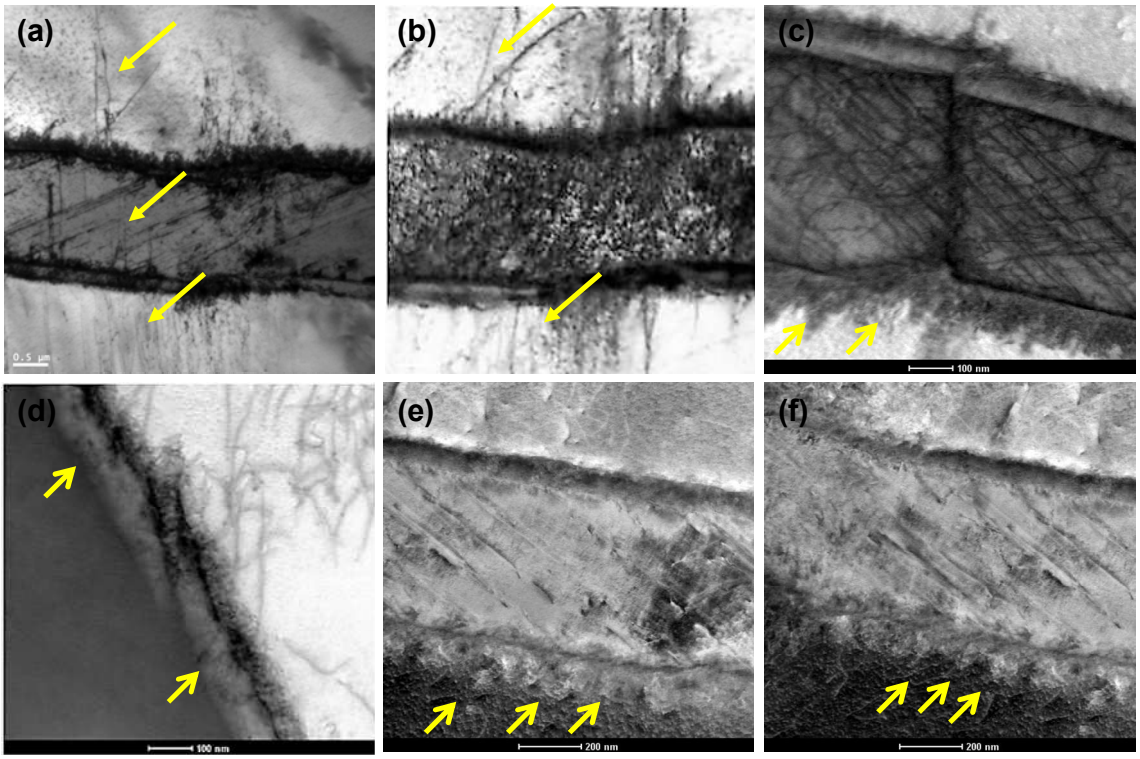

A schematic diagram for dislocation movement throughout the beta phase is presented in Figure 6-27. The curved shape of the dislocations in the side face (see region C on Figure 6-10) indicates dislocations coming into the entry side. The exit side indicates the direction of dislocations going out the broad face.

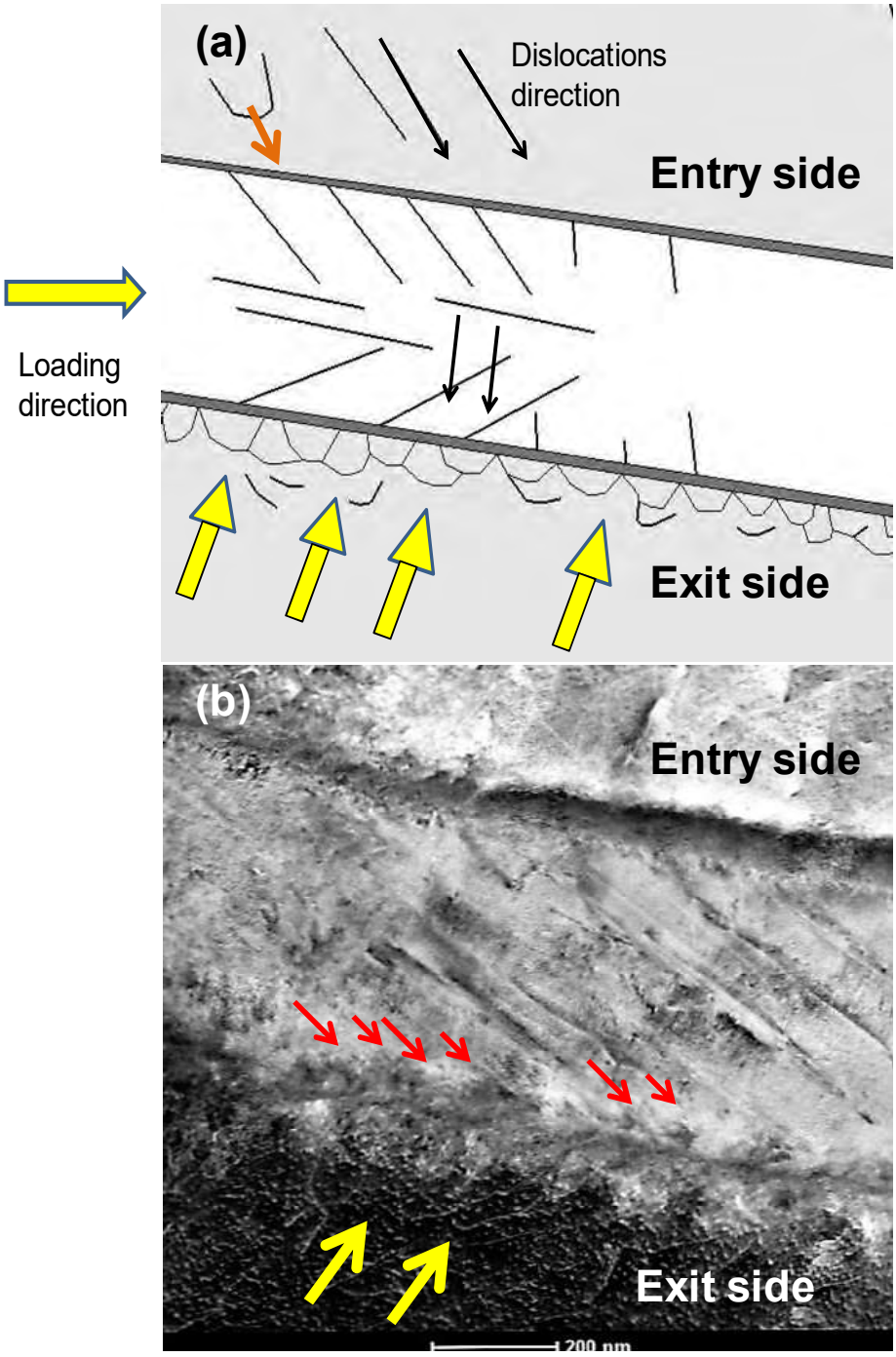
(a)
Dislocations direction
Entry side
Loading direction
Exit side
(b)
Entry side
Exit side
200 nm

6.2.2.3.4. Burgers vector analysis for beta grain

The dislocation microstructure in the β phase was also analysed. Figure 6-28 to Figure 6-31 were taken with g vectors within the β-phase to identify the nature of the dislocations. A network of dislocations can be observed forming in the β-phase upon slip transmission through the α/β interface, as shown in Figure 6-26 (c). These bright field TEM micrographs were taken with different g vectors. In Figure 6-26 (c), all $< 111 >$ dislocations within the β-phase are visible. A full g.b analysis of the dislocations within the β-lath indicates that all of the dislocation contrast is consistent with $< 111 >$ dislocation content. Table 6-5 lists the visibility of the dislocations under the chosen diffraction conditions in the beta phase colony in the pillar D.

Table 6-5 Summary of the analysis of the beta phase of 4-µm Pillar D in different diffraction conditions.

Beam direction	g vector	Slip system ½[11$\bar{1}$]	Slip system ½[$\bar{1}$11]	Slip system ½[111]	Slip system ½[1$\bar{1}$1]	Figures
[$\bar{1}\bar{1}\bar{1}$]	$\bar{1}$01	V	V	I	I	Figure 6-28
[$\bar{1}\bar{1}\bar{1}$]	0$\bar{1}$1	V	I	I	V	Figure 6-29
[1$\bar{1}\bar{3}$]	110	V	I	V	I	Figure 6-30
[$\bar{1}\bar{1}\bar{1}$]	$\bar{1}$10	I	V	I	V	Figure 6-31

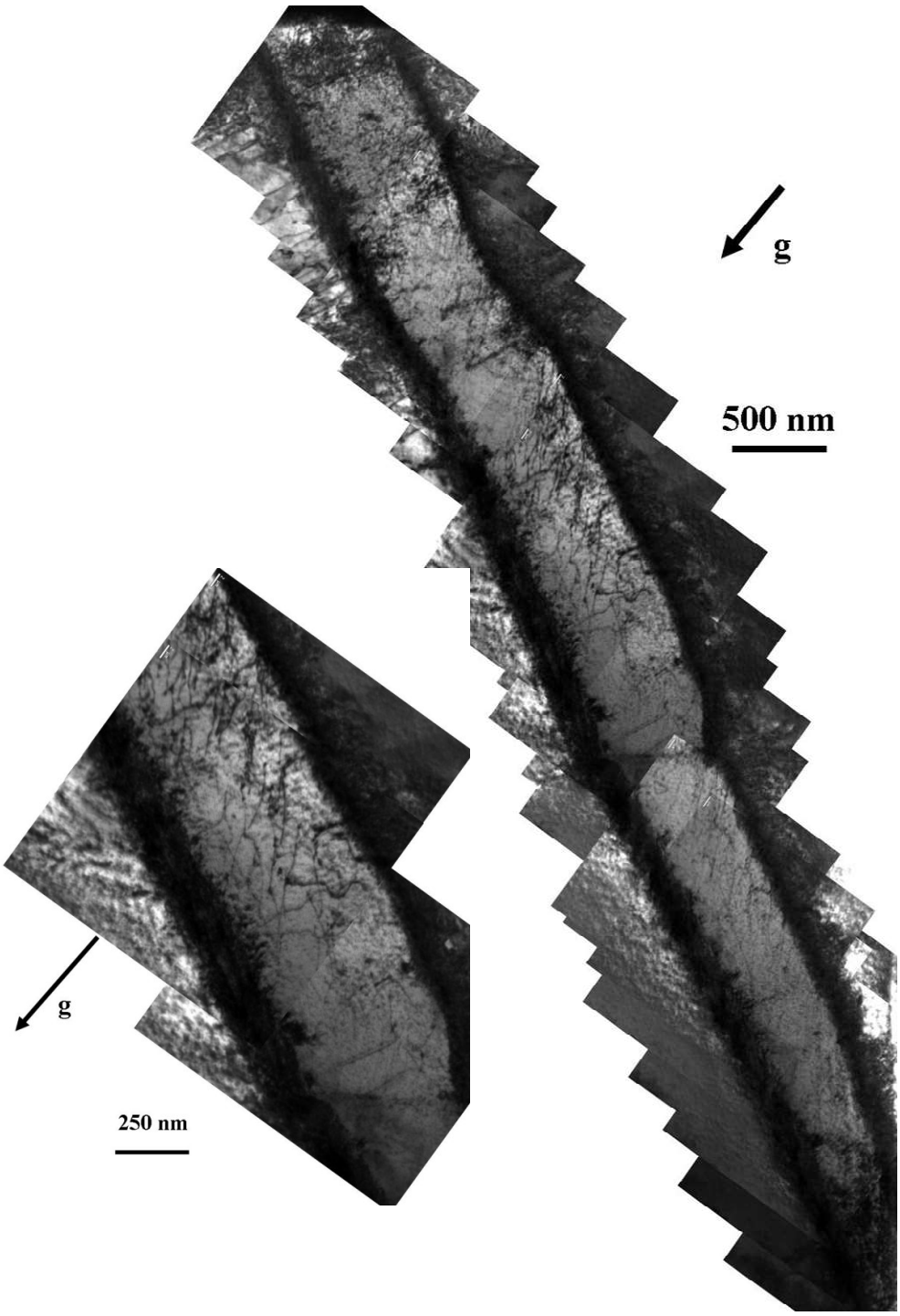

Figure 6-28 BF TEM micrographs taken with g = $\bar{1}01$ near the $[\bar{1}\bar{1}\bar{1}]$ zone axis for the pillar (D) beta phase; showing $\mathbf{b_2} = \frac{1}{2}[\bar{1}11]$ dislocation (due to Burgers Orientation Relationships) segments lying on the primary (101) slip plane. Blue arrows shows $\mathbf{b_2} = \frac{1}{2}[\bar{1}11]$ impinges at the alpha/beta interface (exit side).

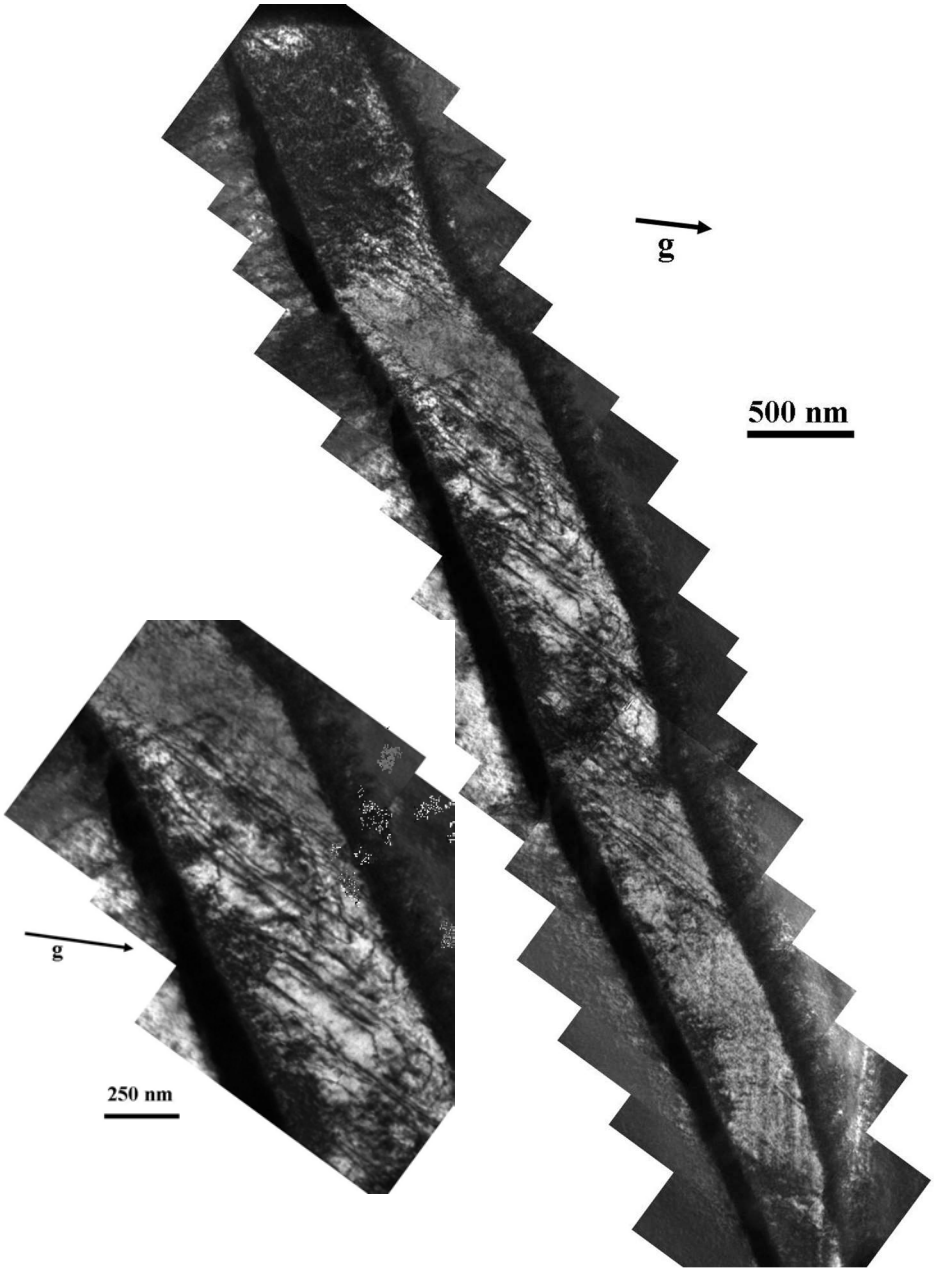

Figure 6-29 BF TEM micrographs taken with g = $0\bar{1}1$ near the $[111]$ zone axis for the pillar (D) beta phase; showing that $\mathbf{b}_4 = \frac{1}{2}[1\bar{1}1]$ and $\mathbf{b}_1 = \frac{1}{2}[11\bar{1}]$ dislocations are visible.

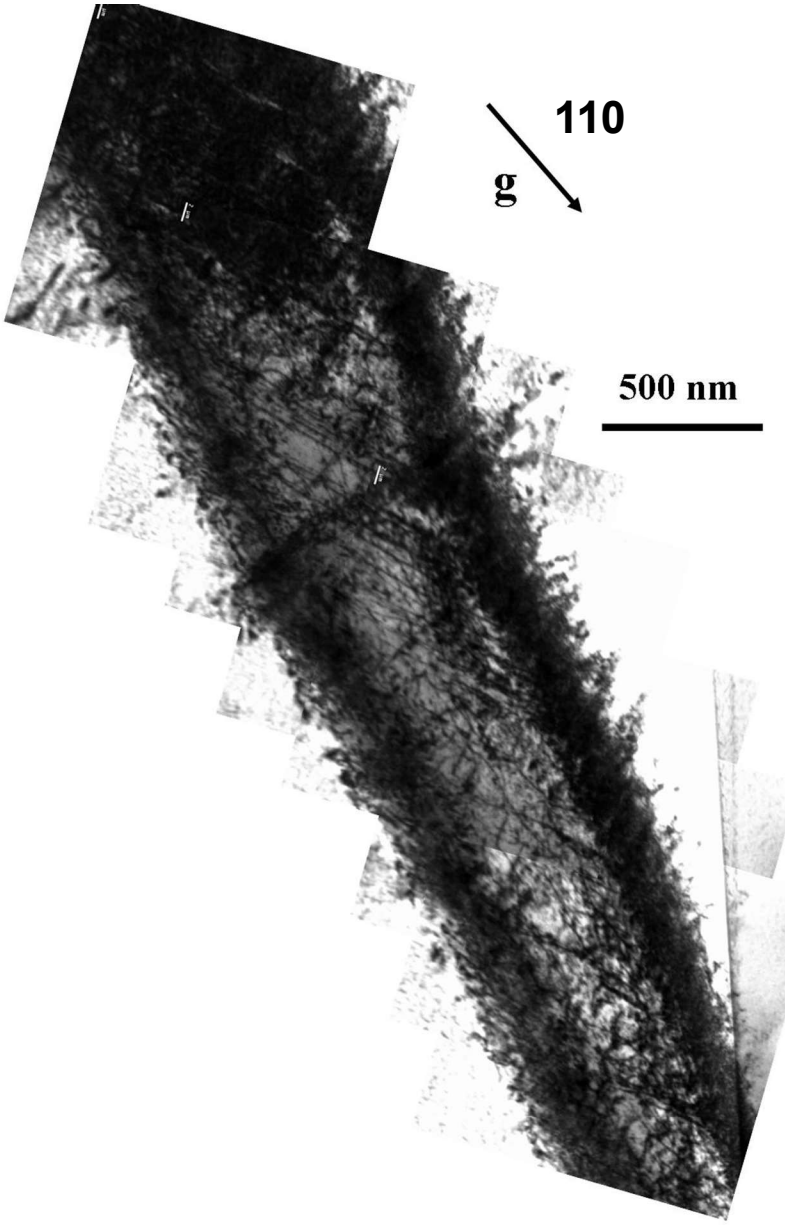

Figure 6-30 BF TEM micrographs taken with g = 110 near the $[1\bar{1}\bar{3}]$ zone axis for the pillar (D) beta phase; showing that $\mathbf{b}_3 = \frac{1}{2}[111]$ and $\mathbf{b}_2 = \frac{1}{2}[\bar{1}11]$dislocations are visible.

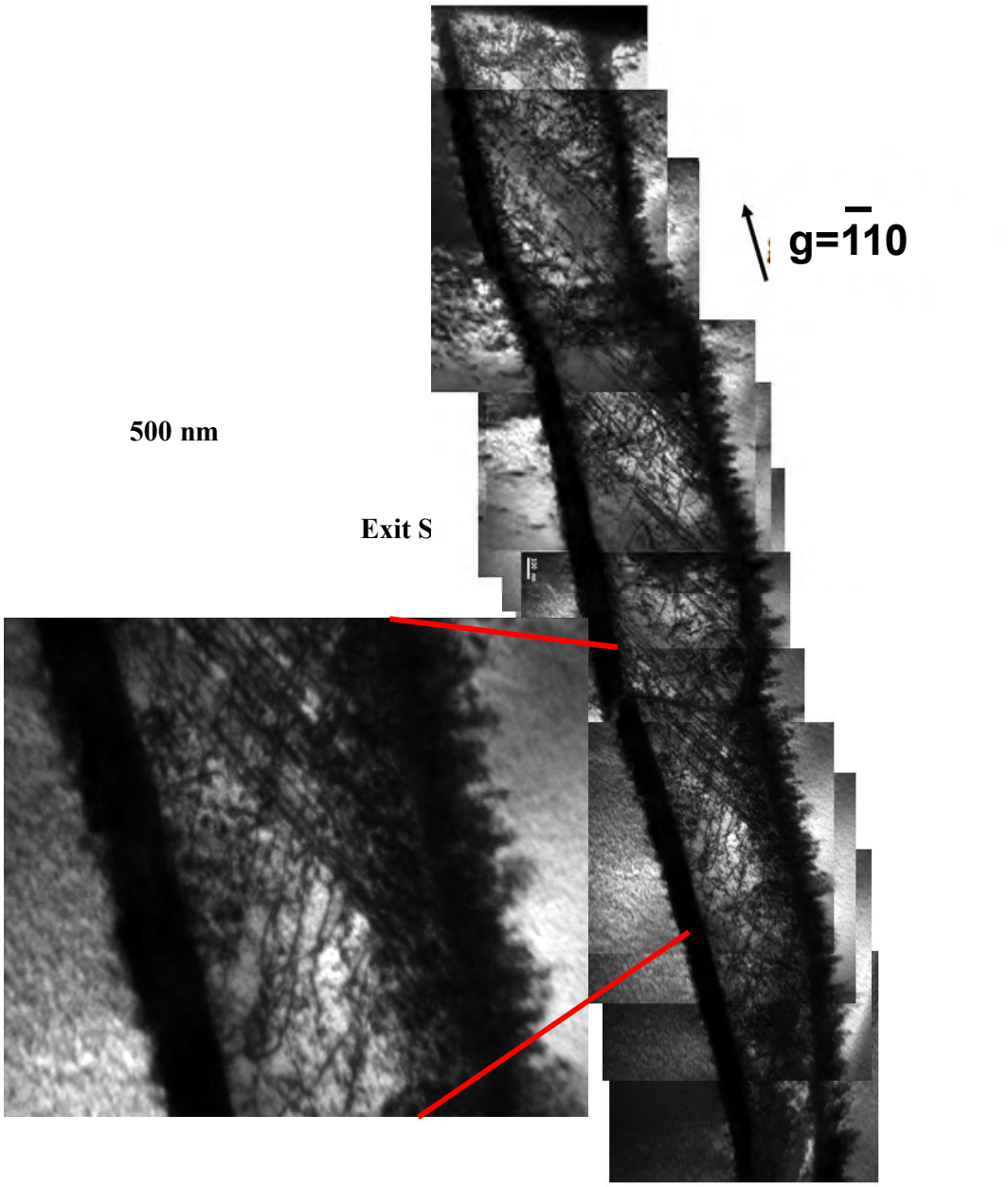

Figure 6-31 BF TEM micrographs taken with g = $\bar{1}10$ near the $[\bar{1}\bar{1}\bar{1}]$ zone axis for the pillar (D) beta phase; showing that $\mathbf{b}_4 = \frac{1}{2}[1\bar{1}1]$ and $\mathbf{b}_2 = \frac{1}{2}[\bar{1}11]$ dislocations are visible.

Figure 6-28 is a BF image of a β lath taken close to the $[\bar{1}\bar{1}\bar{1}]$ zone with a diffraction vector of $g = \bar{1}01$. With this particular vector, dislocations with Burgers vectors $b_1 = \frac{1}{2}[11\bar{1}]$ and $b_2 = \frac{1}{2}[\bar{1}11]$ are both visible. In Figure 6-28, dislocations with the b_2 Burgers vectors are visible and seem to lie on the (101) primary slip plane, depending on the relation between alpha and beta phase and the angle between them as mentioned in the previous chapters.

Figure 6-29 is a BF TEM micrograph of a beta lath taken close to the $[\bar{1}\bar{1}\bar{1}]$ zone with $g = 0\bar{1}1$. With this particular vector, dislocations with Burgers vectors $b_1 = \frac{1}{2}[11\bar{1}]$ and $b_4 = \frac{1}{2}[1\bar{1}1]$ are both visible. The dislocations which are clearly indicated by the yellow arrows in Figure 6-29 are only invisible for $g = \bar{1}01$ in Figure 6-28.

Dislocations with Burgers vectors $b_2 = \frac{1}{2}[\bar{1}11]$ are invisible with g vectors parallel to $g = 0\bar{1}1$ and $g = 110$ respectively taken close to the $[\bar{1}\bar{1}\bar{1}]$ and $[1\bar{1}\bar{3}]$ zone axes as illustrated in Figure 6-29 and Figure 6-30.

The $b_2 = [\bar{1}11](101)$ slip system has the highest resolved shear stress as listed in Table 4-2 (the Schmid factors for the different $^1/_2 < 111 > \{101\}$ slip systems). It is important to point out here that dislocations with Burgers vector $b_1 = [11\bar{1}]$ are visible with the diffraction vectors shown in Figure 6-28 and Figure 6-29. Figure 6-30 shows a micrograph close to the $[1\bar{1}\bar{3}]$ zone axis and $g = 110$.

Figure 6-31 is a BF TEM micrograph of a β lath taken close to the $[\bar{1}\bar{1}\bar{1}]$ zone with a g vector parallel to $g = \bar{1}10$. With this vector, dislocations with Burgers vectors $b_4 = \frac{1}{2}[1\bar{1}1]$ and $b_4 = \frac{1}{2}[1\bar{1}1]$ are both present.

The dislocations in the beta phases for the pillar D were colour coded. Table 6-6 lists the colour chosen for each Burgers vector.

Table 6-6 Activated Burgers vectors in the beta phase for the pillar (D).

No. of slip systems	Burgers vectors	Colour coding
1	$b_1 = \frac{1}{2}[11\bar{1}]$	Blue
2	$b_2 = \frac{1}{2}[\bar{1}11]$	Red
3	$b_3 = \frac{1}{2}[111]$	Green
4	$b_4 = \frac{1}{2}[1\bar{1}1]$	Yellow

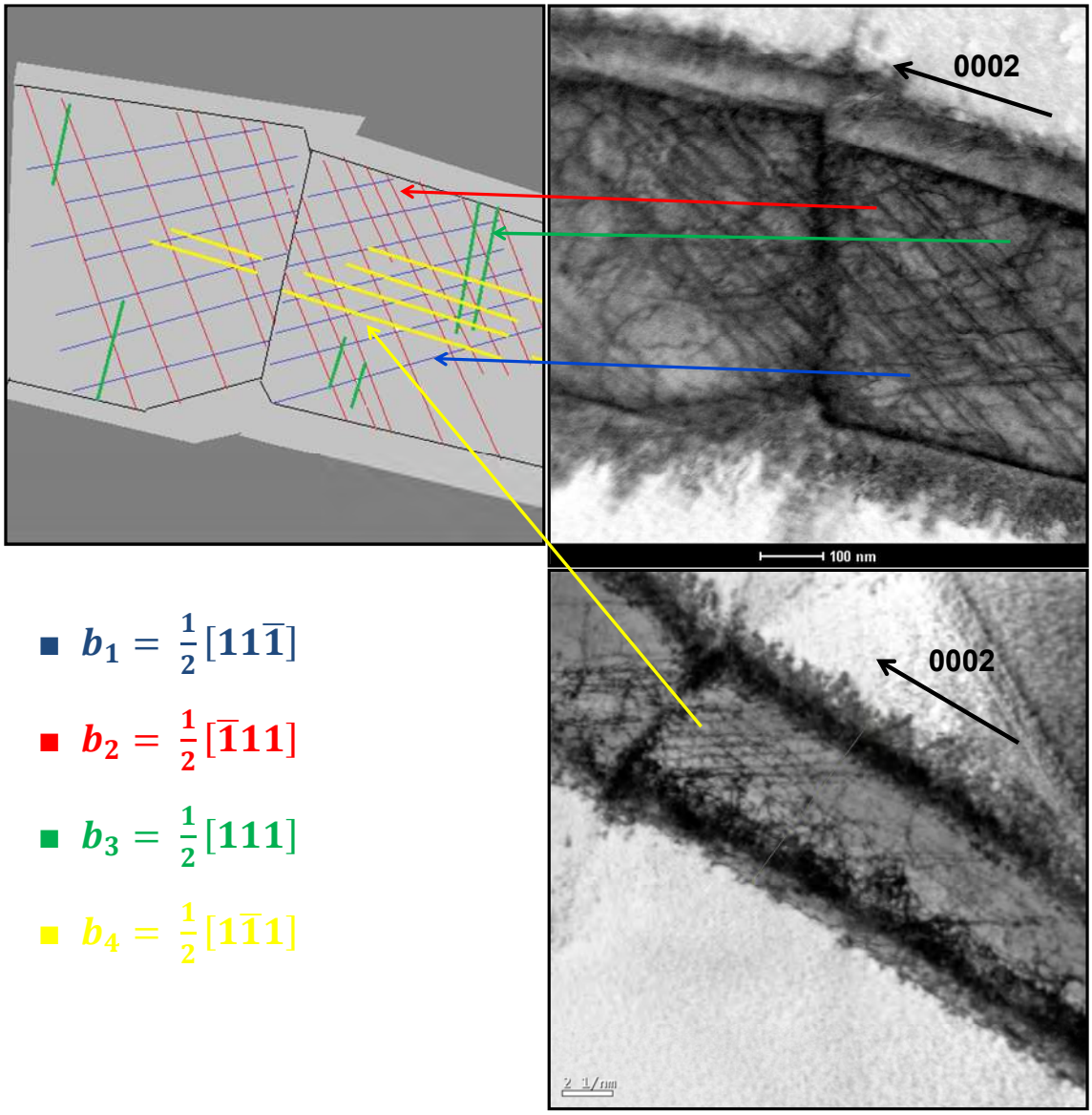

Figure 6-32 Colour coding for the dislocations in the beta phases for the pillar D. Purple arrows shows $b_2 = \frac{1}{2}[\bar{1}11]$ impinges at the alpha/beta interface (exit side).

6.2.3. Characterisation of interface

BF-images have been taken every ~ 5 degrees of tilt about g vector 0002 which is parallel to the alpha/beta interface as illustrated in Figure 6-33. Since the tilting was limited, the sample was re-inserted upside down and then the BF-image was taken at the same place as shown in Figure 6-34 below. It is observed that the beta phase gets wider and the alpha/beta interface changes with tilting from beam directions (BD) $[1\bar{2}10]$, as listed in Table 6-7.

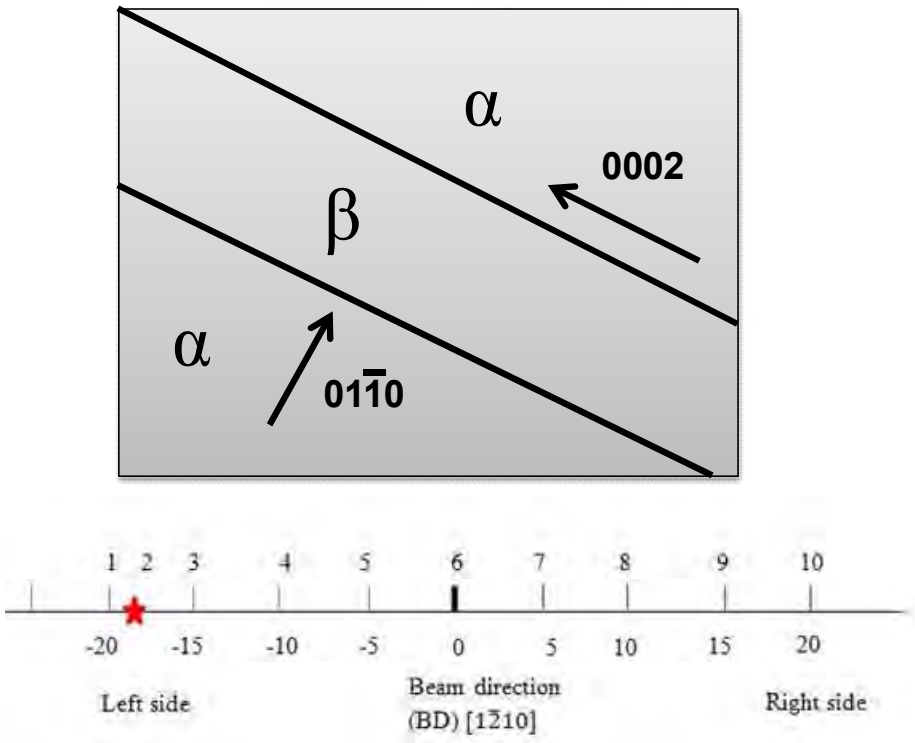

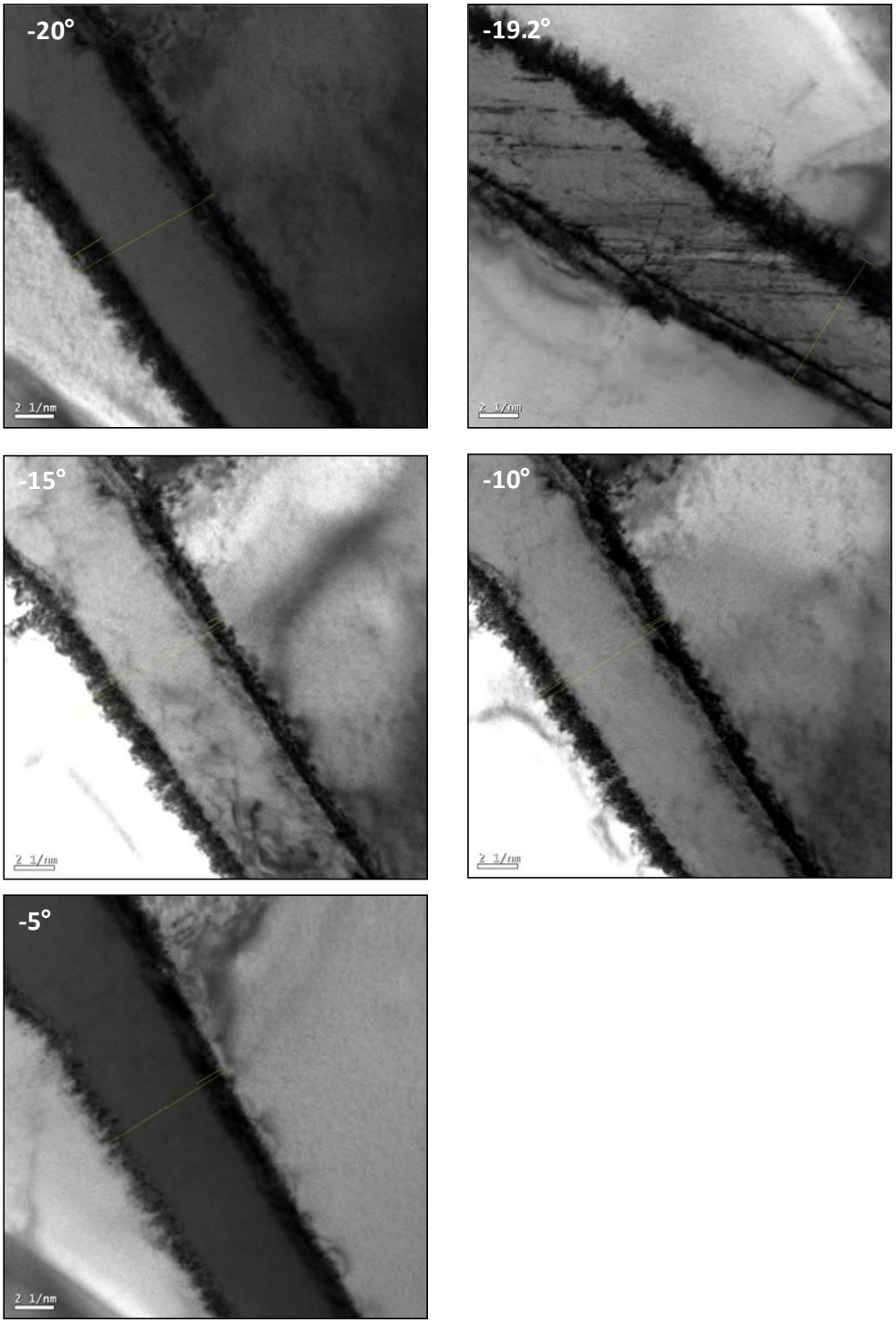

(a)

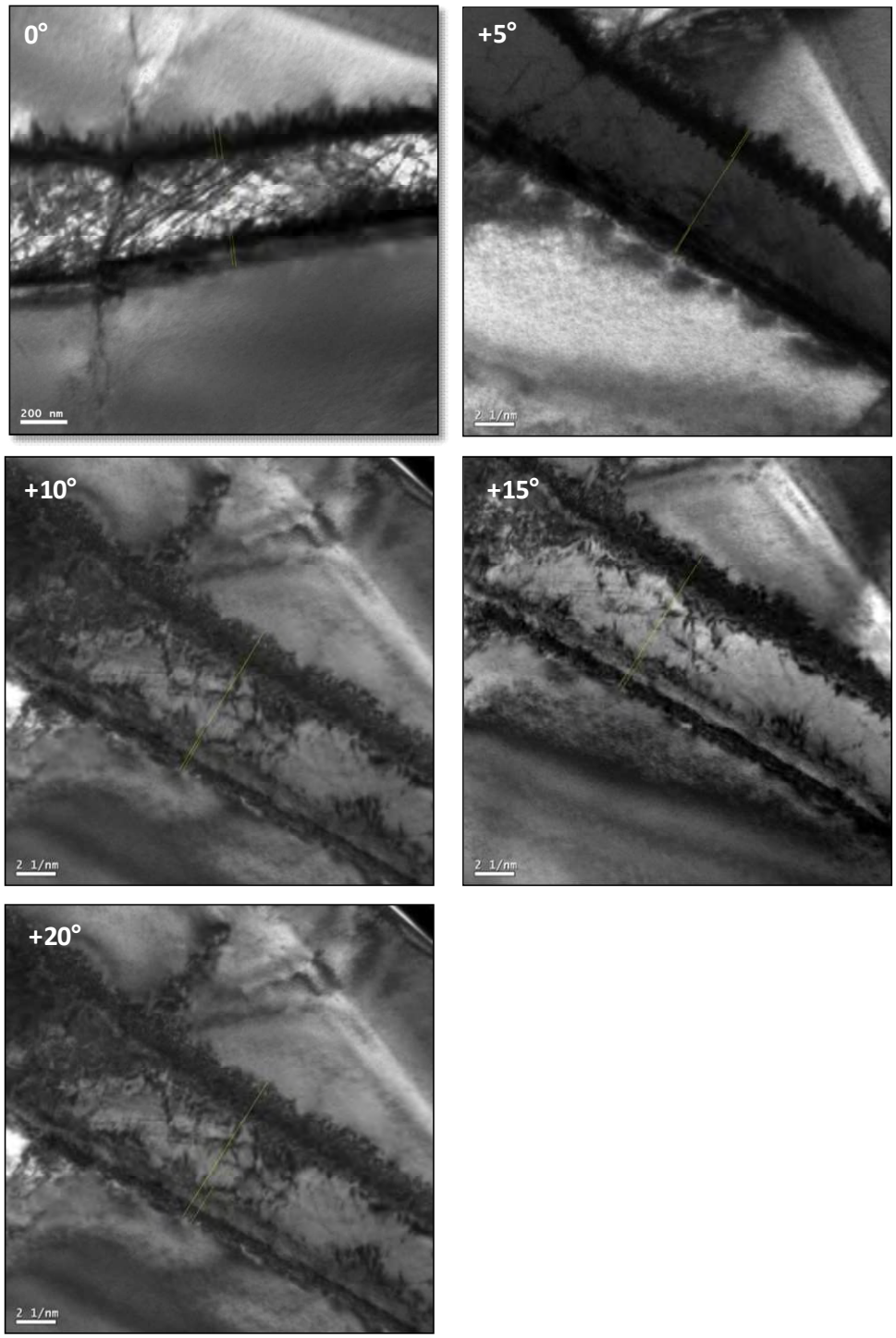

(b)

Figure 6-34 BF TEM micrographs taken with g = $01\bar{1}0$ starting tilt near the [$1\bar{2}10$] zone axis for the pillar (D) beta phase. (a) Left side based on Figure 6-33, (b) right side based on Figure 6-33 of the beam direction (BD) [$1\bar{2}10$].

Table 6-7 Width of the beta phase and the broad and side faces versus tilting angle from beam directions $[1\bar{2}10]$.

0-110 g vector parallel to Broad face	Starting from left side of BD to right side			
No.	Tilting degree	Beta phase width (nm)	Broad face width (nm)	Side face width (nm)
1	-20	779	62	193
★ 2	-19.2	-	25	205
3	-15	763	76	158
4	-11	749	81	149
5	-5	680	143	122
6	0	630	145	135
7	+5	698	144	148
8	+10	712	179	182
9	+15	766	182	215
10	+20	789	213	235

From Figure 6-34 it can be seen that the residual dislocation density in the pillar D is increased at the side face of the α/β interface which is effective in impeding slip movement as shown in the priveous figure with zero tilt angle, while slip movement in the beta phase is obstructed by exit side before crossing through the α/β interface due to the difference in the lengths of the Burgers vectors in the two planes. Thus, the observation provides further support to the slip in pillar D starting inside the alpha phase toward to the alpha/beta interface and then crossing through the beta phase to the alpha phase in the other grain leaving behind some residual dislocations at entry and exit sides.

6.3. **TEM Examination for <c+a> dislocations**

In order to the investigate activation of slip systems with the highest Schmid factor in the micropillar oriented for <c+a> pyramidal slip it is convenient to make the column direction [0001] or nearly 45° to the <c+a> Burgers vectors. A TEM specimen was therefore cut parallel to the c-axis of pillar 12 (the TEM foil cuts the slip band normally and normal to the TEM foil is close to $[12\bar{3}0]$ in fact), thus giving access to the possible $a/3 < 11\bar{2}3 >$ beam directions, which are the six possible <c+a> Burgers vectors. Such a cross-sectional analysis of a deformed <c+a> column is extremely helpful in assessing the CRSS value with cross slips in the column and comparing with the CRSS value for the <a> slip planes. A typical micro-pillar of mid-plane diameter of 4 micron and its corresponding FIB'd cross section is shown in Figure 6-35.

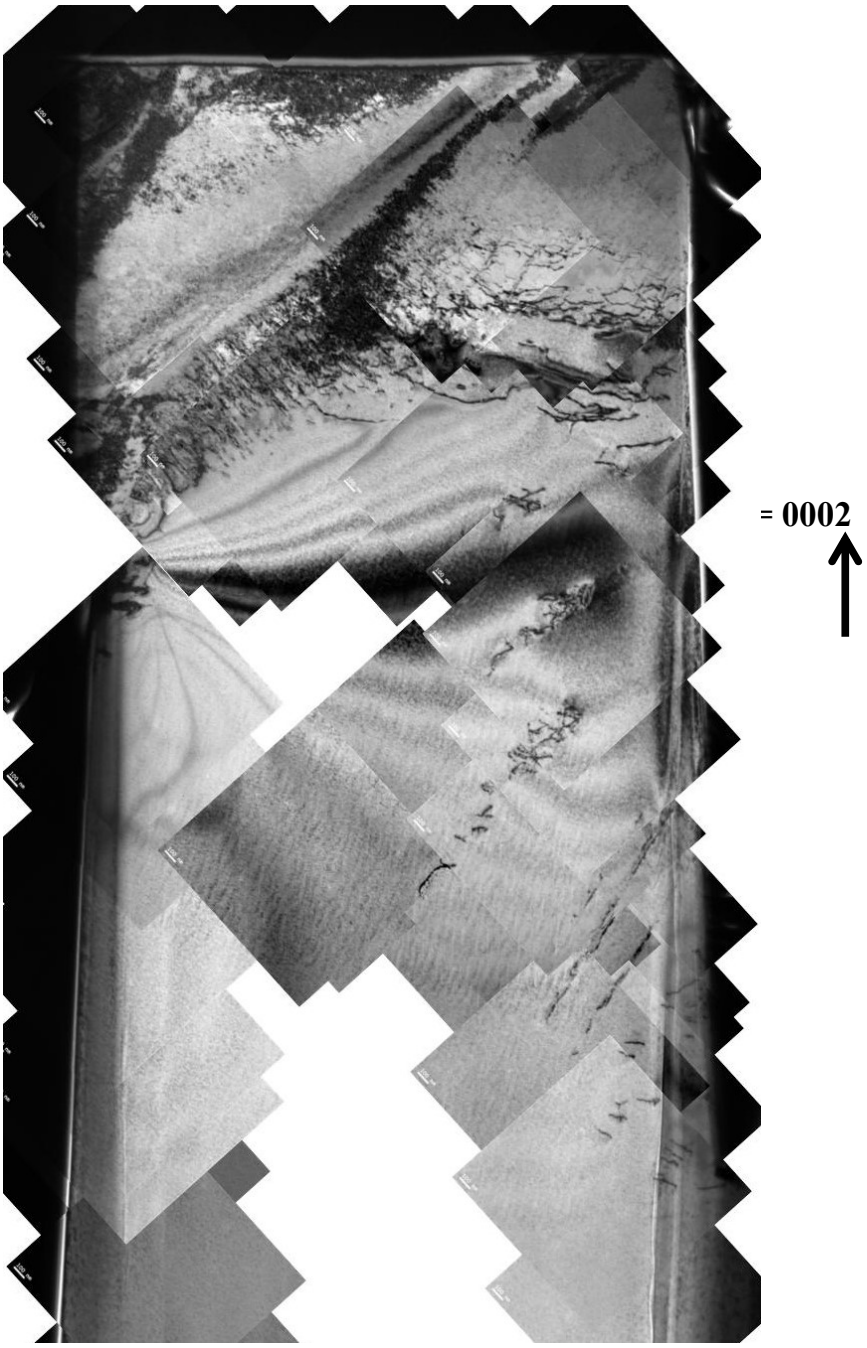

Figure 6-35 A montage of bright field TEM micrographs taken with $g = 0002$ near the $[11\bar{2}0]$ zone axis for pillar 12. (A), (B) and (C): three different slip systems.

6.3.1. Burgers vector analysis of dislocations in the alpha slip colony

The follow five different reflection micrographs (Figure 6-36 - Figure 6-41) taken from pillar 12.

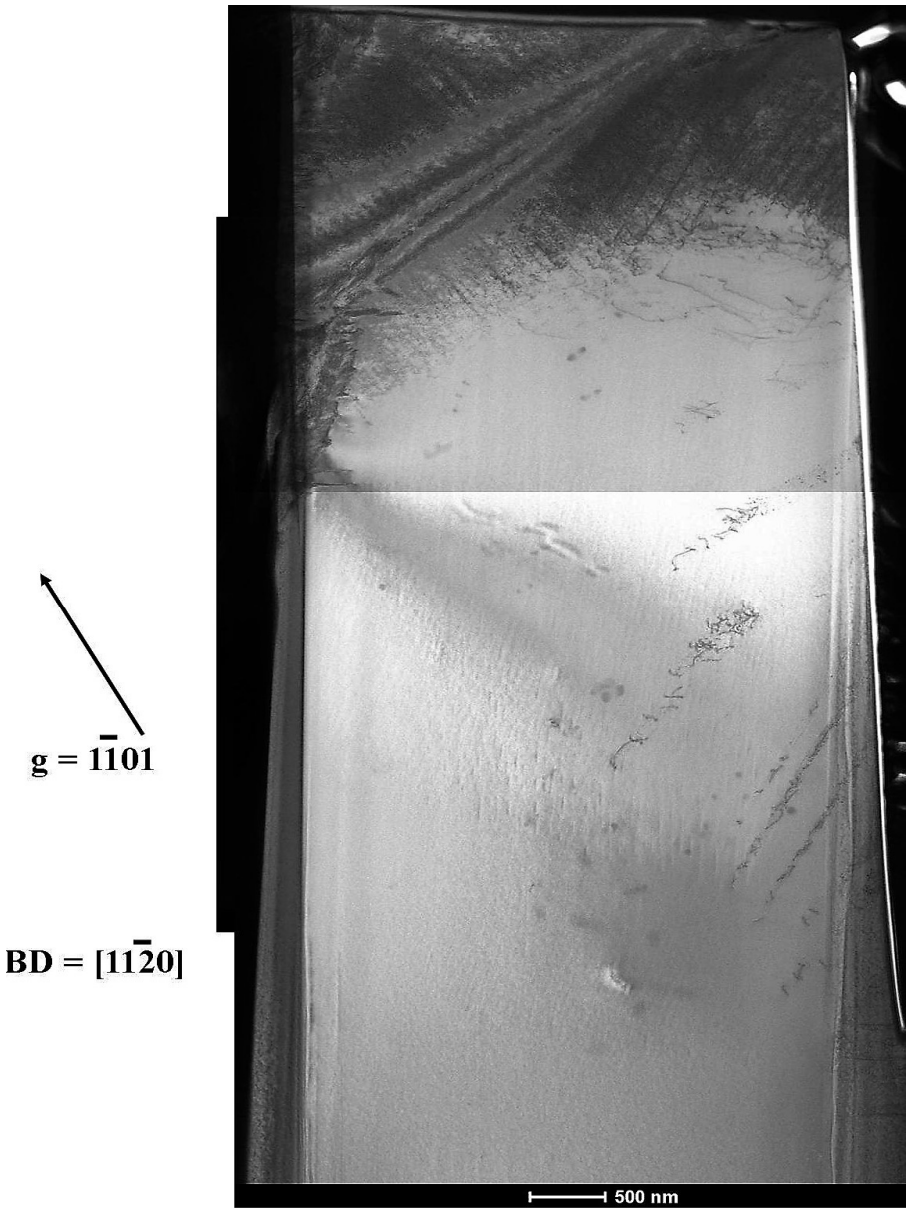

Figure 6-36 A montage of BF-STEM micrographs taken with $g = 1\bar{1}01$ near the $[11\bar{2}0]$ zone axis for pillar (12).

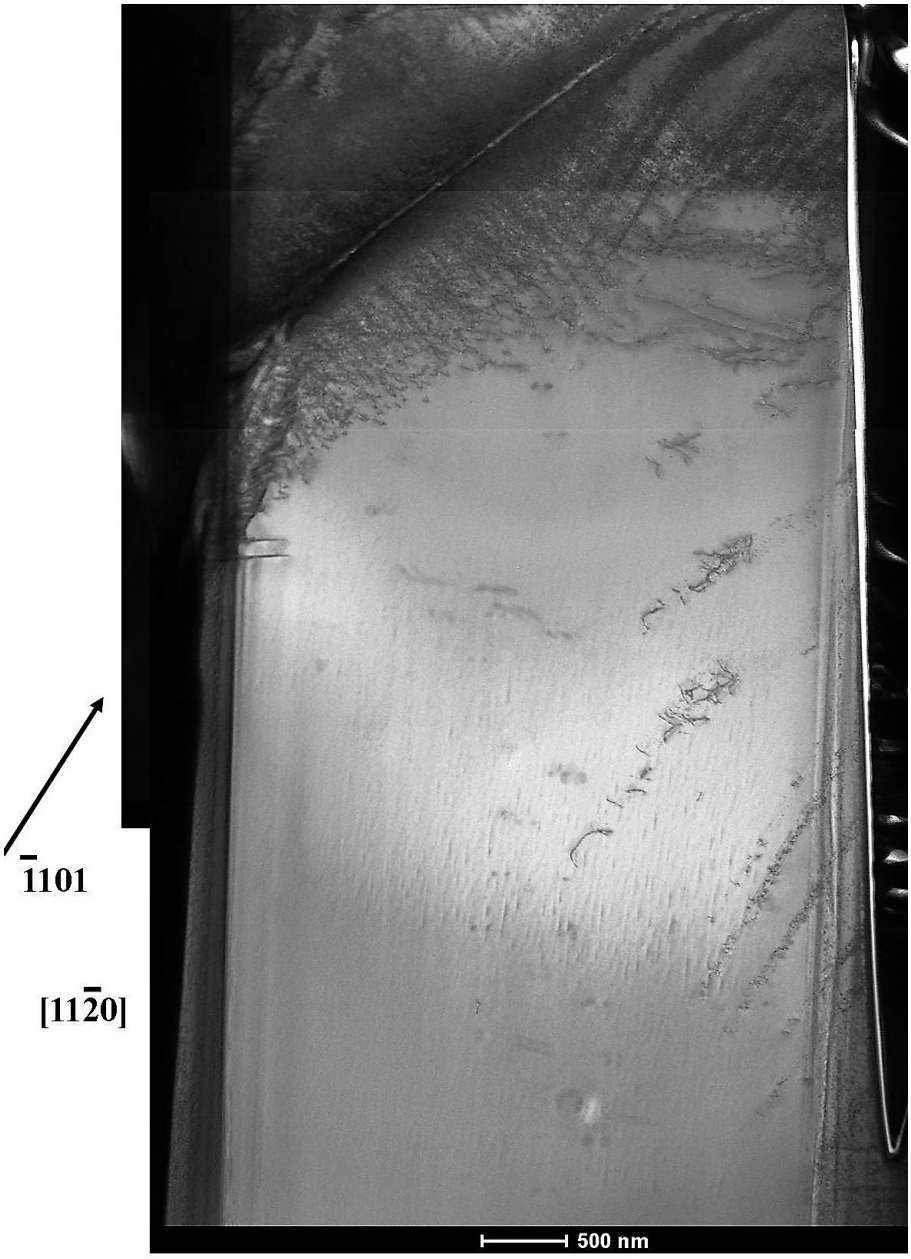

Figure 6-37 A montage of BF-STEM micrographs taken with $g = \bar{1}101$ near the $[11\bar{2}0]$ zone axis for pillar (12).

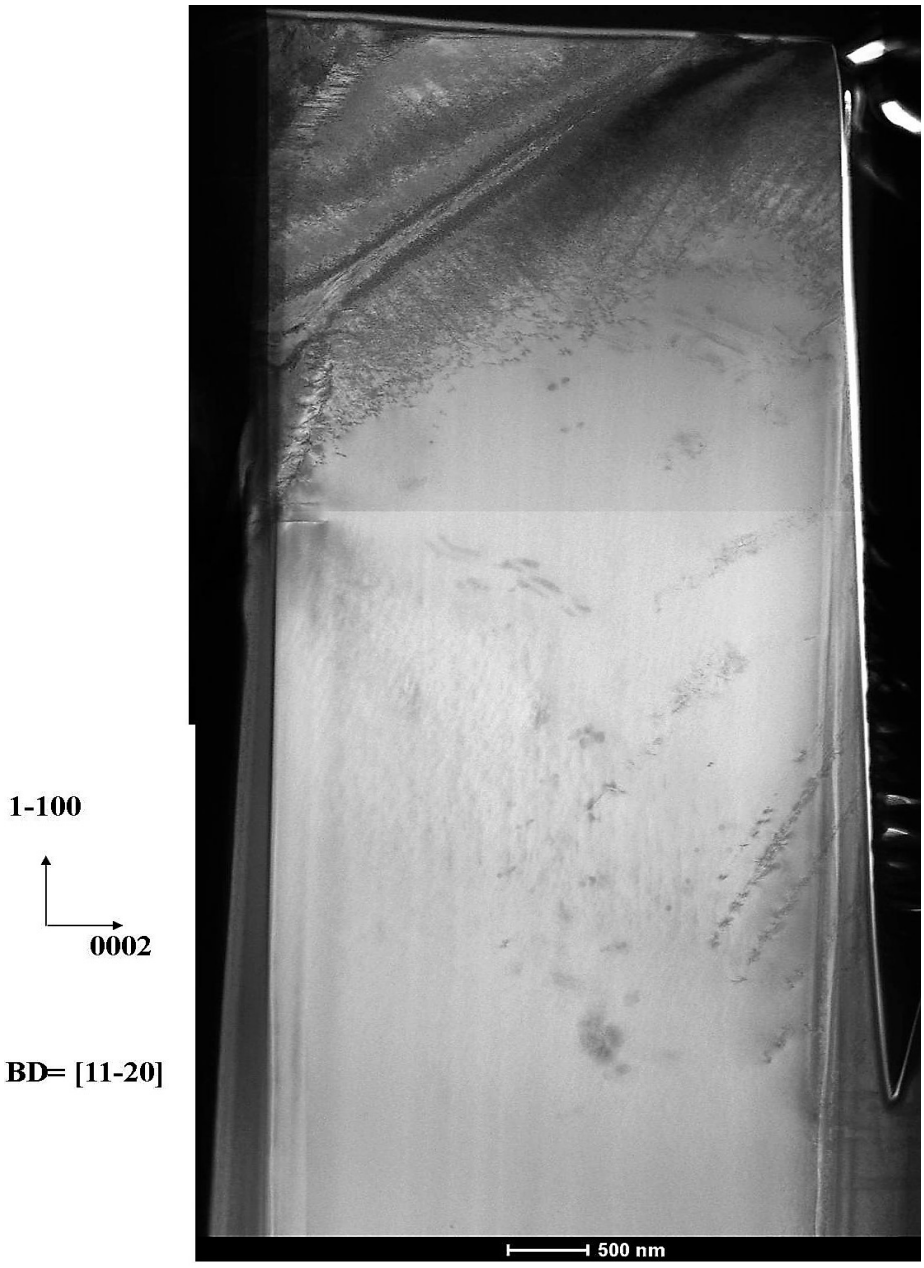

Figure 6-38 A montage of BF-STEM micrographs taken with $g = 1\bar{1}00$ near the $[11\bar{2}0]$ zone axis for pillar (12).

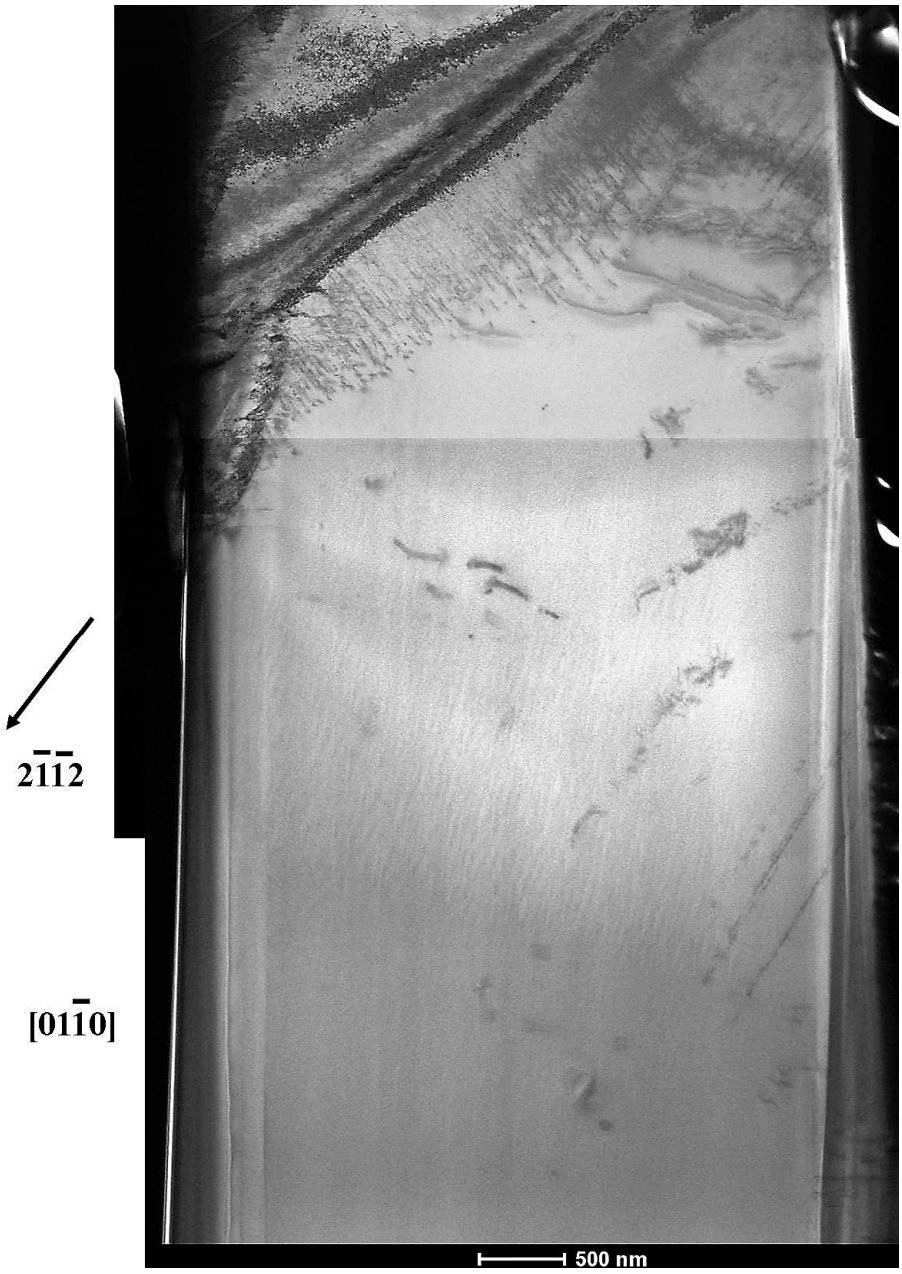

Figure 6-39 A montage of BF-STEM micrographs taken with $g = 2\bar{1}\bar{1}2$ near the $[01\bar{1}0]$ zone axis for pillar (12).

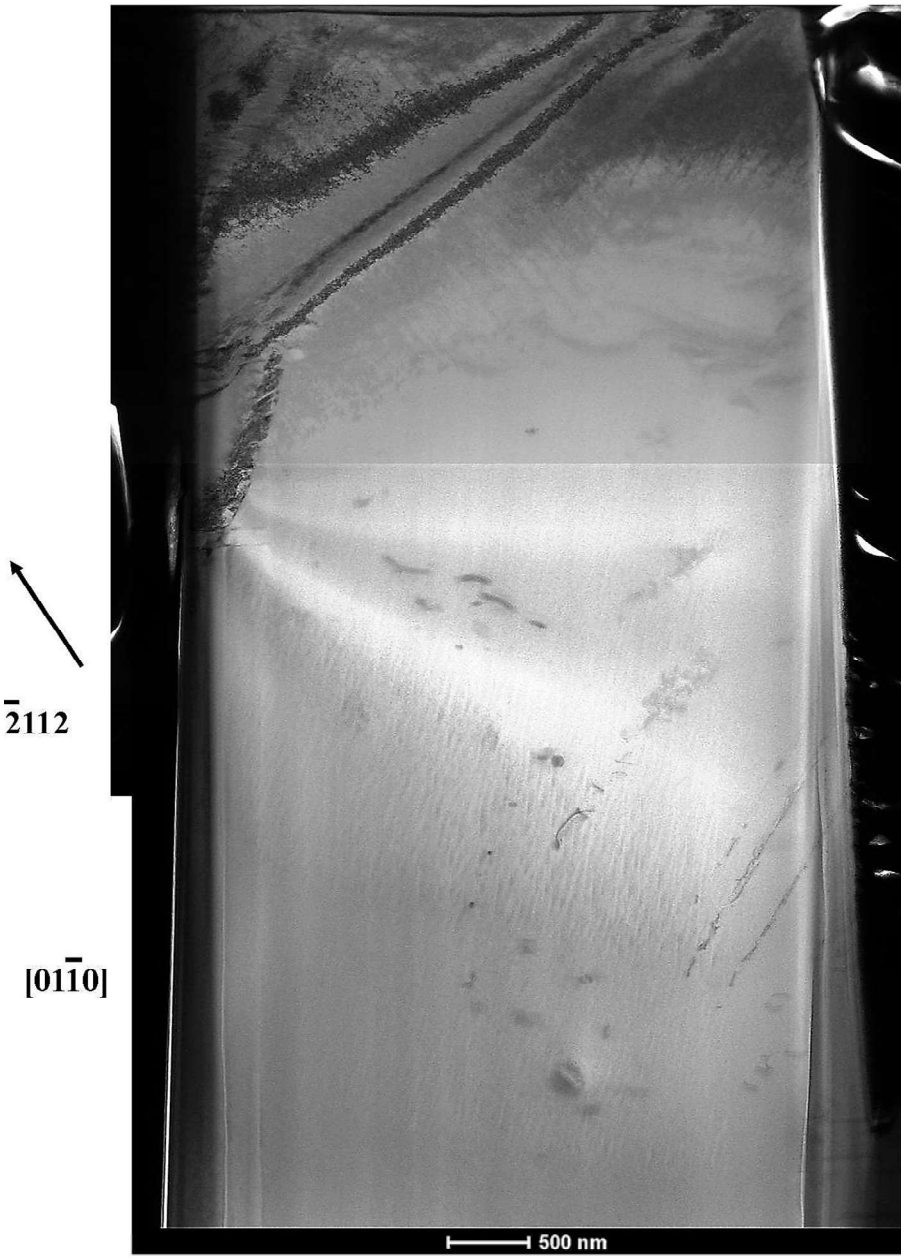

Figure 6-40 A montage of BF-STEM micrographs taken with $g = \bar{2}112$ near the $[01\bar{1}0]$ zone axis for pillar (12).

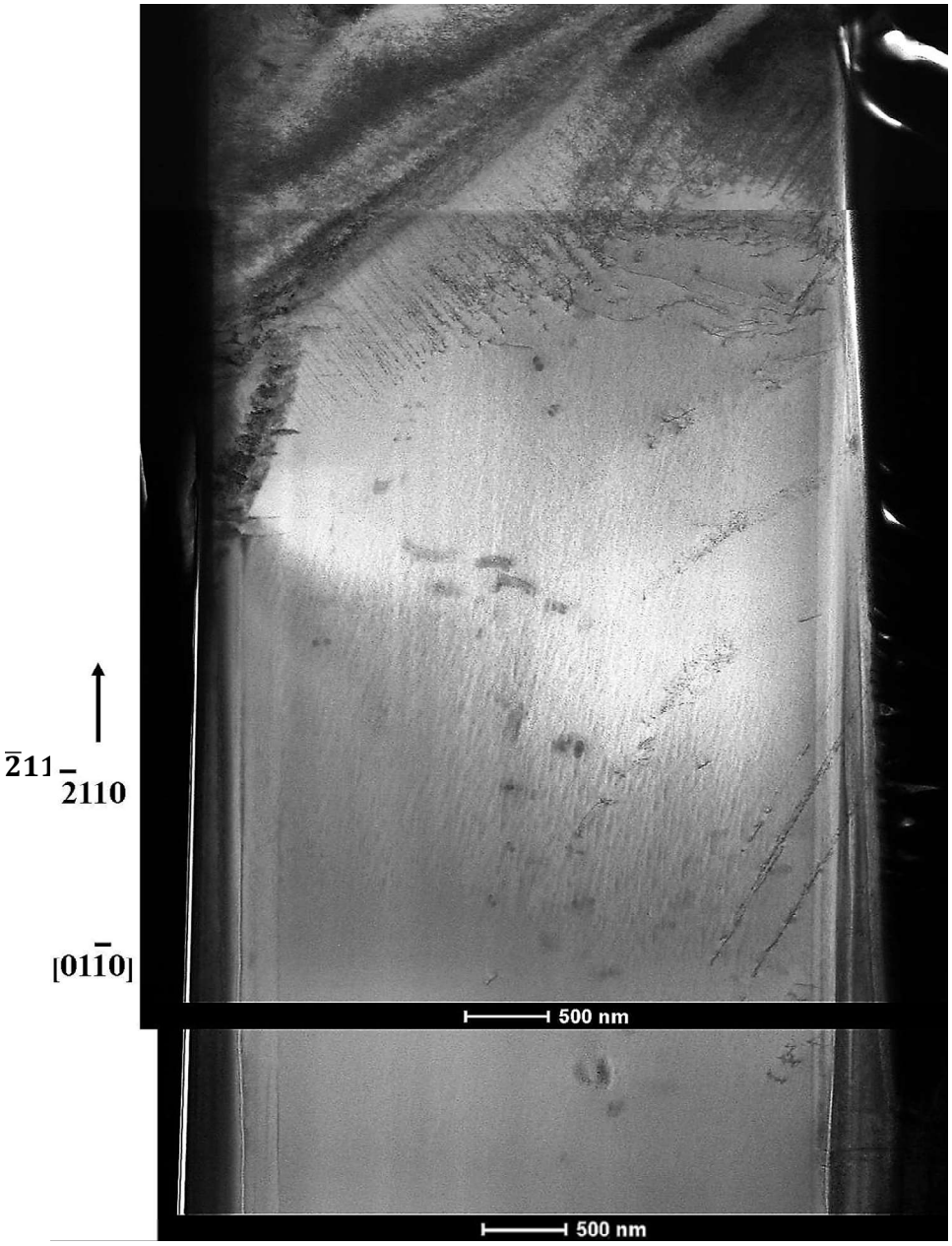

Figure 6-41 A montage of BF-STEM micrographs taken with $g = \bar{2}110$ near the $[01\bar{1}0]$ zone axis for pillar (12).

The dislocations shown in Figure 6-35 must be <c+a> dislocations. Figure 6-36 provides an example of the invisibility for the dislocations in the region (A) of dislocations shown in Figure 6-35. That indicates that the dislocations in the region (A) have Burgers vectors $b = \frac{1}{3}[\bar{1}2\bar{1}3]$ and $b = \frac{1}{3}[\bar{2}113]$. Figure 6-37 shows a bright field STEM micrograph taken with g = $\bar{1}101$ near the beam direction $[11\bar{2}0]$. With this particular g vector, dislocations in the region (A) with Burgers vectors $b = \frac{1}{3}[\bar{1}2\bar{1}3]$ and $b = \frac{1}{3}[\bar{2}113]$ are both visible. However, dislocations with Burgers vectors $b = \frac{1}{3}[\bar{2}113]$ are visible in Figure 6-39. Therefore, the only possible Burgers vectors for the dislocations in the region (A) is $b = \frac{1}{3}[\bar{1}2\bar{1}3]$.

Figure 6-39 shows micrographs with g vectors $2\bar{1}\bar{1}2$. With this reflection, dislocations in the region (B) are invisible, thus the dislocations in the region (B) have Burgers vectors $b = \frac{1}{3}[\bar{2}11\bar{3}]$. The dislocations in the region (C) are invisible in the reflection vector $g = 1\bar{1}00$ as shown in Figure 6-38. Therefore, dislocations in the region (C) have one of two Burgers vectors $b = \frac{1}{3}[11\bar{2}3]$ and $b = \frac{1}{3}[11\bar{2}\bar{3}]$, while Figure 6-39 shows $g.b$ for $b = \frac{1}{3}[11\bar{2}\bar{3}]$ is not equal to ±3 like Burgers vectors $b = \frac{1}{3}[11\bar{2}3]$ (see Ref. [118] for details). As a result, this suggests that $b = \frac{1}{3}[11\bar{2}3]$ is the Burgers vector for dislocations in the region (C).

6.3.1.1. Identification of slip planes

All the alpha phase dislocations were in contrast with $g = 0002$ (Figure 6-35). This indicates that the dislocations were <c+a>. In order to identify the slip planes, a line approaches have been used (see section 6.2.2.2).

Based on Figure 6-35, the true direction for <c+a> dislocations in the area (A), was obtained then by cross product between project of dislocation in two different g vectors and in two beam direction $[01\bar{1}0]$, $[11\bar{2}0]$, respectively. Then, cross product between the Burgers vector $\frac{1}{3}[\bar{2}11\bar{3}]$ and normal to both lines were getting the slip plane. Dislocations in the area (B) are edge on therefore, the slip plane for dislocations is ~ $(\bar{1}011)$; also it has been confirmed the angle between dislocations (A) and (B) is equal to ~ 60°. Finally, the slip plane for dislocations in the area (C) was $(0\bar{1}11)$, which contains the Burgers vector $\frac{1}{3}[11\bar{2}3]$ and normal to the true direction. The operative slip systems in the samples that were analysed are presented in Table 6-8.

Table 6-8 Summary of the results obtained from the <c+a> dislocations analyses in the alpha phase for pillar 12 using different diffraction conditions (see Figure 6-35 to Figure 6-41)

Beam direction	g vector	Slip system $\mathbf{1/3[\bar{1}2\bar{1}3](1\bar{1}01)}$	Slip system $\mathbf{1/3[\bar{2}113](\bar{1}011)}$	Slip system $\mathbf{1/3[11\bar{2}3](0\bar{1}11)}$	Figures
$[\mathbf{11\bar{2}0}]$	0002	V	V	V	Figure 6-35
	$1\bar{1}01$	I	V	V	Figure 6-36
	$\bar{1}101$	V	I	V	Figure 6-37
	$1\bar{1}00$	V	V	I	Figure 6-38
$[\mathbf{01\bar{1}0}]$	$2\bar{1}\bar{1}2$	V	I	V	Figure 6-39
	$\bar{2}112$	V	V	V	Figure 6-40
	$\bar{2}110$	V	V	V	Figure 6-41

6.4. **Summary**

1. In the undeformed specimen the dislocation density was $1.2 \times 10^{13} \mathrm{m}^{-2}$ in the alpha phase and $2.7 \times 10^{16}\ \mathrm{m}^{-2}$ in the beta phase.

2. The two slip bands for pillar D (basal slip) corresponding to those seen in the SEM could clearly be seen in the TEM.

3. The slip plane was confirmed as basal overall, with one excursion due to cross-slip.

4. The distribution of dislocations along the slip plane was homogeneous.

5. The <a> basal slip sample orientation incorporates a significant misorientation between the $\mathrm{a}/3[1\bar{2}10]$ and $\mathrm{a}/2[\bar{1}11]$ slip vectors (11.5° and a 5.2% mismatch in magnitude). Large $a/2 < 111 >$ dislocation pileups were observed on the (101) primary slip plane and (211) cross slip planes within the beta laths in TEM foils prepared from the a_2 basal slip sample.

6. The major Burgers vector was a_2 (from Figure 6-21). This is consistent with the highest Schmid factor (see Table 4-1). Therefore, SEM and TEM observations support the significance of the Schmid factor. Close to the alpha/beta interfaces, there are small, non-planar distributions of a_1 dislocation which react with the next dislocation to form a_3 at the exit side.

7. TEM observations also indicate that the screw component of the dislocation near the exit side of the alpha/beta interface cross-slips onto the $(1\bar{1}01)$ pyramidal slip plane. The waviness of the slip represents the path of screw dislocations and the waviness suggests that screw dislocations undergo a number of cross-slip events. In Figure 6-25

a_2 dislocations along the alpha/beta interface are observed to lie on the pyramidal plane providing further support for the cross-slip mechanism.

8. The dislocations tend to be screw then their tendency to follow the alpha/beta interface.

9. In the β phase the dislocations were of all four types (fig. 6-32). Most of them were not obviously to do with the two slip bands.
10. The heavily dislocated interfaces were on the entry side face and exit broad face.
11. <c+a> dislocations have been analysed successfully.
12. The cross-slip dislocation nascent in the alpha phase provides further supports to the CRSS value for <c+a> slip on the pyramidal planes for the Ti alloys is higher than <a> basal and prismatic planes.
13. The observation of cross-slip <c+a> dislocations on the first order pyramidal planes supports the orientation size effects and close slip bands on the surface of the pillar.
14. Direct correlation between the SEM micrographs of pillars and TEM prepared with a FIB (which was discussed in Chapter 4) was possible for the slip lines on the samples.

Chapter Seven

7. Discussion

7.1. Introduction

This chapter will discuss how the evolution of the dislocation structure is responsible for the micromechanical properties. Section 7.2 describes the mechanisms governing or contributing to the size effect observed in micro-compression experiments. Section 7.2.1 to 7.2.5 discusses the deformation of the single and tri-crystals at constant strain rate. Section 7.3 and 7.5 describes the characterization of the slip traces and slip steps using SEM. Section 7.6 details the characterization of the dislocations in the alpha and the beta phases of the pillar using transmission electron microscopy. In particular, section 7.6.3 discusses a possible mechanism of slip transmission, based on experimental observations, across the alpha/beta interface for the two colony crystals. Lastly, section 7.7 describes the characterization of the <c+a> dislocation.

7.2. Micromechanical results: the anisotropy and the strength of the α/β interface

The samples were oriented to activate single slip in the alpha phase by orienting specific samples to have the highest Schmid factor for the particular system.

The CRSS data reported is determined from the proportional limit of the stress-strain curves where the onset of plasticity likely occurs or exactly from the proof stresses for the three different orientations. The elastic slope in the micropillars is commonly measured to be lower than the bulk Young's modulus, due to the uncorrected stiffness of the load frame, dislocation removal from the free surfaces and any slight misalignment between the sample and the nanoindenter tip [119].

From the CRSS data obtained from the deformation of Ti64 alpha and beta single phase crystals and alpha/beta/alpha tri-crystals described in Chapter Four one can make three key observations (as will be discussed in the following sections): (a) the CRSS for the <a> type vectors is different for each orientation for both alpha single phase crystals and alpha/beta/alpha tri-crystals, (b) the CRSS values in <a> alpha/beta/alpha tri-crystals are larger than those for single alpha phase crystals, and (c) <c+a> single phase crystals have a higher CRSS than <a> and <c+a> alpha/beta/alpha tri-crystals: this is discussed in detail this in section.

The mechanical properties within the alpha–beta colonies, single alpha and beta phase have been measured to elucidate the role of the alpha/beta interfaces in determining critical resolved shear stress. For <a> slip the alpha/beta interfaces cause a higher critical resolved shear stress in the expected slip system compared with the single alpha phase, so the alpha/beta interfaces within these colonies were considered to hinder to slip. In spite of the very close crystallographic orientations of the different microstructural elements (alpha and beta), the effectiveness of the beta laths in restricting slip motion is very obvious, and thereby

the strength is increasing. The results obtained from the mechanical analysis are shown in Table 7-1.

Table 7-1 Mechanical data for compression of alpha/beta/alpha, alpha and beta micro-pillars.

Type of slip in α	Specimen	Diameter of pillar (μm)	Proof stress (MPa)	CRSS (MPa)	Comments
Basal <α>	α/β/α	2	897	422 ± 5	CRSS for α phase
		4	843	396 ± 15	
		5	802	375 ± 10	
		6	767	360 ± 5	
	α	1	923	433 ± 10	
		2	865	407 ± 10	
		3	820	385 ± 5	
		4	779	366 ± 10	
		5	752	353 ± 10	
	β	1	854	418	CRSS for β phase assuming {110} slip corresponding to largest Schmid factor
		2	760	372 ± 8	
Prismatic <a>	α/β/α	2	782	336 ± 20	CRSS for α phase
		4	700	301 ± 15	
		5	653	278 ± 5	
		6	627	269 ± 5	
	α	1	790	340 ± 5	
		2	727	312 ± 15	
		3	666	282 ± 5	
		4	626	268 ± 10	
		5	575	247 ± 3	
	β	2	687	302 ± 10	CRSS for β phase assuming {110} slip corresponding to largest Schmid factor
Pyramidal <c+a>	α/β/α	2	1969	888 ± 10	CRSS for α phase
		3	1820	821 ± 20	
		4	1684	770 ± 20	
		5	1558	702 ± 10	
		6	1398	630 ± 10	
	α	2	2346	1057 ± 15	
		3	2082	938 ± 15	
		4	1953	880 ± 20	
	β	1	989	446 ± 10	CRSS for β phase assuming {110} slip corresponding to largest Schmid factor
		2	867	391 ± 20	

7.2.1. Size effects

Many efforts have been made to understand the specimen size effect for the different slip systems in FCC and BCC [14, 15], with morphology and orientation of the crystal controlled. In reviewing the literature, according to our current knowledge, no data was found on the association between size effect and orientation in HCP, Ti or Ti alloys.

Interestingly, the evolution of the flow stress at 0.2% strain, as a function of micropillar diameter, is plotted in Figure 4-44 and Figure 4-45. The plots show a noticeable size effect on the mechanical response for all the micro-pillars tested. The CRSS is found to follow a power law relationship as shown in Table 7-2. From Figure 4-44 and Figure 4-45, we can see that the CRSS is inversely dependent on the pillar diameters, which therefore could be summarised as "smaller is stronger".

Table 7-2 Summary of orientation size effects for the basal, prismatic and pyramidal planes for single crystal α phase and tri-crystal α/β/α phase .

Type of slip in α	Specimen	σ_0	n
Basal <a>	α/β/α	992	0.132
	α	935	0.130
Prismatic <a>	α/β/α	903	0.194
	α	805	0.192
Pyramidal <c+a>	α/β/α	2458	0.290
	α	2822	0.271

The research community agrees upon the nature of the operative dislocation sources in the micron-sized samples as single-armed spirals and that there is an effect due to the sample volume. Several sources have reported spiral dislocation sources in a number of *in-situ* TEM deformation investigations [120,121].

As a few emitted dislocations still remain in the large pillars, they need less stress to achieve deformation. Contrarily, small pillars are less likely to contain existing dislocations or sources, meaning that it is more likely that fresh nucleation is required before any plastic deformation can occur.

The dislocation sources can readily be truncated by the free surfaces in the 1 μm pillars for single phase and the 2 μm pillars for alpha/beta/alpha pillars; they are unlikely to serve as dislocation sources and thus smaller pillar takes a longer time than a larger pillar to generate dislocations which restricts the deformation response.

Furthermore, increasing sample size leads to an increase in the probability of dislocation interactions inside the pillar: in other words, the free surfaces have less influence on the plastic flow of the larger samples.

As reported by Volkert and Lilleodden [87] the apparent strain hardening rate for Au single crystals increases strongly with decreasing column diameter, following a power law trend.

They suggest that the dislocation density decreases with decreasing sample volume due to dislocation starvation and that therefore more stress is needed to nucleate or activate new dislocation sources inside the pillar. The current study supports these observation.

The findings of the current study are also consistent with those of Gong and Wilkinson [12,62] and Sun *et al*. [122] who found that Ti and Ti64 microcantilievers and single crystalline Ti micropillars, respectively, oriented for prismatic slip are prone to size effects. These results differ from those of Byer *et al*. [102] who reports no size effect for microcompression testing of [0001] Mg, but they are broadly consistent with Lilleodden [95], who concurrently published the results of similar compression experiments on Mg [0001] oriented micropillars. Lilleodden showed a size effect in the flow stress, while no size effect was found for strain hardening [95]. Thus the two groups report diametrically opposite size-dependent strengths and there is therefore a need to examine the size effect for (HCP) Ti-6Al-4V.

From the data in Figure 4-44 and Figure 4-45, in comparison with BCC Mo [9] and FCC pillars [11], it is apparent that the power law exponent for HCP is less pronounced. The power law exponent (n) for the FCC and BCC studies are in the range of -0.6 to -0.9 [11] and -0.4 to -0.8 [9], respectively, significantly steeper than observed for Ti64; this is clearly shown in Figure 4-44 and Figure 4-45. It has been recognized that HCP materials (Ti-64) become less size-sensitive to the flow stress than BCC and FCC materials. This lead to the (n) power law exponent for HCP is less pronounced than BCC and FCC materials.

The sample oriented for pyramidal <c+a> slip achieves a considerably higher power law exponent (n) compared to the other orientations (prismatic and basal slip), as shown in Figure 4-44. The reasons for the difference in the power law exponent (n) between the three orientations are suggested to be as follows:

1. Basal <a> plane: the $[\bar{1}5\bar{4}6]$ pillars exhibited primarily single slip along a preferred <a> slip system.

2. Prismatic <a> plane: the $[01\bar{1}0]$ micropillars were cut from a grain, which had the possibility to activate two prism planes with 120° between each other in the pillars. The pillars oriented for prismatic slip were aligned so that two prismatic planes were at ±60° to the loading directions, and so were both subjected to the same maximum shear stress.

3. Pyramidal <c+a> planes: compression along [0001]: such a high symmetry orientation activates multiple non-parallel slip systems, which would lead to a relatively homogeneous deformation, non-localized deformation, and high flow stresses.

The difference power law exponents for each of the three orientations could be related to activation of single or multiple slip planes. For example, for basal slip, one slip system is preferred and for compression along [0001] six c+a systems are equally favoured.

Another possible reason for the different power law exponents for the basal, prismatic and pyramidal planes micropillars is in to terms of Peierls stresses [123] or temperatures [124]. Peierls stress decreases with increasing distance between atomic planes, because it depends on

the size and width of a dislocation and the distance between the planes. Lee *et al*. [125] also reported that as the friction stress (his terminology) is higher, the power-law exponent is lower. Rao *et al* [126], identify the dislocation density as an important parameter affecting the power law exponent since the operation stress of the weakest single arm dislocation sources depends on the initial dislocation density [126].

It can be seen from the data in Table 7-2 that the (n) power law exponent for alpha/beta/alpha phase is higher than a single alpha phase for three different planes, which is affected by the presence of the beta phase. However, the basal and prismatic planes are less sensitive size effect regards to the <c+a> pyramidal plane, thus the difference (n) value in the pyramidal plane is higher than the basal and prismatic planes.

This finding is consistent with the findings of the previous studies by Schneider *et al.* [9,10], which focus on the effect of BCC crystal structure on the size effect, through compression testing of [001] and [235] Molybdenum (Mo) small scale pillars. On the other hand, this is surprising; as similar multiple orientation studies in FCC of the sample size effect on FCC does not show sample orientation dependency [11]. In addition, the exponents from a power law expression caused by the size effect for alpha/beta/alpha prismatic slip (- 0.194) is also accords with earlier observations by Gong and Angus [12], who showed that the power law exponent for prismatic slip is equal to (- 0.21).

To conclude, in our study, the compression experiments exhibited a strong size effect on the flow stress. All the micro-pillars tested were found to follow a power law relationship which is also in agreement with the model of Taylor-type interaction mechanisms. The strength of the pillars correlates well with the dislocation interaction increasing as the sample size is increased, which considers the increase in the CRSS value due to the interaction of dislocations at the interface or via cross-slip to another slip system. Small pillars cannot trap dislocations effectively, but an capable of producing a significant strengthening effect, suggesting that dislocation nucleation in a small size of the pillar is more difficult than for larger sizes.

7.2.2. Anisotropy

Typical stress-strain curves for microcompression of (α/β/α) and (α) pillars for three different directions are shown in Figure 7-1. This should give an insight into the anisotropy of the materials. Strength differences were observed between <a> prismatic, <a> basal and <c+a> pyramidal slip for thealpha and alpha/beta/alpha pillars. The yield and flow strengths for the prism and basal orientations are close to each other, while the pyramidal <c+a> slip shows a much greater yield strength. Slip line analysis using SEM confirmed that single basal and prism slip systems were dominant for these two crystal orientations, while for the [0001] orientation, multiple <c+a> slip occurs on first-order pyramidal planes [13].

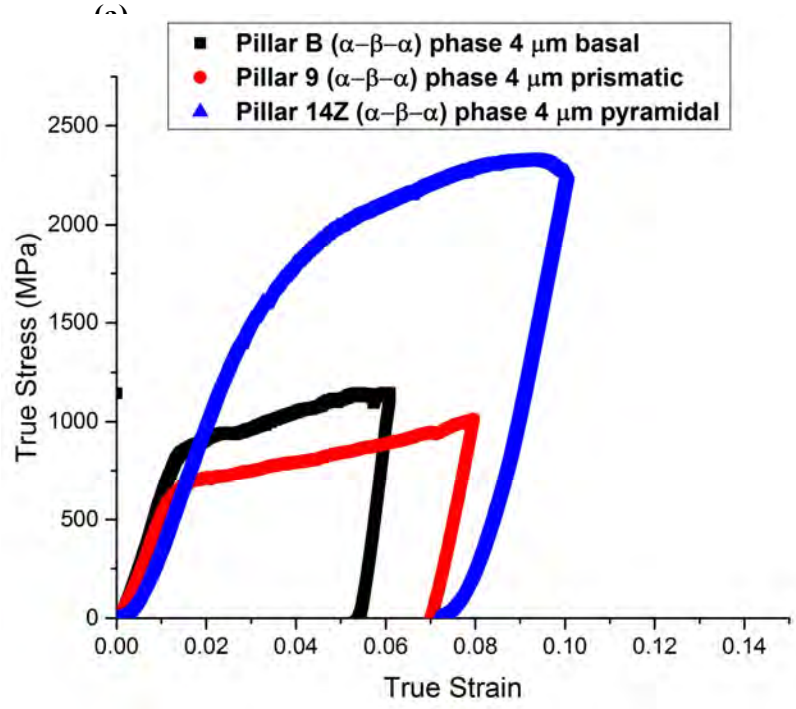
Pillar B (α–β–α) phase 4 μm basal
Pillar 9 (α–β–α) phase 4 μm prismatic
Pillar 14Z (α–β–α) phase 4 μm pyramidal
True Stress (MPa)
True Strain
0
500
1000
1500
2000
2500
0.00
0.02
0.04
0.06
0.08
0.10
0.12
0.14

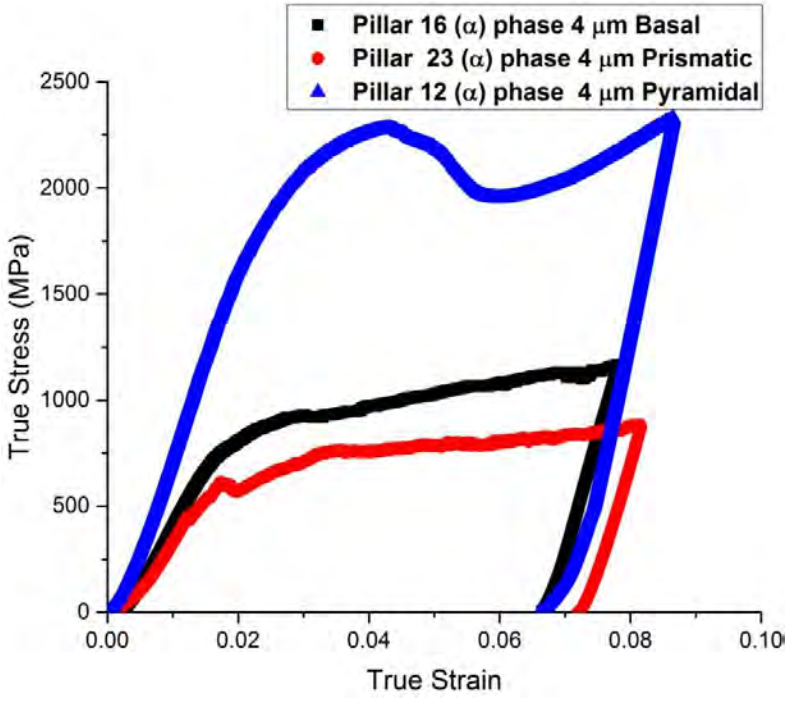
Pillar 16 (α) phase 4 μm Basal
Pillar 23 (α) phase 4 μm Prismatic
Pillar 12 (α) phase 4 μm Pyramidal
True Stress (MPa)
True Strain
0
500
1000
1500
2000
2500
0.00
0.02
0.04
0.06
0.08
0.10

Figure 7-2 shows a summary of CRSS versus slip system for the micro-compression 4 μm samples.

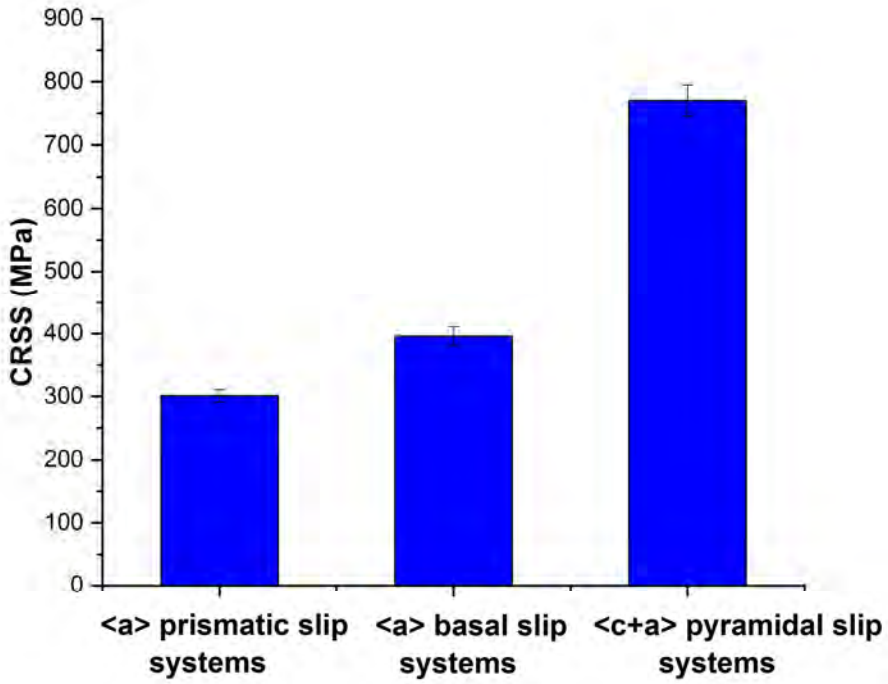

Load drops were observed both at the end of the elastic regime and at high stress compression. The load drops at larger strain were typically larger in magnitude, and shown by *in-situ* SEM to be associated with the formation of intense localized slip bands on the pillars.

Table 7-3 presents reported values of the proof stress for alpha/beta colonies in Ti-64, Ti–6242 and Ti–5–2.5, under the same compression test conditions and at the same deformation temperature.

Table 7-3 Summary of the proof stress of slip systems at room temperature for Ti alloys.

Materials / Compression testing	Basal (MPa)	Prismatic (MPa)	Pyramidal <c+a> (MPa)	Ref.
Polycrystal Ti64	998	903	2458	This study
Polycrystal Ti64	1020	906	1557	[13]
Polycrystal Ti64	1180	779	-	[111]
Polycrystal Ti64	-	960	2587	[2,4]
Polycrystal Ti–6242	824	-	-	[15,56,69]
Polycrystal Ti–5-2	-	755	-	[17]

Note: the proof stress for this study are obtained from fitting power law exponent

Table 7-3, compared the proof stress reported for basal, prismatic and pyramidal slip which shows reasonable agreement with a great deal of the previous work in this field given also much effect heat treatment has on Ti-64 . For example there are similarities between the proof stress by the basal and prismatic slips in this study and those described by Jones and Hutchinson [13] who report CRSS values for <a> slip on the basal and prismatic planes for

Ti-6Al-4V macrocompression. Although, the absolute value for pyramidal slip differs here from Jones and Hutchinson [13], their material was very stromgly textured. My results are very close to those described of Ding *et al*. [4] who tended to focus on the deformation mechanisms in microcantilever polycrystalline two-phase Ti-6Al-4V samples.

The CRSSs are controlled by plane spacing and magnitude of Burgers vector according to Peierls [127]. The <c+a> pyramidal plane has low packing density and a large Burgers vector. The <c+a> pyramidal is hard to activate (2–3 times harder than <a> slip due to its Burgers vectors, which is equal to $\left(\sqrt{(a)^2 + (c)^2} = 0.553 \text{ nm}\right)$.

7.2.3. The beta phase strengthening for <a> slip

Table 7-1 shows that the beta phase is somewhat weaker than <a> slip in the alpha phase, but the alpha/beta/alpha pillar are *stronger* than the alpha phase. Thus, the beta phase hinder dislocation glide at the α/β interfaces, which provide resistance to slip movement across the colony structure and in turn lead to an increase in the strength [15,17].

The slip transmission of <a> type dislocations on the basal plane in the alpha phase via a/2<111> dislocations on the (101) slip plane in the beta phase ideally should be coplanar. This planar arrangement should allow for the easy annihilation of residual dislocations and little work hardening.

However, micropillars with alpha/beta interfaces between alpha lamellae are considerably stronger than alpha crystals: for example a CRSS of 396 MPa for alpha/beta/alpha and 366 MPa for alpha columns for 4 μm pillar in basal slip. Therefore, the 30 MPa difference between alpha/beta/alpha pillars and single alpha phase pillar represents the additional strengthening from the beta phase as shown in Table 7-1. This additional strengthening confirms that the α/β interface is effective in impeding slip movement regardless of slip direction.

The same observations are found for prismatic slip. The CRSS for micropillars with a nominal diameter of 4 μm were 301 MPa (alpha/beta/alpha) and 268 MPa (single alpha phase). Thus 33 MPa corresponds to the additional strengthening from the beta phase.

This finding is consistent with past studies by Gong and Wilkinson [12], which found that the interfaces in Ti–6Al–4V cause an additional strengthening compared to the Ti–6Al matrix. However, the a_3 Burgers vector was selected in the alpha phase which does not have a close correspondence to any of the Burgers vectors within the bcc phase and so the interface is likely to generate a significant barrier to continued slip [12]. Lower strengthening contribution has been found here for the a_2 Burgers vectors in basal and prismatic slip, for which the Burgers vectors within the beta phase are more closely aligned [12].

The result is consistent also with those found by Suri *et al*. [17] during the room temperature deformation of single colonies of Ti–5Al–2.5Sn–0.5Fe oriented for prismatic slip. A similar

anisotropy was reported by Savage *et al.* [15,56,69] who showed that a_3 is stronger than $a_2$which is stronger than a_1 [15]. Salem and Semiatin [16] found the same thing.

The single most striking observation to emerge from the single alpha phase data comparison was that the CRSS was lower than for the alpha/beta/alpha phases, but still higher than for single beta phase. The alpha structure is harder than the more symmetrical beta structure partly because the addition of substitutional aluminium make the alpha phase harder.

The slight variations in the 0.2% flow stress levels from the same pillar size and orientation are due to differences in the initial dislocation densities. The dislocation density measured experimentally was reported to be $1.2 \times 10^{13}\ /m^2$, which obviously include the density of dislocations in the undeformed pillar.

We will be discussing the possible sources of anisotropy and strength of the α/β interfaces in accordance with our experimental results and also presenting our knowledge of the physical properties of the alpha and beta phases. Further discussion includes the magnitude and direction of accumulated residual dislocations found near the α/β interfaces, which has been suspected to be responsible for the observed strength [15].

Ankem and Margolin [128] have reported that the beta phase can be three times stronger than the alpha phase. However, the findings of the current study do not support Ankem and Margolin [128]. The CRSS for the beta phase is lower than for the alpha phase of the three selected orientations: thus beta phase cannot be harder than alpha phase. This also accords

with Suri *et al.*'s [17] earlier observations, which showed that the effective thickness of the β lath is actually larger in 'OA' than in 'OB' crystals. If the β phase were the stronger phase at lower temperatures [128], then this would suggest that OA might have a higher strength than OB.

Ankem and Margolin [129] reported that the influence of an applied stress on the alpha/beta interface generates elastic compatibility stresses which when resolved on to the prismatic systems could support or oppose the onset of glide in bicrystal and tricrystals. Ankem and Margolin [6,7,8] have categorised elastic interaction stresses at the alpha/beta interfaces with respect to various orientations of the stress axis into three compression axes (X_{20}, X_{29} and X_{58} [131]) and these are closely related to prismatic, pyramidal and basal planes respectively. However, the interaction of the elastic compatibility stresses with the primary slip systems in the alpha phase was found to be negligible for three grain orientations.

This seems to suggest that there may be other aspects that influence the interfacial dislocation transmission process.

Other possible causes of strength at the alpha/beta interface have been attributed to the details of the Burgers OR exists between the alpha and beta phase which has been extensively reported by researchers [1,5,6,7,8,9,10]. The Burgers OR suggests that there should be easy slip transmission across the alpha/beta interface. Figure 5-3 shows a selected area diffraction pattern from the two phases taken along $[0001]_a // [101]_\beta$. The Burgers vectors a_1 and b_1 in the alpha and beta phase are nearly parallel to each other with 0.7° misalignment between the two Burgers vectors having $[101]_\beta$ as the apparent rotation axis as discussed in Chapter 5. One setback attributed to the Burgers OR is that there is an a misorientation of about 11.5°,

$[0001]_\alpha$ between the slip vector a_2 in the alpha and b_2 in the beta phase. The third <a> type slip direction in the alpha phase does not have a closely aligned $< 111 >_\beta$ direction in the beta phase at all. It is clear from these simple geometrical considerations that the beta laths could provide a different resistance to slip transmission for these three slip directions due to a larger misalignment of the slip directions in the alpha phase and beta phase. The mechanism of this process was proposed to be similar to the prismatic plane in Ti-64. These three slip directions were always observed to be aligned at the same angle to the broad face of the beta-lath structure, as has been predicted using the invariant line construction [51,113].

The difference in the lengths of the Burgers vectors in the two planes has been found to contribute to the anisotropy and strength of the interface. There exists a difference in the lengths of the Burgers vectors in the two phases.

$$|\boldsymbol{b_\alpha}| \,/\, |\boldsymbol{b_\beta}| = 1.04$$

It has been argued (Suri *et al*., [17] and Savage *et al*., [15,56,69]) that the CRSS for the lamellar prismatic and basal systems depends on the magnitude of the residual dislocation that is left behind at the α/β interface after dislocation transmission. The magnitude of the residual dislocation is related to the misalignment of Burgers vectors in the α and β phases and can be calculated using the BOR. The argument is that leaving behind a larger net residual dislocation should result in a higher CRSS for that system. This hypothesis has been tested by Savage *et al*., [15,56,69] on a single colony crystal of the alpha/beta alloy Ti-6246. The alpha/beta morphology in these experiments were lamellar structure for basal and pyramidal planes, and while it is not a true lamellar structure for prismatic plane, the BOR is maintained with respect to the alpha/beta interface plane. The results of our research agree with the

residual dislocation argument reasonably well for the basal slip system that is expected to leave behind the net residual dislocation; also, the prismatic slip systems, which are suppose to have the lowest value of CRSS. It is accepted that the alpha/beta interface will lead to an increase in the rate of hardening, it is a sessile defect acting as an obstacle to dislocation motion.

Also lack of corresponding parallel slip planes in the hcp and bcc phases cause impedance of the slip transmission. Therefore, the soft deformation modes are described as the slip systems which either glide parallel to the α/β interface or have parallel slip planes in both the α and β phases.

7.2.4. Beta phase in <a> slip

The beta phase thickness in the microstructure (lamellar or equiaxed microstructure) is small (width of ≤ 2 μm) compared to alpha phase even after heat treatment and a very slow cooling rate. Therefore, two pillar diameters were tested to measure the mechanical properties in order to quantify how these microstructural changes contributed to the overall strength of the material as can be seen from the data in Table 7-1. Lower values of the CRSS value were measured for the beta phase in the basal and prismatic plane compared to the single alpha phase and alpha/beta/alpha phase. Symmetry of the beta crystal structure could be a major factor, if not the only one, causing to deform easier than a single alpha phase. Thus, the single beta phase has lower CRSS values than the single alpha and alpha/beta/alpha crystal structures as shown in Figure 7-3.

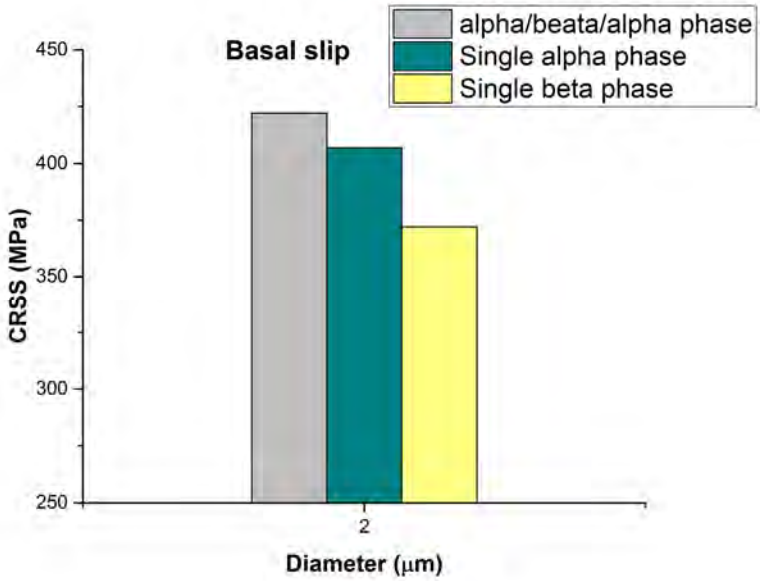
Basal slip
alpha/beata/alpha phase
Single alpha phase
Single beta phase
CRSS (MPa)
450
400
350
300
250
2
Diameter (μm)

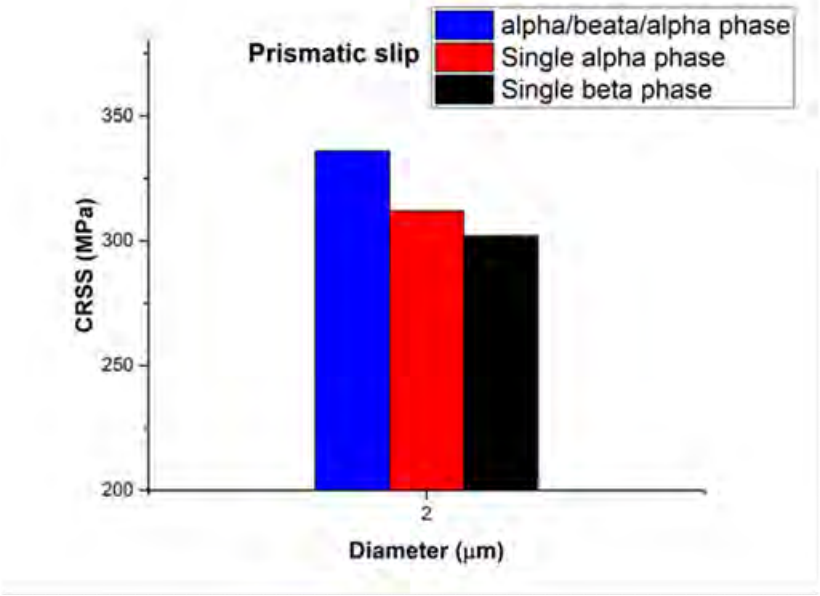
Prismatic slip
alpha/beata/alpha phase
Single alpha phase
Single beta phase
CRSS (MPa)
350
300
250
200
2
Diameter (μm)

Comparing the CRSSs for the beta phase in Table 7-1, the CRSS for the beta phase in a prismatic colony look smaller than the beta phase in the basal and, particularly, pyramidal colonies. It should be pointed out that the morphology of the beta phase in the microstructure nature of different slip systems is different, therfore one of the main reasons for the weaker beta phase in the prismatic plane than the basal and pyramidal plane. The morphology of the beta phase in the basal and pyramidal plane is closer to straight as they have a lamellar microstructure (see Figure 4-1 a), thus the preparation of the pure single beta phase pillar is less complex than the beta pillar from the prismatic colony. The beta morphology in the prismatic plane has an equiaxed microstructure (see Figure 4-1 b). Possibly there is some alpha sticking to it. In order to address this problem, more pillar and TEM analysis of pillar need to confirm single beta phase.

7.2.5. Pyramidal <c+a> slip

From Table 7-1, it is widely observed that the CRSS value for <c+a> slip is much greater than for <a> slip; also the exponent in the power law expression is larger than for the basal and prismatic planes.

Once frequent cross-slip has occurred in the alpha phase, the <c+a> dislocations will not be localised to one unique slip plane, as all the <c+a> slip systems are symmetrically compressed [4]. Consequently, more dislocations will nucleate and move. Thus, another reason making the CRSS value of <c+a> slip systems significantly higher than for <a> slip systems.

Comparing the mechanical data for alpha/beta/alpha and single alpha phase with the <c+a> pyramidal slip as summarised in Table 7-1, we can see that single alpha phase micro-pillars have a larger CRSS value than alpha/beta/alpha crystal which is in contrast to the <a> slip systems. This is because the beta phase is much weaker in this situation than alpha phase. For <a> slip, slip will always start from alpha because the sources are bigger, (and therefore softer). In the <c+a> situation, although this is still true, the enormous difference in strength between beta and alpha means that the slip will initiate in the beta phase and, despite the strengthening effect of the both interfaces, the overall strength of the ensemble will be less than that of single alpha phase.

Similar to the beta phase in the basal and prismatic plane, the beta phase is softer than the single alpha phase and alpha/beta/alpha phases in the pyramidal planes which is an interpretation of size-dependent strengthening as shown in Figure 7-4.

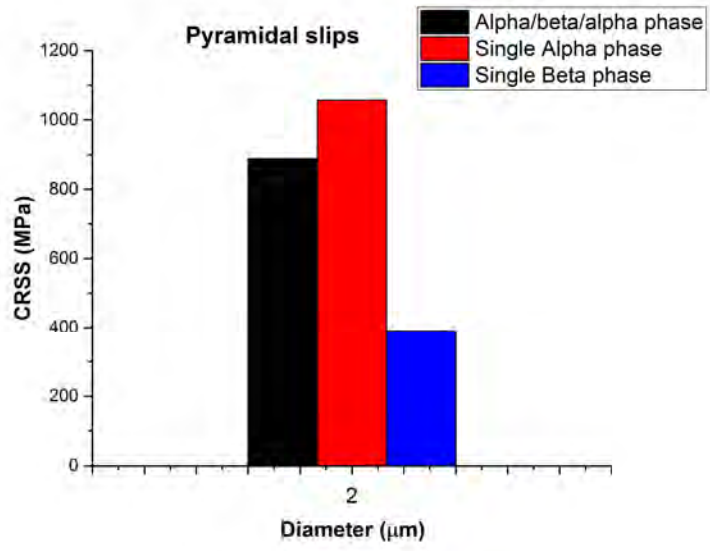

Figure 7-4 Summary of the CRSS for α/β/α, single α and β phase the micro-pillar with a nominal diameter of 2 μm for pyramidal slip systems

7.3. **How many slip bands?**

From the SEM micrographs in Chapter Four and Chapter Five, pillars selected to activate <a> dislocations in the basal plane usually show two parallel slip bands in the upper half of the crystal (see Figure 5-14). The number of slip bands and the positions of the slip bands can be attributed to the limited number of dislocation sources in these small specimens. Also, due to the crystal orientation and loading direction the normal to the basal plane is 40° from the loading direction $[\bar{1}5\bar{4}6]$ and from the taper of the column one would expect slip to initiate nearer the top of the column, therefore the slip bands are formed in the upper half of the pillar. For prismatic slip, more slip bands were distributed throughout the whole pillar, with different slip steps on parallel planes at the surface of the micropillar, despite the comparable pillar diameters and the strain level (between 6% and 7%). It would seem that the easier the slip (lower CRSS) the more slip bands there are, which seems reasonable.

The relation between the slip directions and the alpha/beta interface is consistent with the crystallographic orientation of the crystals (see Chapter 4 for details). The shear traces for the basal plane are at around 33° to the alpha/beta interface, while they are at a shallow angle ~ 80° to the beta laths for the prismatic slip. Thus, the shear bands are normal to the beta lath for prismatic slip. Only one set of slip traces is observed in the basal slip crystals which confirmed that only a single slip system is active even at the high strain levels due to the high Schmid factor.

For micropillars selected to activate <c+a> dislocations many slip bands are activated in different directions (see Figure 5-28) for a strain around 7%. All the <c+a> slip planes are equally stressed, but only a limited number is activated. The uncertainty over single or multiple slip planes can be attributed to the limited number of <c+a> dislocation sources in these small specimens, also from the unavoidable taper of the column since the stress at the top of the pillar is more than at the bottom of the pillar. The reason why the slip bands are formed right at the top of pillars is also because the pyramidal planes are at 47.5° to the loading direction [0001].

The effect of slip line spacing on the observed CRSS of basal, prismatic and pyramidal slip systems in single alpha/beta colonies of Ti-alloys was that CRSS increases sharply with decreasing slip line spacing, regardless of the microscopic slip plane. Chan *et al,* [59] state that more frequent cross slip events are likely to occur on closely spaced slip bands. These dislocation interactions are cited to be a source of significant strengthening in a colony structure. According to these arguments, the wide spacing between the intense, planar slip lines observed in this study for prism slip (see Figure 5-19) are likely to encourage little interaction between slip lines and thus minimal cross slip. The fine, not parallel slip lines observed for pyramidal slip (see Figure 5-28) are likely to result from frequent interactions between adjacent slip planes, resulting in frequent cross slip. These frequent interactions and cross slip events are likely to result in an increased CRSS value for microscopic plastic flow. This phenomenon again supports our argument that the difference in power law exponent between the three orientations is related to activation of single or multiple slip.

7.4. **Slip systems**

From the SEM images, it is possible to determine that the active <a> slip planes are $\{0001\}$ and $\{1\bar{1}00\}$ planes for basal and prismatic slip, respectively, and $\{10\bar{1}1\}$ for <c+a> pyramidal slip. Literature sources suggest that the Burgers vector in Ti alloys always has the form $^1/_3 < 11\bar{2}0 >$ and $^1/_3 \langle 11\bar{2}3 \rangle$ for <a> and <c+a> dislocations, respectively [2,4,13,14,17,56,62]. The active slip plane was identified by measuring the angle between the line of intersection with the loading axis. The slip planes visible in Figure 5-9 were identified, by the method described in Chapter Five for basal slip. The slip lines attributed to basal slip correspond to the slip system with the highest Schmid factor.

The active slip system is therefore believed to be $(0001)\,[1\bar{2}10]$ for a pillar with a loading direction $[\bar{1}5\bar{4}3]$. This slip system has the highest resolved shear stress for this colony orientation, with a Schmid factor of 0.47. From the crystallography of the colony crystal the basal slip plane (0001) should be at 45° to the surface. However, for the area scanned in Figure 5-9, the slip traces exhibit angles of less than 45° probably due to the somewhat diffuse nature of the slip trace, diffuse slip bands, possibly due to the slip taking place on a number of neighbouring slip planes, thus lowering the angle with the loading direction as shown in Figure 5-9 (a).

For a micropillar with loading direction $[01\bar{1}0]$ the slip system was found to be $(10\bar{1}0)\,[\bar{1}2\bar{1}0]$. That conforms with slip plane and EBSD data with regard to the loading direction as presented on the stereogram (see Figure 5-23). However, unactivated $(1\bar{1}00)$ slip

is commonly attributed to a small misalignment between the flat punch indenter and the pillar, causing uneven compression. Therefore, it is likely that the $(10\bar{1}0)\,[\bar{1}2\bar{1}0]$ system is the softest slip system activated at room temperature. This conclusion is in agreement with most literature sources [3,14,15,17,62,69,133].

Measurement of the incident angle of these slip lines with respect to the loading direction and the broad face of the alpha/beta interface also confirmed the activation of the <c+a> pyramidal slip systems. The corresponding surface morphology, displayed in Figure 5-28, reveals that two only slip planes are activated, even though all the <c+a> slip systems are equally stressed, see Table 4-1. There are, in Figure 5-28, only a limited set of slip bands obviously present for <c+a> pyramidal slip. The uncertainty over two or six slip planes can be attributed to a contact misalignment between the micropillars head and the flat punch and also a limited number of dislocation sources in these small specimens.

7.5. SEM measurements

7.5.1. Strain measurements

The plastic strain was measured in three different ways: (i) micromechanically (ii) $\frac{\delta l}{l}$ from SEM and (iii) size of slip steps (SEM). All three show good overall agreement. The total plastic strain imposed on the samples, as determined from the stress-strain curves for several tests((i) above), matches well with the plastic strain values determined by measuring the total change in the micropillar for all of the microcompression tests (see Figure 5-15) ((ii) above).

Table 5-3, Table 5-6 and Table 5-9 list the uniaxial strain measured by SEM of some typical pillars of each phase and orientation, before and after testing. These measurements were made by SEM using a precision x-z translation stage equipped with SEM/FIB tilt corrections. Therefore, the SEM images can be used to calculate the strain caused by slip traces at the pillars along loading directions, which is in general agreement with the strain worked out from the stress-strain curves.

7.5.2. The number of dislocations

For basal slip we can also determine the number of dislocations in each slip band. If one follows the profile across the yellow arrows on the pillar D (see Figure 5-17), a total step of 965 nm is measured which corresponds to about 3275 <a> type dislocations with 2710 dislocations leaving the pillar. Thus 560 <a> type dislocations remain inside the pillar. It has also been confirmed that the dislocation density increases using FIB-TEM.

The sums of the magnitudes of the entrance slip steps (Table 5-3 and Table 5-9) agree well with the strains reported. Dislocation counts from slip steps for prismatic slip (Table 5-6), however are not consistent with the expected value, because the initiation and end of the slip steps were not very obvious on pillar 19 (see Figure 5-24 (b)).

<c+a> dislocations have the same characteristics as the <a> basal dislocation. The entrance slip steps (higher up the pillar) are larger than the exit slip steps and thus some dislocations remain inside a pillar (see Figure 5-28). Thus, again the dislocations initiate at the top of the pillar. The dislocations then move through the pillar till they reach the free surface on the

other side of the pillar (in principle). This is consistent with the results and the pillar taper angle. Pillars with a taper will start to deform in the top of the pillar and then gradually down.

The analysis of slip step heights and numbers of dislocations remaining in the foil afforded by the micropillar structure allows a quantitative geometric analysis of the applied strain. This level of quantification for micropillar sliding is an attractive feature of this approach.

7.5.3. Slip direction

Slip directions can be determined from the EBSD data, which allows the orientation of the pillar to be determined in 3D space and form SEM micrographs (see section 5.3.4).

The slip directions were found, using EBSD, to be $< 11\bar{2}0 >$ type, for basal and prismatic planes consistent with the literature (see [13,15,16,56]). Once again, all of the possible slip systems have $1/3 < 11\bar{2}0 >$ Burgers vectors; the active slip system is determined to be $(0001)1/3[1\bar{2}10]$ for the basal plane and $(10\bar{1}0)\ 1/3[11\bar{2}0]$ for the prismatic plane. These slip directions attributed to basal and prismatic slip correspond to the slip systems with the highest Schmid factor. Furthermore, the number of dislocations at the top of pillar is higher than in the middle of the pillar which indicates the dislocations coming from the top of the pillar to the middle (i.e strongly consistent with directions for highest Schmid factor). For pyramidal planes the slip directions were found to be of $1/3 < 11\bar{2}3 >$ type. Again, these are possible slip directions identified for pyramidal planes in Ti64. The active slip systems are

therefore those reported by Jones and Hutchinson [13] [$(10\bar{1}1)\ {}^{1}/_{3}\ [\bar{2}113]$ in Ti-64, therefore $(1\bar{1}01)\ {}^{1}/_{3}\ [\bar{2}113]$, $(1\bar{1}01)\ {}^{1}/_{3}\ [\bar{1}2\bar{1}3]$ and $(10\bar{1}1)\ {}^{1}/_{3}\ [\bar{1}\bar{1}23]$]. Compression along the c-axis and the resultant cross-slip made identification of the slip systems more difficult. The uncertainty over the identity of all possible slip systems can be attributed to a contact misalignment between the micropillars head and the flat punch and also to a limited number of dislocation sources in these small specimens. For that reason, it is tentatively suggested that they be interpreted in terms of dislocations initiating from the beta phase.

7.6. TEM studies

7.6.1. The correlation between the mechanical behaviour and the SEM results with the TEM results

An attempt will be made in this section to confirm a correlation between the mechanical behaviours and the SEM characteristics of the three different crystal orientations with the deformation microstructure observed by the TEM. The mechanical behaviour of the three different orientations can be summarised as follows. <a> dislocations have a slightly straighter dislocation movement and lower CRSS than <c+a> dislocations. Additionally, the slip systems with the highest Schmid factor for <a> dislocations were activated. <c+a> dislocations experience symmetrical stresses on all planes of the pyramidal planes, but a limited number of planes is activated because of the misalignment between the micropillar head and the flat punch and also because of a limited number of dislocation sources in these small specimens as has been mentioned earlier.

Turning now to the experimental evidence on dislocation transmission through the narrow beta lath, it appears to happen readily for example Figure 6-8 shows an example of the interaction of these a_2 dislocations with the entry face of the beta lath structure of the pillar D. The (a) dislocations are a_2 the (b) are as b_2 ($a_2 // b_2$) which inplies a nearly one to one correspondence of screw dislocations through the beta lath. A shearing event of the beta lath is shown in Figure 6-28 and at higher magnification in Figure 6-31. Within the beta phase bowing b_2 ($b_2 = {}^{a}/_{2}\,[\bar{1}11]$) dislocations are visible on the primary $(101)_\beta$ slip plane, which is well aligned with the $(0001)_\alpha$.

The positive correlation between the slip system with the highest Schmid factor (see Table 4-1) and the SEM and TEM characteristics shows activation of a_2 dislocations in the basal plane for pillar D, which has a highest Schmid factor. The Burgers vector is confirmed by SEM and TEM to be also almost parallel to $b_2 = {}^{a}/_{2}\,[\bar{1}11]$ in $(101)_\beta$. Further analysis found strong evidence of the Burgers orientation relationship between ($a_2 // b_2$) when the Burgers vectors were analysed in the alpha and beta phases; this conforms well with the SEM analysis. Another important finding was that the slip planes and slip directions for <a> and <c+a> dislocations analysed by the TEM are in a very strong correlation with the SEM analyses.

These findings of the current study are consistent with the TEM studies of Ding *et al.* [2–4] who shed some additional light on deformation processes in $\{1\bar{1}00\}$ oriented Ti alloy microcantilever.

7.6.2. Dislocation sources and their operation

In order to understand the observed deformation microstructure and the dislocation processes causing the transmission through alpha/beta interface during microcompression, one needs to

understand the dislocation sources and their operation in the Ti-64 alloy. Figure 6-4 shows a montage of the alpha/beta grains in an undeformed micropillar specimen. There are only a few grown-in dislocation present in the alpha grains, but a lot of dislocations in the beta phase. Furthermore, Figure 6-26 and Figure 6-27 (basal slip) show that the dislocations are coming from the alpha phase from the right side (entry side) and going through the beta phase, and then the exit side as indicated by the yellow arrow in Figure 6-26 (d to f). Both the incoming and outgoing dislocations were found by diffraction contrast analysis to be <a> type with Burgers vectors $\mathrm{b} = \pm {}^{\mathrm{a}}/_{3}\,[1\bar{2}10]_{\mathrm{in}}$ and $\mathrm{b} = \pm {}^{\mathrm{a}}/_{3}\,[1\bar{2}10]_{\mathrm{out}}$ and $\mathrm{b} = \pm {}^{\mathrm{a}}/_{3}\,[11\bar{2}0]_{\mathrm{out}}$, respectively. Similarly a_2 screw dislocations are observed on the opposite side of the alpha/beta interface, indicating that slip transmission through the beta lath has occurred. This supports the concept that the transmitted dislocation is accommodated in the alpha/beta interface and a new dislocation is generated and emitted by the beta interface to achieve the slip transfer.

Further, during *in-situ* deformation in the SEM via <a> slip, it was observed that there were no dislocation sources operating inside the beta laths initially, very different from the cracking or initiation of slip bands founds in the alpha grain. Therefore, dislocations were found to be generated from the edge of the pillar. All the SEM micrographs show <a> slip bands in the alpha/beta/alpha phase; no slip bands started from the beta to the alpha. That indicates that the <a> dislocations start from alpha and propagate to the beta interface. The logical explanation for the dislocation sources in the alpha/beta/alpha phase is as follows. The alpha phase is harder than the beta phase, so when the indenter compresses on the top of the pillar, the beta cannot deform plastically before the alpha phase as it is between two alpha grains. Another interesting feature to note from Figure 6-25 is that the dislocations are elongated in the screw

orientation even at the source. This is due to the low mobility of screw segments, as will be discussed in section 7.6.4. Therefore, this suggests that the dislocation sources have to be present in the alpha grain in this alloy, at least initially, and then the dislocations move toward the alpha/beta interface, crossing through the beta phase to the new alpha phase, as shown in Figure 6-25.

7.6.3. Slip transmission

The strong anisotropies in the CRSS values indicate that grain to grain slip transmission processes are quite different under different orientations in compression. In order for transmission to occur through alpha/beta grain boundary, residual dislocations with a total vector that accounts for the differences between the incoming and outgoing slip systems must be deposited at the alpha/beta interface.

We can use a simple model proposed by Mills and Neeraj [133] and [134] to explain the observed movement of dislocations across the alpha-beta interface on the basal plane. Figure 7-5 (a-g) are schematics showing the possible mechanism of slip transfer across the alpha/beta interface for basal slip. Figure 7-5 (a) shows an a_2 dislocation moving towards the alpha-beta interface. It impinges on the side face of the alpha/beta interface because of the relative misorientation between the slip directions of the alpha and beta phases.

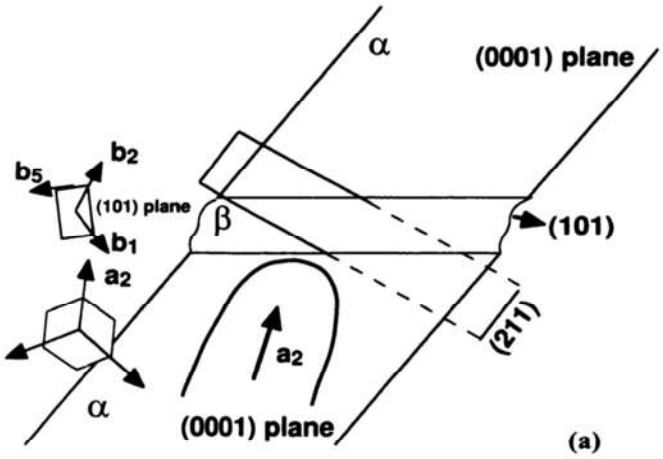

Figure 7.5 (a) (Caption later)

It is also interesting to note that a slip trace close to the entry side of the beta lath of the pillar D deviates away from the interface (indicated by the red arrow in Figure 6-8 (a)) which showed a tendency to follow the alpha/beta interface.

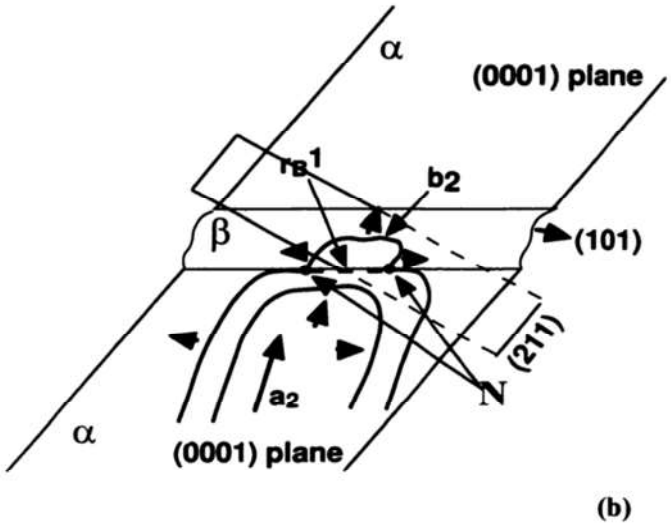

Figure 7.5 (b) (Caption later)

The propagation nature of the slip movement suggests the tendency of the screw dislocations to follow the alpha/beta interface. As is shown in the TEM observations (see Figure 6-25), the slip movement can be associated with to frequent cross slip events, both within the grain interiors and also due to the presence of the alpha/beta interface (presumably due to the internal beta laths).

Dislocations continue to move across the beta phase as b_2 dislocations, leaving a residual dislocation (rb1) at the interface as shown in Figure 7-5 (b). There are two possible slip planes in the beta phase, namely the (101) primary slip plane and the (211) secondary slip plane shown in Figure 7-5 (b and C).

Figure 7-5 (b) and (c) consider the initial portion of the transmission process where the b_2 dislocations lie on the (101) slip plane. Initially the b_2 dislocation lies on the (101) slip plane as it is parallel to the alpha basal plane.

An example of an experimental observation of $b_2$dislocations loops lying on the (101) plane is shown in Figure 6-31 and (purple arrows) Figure 6-32. When the $b_2$dislocation grows, the node N is pulled along the interface and b_2 impinges at the alpha-beta interface on the other side. As more dislocation loops arrive at the exit face, pile up of b_2 dislocations occurs, which eventually leads to the formation of an a_2 dislocation at the alpha phase as shown in Figure 7-5 (c). A residual dislocation (-rb1), which is equivalent to the previous residual dislocation (rb1) but with opposite sign, is left on the exit face as can be seen (blue arrow) in Figure 6-28.

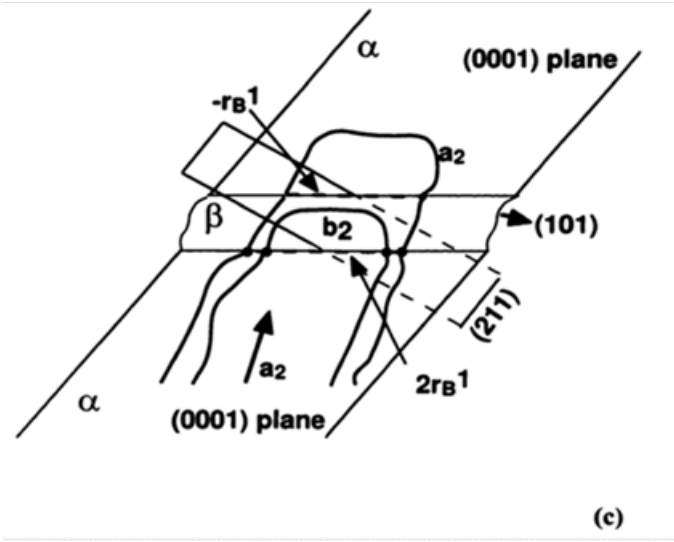

Figure 7.5 (c) (Caption later)

This is experimentally observed in Figure 6-17 where the outward motion of the b_2 screw dislocations seems to drag the nodes along.

Figure 6-28 to Figure 6-31 show a series of TEM micrographs from the beta lath region with all of the g vectors taken within the beta phase. Significant shearing of the beta laths has been observed in two regions of the pillar D, with residual dislocation content present in the alpha phase. A second dislocation loop is also seen approaching the alpha/beta interface at the exit face. Pile-up configurations shown in Figure 6-26 (e and f) (Red arrow) and Figure 6-27 (b) are commonly observed in pillar D suggesting that the slip within the alpha phase is planar in nature.

It is also interesting to note here that such a transmission process will lead to a one to one correspondence of the screw segments in the alpha phase on either side of the beta lath. In

both Figure 6-17 and Figure 6-18, a one to one correspondence of the screw dislocation segments on either side of the beta laths is observed. This provides additional support for a planar transmission process from the basal to the (101) plane across the alpha/beta interface.

Figure 7-5 (d) schematically illustrates a possible cross-slip of a b_2 screw dislocation onto a (211) type plane. An example of a cross-slip process can be seen in Figure 6-28 and also in Figure 6-31. As the cross-slip advances across the (211) plane, the edge segments run outwards as illustrated in Figure 7-5 (d).

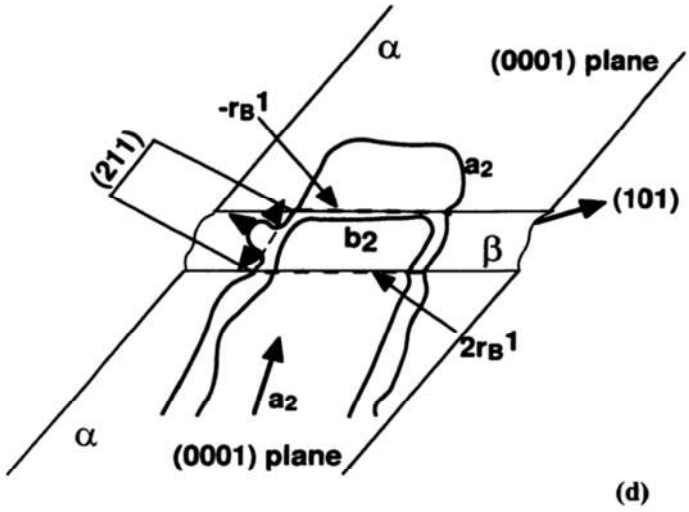

Figure 7.5 (d) (Caption later)

The edge segments of the dislocation loop unzip the b_2 screw segment and the node N is formed in the interface plane. The node N connects the b_2 dislocation on the (211) plane with the a_2 dislocation on the (0001) plane as shown in Figure 7-5 (e). A number of such examples can be seen in the experimental observations shown in Figure 6-17 and Figure 6-28 to Figure

6-31. It is also interesting to note that the node N cannot move in the interface plane. As the b_2 dislocation on the (211) plane expands, it deposits b_2 dislocation segments along the interface. Also, the (211) plane is not parallel to the (0001) plane, and therefore it is not favourable for b_2 dislocations to transmit to the (0001) plane. Instead, the b_2 dislocation on the (211) plane continues to glide until it cross-slips back to the (101) plane (second cross-slip event) as shown in Figure 7-5 (f).

This b_2 dislocation in (101) now impinges on the alpha-beta interface on both the entry and exit side and the outward motion of the a_2 screw dislocations also results in the formation of segments along the alpha/beta interface. The a_2 dislocation segments seen along the alpha/beta interface in Figure 6-17 and Figure 6-18 can possibly be due to this process.

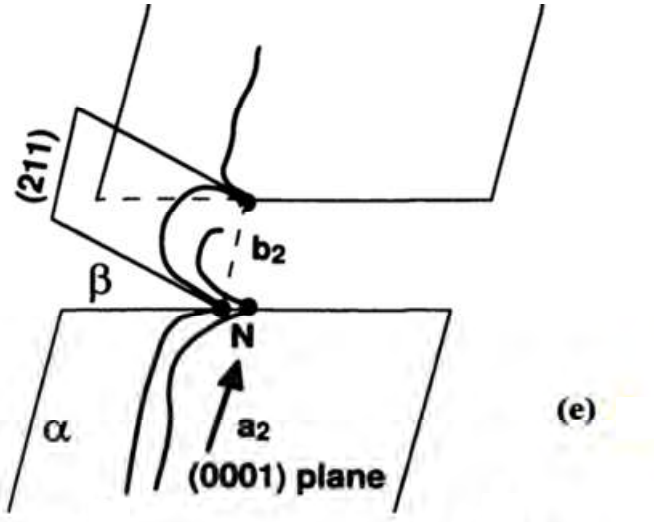

Figure 7.5 (e) (Caption later)

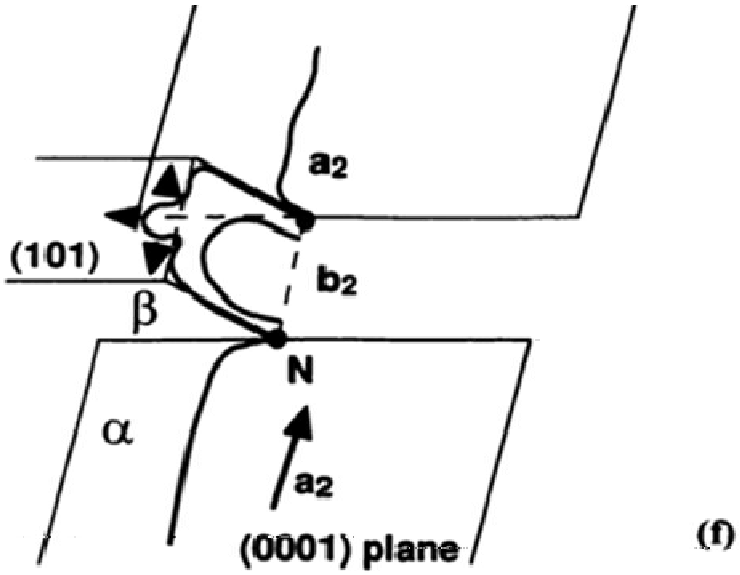

Figure 7.5 (f) (Caption later)

Figure 7-5 (g) shows a schematic for the dislocation on the (101) impinging on the alpha/beta interface, where it can form a_2 dislocations and leave the beta lath on both the entry and the exit side.

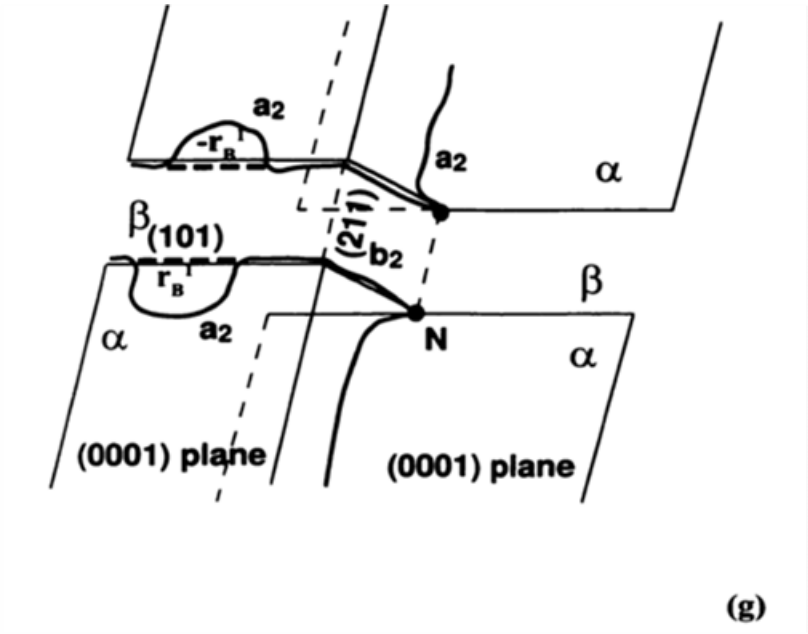

(g)

The a_3 residual matrix dislocations on the exit face of the alpha/beta interface is seen as a red line in Figure 6-24 and provides additional support for the mechanism suggested by Mills and Suri [17]. It is also interesting to point out here that these a_3 residual matrix dislocations also lie on the basal slip plane and their interaction with the a_2 dislocations can cause strengthening to occur as shown in Figure 7-6.

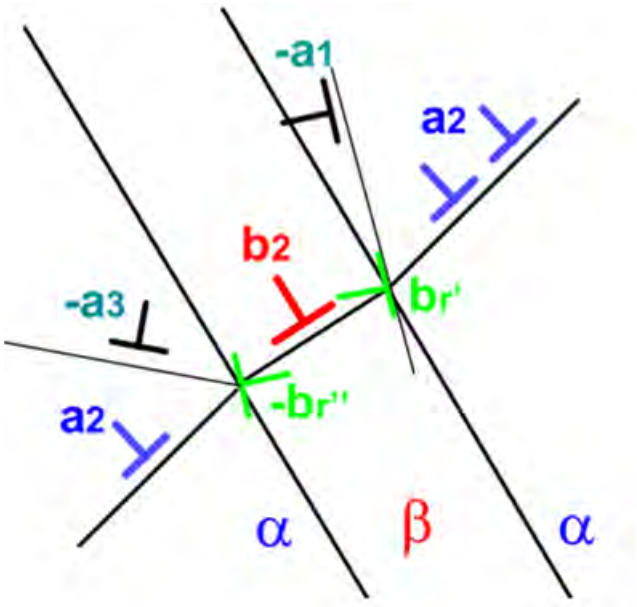

Figure 7-6 Schematic of the slip transmission and residual dislocation formation for Pillar D. Passage of a_2 dislocations causes the residual content of $2b_{r'}$ at the entry side and $-b_{r''}$ at the exit side. The a_1 dislocation at the entry side react with the next dislocation to form a_3 at the exit side. Reproduced from Mills [17].

The observed slip lines and observed mechanical behaviour are consistent with such a slip transfer mechanism in pillar D and pillar E.

Residual dislocation content is apparent near the alpha/beta interfaces within the alpha phase. The residual dislocations in Figure 6-24 appear to be not a_2 dislocations, but this observation cannot be confirmed from this series of micrographs due to the close proximity of the dislocations to the alpha/beta interface. g.b analysis confirms that the residual dislocations observed near the alpha/beta interface in the basal slip sample are typical a_3 and a_1 types, in contrast to the <c+a> dislocations, which are found to be in tangled configurations due to cross-slip (see Figure 6-35).

Studies of the dislocation structures within the beta phase were only performed on basal slip samples (pillar D) which were oriented for a_2 basal slip. Significant $a/2 < 111 >$ dislocation activity was observed on $\{101\}$ and $\{211\}$ planes in the a_2 basal slip oriented sample. Frequent large b_2 dislocation pileups were observed on these planes at the exit alpha/beta interface. An intrinsic non-Schmid effect has been observed due to the inherent crystal symmetry of BCC metals, specifically the fact that the $\{211\}$ cross slip plane is not a mirror plane. This gives rise to an asymmetry in the $a/2 < 111 >$ directions on these planes. Slip on these $\{211\}$ cross slip planes is likely subject to the intrinsic non-Schmid effects mentioned above, and should contribute to any observed compression asymmetry. Dense dislocation tangles of $a/2 < 111 >$ dislocations were observed upon significant slip transmission through the beta laths in the pillar D. These tangled structures imply that frequent cross slip has occurred on $\{101\}$ and $\{211\}$ planes. Again, these cross slip events will exhibit similar intrinsic non-Schmid effects. However, they are less likely to contribute to a microscopic observed compression asymmetry since they are occurring on many different $\{211\}$ cross slip planes in compression to achieve the complex tangled structure.

7.6.4. The mobility of edge and screw a-type dislocations

Figure 6-18 shows a bright field TEM micrograph taken with $g = 01\bar{1}1$ near the $[1\bar{1}01]$ zone axis. Long line lengths of the screw character a_2 dislocations are visible with less frequent observations of the more mobile edge segments, as indicated on the micrograph illustrated in Figure 6-25.

The role of the mobility of <a> type ($b = a/3 < 2\bar{1}\bar{1}0 >$) dislocations may be attributed to the <a> type dislocation core being spread onto basal or prism slip planes. The explanation for this effect may lie in the nature of the core structure of the <a> screw dislocation. These non-planar core effects have been studied by several groups. The frictional stresses opposing glide are increased due to a non-planar spreading of the screw dislocation core onto either the basal and prism planes [135–138] or the prismatic and first order pyramidal planes [67,135,139]. Naka *et al*. [67] performed a detailed dislocation structure analysis on alpha Ti single crystals with varying interstitial contents. Naka *et al*. [67] investigated the dislocation structure after deformation as well as during *in-situ* straining experiments in the TEM. They observed a high mobility for edge segments of $a/3 < 1\bar{2}10 >$ dislocations on prism planes, but long line lengths of screw character dislocations with apparently very low mobility. They believe that this difference in mobility is due to a non-planar spreading of the $a/3 < 1\bar{2}10 >$ screw core onto the prism and pyramidal planes. They cite three reasons for the likelihood of a dislocation core effect: the observed deviation from Schmid's law for alpha Ti single crystals, the observed cross slip of screw dislocations from prism to pyramidal planes, and the strong temperature dependence and high lattice resistance for $a/3 < 1\bar{2}10 >$ screw mobility on prism planes.

Similar observations on the lower mobility screw character dislocations were found in pillar D and pillar E (basal plane). The beta phase where {110} phase has a misorientation with the basal plane in the alpha phase, obstructed the movement of dislocations and hence most of the dislocations remaining in the pillar D were of screw dislocation. That indicates that the edge dislocations can move faster than screw dislocations in the basal plane.

The absolute mobility of the non-planar core structure of <a> type dislocations in the alpha phase and beta phase presented above could be expected to be strongly dependent on the nature of the applied stress.

7.6.5. TEM Observations of the Broad and Side faces

Based on the observed deformation microstructure, intersections between screw pile-ups of <a> type dislocations are the most common dislocation intersections. Since, the basal and beta planes are almost parallel to each other with a small misorientation between them (for details see Chapter Five).

The possibility is that the basal slip bands are established first. The lead dislocation will bow between the pinning points due to the jogs and can expand on many different slip planes. In such a process the slip band will become diffuse after the intersection with the alpha/beta interface. Dislocations parallel to slip trace (0001) can be seen around the slip bands (red line in Figure 6-8 a). When the slip band intersects the beta laths, the dislocations will have to cut through the beta lath domains on parallel planes. This could be a difficult process. The dislocation segment lying on the original slip plane will be able to cut preferentially through

the alpha/beta interface because it can be assisted by the self stresses of the dislocations in the pile-up, which will be maximised on this plane. Due to the motion of that segment, the applied stress on the basal plane can assist in the lateral motion of the jogs. This process will help the dislocation to straighten itself on the original glide plane. The trailing dislocations will be biased to continue on the original glide plane, because of the glide on the preferred slip system that has taken place in the original slip plane. The slip band will remain planar even after such an intersection process a beta lath.

This is consistent with this research. In the pillar D and pillar E <a> basal plane and pillar 18 and 19 prismatic planes. Hence, <a> basal and prismatic slip bands intersections with the beta laths provide significant strengthening in many instances compared to the single alpha phase and same volume fraction in the pillar. Moreover, slip band intersections in Figure 6-8 that showed the dislocations on intersecting slip bands are able to cut through the beta phase and continue propagating, bowing around the bands as suggested earlier in section 7.6.3. In contrast, the slip bands in pyramidal planes are probably established first in the beta phase and then intersect with the alpha phase as shown in Figure 6-35. This is because the beta phase is much weaker in the <c+a> situation than the alpha phase. The enormous difference in strength between beta and alpha means that the slip will initiate in the beta phase first then move across alpha phase.

7.7. **Pyramidal <c+a> slip systems**

Schmid factor values were very helpful in assessing the possible deformation substructures in the grains investigated. Figure 6-35 shows the SF values (consequently, the resolved shear stress) to be very low for any <a> type $1/3 < 11\bar{2}0 >$ slip. These grains are oriented at [0001] direction and hold very low resolved shear stress values for <a>-types $1/3 < 11\bar{2}0 >$ slip on (0001) basal and $\{10\bar{1}0\}$ prismatic planes which therefore cannot be activated. This is consistent with the increased <c+a> activity in this grain. On the other hand, Figure 6-36 to Figure 6-37 shows activated <c+a> dislocations on $\{\bar{1}011\}$ pyramidal slip systems that can confirm our results about micromechanical properties considering that the CRSS values for <c+a> pyramidal slip planes were higher than for <a> slip planes. In addition, the presence of multiple <c+a> slip in this grain would result in cross slip between pyramidal planes, therefore, the SEM slip plane analysis are confirmed as there are many slip bands generated on the surface of the pillar (see Figure 5-28) and the distance between slip bands were very small compared with the pillars compressed to activate <a> dislocations.

Chapter Eight

8. Conclusions

1. Judicious alloying to slow the kinetics of the α-phase on cooling across the β transus and control of the cooling rates allows considerable control of the α/β microstructural length scale, with slow kinetics leading to fine microstructures and high strength. Microstructural variations caused by a range of the cooling rates from the β phase field are investigated. For most cooling rates ranging from 0.5 °C/min to 1 °C/min, the observed microstructure consists of both the equiaxed and lamellar microstructures; the equiaxed microstructure is dominant for slower cooling rates. The equiaxed and lamellar microstructures are normally formed in the middle of the same grains, which depends on the morphology of the beta phase in the colony.

2. Measurements of the CRSS values from the proof stresses for the three different orientations exposed a strong dependence of mechanical behaviour on colony orientation and activated slip system. Based on these results, for polycrystal Ti-6Al-4V (hexagonal closed packed structure) the critical resolved shear stress (CRSS) for $\{10\bar{1}0\} < 1\bar{2}10 >$ prismatic slip is lower than that $\{0001\} < 1\bar{2}10 >$ basal slip, and much lower than that for $\{10\bar{1}1\} < \bar{2}113 >$ pyramidal <c+a> slip.

3. Another important aspect to consider in the colony study is the relative strength of the alpha/beta interfaces for <a> type dislocations. Based on these results, it becomes clear that for any successful modelling of the micro-compression effect in the alpha/beta titanium alloys to proceed efficiently, a full understanding of the mechanical behaviour of the single alpha and beta phase and the alpha/beta/alpha crystal has important implications for the deformation behaviour in these alloys at room temperature. This includes ascertaining the relative ease of slip and deformation rates for the basal, prism and pyramidal slip in alpha, aligned-alpha and single transformed beta colonies under constant strain rate.

4. Micropillars are a more effective method of measuring true stress and strain curves than the microcantilever methods used. This is achieved by converting load and displacement measurements of the pillar cross-section and height, although the strains are typically overestimated owing to deformation of the top of the pillar which effectively acts as a blunt punch.

5. In Ti alloys, an obstacle controlled material, an increase in the dislocation density was observed at smaller sample sizes; such densities was sufficient in explaining the observed flow stresses based on a Taylor based model.

6. Unlike BCC and FCC materials, HCP materials (Ti-64) are less size-sensitive to the flow stress. Thus the (n) power law exponent for HCP is less pronounced than for BCC and FCC materials.

7. The plastic strain corresponding to the dislocations in the micro-sample can be measured in three different ways: (i) micromechanically (ii) $\frac{\delta l}{l}$ from SEM and (iii) size of slip steps (SEM). All three show good overall agreement.

8. Dislocation analyses indicated that the deformation in individual grains conformed to the Schmid factor analysis where slip primarily occurs on those slip systems where RSS (SF) values are highest.

9. A higher CRSS value was observed for the a_2 basal slip than the prismatic slip sample tested in compression. In this orientation, there exists a significant misorientation between the $a/3\ [1\bar{2}10]$ and $a/2\ [\bar{1}11]$ slip vectors (11.1° and a 5.1% mismatch in magnitude). Large $a/2 < 111 >$ dislocation pileups were observed on the (101) primary slip plane and (211) cross slip planes within the β-lath in TEM foils prepared from the a_2 basal slip sample (pillar D).

10. A higher CRSS value is found in pillars with a beta lath (for <a> dislocations). The non-planarity and cross-slip from (101) onto the (211) plane are likely the cause of

more difficult slip transmission from alpha to beta then to alpha again. This non-planarity of slip also prevents annihilation of residual dislocation content within the β-phase. This is evidenced by the dislocation pile-ups at the alpha/beta interfaces whereby annihilation of residual dislocation content was found through the presence of a_1 and a_3 residual dislocations.

Chapter Nine

9. Future Work

Several fundamental questions regarding room temperature deformation behaviour of titanium alloys remain answered by this research, but several new phenomena have been discovered and new questions have been raised which need to be resolved in order to develop a better understanding of the deformation behaviour in these alloys.

1. Given the importance of the grain and the colony scale factor and the beta and alpha lath thicknesses, a dislocation analysis of the grain/grain boundary, the colony/colony interface and the lath/colony interface should provide valuable information on the important slip mechanisms controlling the compression behaviour.

2. Future work could also consider the slip system anisotropy of the CRSS and stress–strain behaviour for possible <a> slip systems and the <c+a> pyramidal slip system during cold working and hot working of Ti–6Al–4V using uniaxial compression testing. Such studies should help improve our understanding of the deformation characteristics of these alloys, and may provide additional directions to pursue for improving the properties of these alloys.

3. Towards a better understanding of the effect of sample geometry, taper-free cylindrical pillars using a more accurate AUTOFIB milling process (Auto lathe milling), need to be fabricated to reflect a more accurate interpretation of the microcompression tests. This should provide a more accurate interpretation of the CRSS for micro-compression tests.

4. The fabrication of Ti-64 nano-crystals smaller than 1 μm is needed to study the stress flow and subsequent Hall-Petch relationship behaviour at nano sizes. Coupling TEM with these results, insights into the relationship between plasticity and the transformation may be achieved.

5. Regarding FIB induced ion damage, does the Ga ion damage from the FIB machining play a significant role on the strengthening of Ti-6Al-4V or not? It is suggested that future work should investigate through TEM analysis the ion damage layer to determine the nature of the strain fields associated with gallium ions in titanium. This could reveal the difference in mechanical behaviour between different orientations in titanium micro-crystals.

6. It was suggested that tension/compression asymmetry may be related to the mobility of <a> type dislocations, and to the generation and motion of <c+a> dislocations. It is suggested that the study of possible tension/compression asymmetry, and "non-Schmid" effects in general, may be an extremely interesting topic for atomistic

simulation. The role of <c+a> dislocations in this effect, and their generation near grain boundaries, should be more thoroughly understood. Experiments exploring the tension/compression asymmetry as a function of grain size may be valuable for exploring more fully the role of <c+a> dislocations.

References

[1] V. A. Joshi, Titanium alloys : an atlas of structures and fracture features, Taylor & Francis Group, Boca Raton, 2006.

[2] R. Ding, J. Gong, A.J. Wilkinson, I.P. Jones, Transmission electron microscopy of deformed Ti – 6Al – 4 V micro-cantilevers, Philosophical Magazine. 92 (2012) 3290–3314.

[3] R. Ding, J. Gong, A.J. Wilkinson, I.P. Jones, A study of dislocation transmission through a grain boundary in hcp Ti–6Al using micro-cantilevers, Acta Materialia. 103 (2016) 416–423.

[4] R. Ding, J. Gong, A.J. Wilkinson, I.P. Jones, 〈c+a〉 Dislocations in deformed Ti–6Al–4V micro-cantilevers, Acta Materialia. 76 (2014) 127–134.

[5] D.M. Dimiduk, M.D. Uchic, T.A. Parthasarathy, Size-affected single-slip behavior of pure nickel microcrystals, Acta Materialia. 53 (2005) 4065–4077.

[6] M.D. Uchic, D.M. Dimiduk, A methodology to investigate size scale effects in crystalline plasticity using uniaxial compression testing, Materials Science and Engineering: A. 400–401 (2005) 268–278.

[7] M.D. Uchic, P. a. Shade, D.M. Dimiduk, Micro-compression testing of fcc metals: A selected overview of experiments and simulations, Jom. 61 (2009) 36–41.

[8] M.D. Uchic, P.A. Shade, D.M. Dimiduk, Plasticity of Micrometer-Scale Single Crystals in Compression, Annual Review of Materials Research. 39 (2009) 361–386.

[9] A.S. Schneider, C.P. Frick, B.G. Clark, P.A. Gruber, E. Arzt, Influence of orientation on the size effect in bcc pillars with different critical temperatures, Materials Science and Engineering A. 528 (2011) 1540–1547.

[10] A.S. Schneider, B.G. Clark, C.P. Frick, P.A. Gruber, E. Arzt, Effect of orientation and loading rate on compression behavior of small-scale Mo pillars, Materials Science and Engineering A. 508 (2009) 241–246.

[11] J.H. Wu, W.Y. Tsai, J.C. Huang, C.H. Hsieh, G.R. Huang, Sample size and orientation effects of single crystal aluminum, Materials Science and Engineering: A. 662 (2016) 296–302.

[12] J. Gong, A.J. Wilkinson, A microcantilever investigation of size effect, solid-solution strengthening and second-phase strengthening for 〈a〉 prism slip in alpha-Ti, Acta Materialia. 59 (2011) 5970–5981.

[13] I. P. Jones and W.B. Hutchinson, Stress-state dependence of slip in Titanium-6Al-4V and other H.C.P. metals, 29 (1981).

[14] J. Gong, A.J. Wilkinson, Anisotropy in the plastic flow properties of single-crystal α titanium determined from micro-cantilever beams, Acta Materialia. 57 (2009) 5693–5705.

[15] M.F. Savage, J. Tatalovich, M.J. Mills, Anisotropy in the room-temperature deformation of α – β colonies in titanium alloys: role of the α – β interface, Philosophical Magazine. 84 (2004) 1127–1154.

[16] A. a. Salem, S.L. Semiatin, Anisotropy of the hot plastic deformation of Ti–6Al–4V single-colony samples, Materials Science and Engineering: A. 508 (2009) 114–120.

[17] S. Suri, G.B. Viswanathan, T. Neeraj, M.J. Mills, Room temperature deformation and single-colony crystals of an α/β titanium alloy, Acta Materialia. 47 (1999) 1019–1034.

[18] S. Banerjee and P. Mukhopadhyay, Phase Transformations Examples from Titanium

and Zirconium Alloys, First ed., Elsevier, Oxford, 2007.
[19] L. Gerd and W. C. James, Engineering Materials and Processes: Titanium, 2nd editio, Springer-Verlag, New York, 2003.
[20] L. Christoph and P. Manfred, Titanium and Titanium Alloys: Fundamentals and Applications, WILEY-VCH, Weinheim, 2003.
[21] J. Matthew J. Donachie, Titanium A technical Guide, First Ed., ASM INTERNATIONAL, Metals Park, Ohio, 1988.
[22] D. M. Hill, Microstructure and mechanical properties of titanium alloys reinforced with titanium boride, The Ohio State University, 2006.
[23] S.K. Kar, Modeling of Mechnical Properties in Alpha/Beta Titanium Alloys, (2005).
[24] Z. Fan, The β---ω transformation during room temperature aging in rapidly solidified Ti-6A1-4V alloy, Scripta Metallurgica et Materialia. 31 (1994) 1519–1524.
[25] Jacek Chraponski and Wojciech Szkliniarz, Quantitative metallography of two-phase titanium alloys, Materials Characterization. 46 (2001) 149–154.
[26] G. Lutjering, Property optimization through microstructural control in titanium and aluminum alloys, Materials Science and Engineering. A263 (1999) 117–126.
[27] E. Lee, MICROSTRUCTURE EVOLUTION AND MICROSTRUCTURE / MECHANICAL PROPERTIES RELATIONSHIPS IN α + β TITANIUM ALLOYS, The Ohio State University, 2004.
[28] G. Lutjering, Influence of processing on microstructure and mechanical properties of (α + β) titanium alloys, Materials Science and Engineering. A243 (1998) 32–45.
[29] G. Lutjering, J. Albrecht, Influence of Cooling Rate and β Grain Size on the Tensile Properties of (α+β) Ti -Alloys, in: Proceedings of the 8th World Titanium Conference, 1995: p. 1995.
[30] M.W. Kearns and C.M.Ward Close., Structure property relationships in centrifugally cast IMI 550 (Ti-4Al-4Mo-2Sn-0.5 Si), SAMPE Journal. 22 (1986) 7–11.
[31] H. Iargolin, P. Farrar, The physical metallurgy of titanium alloys, Ocean Engng. 1 (1969) 329–345.
[32] M. Peters, Titanium and Titanium Alloys, 2003.
[33] E. P. Barry, Three-dimensional reconstruction of microstructures in α + β titanium alloys, The Ohio State University, 2008.
[34] T.R. Bieler, S.L. Semiatin, The origins of heterogeneous deformation during primary hot working of Ti – 6Al – 4V, International Journal of Plasticity. 18 (2002) 1165–1189.
[35] D. Hull and D. J. Bacon, Introduction to Dislocations, Fifth Edit, Elsevier Ltd, Oxford, 2011.
[36] B. E. O. Hall, The Deformation and Ageing of Mild Steel: III Discussion of Results, Proceedings of the Physical Society. Section B. 64 (1951) 747.
[37] N.J. Petch, The cleavage strength of polycrystals, J. Iron Steel InstInst. 174 (1953) 25–28.
[38] J.G. Sevillano, Intrinsic and Extrinsic Size Effects in Plasticity by Dislocation Glide, MRS Proceedings. 653 (2000) 1–12.
[39] R.A. Jago, N. Hansen, Grain size effects in the deformation of polycrystalline iron, Acta Metall. 34 (1986) 1711–1720.
[40] K.H. Chia, K. Jung, H. Conrad, Dislocation density model for the effect of grain size on the flow stress of a Ti–15.2 at.% Mo β-alloy at 4.2–650K, Materials Science and Engineering: A. 409 (2005) 32–38.
[41] K. Kako, E. Kawakami, J. Ohta, M. Mayuzumi, Effects of Various Alloying Elements on Tensile Properties of High-Purity Fe – 18Cr –(14 – 16) Ni Alloys at Room

Temperature, Materials Transactions. 43 (2002) 155–162.
[42] L. Anand, J. Gurland, Effect of Internal Boundaries on the Yield Strengths of Spheroidized Steels, Metallurgical Transactions AA. 7 A (1976) 191.
[43] M. Meyers, K. Chawla, Mechanical Behavior of Materials, Cambridge University Press, 2009.
[44] W.G. Burgers, The process of transition of the cubic-body-centered modification into the hexagonal-close-packed modification of zirconium, Physica I. 1 (1933) 561–586.
[45] T. Bieler, R.L. Goetz, S.L. Semiatin, Anisotropic plasticity and cavity growth during upset forging of Ti–6Al–4V, Materials Science and Engineering: A. 405 (2005) 201–213.
[46] Y. Guo, Microstructure and texture characterisation of linear friction welding of Ti-6Al-4V and Ti-6Al-2Sn-4Zr-6Mo, University of Birmingham., 2013.
[47] M.R. Plichtai, H. Aaronson, Crystallography and morphology of the β -- ζ , massive transformation in Ag-26 a/o A1, Acta Meiallurgica. 28 (1980) 1041–1057.
[48] V. PEROVIC and G. C. WEATHERLY', the β to α transformation zr-2 . 5 wt % nb alloy, Acta Metallurgica. 37 (1989) 813–821.
[49] T. FURUHARA and H. 1. AARONSON, computer modeling of partially coherent b.c.c. :h.c.p. boundaries, Acta Metall, Mater. 39 (1991) 2857–2872.
[50] T. Furuhara, T. and Ogawa, T. Maki, Atomic structure of interphase boundary of an a precipitate plate in a β Ti [sbnd] Cr alloy, Philosophical Magazine Letters. 72 (1995) 175–183.
[51] U. Dahmen, Orientation relationships in precipitation systems, Acta Metallurgica. 30 (1982) 63–73.
[52] M.Yiwen Mou and H. I. Aaronson, O-lattice modeling of ledged, partially coherent b.c.c.:h.c.p. boundaries, Acta Metall, Mater. 42 (1994) 2133–2144.
[53] S. Zherebtsov, G. Salishchev, S. L. Semiation, Loss of coherency of the alpha/beta interface boundary in titanium alloys during deformation, Philosophical Magazine Letters. 90 (2010) 903–914.
[54] M. Cabibbo, S. Zherebtsov, S. Mironov, G. Salishchev, Loss of coherency and interphase α/β angular deviation from the Burgers orientation relationship in a Ti–6Al–4V alloy compressed at 800 °C, Journal of Materials Science. 48 (2012) 1100–1110.
[55] T. Furuhara, J. M. Howe, H. I. Aaronson, Interphase boundary structures of intragranular proeutectoid α plates in a hypoeutectoid Ti-Cr alloy, Acta Metall, Mater. 39 (1991) 2873–2886.
[56] M.F. Savage, T. Neeraj, M.J. Mills, Observations of Room-Temperature Creep Recovery in Titanium Alloys, Metallurgical and Materials Transactions A. 33 (2002).
[57] T. Neeraj, M.F. Savage, J. Tatalovich, L. Kovarik, R.W. Hayes, M.J. Mills, Observation of tension–compression asymmetry in α and titanium alloys, Philosophical Magazine. 85 (2005) 279–295.
[58] D. Bhattacharyya, G.B. Viswanathan, R. Denkenberger, D. Furrer, H. L. Fraser, The role of crystallographic and geometrical relationships between α and β phases in an α/β titanium alloy, Acta Materialia. 51 (2003) 4679–4691.
[59] K. Chan, C. Wojcik, D. Koss, Deformation of an alloy with a lamellar microstructure: experimental behavior of individual widmanstatten colonies of an α-β titanium alloy, Metallurgical Transactions A. 12 (1981) 1899–1907.
[60] B. Bhattacharya, M. Niewczas, Work-hardening behaviour of Mg single crystals oriented for basal slip, Philosophical Magazine. 91 (2011) 2227–2247.
[61] D. Shechtman, D. G. Brandon, Orientation dependent slip in polycrystalline titanium,

Journal of Material Science. 8 (1973) 1233–1237.
[62] J. Gong, A.J. Wilkinson, Micro-cantilever testing of ⟨a⟩ prismatic slip in commercially pure Ti, Philosophical Magazine. 91 (2011) 1137–1149.
[63] G.B. Viswanathan, E. Lee, D.M. Maher, S. Banerjee, H.L. Fraser, Direct observations and analyses of dislocation substructures in the α phase of an α/β Ti-alloy formed by nanoindentation, Acta Materialia. 53 (2005) 5101–5115.
[64] M.F.Savage, Microstructural and mechanistic study of low temperature creep and dwell fatigue in single colony alpha/beta titanium alloys, The Ohio State University, 1999.
[65] Y.M. and M.K. H. Numakura, <11-23> {10-11}Slip in titanium polycrystals at room temperature, Scripta Metallurgica. 20 (1986) 1581–1586.
[66] T.B. Britton, F.P.E. Dunne, A.J. Wilkinson, On the mechanistic basis of deformation at the microscale in hexagonal close-packed metals, The Royal Society. A471 (2015).
[67] S. Naka, A. Lasalmonie, P. Costa, L.P. Kubin, The low-temperature plastic deformation of α-titanium and the core structure of a-type screw dislocations, Philosophical Magazine A. 57 (1988) 717–740.
[68] M.H. Yoo, S.R. Agnew, J.R. Morris, K.M. Ho, Non-basal slip systems in HCP metals and alloys: Source mechanisms, Materials Science and Engineering A. 319–321 (2001) 87–92.
[69] M.. Savage, J. Tatalovich, M. Zupan, K.. Hemker, M.. Mills, Deformation mechanisms and microtensile behavior of single colony Ti–6242Si, Materials Science and Engineering: A. 319–321 (2001) 398–403.
[70] J. A. M.Perilla, J. G. Sevillano, Two-dimensional sections of the yield locus of a Ti-6%Al-4%V alloy with a strong transverse-type crystallographic alpha-texture, Materials Science and Engineering A. 201 (1995) 103–110.
[71] F. Bridier, P. Villechaise, J. Mendez, Analysis of the different slip systems activated by tension in a alpha/beta titanium alloy in relation with local crystallographic orientation, Acta Materialia. 53 (2005) 555–567.
[72] T. Dick, G. Cailletaud, Fretting modelling with a crystal plasticity model of Ti6Al4V, Computational Materials Science. 38 (2006) 113–125.
[73] J. Gong, T.B. Britton, M.A. Cuddihy, F.P.E. Dunne, A.J. Wilkinson, ⟨a⟩ Prismatic, ⟨a⟩ basal, and ⟨c+a⟩ slip strengths of commercially pure Zr by micro-cantilever tests, Acta Materialia. 96 (2015) 249–257.
[74] S. Rawat, N. Mitra, Compression twinning and structural phase transformation of single crystal titanium under uniaxial compressive strain conditions: Comparison of inter-atomic potentials, Computational Materials Science. 126 (2017) 228–237.
[75] P.J. Guruprasad, A.A. Benzerga, Size effects under homogeneous deformation of single crystals: A discrete dislocation analysis, Journal of the Mechanics and Physics of Solids. 56 (2008) 132–156.
[76] a. Akhtar, E. Teghtsoonian, Prismatic slip in Alpha-titanium single crystals, Metallurgical and Materials Transactions A. 6 (1975) 2201–2208. doi:10.1007/BF02818644.
[77] J.C. Williams, R.G. Baggerly, N.E. Paton, Deformation behavior of HCP Ti-Al alloy single crystals, Metallurgical and Materials Transactions A. 33 (2002) 837–850.
[78] E. Tarleton, D.S. Balint, J. Gong, A.J. Wilkinson, A discrete dislocation plasticity study of the micro-cantilever size effect, Acta Materialia. 88 (2015) 271–282.
[79] D.M. Norfleet, D.M. Dimiduk, S.J. Polasik, M.D. Uchic, M.J. Mills, Dislocation structures and their relationship to strength in deformed nickel microcrystals, Acta Materialia. 56 (2008) 2988–3001.

[80] Q. Sun, Q. Guo, X. Yao, L. Xiao, J.R. Greer, J. Sun, Size effects in strength and plasticity of single-crystalline titanium micropillars with prismatic slip orientation, Scripta Materialia. 65 (2011) 473–476.
[81] J. Zhang, K.T. Ramesh, S.P. Joshi, Stochastic Size Dependent Slip-Twinning Competition in Hexagonal Close Packed Single Crystals, Modelling and Simulation in Materials Science and Engineering. 22 (2014) 1–24.
[82] H. Fei, A. Abraham, N. Chawla, H. Jiang, Evaluation of Micro-Pillar Compression Tests for Accurate Determination of Elastic-Plastic Constitutive Relations, Journal of Applied Mechanics. 79 (2012) 61011.
[83] H. Fei, A. Abraham, N. Chawla, H. Jiang, Evaluation of Micro-Pillar Compression Tests for Accurate Determination of Elastic-Plastic Constitutive Relations, 2012.
[84] J.R. Greer, J.T.M. De Hosson, Plasticity in small-sized metallic systems: Intrinsic versus extrinsic size effect, Progress in Materials Science. 56 (2011) 654–724.
[85] J.R. Greer, W.C. Oliver, W.D. Nix, Size dependence of mechanical properties of gold at the micron scale in the absence of strain gradients, Acta Materialia. 53 (2005) 1821–1830.
[86] S.W. Lee, S.M. Han, W.D. Nix, Uniaxial compression of fcc Au nanopillars on an MgO substrate: The effects of prestraining and annealing, Acta Materialia. 57 (2009) 4404–4415.
[87] C.A. Volkert, E.T. Lilleodden, Size effects in the deformation of sub-micron Au columns, Philosophical Magazine. 86 (2006) 5567–5579.
[88] L. Jiang, N. Chawla, Mechanical properties of Cu6Sn5 intermetallic by micropillar compression testing, Scripta Materialia. 63 (2010) 480–483. doi:10.1016/j.scriptamat.2010.05.009.
[89] N.A. Mara, J. Crapps, T.A. Wynn, K.D. Clarke, A. Antoniou, P.O. Dickerson, et al., Microcantilever bend testing and finite element simulations of HIP-ed interface-free bulk Al and Al–Al HIP bonded interfaces, Philosophical Magazine. 93 (2013) 2749–2758.
[90] S.M. Han, M. a. Phillips, W.D. Nix, Study of strain softening behavior of Al–Al3Sc multilayers using microcompression testing, Acta Materialia. 57 (2009) 4473–4490. doi:10.1016/j.actamat.2009.06.007.
[91] P.J. Phillips, M.J. Mills, Fine-scale structure of dislocations and debris in deformed Ni-based superalloy, Philosophical Magazine. 93 (2013) 37–41.
[92] Z.W. Shan, R.K. Mishra, S. a Syed Asif, O.L. Warren, A.M. Minor, Mechanical annealing and source-limited deformation in submicrometre-diameter Ni crystals., Nature Materials. 7 (2008) 115–9.
[93] D.M. Norfleet, D.M. Dimiduk, S.J. Polasik, M.D. Uchic, M.J. Mills, Dislocation structures and their relationship to strength in deformed nickel microcrystals, Acta Materialia. 56 (2008) 2988–3001.
[94] D. Catoor, Y.F. Gao, J. Geng, M.J.N.V. Prasad, E.G. Herbert, K.S. Kumar, et al., Incipient plasticity and deformation mechanisms in single-crystal Mg during spherical nanoindentation, Acta Materialia. 61 (2013) 2953–2965.
[95] E. Lilleodden, Microcompression study of Mg (0001) single crystal, Scripta Materialia. 62 (2010) 532–535.
[96] D.J. Lloyd, S. a. Court, Influence of grain size on tensile properties of Al-Mg alloys, Materials Science and Technology. 19 (2003) 1349–1354.
[97] W. a. Soer, J.T.M. De Hosson, A.M. Minor, J.W. Morris, E. a. Stach, Effects of solute Mg on grain boundary and dislocation dynamics during nanoindentation of Al–Mg thin

films, Acta Materialia. 52 (2004) 5783–5790.
[98] E. Lilleodden, Microcompression study of Mg (0001) single crystal, Scripta Materialia. 62 (2010) 532–535.
[99] M.H. Yoo, J.R. Morris, K.M. Ho, S.R. Agnew, Nonbasal deformation modes of HCP metals and alloys: Role of dislocation source and mobility, Metallurgical and Materials Transactions A. 33 (2002) 813–822.
[100] Q. Yu, Z.-W. Shan, J. Li, X. Huang, L. Xiao, J. Sun, et al., Strong crystal size effect on deformation twinning., Nature. 463 (2010) 335–8.
[101] W.S. Choi, B.C. De Cooman, S. Sandlöbes, D. Raabe, Size and orientation effects in partial dislocation-mediated deformation of twinning-induced plasticity steel micro-pillars, Acta Materialia. 98 (2015) 391–404.
[102] C.M. Byer, B. Li, B. Cao, K.T. Ramesh, Microcompression of single-crystal magnesium, Scripta Materialia. 62 (2010) 536–539.
[103] W.D. Nix, H. Gao, indentation size effects in crystalline materials : a law for strain gradient plasticity, Journal Mech. Phys. Solids. 46 (1998) 411–425.
[104] C. Motz, D. Weygand, J. Senger, P. Gumbsch, Micro-bending tests: A comparison between three-dimensional discrete dislocation dynamics simulations and experiments, Acta Materialia. 56 (2008) 1942–1955.
[105] T.A. Parthasarathy, S.I. Rao, D.M. Dimiduk, M.D. Uchic, D.R. Trinkle, Contribution to size effect of yield strength from the stochastics of dislocation source lengths in finite samples, Scripta Materialia. 56 (2007) 313–316.
[106] J.R. Greer, W.D. Nix, Nanoscale gold pillars strengthened through dislocation starvation, Physical Review B - Condensed Matter and Materials Physics. 73 (2006) 1–6.
[107] H. Zhang, B.E. Schuster, The design of accurate micro-compression experiments, 54 (2006) 181–186.
[108] G. Dehm, H.P. Wörgötter, S. Cazottes, J.M. Purswani, D. Gall, C. Mitterer, et al., Can micro-compression testing provide stress–strain data for thin films?, Thin Solid Films. 518 (2009) 1517–1521.
[109] D. Kiener, C. Motz, G. Dehm, Micro-compression testing : A critical discussion of experimental constraints, 505 (2009) 79–87.
[110] D. Raabe, D. Ma, F. Roters, Effects of initial orientation , sample geometry and friction on anisotropy and crystallographic orientation changes in single crystal microcompression deformation : A crystal plasticity finite element study, 55 (2007) 4567–4583.
[111] T.-S. Jun, G. Sernicola, F.P.E. Dunne, T.B. Britton, Local deformation mechanisms of two-phase Ti alloy, Materials Science and Engineering: A. 649 (2016) 39–47.
[112] C.P. Frick, B.G. Clark, S. Orso, A.S. Schneider, E. Arzt, Size effect on strength and strain hardening of small-scale [1 1 1] nickel compression pillars, 489 (2008) 319–329. doi:10.1016/j.msea.2007.12.038.
[113] and G.B.V. M.J. Mills, D.H. Hou, S. Suri, orientation relationship and structure of alpha/beta interfaces in conventional titanium alloys, in: Boundaries and Interfaces in Materials, TMS, Warrendale, PA, 1998: pp. 295–301.
[114] J. E. Bailey, P. B. Hirsch, The dislocation distribution, flow stress, and stored energy in cold-worked polycrystalline silver, Philosophical Magazine. 5 (1960) 485–497.
[115] D.B. Williams, C. Barry Carter, Transmission Electron Microscopy, 2009.
[116] M.H. Loretto, Electron Beam Analysis of Materials, 1984.
[117] J. Kacher, I.M. Robertson, In situ and tomographic analysis of dislocation/grain

boundary interactions in α-titanium, Philosophical Magazine. 94 (2014) 814–829.
[118] M.H. Loretto, R.E. Smallman, Defect analysis in electron microscopy, in: 1975: pp. 1–144.
[119] X. Zhao, fabrication and plastic deformation of copper at small scales, University of Birmingham, 2014.
[120] D. Kiener, A.M. Minor, Source Truncation and Exhaustion : Insights from Quantitative in situ TEM Tensile Testing, (2011) 3816–3820.
[121] S.H. Oh, M. Legros, D. Kiener, G. Dehm, In situ observation of dislocation nucleation and escape in a submicrometre aluminium single crystal, Nature Materials. 8 (2009) 95–100. doi:10.1038/nmat2370.
[122] Q. Sun, Q. Guo, X. Yao, L. Xiao, J.R. Greer, J. Sun, Size effects in strength and plasticity of single-crystalline titanium micropillars with prismatic slip orientation, Scripta Materialia. 65 (2011) 473–476.
[123] J.Y. Kim, D. Jang, J.R. Greer, Insight into the deformation behavior of niobium single crystals under uniaxial compression and tension at the nanoscale, Scripta Materialia. 61 (2009) 300–303.
[124] A.S. Schneider, D. Kaufmann, B.G. Clark, C.P. Frick, P.A. Gruber, R. Monig, et al., Correlation between critical temperature and strength of small-scale bcc pillars, Physical Review Letters. 103 (2009) 1–4.
[125] S.-W. Lee, W.D. Nix, Size dependence of the yield strength of fcc and bcc metallic micropillars with diameters of a few micrometers, Philosophical Magazine. 92 (2012) 1238–1260.
[126] S.I. Rao, D.M. Dimiduk, T. a. Parthasarathy, M.D. Uchic, M. Tang, C. Woodward, Athermal mechanisms of size-dependent crystal flow gleaned from three-dimensional discrete dislocation simulations, Acta Materialia. 56 (2008) 3245–3259.
[127] R. Peierls, The size of a dislocation, Proceedings of the Physical Society. 52 (1940) 34–37.
[128] S. Ankem, H. Margolin, Alpha-Beta Interface Sliding in Ti-Mn Alloys, Metallurgical Transactions A. 14 (1983) 500–503.
[129] S. Ankem, H. Margolin, A rationalization of stress-strain behavior of two-ductile phase alloys, Metallurgical Transactions A. 17 (1986) 2209–2226.
[130] A. Jaworski Jr, S. Ankem, Influence of the second phase on the room-temperature tensile and creep deformation mechanisms of α-β titanium alloys, part II: Creep deformation, Metallurgical and Materials Transactions A. 37 (2006) 2755–2765.
[131] S. Ankem, H. Margolin, The role of elastic interaction stresses on the onset of plastic flow for oriented two ductile phase structures, Metallurgical Transactions A. 11 (1980) 963–972.
[132] V.S. Deshpande, A. Needleman, E. Van Der Giessen, Plasticity size effects in tension and compression of single crystals, Journal of the Mechanics and Physics of Solids. 53 (2005) 2661–2691.
[133] M.J. Mills, Microstructural and Mechanistic Study of Primary Creep in Titanium Alloys at Lower Temperatur, 1998.
[134] Neeraj Srinivas Thirumalai, low temperature creep of titanium alloys: microstructure, deformation mechanisms and modeling, The Ohio State University, 2000.
[135] M. Sob and J. Kratochvil, theory of strengthening of alpha titanium by interstitial solutes, Chekhoslovatskii Fizicheskii Zhurnal. 25B (1975) 872.
[136] V. Vitek, M. Igarashi, Core structure of 1/3 <1120> screw dislocations on basal and prismatic planes in h.c.p. metals: An atomistic study, Philosophical Magazine A. 63

(1991) 1059–1075.
[137] M. Aoki, D. Nguyen-Manh, D.G. Pettifor, V. Vitek, Atom-based bond-order potentials for modelling mechanical properties of metals, Progress in Materials Science. 52 (2007) 154–195.
[138] Takllshi Goto, Shinji Ando and Hideki Tonda, Computer Simulation for a-Type Dislocation Core Structures in hcp Metals Using the Molecular Dynamics Method, Journal of the Japan Institute of Metals. 64 (2000) 391–394.
[139] T. Sakai, E. Fine, plastic deformation of ti-al single crystals in prismatic slip, Acta Meiallurgica. 22 (1974) 1359–1372.

Appendix

Appendix A: The alpha phase has the hexagonal structure with Burgers orientation relationship to the body centre cubic beta matrix.

The Burgers orientation relationship between HCP and BCC.

No.	α phase (HCP)	β phase (BCC)	Rough equivalent
1	(0001)	1.1243, 0, 1.1243	(101)
2	$\frac{1}{3}[0\bar{1}10]$	0.71, -1.411, -0.71	$\frac{1}{2}[1\bar{2}\bar{1}]$
3	$\frac{1}{3}[\bar{1}010]$	0.71, 0.71, -1.411	$\frac{1}{2}[11\bar{2}]$
4	$\frac{1}{3}[\bar{1}100]$	-1.411, 0.71, 0.71	$\frac{1}{2}[\bar{2}11]$
5	$\frac{1}{3}[\bar{2}110]$	-0.5774, -0.5774, 0.5774	$\frac{1}{2}[\bar{1}\bar{1}1]$
6	$\frac{1}{3}[1\bar{2}10]$	0.6422, -0.4185, -0.64223	$\frac{1}{2}[5\bar{3}\bar{5}]$
7	$\frac{1}{3}[11\bar{2}0]$	-0.06488, 0.9958, 0.06488	$\frac{1}{2}[010]$
8	$(0\bar{1}11)$	0.9161, –0.9428, –0.0266	$(1\bar{1}0)$
9	$(01\bar{1}1)$	–0.0266, 0.9428, 0.9161	(011)
10	$(\bar{1}011)$	0.1030, –1.0487, 0.7863	
11	$(10\bar{1}1)$	0.7863, 1.0487, 0.1030	
12	$(\bar{1}101)$	–0.3683, –0.1059, 1.2577	
13	$(1\bar{1}01)$	1.2577, 0.1059, –0.3683	
14	$\frac{1}{3}[\bar{2}113]$	0.5469, –0.5773, 1.7016	$\frac{1}{2}[1\bar{1}3]$

15	$\frac{1}{3}[1\bar{2}13]$	1.7665, –0.4184, 0.4820	$\frac{1}{2}[4\bar{1}1]$
16	$\frac{1}{3}[1\bar{2}1\bar{3}]$	-0.4821, -0.4821, -1.7665	$\frac{1}{2}[\bar{1}\bar{1}\bar{4}]$
17	$\frac{1}{3}[11\bar{2}3]$	1.0594, 0.9957, 1.1891	$\frac{1}{2}[111]$
18	$\frac{1}{3}[2\bar{1}\bar{1}3]$	1.7016, 0.5773, –0.5469	$\frac{1}{2}[311]$
19	$\frac{1}{3}[\bar{1}2\bar{1}3]$	0.4822, 0.4184, 1.7665	$\frac{1}{2}[114]$
20	$\frac{1}{3}[\bar{1}\bar{1}23]$	1.1891, –0.9957, 1.0594	$\frac{1}{2}[1\bar{1}1]$
21	$\frac{1}{3}[\bar{1}5\bar{4}6]$	0.9, 1.83, 3.6	$\frac{1}{2}$ $[124]$
22	$\frac{1}{3}[4\bar{5}13]$	3, -0.261, -0.742	$\frac{1}{2}$ $[12\bar{1}\bar{3}]$

Appendix B: The pillar has been tilted 52° about the slip direction/Burgers vector. In order to identified the active slip plane the angle between the line of intersection with the loading axis has been measured:

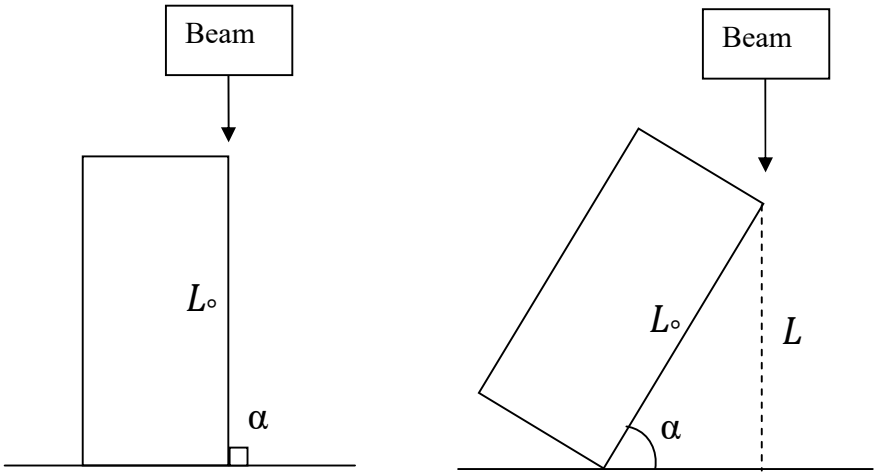

$$L_\circ = L \,.\sin\alpha \qquad (1)$$

$L_\circ$: is the initial length for pillar

L: is the obvious length for pillar

α : is the tilting angle along the x axis

D: Diameter of pillar

θ :obvious angle between slip plane and diameter.

$H_\circ$: is the initial height between slip plane and diameter

H: is the obvious diameter

φ : is the inclination corrected angle after tilting.

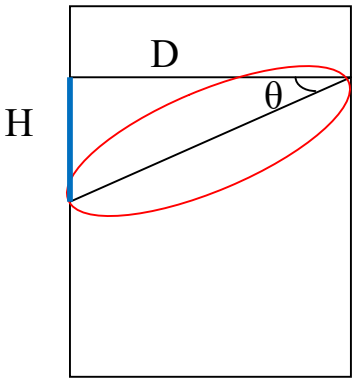

$$\tan\varphi = \frac{H}{D} \qquad (2)$$

From equation (1)

$$H = \frac{H_\circ}{\sin \alpha} \qquad (3)$$

$$\tan \theta = \frac{H_\circ}{D} \qquad (4)$$

Substitution equations (3) and (4) in to equation (2)

$$\varphi = \tan^{-1}\left(\frac{H_\circ / \sin \alpha}{H_\circ / \tan \theta}\right)$$

$$\varphi = \tan^{-1}\left(\frac{\tan \theta}{\sin \alpha}\right)$$